THE UNIVERSITY
OF ADELAIDE
AUSTRALIA

Department of Mechanical Engineering

On the Structure and Mixing of a Jet in Crossflow

Ph.D. Thesis

Philip Robert Edward Cutler

July 2002

Abstract

In the current thesis a comparison is made between the mixing and structure of two forms of transverse jet. The configurations investigated were the elevated jet and the flush-mounted jet. These cases shared identical flow conditions so that the difference lay in the presence or absence of a flat wall adjacent to the jet exit. Although the elevated case of the transverse jet occurs in many industrial applications it has received far less attention than the flush-mounted jet. In addition, a detailed comparison of the mixing and structures of the two flows had not been previously attempted. Volumetric flow measurement techniques and dye visualisation were used to investigate the differences between the two flow cases. The volume techniques allowed the mean three-dimensional concentration field and instantaneous flow structures to be captured and analysed on various planes within the flow.

The most significant finding from the study was that the elevated jet forms one of two distinct structures based on the velocity ratio and Reynolds number of the flow. At lower velocity ratios and Reynolds numbers the elevated jet structure is substantially different to a flush-mounted jet at the same flow conditions. As the Reynolds number or velocity ratio is increased the elevated jet undergoes a transition, and evolves into a flow that appears very similar to the flush-mounted jet at the same flow conditions. The difference in structure of the elevated jet affects both the characteristics of the jet (i.e. trajectory, lateral spreading) as well as the mixing. The interaction of the wall boundary layer circulation and the leading edge jet shear was also investigated, in addition to which the mechanism by which the jet shear layer roll-up occurs has been clarified.

Table of Contents

ν	Kinematic viscosity (m^2/s)
Q	Flow rate (m^3/s)
θ	Boundary layer momentum thickness (mm)
r	Internal jet pipe radius (mm)
ρ	Density (kg/m^3)
S_o	Distance from the image plane to the focal plane (mm)
τ	Time scale
U_j	Jet bulk velocity (m/s)
U_∞	Free stream (crossflow) velocity (m/s)
x	Spatial coordinate in the streamwise direction (direction of crossflow)
y	Spatial coordinate in the vertical direction (direction of jet)
z	Spatial coordinate in the spanwise direction

Non-Dimensional Parameters

R	Velocity ratio = $\frac{U_j}{U_\infty}$
Re	Crossflow Reynolds number = $\frac{\rho U_\infty d}{\mu}$
Re_j	Jet Reynolds number = $\frac{\rho U_j d}{\mu}$
S_t	Stokes number = $\frac{\tau_p}{\tau_f}$
St	Strouhal number = $\frac{fd}{U}$

Subscripts

∞	Crossflow
a	Air
f	Flow
j	Jet
p	Particle
w	Water

Notation

Abbreviations

AC / DC	Alternating / Direct Current
CCD	Charged Coupled Device
CFD	Computation Fluid Dynamics
CNC	Computer Numerically Controlled
CPT	Critical Point Theory
CVP	Counter-Rotating Vortex Pair
DOF	Depth of Field
JICF	Jet in Crossflow
PLIF	Planar Laser Induced Fluorescence
PVC	Polyvinyl Chloride
TTL	Transistor-Transistor Logic
V/STOL	(Very) Short Take-off and Landing

Symbols

A	Internal jet pipe cross-sectional area (mm^2)
c	Circle of confusion (mm)
d	Internal jet pipe diameter or jet diameter (mm)
δ	Boundary layer thickness (mm)
δ^*	Boundary layer displacement thickness (mm)
f	Frequency (Hz)
f	Focal length of lens (mm)
$f^\#$	f-number of lens
g	Gravitation acceleration (9.81 m/s^2)
h	Hyperfocal distance (mm)
λ	Wavelength (m)
M	Magnification
μ	Dynamic viscosity (Ns/m^2)

Statement of Originality

The work contains no material which has been accepted for the award of any other degree or diploma in any university or other tertiary institution and, to the best of my knowledge and belief, contains no material previously published or written by another person, except where due reference has been made in the text.

Philip Cutler

Permission to Copy

I give consent to this copy of my thesis, when deposited in the University Library, being available for loan and photocopying.

Philip Cutler

Acknowledgments

This work would have been difficult to achieve without the help of a number of people. First and foremost I would like to thank my supervisor, Dr Richard Kelso, for his guidance, support and comments throughout my research.

I also wish to thank the members of the Turbulence, Energy and Combustion Group at the University of Adelaide. My particular thanks goes to Dr Gus Nathan and Professor Sam Luxton for their support and valuable suggestions. I also wish to thank Jordan Parham and Bad Ghazali for their assistance in setting up experiments and their useful technical as well as light hearted social discussions.

I am indebted to the highly skilled electronic and mechanical technicians in the Mechanical Engineering department for the help they have provided. In particular, I wish to thank George Osborne and Anthony Sherry for their assistance manufacturing and assembling my experimental rig, and their continued suggestions on the improvement of the apparatus.

The financial support (scholarship) from the University of Adelaide Postgraduate Office and the large research grant funded by the Australian Research Council for the current jet in cross-flow study are acknowledged.

My very special thanks go to my parents and brother who have always been there and provided so much support. I would like to thank my mother for her time spent proof reading my work. I am very much indebted to my father who has shown me many practical skills that have been so valuable in the accomplishing the experimental work I undertook during my research.

Finally, I would like to express my sincerest and deepest thanks to my family. My partner Dr Thanh Vu for her love, encouragement and support. My daughter, Emilia, who is always so energetic and happy, and always brings a smile to my face.

1 Introduction

1.1 Background and Motivation

1.1.1 A Jet in Crossflow or Transverse Jet

Jet flows occur in a large number of natural and industrial systems spanning an extensive range of scales and geometries. Although a great deal of research has been undertaken into the structure and mixing of many different configurations of jets, many issues remain to be fully understood. One such flow, most commonly termed either a jet in crossflow or a transverse jet, occurs when a jet-flow is exhausted at a large angle into an unconfined-stream. The flow occurs in many natural as well as industrial systems. However, it is also of significant experimental interest in itself because of its simple geometry, yet complex flow structure. Natural occurrences of the flow can be seen in the plumes of volcanoes and smoke from fires. Since the smoke from both of the mentioned sources can be major health hazards, it is important to be able to predict the smoke distribution at ground level and downstream from the source. The concentration of the smoke and therefore the level of pollution are of a primary interest to people around the smoke source.

Industrial applications of a jet in crossflow include a smokestack exhausting into the atmosphere, as shown in Figure 1-1, or pipes discharging into bodies of water. In such cases the dispersion of the exhausted material is important. Therefore, industry is interested both in the diffusion of the jet fluid and the ability to determine the downstream concentration levels in order to ascertain the extent of the impact in terms of environmental pollution from a discharge. The flow is also found in many aeronautical situations, examples of which are the roll control of rockets or missiles, the cooling of gas turbine blades and combustors, turbofan thrust reversers and turbojet thrust vectoring. In applications such as these the extent of jet penetration and mixing characteristics of the two streams are important. Many different variants of the flow exist in the study of the exhaust from V/STOL aircraft. Significant issues arise from ground effects when an aircraft is close to the ground with the engine exhaust directed downwards. Such issues include the damage caused to the ground by the exhaust jets, the generation of upwash fountains that affect the aerodynamics of the aircraft, and the ingestion of the exhaust gas back into the engines. During flight the interaction of the exhaust jets and the ambient air also causes aerodynamic losses and problems with aircraft stability during the transition from hover to wing-sustained flight.

Figure 1-1 A typical example of an industrial jet in crossflow; the discharge of smoke into the atmosphere from a chimneystack (photo curtesy of Dr Gus Nathan).

A recent review, Margason (1993), which contains over 300 references, highlights the fact that a large amount of research has been undertaken on the structure, mixing, and characteristics of a jet in crossflow. It is documented that the initial systematic studies of the flow took place in the 1930s on chimney plumes, but the emphasis of most research moved toward aeronautical applications during the 1940s. A very extensive research program into the jet in crossflow, as a basis for investigations into V/STOL aircraft, took place in the 1950s and 1960s in the USA and Europe. A symposium on jets in crossflow took place in 1969, at which an agreement on the jet cross-section shape, appropriate correlation parameter and jet path was formed. However, a detailed description of the flow structure was not available at the time.

During the 1970s detailed investigations of the flow field of the jet in crossflow were made and many parameters were studied, including the effect of jet deflection angle, jet exit geometry and multiple jet configurations. Quantitative analyses were also undertaken in which the jet dynamic pressure decay profile and jet temperatures were studied. The research in this period was again largely influenced by the military interests in rocket reaction control and in V/STOL aircraft.

The emphasis of the research carried out during the 1980s moved toward the computational modelling of the jet in crossflow and the experimental studies undertaken were centred on providing the data required for CFD verification. Margason (1993) highlights the need for high quality and extensive jet in crossflow experimental data, particularly from the very near-field region of the jet exit, and the surface region downstream of the jet exit. Quantitative velocity data are also required for both the steady and unsteady fields. It is claimed in the review that although the mean flow characteristics of the jet in crossflow had been modelled, the unsteady flow features were not yet fully resolved.

1.1.2 Structure

A jet in crossflow, in its broadest sense, describes a jet that issues into a secondary flow at a large angle. The interaction that occurs between the two flows is complicated and highly unsteady. Schematic diagrams of the resulting flow are shown in Figure 1-2 and Figure 1-3, for the case when a jet-flow exits from a flush-mounted pipe. Four major regions exist in the flow as proposed by Fric & Roshko (1994). These are: (1) the jet shear layer; (2) the system of horseshoe vortices; (3) the counter-rotating vortex pair (CVP); and (4) the wake vortices.

When the jet-flow encounters the crossflow, two counter-rotating vortices are formed that appear to originate from inside the pipe, and persist far downstream of the jet pipe exit. The entrainment of crossflow fluid into the jet causes the jet to deflect in the direction of the crossflow. In the flush-mounted case, along the wall upstream of the jet pipe exit, a horseshoe vortex system is produced in a similar manner to that produced by a wall mounted circular cylinder. A wake region, which contains two vortex systems, exists downstream of the jet exit. A set of streamwise vortices, referred to here as wall vortices, develops close to the wall. Periodic upright wake vortices bridge between the wall vortices and the counter rotating vortex pair.

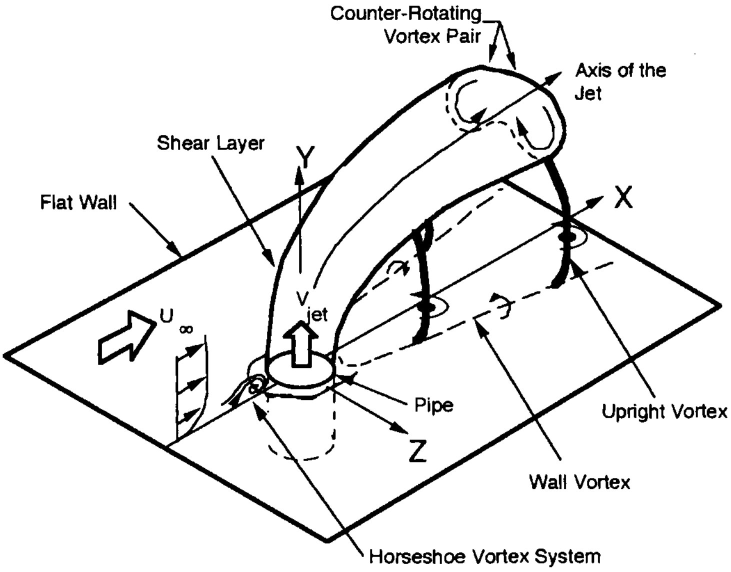

Figure 1-2 Schematic diagram showing the many vortex systems of a wall mounted jet in crossflow (reproduced from Kelso, Lim & Perry 1995).

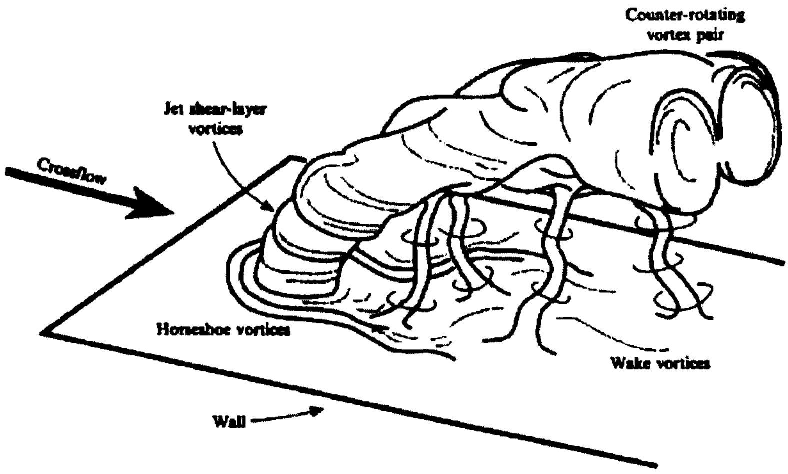

Figure 1-3 Schematic diagram showing the vortex systems as described by Fric & Roshko (reproduced from Fric & Roshko 1994).

Although the features of the flow have been identified by many authors, Morton (1995), Fric & Roshko (1994), Kelso (1991) and others, there is still much contention about the mechanism of formation and importance of each of the flow features.

1.1.3 Flow Cases

The coordinate system used in this thesis is shown in Figure 1-2. The coordinate in the free stream direction is denoted x. Component y is in the direction of the jet and z is in the spanwise (transverse) direction. In order to categorise different cases of the flow, a number of parameters have been used. The major characteristics of the flow are dependent upon the ratio of the momentum flux from the jet orifice to the momentum flux of the crossflow over equal areas, defined as

$$R^2 = \frac{\int_A \rho_j U_j^2}{\int_A \rho_\infty U_\infty^2},$$

where ρ is the density, U is the velocity and the subscripts j and ∞ refer to the jet properties and crossflow properties respectively.

This ratio, however, may be simplified to the velocity ratio between the jet and the crossflow,

$$R = \frac{U_j}{U_\infty},$$

if the fluids are the same, and at the same temperature and if the jet exit velocity profile is close to the classical top-hat profile.

Two Reynolds numbers, the jet Reynolds number and the crossflow Reynolds number, are also parameters of primary importance. The jet Reynolds number is based on the jet velocity and jet diameter, and is defined as

$$\mathrm{Re}_j = \frac{\rho U_j d}{\mu} = \frac{U_j d}{\nu}.$$

The crossflow Reynolds number, however, is a function of the crossflow velocity and the jet diameter, defined as

$$\mathrm{Re} = \frac{\rho U_\infty d}{\mu} = \frac{U_\infty d}{\nu}.$$

Historically, to define a flow case, only the crossflow Reynolds number is used, along with the velocity ratio. This is probably due to the misconceptions about the behaviour of the jet in crossflow and the comparison of it to the flow around a cylinder.

In the case of the flush-mounted jet, the thickness and state of the flat wall boundary layer profile will also affect the jet-crossflow interaction. Relevant parameters describing these effects may be the ratio of boundary layer thickness parameters (such as thickness, δ, displacement thickness, δ^* and momentum thickness, θ) to the jet diameter. In the following work, this will be recognised by the parameter δ/d, and knowledge of the laminar/turbulent state of the flat wall boundary layer.

Other variables and configurations that have previously been investigated by various researchers include;

- the effect of the geometry of the jet exit on the flow structure (Haven & Kurosaka 1997, Vogel 1996, McMahon *et al.* 1971);
- the effect of multiple jet arrangements on the flow structure and mixing (Jansson & Davidson 1996, Toy *et al.* 1993);
- the changes in the jet structure due to the interaction of the jet flow with other surfaces (Mikolowsky & McMahon 1973, McMahon *et al.* 1971);
- the effect on flow separation due to changes in the angle at which the jet discharges into the free-stream (Krothapalli & Shih 1993); and
- jet flow conditions (buoyancy: Papaspyros *et al.* 1996, swirl: Niederhaus *et al.* 1997, Kavsaoglu & Schetz 1989, pulsed: Diep & Sigurdson 2001, Johari *et al.* 1999, Lim *et al.* 1998, Kelso *et al.* 1996).

1.1.4 Defining the Flow to be Investigated

The jet in crossflow configurations examined in this thesis are limited to a circular, isothermal jet, of the same fluid as the cross-stream, exhausted perpendicularly into the crossflow. The work includes the study of a jet discharging from a pipe mounted flush to a flat wall and the case of the flow from a chimney, in which the pipe extends into the crossflow.

Most of the flow cases occurring in industrial situations are large-scale flows that will, in the main, be turbulent and occur at Reynolds numbers greater than 10,000, and jet have velocity ratios above 10. To replicate such flows in the laboratory is not feasible and would make the analysis very much more demanding. The flows studied in the laboratory are therefore not meant to be direct comparisons of industrial flows, but are used to gain as much information as possible about the flow structure. The information will then form a basis for gaining a better insight into the characteristics of the large-scale flows. On the other hand, since the flow is very common and will occur in many cases by accident rather than design, applications with similar flow properties are also almost certainly going to exist.

Many studies have been undertaken on jets in crossflow, attempting to explain the formation of the features or 'structures' in the flow. However, the significance of each structure to the mixing characteristics of the flow or the relative strength of the structures under varying flow conditions has not been adequately dealt with. This work will provide a better understanding of the flow and its mixing characteristics using modern imaging equipment together with some innovative flow visualisation. In addition, many fundamental questions remain in fluid mechanics concerning the interactions between vortices and the mixing of fluids. A better understanding of both of these mechanisms is vital if the current control or modelling of transverse jet flows is to be advanced.

1.2 Research Objectives

The current study investigates two configurations of a single round jet in crossflow. The two cases considered are that of a flush-mounted jet, in which the jet pipe exit is mounted flush with the crossflow wall, and the case of an elevated jet, in which the jet pipe extends into the crossflow. There are a number of reasons for undertaking this comparison. The most significant is that although both cases of the flow have been studied separately and differences noted between them, a study that directly compares the two cases using the same experimental apparatus has not been undertaken. The work will also focus on the effect of the wall boundary, and its associated vorticity, which will not be present in the case of the elevated jet. In addition, since it has been established that there are important interactions between the crossflow and jet-flow occurring within the jet pipe, it would be of benefit to observe this interaction. Although it is difficult to study the flow within the jet pipe for the flush-mounted jet due to the presence of the wall, in the elevated case it is possible to observe the flow structures within the jet pipe in detail.

The current investigation will focus on the development of the transverse jet in the jet exit (or vortex interaction) region and in the near-field. The definition of the near-field, as given by Smith & Mungal (1998), is discussed in Section 2.6. The size of the near-field is shown to be dependent on the square of the velocity ratio. For the velocity ratios considered in this thesis the near-field resides within 1.2d (R=2), 4.8d (R=4) and 10.8d (R=6).

The work presented in this thesis also focuses on the experimental aspects of flow visualisation. Therefore, as part of the research, experimental techniques have been developed in order to enable a better understanding of the overall three-dimensional structure of the flow. Two laser-based volume experimental techniques have been developed and applied in order to assist in with the comparison between the flush-mounted jet and the elevated jet. The first technique, termed the volume quantitative time-averaged scalar field technique, has allowed scalar concentration data to be obtained in three-dimensions. This allows the mixing of jet and crossflow fluids to be investigated. The second technique, volume visualisation, allows a time-series of detailed quasi-instantaneous snapshots of the jet structure to be obtained in three-dimensions. This allows us to investigate the evolution of the vortical structures within the jet.

The aim of the current research is to establish a definitive understanding of the flow mechanisms which produce vortical structures within a jet in crossflow. As the flow exists in many natural and industrial systems, the understanding of the mechanisms is useful for many natural phenomena or industrial applications where two or more fluids are mixed. Without the detailed knowledge of the mechanisms of the flow, it is difficult to predict the behaviour of the flow or design an optimal mixing system.

The research aims to:

- Determine the vortical structure of the elevated jet in crossflow.
- Compare the elevated and flush mounted cases of jets in crossflow in order to determine how the flat wall influences the structure and mixing of the jet.
- Determine the origin of the CVP.

- Determine in greater detail how the jet's shear layer rolls up to form leading edge and trailing edge vortices.
- Determine the differences between the concentration decay on the jet centreline trajectory and the decay along the cores of the counter rotating vortices.

1.3 Thesis Outline

The thesis is divided into two main sections. The first section covers the apparatus and experimental techniques, and the second section the experimental results and interpretation of the data.

Section 1 begins with Chapter 2 in which a review of transverse jet literature is presented to form a background to the current work. In Chapter 3, a detailed description of the experimental apparatus used for the experiments is presented. Following this, Chapter 4 provides a summary of experimental techniques used for flow visualisation. An account of critical point theory is included as a means of providing a standard way of interpretation flow visualisation results. The two volume visualisation techniques are introduced and then discussed in depth along with the additional apparatus and data processing designed to implement the techniques.

The second section is in three chapters in each of which a different experimental technique is applied to investigate the flow cases. Chapter 5 presents the results from the time-averaged scalar concentration experiments. In Chapter 6, the structure of the jet is investigated using the volume visualisation technique. The results of a dye and hydrogen bubble wire visualisation study are then presented in Chapter 7, to provide details of the differences between the elevated and flush-mounted jet flows.

A summary including the discussion, conclusions and suggested future work is then presented in Chapter 8.

2 A Review of Transverse Jet Literature

2.1 The Overall Structure of the Flow

From simple initial conditions, the interaction of a jet and crossflow results in a complex flow that contains numerous vortex systems, all of which are somehow connected (Kelso *et al.* 1996). Moussa *et al.* (1977, p.60) categorised a jet in crossflow into three regions: the free-stream, the deflected jet and the wake. The wake region was further divided into three parts; the "turbulent wake due to separation and shear on the surface of the jet, the shedding wake due to the roll-up of some of the mean vorticity at the boundary surface, and the bound vortex system attached to the trailing surface of the jet". However, a more recent classification of the vortical structures made by Fric & Roshko (1989) has subsequently been adopted by most researchers (Kelso *et al.* 1996, Yuan *et al.* 1999, Lim *et al.* 2002, and others). For the case of a wall- (or flush-) mounted jet, Fric & Roshko identified four distinct vortical structures. These are a pair of counter-rotating vortices (CVP) embedded within the jet, ring-like vortices in the jet's cylindrical shear layer, a system of horseshoe vortices near the wall upstream of the jet exit and a system of wake vortices. Although the case of an elevated jet has not been so comprehensively investigated it has been established that a similar set of vortex systems exist as in the flush-mounted case. The main differences are the lack of the horseshoe vortices and structural differences in the jet-wake due to the absence of the crossflow wall (Eiff & Keffer, 1997).

Although the overall flow structure of jets in crossflow is relatively well accepted, the formation mechanisms of the many vortex systems and the vorticity sources from which they originate are not yet fully established. Further, the dominance of the individual vortex systems and their interaction with one another has not been resolved.

During the review of the literature on jets in crossflow there appeared to be little data referring to the flow structure within the jet pipe, upstream of the jet exit plane. In fact, most diagrams and interpretations of the flow begin above the exit plane of the jet, and do not consider the upstream flow or structures that may be present.

Andreopoulos & Rodi (1984, p. 94) studied wall mounted jets and observed that for low velocity ratios, R < 0.5, "the flow behaves as if a partial, inclined 'cover' were put over the front part of the exit hole...". The jet was reported to be bent over completely, right above the exit and the crossflow was observed to be lifted over the jet. For high velocity ratios, R > 2, the jet was found to be only weakly affected near the exit, and penetrates into the crossflow before being bent over.

A surface streamline pattern was proposed by Kelso (1991) for the flow inside the pipe, based on a dye visualisation study that demonstrated that boundary layer separation occurs within the jet pipe. It was also suggested that the formation of the CVP was initiated within the pipe. It would therefore be of interest to learn whether the details of the flow within the pipe affect the eventual mixing of the jet and crossflow fluids. Furthermore, it is of interest to discover the influence of jet pipe protrusion on the mixing of the fluids. Is a chimney jet or flush-mounted jet a more efficient mixer, and therefore what role does the wall or wall-generated turbulence play in the mixing? Undertaking the work on an elevated jet will also aid in understanding and resolving the details of the flow structures within the jet pipe due to the increased visibility of the pipe interior.

2.2 Vorticity Sources

Understanding the source of the vorticity for each of the vortex systems arising in a jet in crossflow is a vital step in understanding the mechanisms governing the flow. Morton (1984, p.23) described a number of properties that must be taken into account in developing any comprehensive treatment of the generation and decay of vorticity. These properties are made up of the requirements that the generation of vorticity results from tangential acceleration of a boundary, from "tangential initiation of boundary motion and from tangential pressure gradients acting along a boundary". The generation of vorticity is instantaneous and, once generated, vorticity cannot "subsequently be lost by diffusion to boundaries". A "reversal of the sense of acceleration or of the sense of pressure gradient, results in reversal of the sense of vorticity generated". Also, the "generation process is independent of the prior presence of vorticity". Vorticity decay takes place only in the fluid interior and is the result of cross-diffusion of vorticity of opposite sign, leading to annihilation. If the net vorticity is always zero, then the flow must generate vorticity of opposite sign in equal quantities.

The source of the vorticity responsible for the formation of the flow features in a jet in crossflow is a contentious issue. Fric & Roshko (1989) established, by considering the vortex transport equation for a Newtonian barotropic and incompressible flow with no body force, that vorticity may only be created from the imposed initial conditions, i.e. from wall boundaries. The result comes about since the equation does not contain any terms for vorticity generation; there are terms only for the convection, stretching, turning and diffusion of the vorticity. Therefore, in the case of a wall mounted jet in crossflow the only sources of vorticity are the jet pipe and the crossflow boundary layer, whereas in an elevated case, the external and internal surfaces of the pipe are the principal sources of vorticity. The majority of the research into the formation and modelling of the flow, such as that undertaken by Fric & Roshko (1989), Andreopoulos (1982, 1983, 1984, 1985) and Kelso *et al.* (1996), is therefore focused on determining from which sources of vorticity each flow feature arises.

An important result from the analyses of Fric & Roshko (1989) and others, is that although the jet in crossflow shows some features similar to those of a wall mounted cylinder, the jet does not continuously generate and shed vorticity as a cylinder does. This result has profound implications for various vortex systems as discussed in subsequent sections.

2.3 Pipe Shear Layer

As discussed above, the pipe flow is one of the main sources of vorticity. Thus, it is to be expected that the shear layer emanating from the pipe will carry the vorticity that will be redistributed once the pipe flow and crossflow interact. Two main types of vortical structures have been identified as evolving from the pipe shear layer; a counter rotating vortex pair (CV) and the 'ring-like' jet shear layer vortices (Fric & Roshko 1989, Kelso *et al.* 1996, Yuan *et al.* 1999). The two structures are believed to be strongly related although the details of the relationship are not fully resolved. The structures are discussed separately in the following two sections.

In the literature there have been numerous comparisons made between a free jet and a jet in the presence of a crossflow. Although such comparisons are useful, they do not account for the influence of the crossflow on the flow within the pipe. Andreopoulos (1982) showed a measurable influence of the crossflow on the pressure distribution up to 4 jet diameters ahead of the jet exit, albeit at low velocity ratios. Furthermore, the observations by Andreopoulos (1982) and Kelso *et al.* (1996) of intermittent and steady separation regions within the pipe, suggest that the pressure distribution imposed by the crossflow can have a significant influence within the pipe. Therefore, it is to be expected that the imposed pressure distribution will influence the distribution of vorticity, or vortex lines, within the pipe.

2.3.1 Shear Layer Vortices

Observations and investigations into the mechanisms of formation of the jet shear layer vortices have been undertaken by many authors including Moussa *et al.* (1977), Andreopoulos (1982, 1983, 1984, 1985), Fric & Roshko (1989, 1994), Morton (1995), Kelso *et al.* (1996), Lim *et al.* (1998), Blanchard, Brunet & Merlen (1999), Yuan, Street & Ferziger (1999), Lim *et al.* (2001) and Cortelezzi & Karagozian (2001). Different authors have used a variety of terms to refer to the vortices: Andreopoulos (1982), "the rolling up of the jet shear layer"; Fric & Roshko (1994), "jet shear layer vortices"; Kelso *et al.* (1996), "ring-like or loop-like vortices"; Blanchard *et al.* (1999), "transverse vortices"; Yuan *et al.* (1999), "spanwise rollers". In the current thesis the structures will be termed "leading edge and trailing edge shear layer vortices". This terminology allows the two sides of the shear layer to be discussed separately and does not assume any connection between them.

In order to identify the vortices discussed in the current section, a PLIF image taken on the plane of symmetry of a transverse jet is shown in Figure 2-1. Here the jet Reynolds number is 4000 and the velocity ratio is 2. The initially cylindrical shear layer can be seen to distort and roll up into a pattern of vortices as it emerges from the jet exit. The large-scale shear layer vortices on both the leading (upstream) and trailing (lee side) shear layers are labelled. The consistency of orientation between the leading and trailing edge vortices suggests that the pattern may be the result of a train of distorted ring vortices, emanating from the pipe exit (Kelso *et al.* 1996). As can be observed there is a substantial tilting of the vortex 'rings' in the near-field of the jet, and the structure breaks down to turbulence in approximately five jet diameters from the jet exit.

Kelso *et al.* (1996) found that the rolling up of the shear layer occurred by one of two mechanisms, depending on the flow conditions. At low velocity ratios and Reynolds numbers, a steady vortex, termed a hovering vortex, formed close to the jet exit. The leading edge shear layer of the jet in this case was laminar with a Kelvin-Helmholtz instability occurring downstream of the jet exit. No roll-up on the trailing edge of the jet was evident. As the Reynolds number was increased (at constant R), the Kelvin-Helmholtz instability occurred closer to the jet exit, until "... the hovering vortex itself begins to shed ring vortices periodically ..." (Kelso *et al.* p. 117).

The leading edge vortices form closer to the jet exit (Andreopoulos 1982, Kelso *et al.* 1996 and Yuan *et al.* 1999) and far more regularly than the trailing edge vortices. Slight differences in the observations and mechanisms of the vortices presented in different studies are likely to result due to the structure of the vortices being dependent on the crossflow Reynolds number and velocity ratio (Andreopoulos 1985 and Kelso *et al.* 1996) as well as the ratio of the boundary layer thickness to the jet diameter. Andreopoulos (1985) determined from flow visualisation of low Reynolds number jets that the shear layer vortices emanating from the leading edge of the pipe appear to be periodic and carry vorticity with the same sign as the pipe vorticity. The size of the vortices was found to be of the order of the pipe boundary layer thickness. As the jet Reynolds number increases, however, it was found that the periodicity of the large-scale leading edge vortices decreases, and these structures begin to occupy a wide range of sizes.

Shear layer vortices occur both in the leading and trailing edges of the jet, although it is uncertain as to whether the two are connected. Researchers such as Kelso *et al.* (1996) who describe the structures as ring-like and suggest that under certain conditions the " ... vortices form by a roll-up of the shear layer around the entire perimeter of the jet" (p. 118) suggest a connection between the two. Yuan *et al.* (1999), however, only observe the formation of the structures on the upstream and downstream edges, and not on the periphery of the jet. Lim *et al.* (2001) also suggest that the leading and trailing edge shear layer vortices are not part of the same vortex ring. The authors point out that the formation of the CVP along the sides of the jet prevents the rolling up of the vortex sheet the entire way around the jet circumference.

Figure 2-1 PLIF image along the jet axis of symmetry of a transverse jet, with a jet Reynolds number of 4000, at a velocity ratio of 2, showing a cross-section of the jet shear layer structures.

In order to understand the way in which the jet shear layer evolves under the influence of the crossflow, the jet has been modelled conceptually by some authors as a series of vortex rings (Moussa *et al.* 1977, Andreopoulos 1985, Sykes *et al.* 1986, Kelso *et al.* 1996). Andreopoulos (1985) proposed the vorticity pattern presented in Figure 2-2. The rolling up of the shear layer was described by vortex rings that carry vorticity of the same sign as the flow inside the pipe. The rings are subjected to symmetrical stretching, transport and tilting due to the crossflow. Andreopoulos makes the observation that in the very near-field the upstream side of the jet is decelerated with respect to the downstream side and that results in a stretching of the vortex lines. The opposite is true further downstream where the upper side of the jet is accelerated with respect to the lower side, resulting in a compression of vortex lines. The difference in the relative speeds of the leading edge and trailing edge vortices has also been noted by Moussa *et al.* (1977) and Kelso *et al.* (1996). Moussa *et al.* added that, as this mechanism occurs to successive rings, the rings will bundle up on the downstream side into two bound vortex tubes joined at infinity, making two counter-rotating helical spiral motions. This mechanism therefore suggests that the formation of the CVP occurs in the lee side of the jet from the vorticity contained within the jet only.

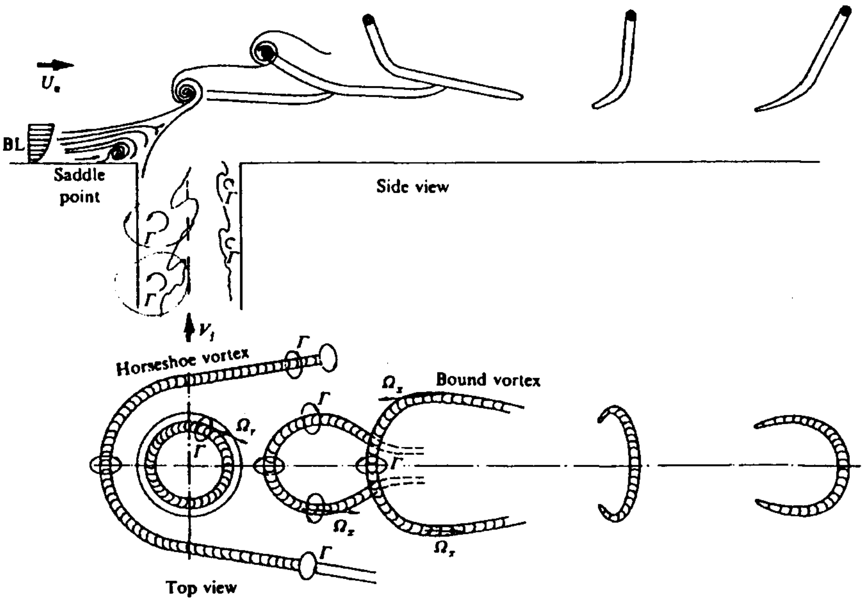

Figure 2-2 Vorticity pattern and flow configuration (reproduced from Andreopoulos 1985).

Lim *et al.* (1998) provided a model of the mechanism by which the shear layer of the jet in crossflow rolls up and distorts, visualised by firing vortex rings into a crossflow. This is included in Figure 2-3. The distortion is shown to involve a complex stretching and looping of the vortex rings into an interlocking arrangement. In the case of a continuous jet, Lim *et al.* (1998) proposed that the process of stretching of the sides of the vortex rings contribute to the counter-rotating vortex pair, see Figure 2-4.

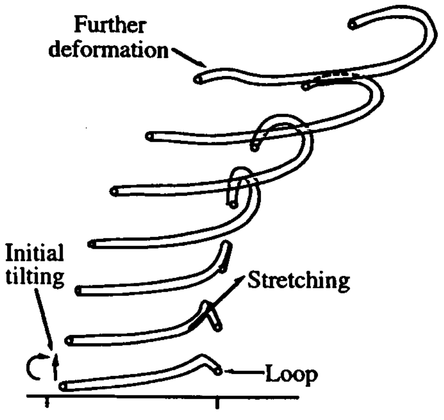

Figure 2-3 Vortex ring evolution of the jet shear layer (reproduced from Lim *et al.* 1998).

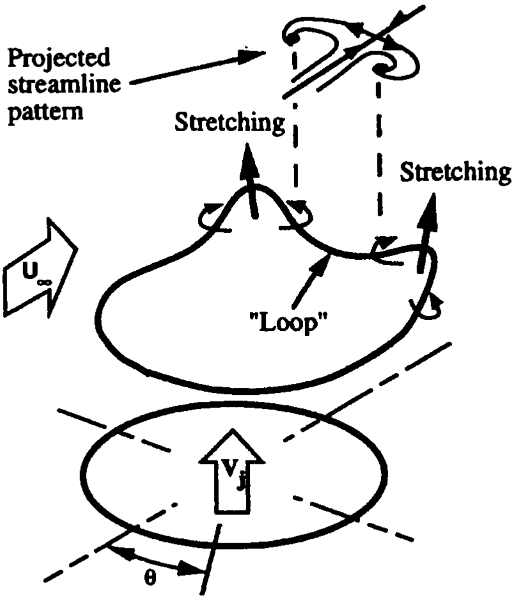

Figure 2-4 Vortex ring deformation process (reproduced from Lim *et al.* 1998)

A different description for the formation of the large-scale structures of the JICF is proposed by Lim *et al.* (2001). Lim *et al.* propose that the large-scale structures are composed of loop vortices rather than being the result of the folding of vortex rings. It is argued that the presence of the CVP prevents the jet shear layer from rolling up into vortex rings, a point also made by Yuan *et al.* (1989). The jet shear layer can therefore only roll up on the upstream and downstream sides since the CVP suppresses the roll-up of the lateral sides of the jet column. The result of this is the presence of two rows of loop vortices separated by the CVP at the sides of the jet. As the jet progresses downstream, the side arms of the vortex loops merge with the CVP. This process is shown in Figure 2-5. The mechanism allows the formation of the vortical structures on the leading and trailing edges of the jet to occur independently and by different mechanisms.

Morton (1995) suggested an alternative model, based on the interaction of the wall-bounded shear layer and jet shear layer, shown in Figure 2-6. The model uses a mechanism similar to that seen by Fohl & Turner (1975) in which two vortex rings are fired along intersecting paths and combine to form a single vortex ring. It was suggested that a similar process of vortex reconnection and annihilation occurs when a vortex filament created in the wall boundary layer is strained over a vortex filament advected from the jet orifice. This model was used principally to explain the formation of the CVP and wall vortices, but it clearly must define the character of the jet shear layer also.

Kelso (1991) contains images showing that when a dye trace is placed within the boundary layer the dye stream is deflected down to a stagnation point located at the leading edge of the pipe. The presence of this persistent feature indicates that the majority of the boundary layer vorticity never meets the jet shear layer vorticity. In fact, the majority of the boundary layer vorticity either contributes to the horseshoe vortices or is convected around the sides of the jet. This is discussed further in Chapter 7.

Bousgarbiès, Brizzi & Foucault (nd) discovered that, at least for low Reynolds number cases of a wall-mounted jet, the vortices formed in the shear layer have some dependence on the jet velocity ratio. A low velocity ratio, $R = 0.66$, produced wake-like leading edge vortices, whereas in the case of a jet velocity ratio of 1.66 the leading edge vortices were jet-like in their sense of rotation. The difference in rotational direction would imply that the magnitude and direction of the vorticity on both sides of the shear layers is important in the overall flow structure. Similar observations have also been made by authors such as Lim *et al.* (2001)

Blanchard *et al.* (1999) and Camussi *et al.* (2002) suggested that for flows with very low Reynolds numbers (< 100) and low velocity ratios, a different mechanism may be responsible for the production of shear layer vortices. The authors suggest that the generation of the shear layer vortices can be better explained by the 'application of the Landman and Saffman theory' (Landman & Saffman, 1987) than by the more established hypothesis of a "Kelvin-Helmholtz" type instability. The flows considered in both publications, however, were at very low Reynolds numbers which may suggest that although the work is valid in its own right, it does not fit the general transverse jet case.

The above discussion demonstrates that the shear layer of the jet in crossflow rolls up to form leading edge and trailing edge vortices and that the nature of these vortices is dependent on parameters such as Reynolds number, velocity ratio and the boundary layer thickness relative to the jet diameter. Most models or descriptions of the flow describe the roll-up of the shear layer in terms of rings or loops comprised of vorticity emanating from the pipe. One mechanism proposes that the flat wall boundary layer is strongly involved in this process also. Three instability mechanisms have been suggested by various authors to describe the process leading to the shear layer vortices. The most relevant of these to the present thesis, based on the flow conditions to which they apply, are those of Kelso *et al.* (1996) and Lim *et al.* (2001).

2.3.2 Counter-rotating Vortex Pair

A principal feature of a jet in crossflow is the formation of a pair of counter-rotating vortices due to the interaction of the crossflow and the jet. The counter-rotating vortex pair (CVP), or bound vortices, are understood to be embedded within, and aligned with, the jet. The vortex pair form in the jet's near-field with the central motion between the vortices in the original direction of the jet. The CVP is known to be the dominant flow feature in the far-field, where it is synonymous with 'the jet'. Pratte and Baines (1967), in fact, were able to detect the presence of the CVP 1000 jet diameters downstream of the jet exit. The origins of the CVP are, however, still not fully resolved.

Broadwell & Breidenthal (1984) provide a description of the formation of the CVP in a global sense. They conclude that the counter-rotating vortex pair is induced in the mean flow field by the impulse of the initially normal jet. The jet provides a transverse force on the crossflow, in a similar way to a lifting wing.

Moussa *et al.* (1977), Andreopoulos (1985), Sykes *et al.* (1986), Coelho & Hunt (1989), Kelso *et al.* (1996) and Yuan *et al.* (1999) among others have suggested mechanisms by which the CVP are formed. Although there is no real consensus on the formation mechanism, it is agreed that the original source of vorticity is the jet shear layer. Sykes *et al.* (1986) determined by numerical simulation, that the source of the streamwise vorticity in the CVP can be traced back to the streamwise vorticity in the sides of the jet. This was also shown by Fric (1990). Moussa *et al.* (1977) states "Most of the mean vorticity issuing from the pipe, tilted and stretched by the flow, bundles up into a pair of vortex tubes bound to [the] lee side surface of the jet." (p. 52).

As with the jet shear layer, authors (Andreopoulos 1985, Sykes *et al.* 1996) have used vortex ring models to explain the formation mechanism of the CVP. They suggest the CVP forms due to the combining of consecutive vortex rings into two line vortices, although the proposed mechanisms by which this occurs differ in detail. Andreopoulos (1985) suggested that the CVP forms due to rapid stretching of the vortex rings during which the 'legs' of successive rings bundle up to form the CVP (bound vortices), as shown in Figure 2-2. Sykes *et al.* (1986) suggest a mechanism where the interaction of the upstream edge of a vortex ring with the downstream edge of the successive rings results in the formation of the CVP along the lateral edge of the jet. The essence of the two

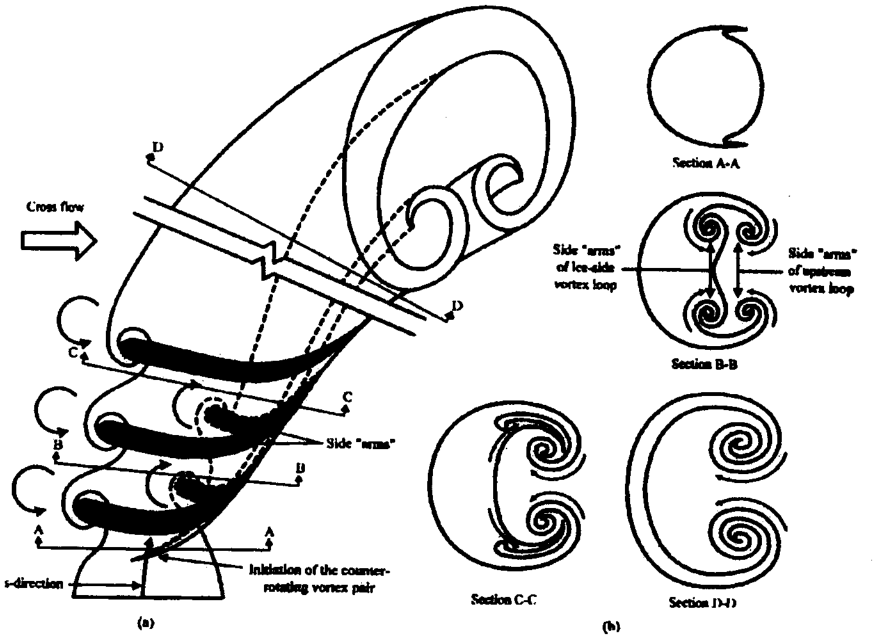

Figure 2-5 Linking mechanism of the vortex loops forming the leading and trailing edge shear layer rollups (reproduced from Lim *et al.* 2001)

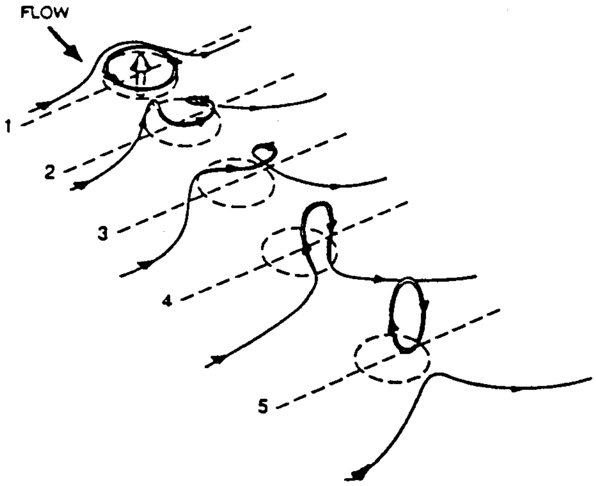

Figure 2-6 Wall and jet vortex filament interaction as proposed by Morton (reproduced from Morton 1995)

mechanisms is essentially the same, being that the longitudinal vorticity emanating from the pipe bundles together to form the CVP. A similar mechanism was proposed by Perry& Lim (1978) to explain the development of longitudinal vorticity in buoyant co-flowing jets and wakes.

Coelho & Hunt (1989) applied a vortex sheet model by which it was proposed that entrainment into the lee side of the jet caused a reorganising of the cylindrical vortex sheet resulting in the initiation of the CVP. Blanchard *et al.* (1999) suggest that the CVP is formed by the shearing along the edges of the jet fluid as the crossflow moves laterally around the jet and then the folding of the face of the jet over itself. Kelso *et al.* (1996) and Lim *et al.* (2001) describe the folding and rolling up of the vortex sheet at the pipe exit as leading to, or contributing to, the formation of the CVP. It is also noted that there may be a connection between the roll-up of the jet shear layer and the *initiation* of the CVP. Kelso *et al.* (1996) and Lim *et al.* (2001) also agree with earlier authors that the longitudinal component of vorticity in the cylindrical shear layer contributes primarily to the formation of the CVP. Kelso *et al.* (1996) suggest that vorticity originating at the flat wall contributes to the CVP also.

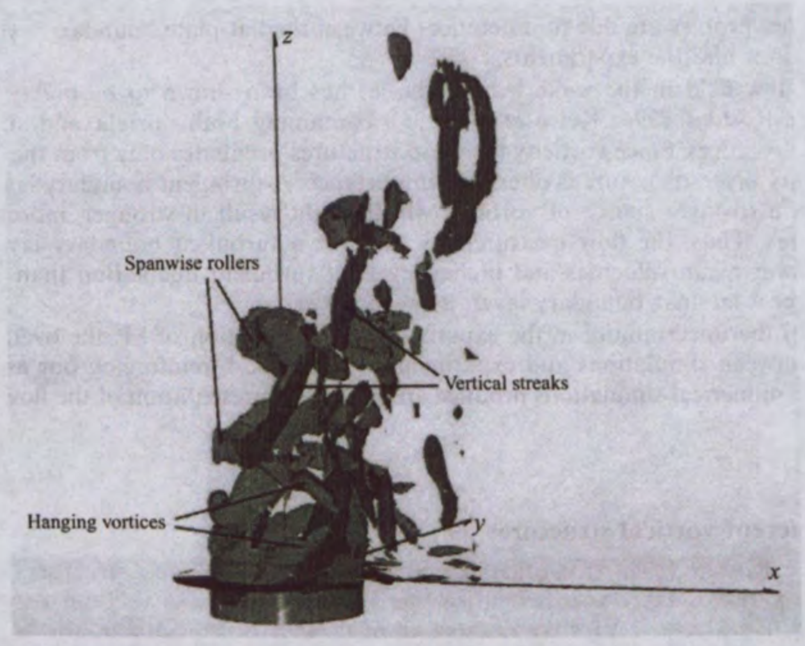

Figure 2-7 Isosurfaces of vorticity showing the coherent vortical structures as discussed by Yuan *et al.* (1999) (reproduced from Yuan *et al.* 1998)

Yuan *et al.* (1999) provide a mechanism for the formation of the CVP somewhat similar to that of Kelso *et al.* (1996). Yuan *et al.* found in their simulation of the flow, two coherent vortical structures present in the near-field of the jet, as shown in Figure 2-7. These were named hanging vortices. The first of the structures occurred on the lateral edges of the jet, directly above the jet exit, and was compared to a feature seen by Kelso *et al.* who described it as the 'folding' of the jet shear layer. This feature was found to be a quasi-steady structure. The second set of structures form further from the jet exit and behave in an unpredictable manner. These structures were compared with the pair of unsteady counter-rotating vortices that were found to be present in non-circular jets investigated by Haven *et al.* (1996). The formation of the hanging vortices is suggested to be the result of the Kelvin-Helmholtz instability between the non-parallel jet and the crossflow mixing layers. It is found by Yuan *et al.* (1999) that the fluid within the lower hanging vortex has a high axial flow that transports a "significant amount of scalar concentration, vorticity, and vertical momentum way from the jet body" (p. 84). The flow visualisation results of Kelso *et al.* (1996) show significant scalar transport by this feature also. In addition, as suggested by Kelso *et al.* (1996) the fluid within the lower hanging vortex was found to undergo vortex breakdown. The breakdown of the 'strong' hanging vortices therefore results in a pair of weak counter-rotating vortices. Although the presence of vortex breakdown and the evolution of the hanging vortices into the CVP seems to fit well with the experimental evidence, the formation of the hanging vortex structures appears to originate from within the jet pipe, possibly before any Kelvin-Helmholtz type instability would occur. The skewed mixing layer concept suggests that there may be differences in the location of the hanging vortices in the flush and elevated jet cases, due to differences in the local velocity components of the crossflow as it approaches the jet.

2.4 Horseshoe Vortex Systems

An important feature of the flush-mounted transverse jet is a system of vortices on the crossflow wall upstream of the jet exit. Authors such as Krothapalli *et al.* (1990), Fric & Roshko (1989, 1994), Kelso & Smits (1993, 1995) and Kelso *et al.* (1996) have undertaken detailed visualisation studies that suggest the structures are a set of vortices resembling horseshoe or necklace vortices. A debate has come about concerning whether or not a set of horseshoe vortices form in the case of a jet in crossflow, and in fact whether they are physically able to form. Morton (1995) suggests that the other authors have misinterpreted the flow and instead suggests the flow field upstream of the jet is integral with the mechanism he proposed for the interaction between the jet shear layer and flat wall boundary layer.

Horseshoe vortices are concentrated U-shaped vortices that form wherever boundary layer vorticity is advected round a surface-mounted obstacle (Mason & Morton 1987). The vortices form due to the adverse pressure gradient experienced by the flow as it approaches the obstacle. This pressure gradient occurs in both the case of a solid cylinder and a transverse jet. The form of the horseshoe vortex system generated is dependent on the Reynolds number (Mason & Morton 1987). With an increasing Reynolds number complex multiple vortical structures form, until the boundary layer becomes turbulent, when a recognisable structure exists only in the mean.

In the case of a wall mounted jet in crossflow the jet is not a rigid body and the boundaries of the jet are compliant and entraining. Moussa, Trischka & Eskinazi (1976) determined that the flow in the case of the jet in crossflow was similar in terms of the velocity distribution to that of the flow past a wall mounted solid cylinder of the same cross section. Kavsaoglu & Schetz (1989) provide pressure distributions that show that an adverse pressure exists that is similar to that induced by a solid obstacle. Additionally, Krothapalli *et al.* (1990) established a jet velocity ratio dependence of the size of the separation of the boundary layer from the wall in the case of a rectangular jet in crossflow. Fric & Roshko (1989) suggest that since the boundary layer separates from the wall, a pressure gradient is indeed induced on the wall, thereby generating additional vorticity. Fric & Roshko point to the crossflow boundary layer as being the source of vorticity for the horseshoe vortices. Doligalski, Smith & Walker (1994) also shows that horseshoe vortices exist and are energetic flow features.

2.5 The Wake

The wake region of the jet in crossflow is the region beneath the counter-rotating vortex pair, and within the area defined by the wall vortices. The general structure of the wake has been investigated by a number of researchers, including McMahon *et al.* (1971), Moussa *et al.* (1977), Wu *et al.* (1988), Fric (1990), Kelso (1991), Fric & Roshko (1994) and Kelso *et al.* (1996). However the mechanisms of the wake structures have not been fully resolved.

Early attempts to understand the wake of the jet in crossflow resulted in analogies being drawn with circular cylinders. The periodic wake was observed to form a Kármán vortex street similar to a cylinder wake, which could be suppressed by the use of a splitter plate (McMahon *et al.* 1971). Similar Strouhal numbers were observed, based on a jet dimension that corrected for entrainment (McMahon *et al.* 1971). Moussa *et al.* (1977) suggested that, similar to solid cylinders, the jet in crossflow should generate vorticity due to shear at the sides of the jet. They proposed that a portion of the mean pipe vorticity, and the additional vorticity generated at the interface of the two flows, roll up into periodically shed vortices, similar to those in a Kármán-Bérnard street. This was refuted by Fric & Roshko (1989) who noted that, in a flow of constant density, vorticity could not be generated within the interior of the fluid. They pointed out that the only sources of vorticity could be the pipe interior and the flat wall. In fact, these researchers showed conclusively that the wake vortices originate within the flat wall boundary layer. This has subsequently been confirmed by Kelso (1991) and Kelso *et al.* (1996). Kelso (1991) also noticed that the wake vortices often contain small traces of dye, or smoke, that originated within the jet. At low jet velocities, however, this can be attributed to the low pressure vortex core drawing fluid down into the wake region. Smith & Mungal (1998) noted jet fluid in the wake vortices of transverse jets with a velocity ratio greater than 10. To explain the occurrence of the jet fluid in the wake, Smith & Mungal (1998) proposed a variation of the Fric & Roshko wake vortex model. The variation reorders the boundary layer separation events proposed by Fric & Roshko, with the effect that the wake structures are transported with the jet instead of attaching to the wall.

Rudman (1995) agrees with the hypothesis of Fric & Roshko through the numerical simulation of a jet in crossflow. The model suggests that a series of structures downstream of the wake exist with a constant Strouhal number. Also highlighted was the fact that when particle markers were placed within the crossflow boundary layer, they were entrained into the wake structures, thus implying the crossflow boundary layer vorticity plays an important role in the formation of the wake system. The simulation therefore agrees with the experiments of Fric & Roshko (1989) and Kelso *et al.* (1996).

An important observation was reported in Kelso (1991), Kelso *et al.* (1993) and Kelso *et al.* (1996). These authors observed from Fric & Roshko's results that different wake flow patterns can occur. They observed that at some conditions the pattern of the wake vortices resembles a Kármán vortex street, but sometimes switches to a pattern of mushroom-like vortex pairs. Kelso *et al.* (1993) investigated structures in the wake region of the jet in crossflow using a three-dimensional imaging technique. Two vortex skeleton models were proposed, one that described the wake vortex roll up process leading to the Kármán vortex street formation, and the other the process leading to the mushroom-like pattern.

For a chimney, or elevated pipe flow the wake structures have been found to differ from the wall mounted jet case. Eiff & Keffer (1997) proposed that two wake vortex systems are present in the case of an elevated jet flow; the jet-wake structures and the pipe-wake structures. The sources of vorticity are different for each. Pipe-wake vortices are produced from the 'shedding' of the flow past the chimney. The source of the vorticity for the jet-wake vortices was found by Eiff & Keffer to be the inside surface of the pipe. Since the jet-wake vortices and the pipe-wake vortices have different sources, it is suggested by Eiff & Keffer that the jet-wake vortices are not extensions of the pipe-wake vortices. The jet-wake vortices were found to lock to the shedding frequency of the pipe-wake, suggesting that the unsteadiness in the wake is dominated by the shedding of vortices from the chimney. Eiff & Keffer's interpretation of the wake structure is shown in Figure 2-8.

2.5.1 Wall Vortices

Downstream of the flush-mounted jet a second counter-rotating vortex pair is formed which is embedded in the crossflow boundary layer with a central motion toward the wall, i.e. opposite to the main CVP. Kelso *et al.* (1996) named these the wall vortices. It is emphasised by Fric and Roshko (1994) that the counter-rotating vortex pair and the wall vortices are distinct structures, and that their origins are not the same. However, evidence has been presented that the vortex systems maybe connected by spin-off vortices (Wu, Vakili & Yu 1988) or upright vortices (Kelso 1991 & Kelso *et al.* 1996).

It was believed by some authors, Andreopoulos & Rodi (1984) and Fric & Roshko (1991), that the wall vortex pair are the trailing arms of horseshoe vortices. However, a different mechanism appears more likely. Wu, Vakili & Yu (1988) proposed that the trailing vortices were induced by the CVP, whereas Kelso *et al.* (1996) suggest that the wall vortices come about due to the separation and roll up of the flat wall boundary layer vorticity.

Morton (1995) suggests that the formation of the wall vortices can be explained by the vortex filament model discussed in Section 3.4.2. Morton proposes that the trailing streamwise vortices come about due to the distortion of vortex lines downstream of the jet. The distortion and stretching of the lines leads to a concentration of vorticity in the wake region, giving rise to the observed vortices. Morton (1995) disagrees with the other authors' interpretations of the wall boundary layer flow upstream of the jet and disputes that horseshoe vortices exist in the flow. Instead he is of the opinion that the key to understanding the physics of deflected jets lies in the interaction of the two shear layers. Morton bases this on his hypothesis that the jet in crossflow produces simultaneous embedded vortex pairs in both the jet and the wall boundary layer.

2.6 Jet Trajectory, Scaling and Mixing

As discussed previously, one of the major characteristics of the transverse jet is the deflection of the jet in the direction of the crossflow. The prediction of the trajectory is of significant importance when the flow is used in real world applications. The trajectory of the jet has been investigated by a number of authors including Pratte & Baines (1967), Broadwell & Breidenthal (1984) and Smith & Mungal (1998). The jet centreline trajectory has been defined by both the locus of the maximum velocity (Moussa *et al.* 1977) and concentration (Smith & Mungal 1998) measured on the plane of symmetry. According to Smith & Mungal, the maximum velocity trajectory penetrates 5-10% further into the flow than the corresponding scalar concentration trajectory. It is well established that the jet will penetrate further into the crossflow for higher velocity ratios, the influence of other factors is less certain. Broadwell and Breidenthal (1984) determined analytically that in the far-field the jet penetration, defined as the jet centreline distance from the jet pipe exit plane (the y-coordinate in this thesis), and the spacing between the counter-rotating vortices, vary with the downstream distance raised to a power close to one-third. An expression for the jet penetration, y, for a streamwise distance, x, was found as

$$\frac{y}{Rd} = A\left(\frac{x}{Rd}\right)^{\frac{1}{3}},$$

where A is a constant, and R is the velocity ratio. No specifications are made about the flow conditions or jet configuration. The Rd relationship, though, fits reasonably well with the experimental data. Pratte and Baines (1967) found the expression

$$\frac{y}{Rd} = 2.05\left(\frac{x}{Rd}\right)^{0.28},$$

fits the jet centreline for data taken at velocity ratios of between 5 and 35 for an elevated jet with two different nozzle diameters. Smith & Mungal (1998) acquired quantitative two-dimensional images of the scalar concentration field, along with mean centreline concentration decay in the near and far-fields. Their work suggests that the jet characteristics scale with three length scales: d, Rd and R^2d. Three different regions of the flow were studied; the vortex interaction region, the near-field, and the far-field. Events within the vortex interaction region (crossflow boundary layer separation and roll up) scale with d. R-dependent variations in this region were found, such as emergence of jet fluid in the wake structure ($R > 10$) and a slower development of the CVP for higher values of R. The trajectory and physical dimensions of the jet were found to scale with Rd in both the near and far-fields. The division between the near and far-fields was proposed to occur at the point where the concentration decay along the jet centreline underwent a transition from enhanced mixing to reduced mixing compared with a simple jet. When the concentration was normalised by R^2d, the transition occurred at uniform jet position $s/R^2d = 0.3$, which was suggested as the division between the near and far-fields. Here the variable s represents the distance from the jet exit along the centreline of the jet.

The conclusions drawn by Smith & Mungal (1998) and other authors have all been based on data obtained at the plane of symmetry, i.e. between the counter-rotating vortices. No studies to date have comprehensively investigated the concentration decay along the cores of the counter-rotating vortices.

Bousgarbiès *et al.* (nd) determined the mean path of the leading edge shear layer vortices for several flow cases. The results demonstrate that the height of the mean leading edge shear layer trajectory increases with increasing Reynolds number at any given velocity ratio.

Andreopoulos (1984) found that changes in the upstream boundary layer conditions cause changes to the flow patterns in the region of the jet exit. The effects are more significant near the jet exit that in the far-field. This illustrates the importance of δ/d as a parameter affecting the development of the flush-mounted jet in crossflow.

The mechanism by which the jet bends was investigated by Coelho & Hunt (1989). In this study it was found that entrainment was required in order for the jet to be deflected. They conclude that the 'pressure-drag' mechanism, as in the case of a bluff body, is negligible compared with the effects of entrainment on the deflection of the jet. The main mechanism for the streamwise deflection of the jet was therefore concluded to be the addition of streamwise momentum due to viscous processes such as entrainment. The main regions of the flow where the entrainment takes place is the CVP and the leading edge shear layer vortices (Yuan *et al.* 1999). Yuan *et al.* conclude that the CVP is responsible for the majority of the entrainment into the jet.

It has been well documented that the entrainment of ambient fluid into deflected jets is substantially greater than into simple turbulent jets in a still environment (Broadwell & Breidenthal 1984, Morton 1995, and others). Broadwell and Breidenthal (1984) state that due to the altered structure of the jet when a crossflow is applied, the vorticity field is a far more efficient mixer. It is surmised that the more rapid mixing, when compared with an axi-symmetric jet, maybe a result of the formation of the CVP and the curved shear layer on the upstream side of the jet. Both structures contain rather large vortices, which results in an enhanced vortex growth rate leading to enhanced mixing. Morton (1995) states that the greatest entrainment is present at a velocity ratio of 5 and exceeds that of a free jet by an order of magnitude.

Measurements and comparisons of the trajectories of elevated jets in crossflow have been reported by very few authors. This is discussed by Moussa *et al.* (1977) who comment that there are " ... considerable variations in the literature in the experimental results for the jet [trajectory] ...". The differences are attributed to the flow conditions at the jet exit, and whether the jet is from a flush-mounted pipe or an elevated pipe. Three reasons are presented to account for the difference between the elevated and flush-mounted cases;

- a difference in the momentum distribution at the jet exit,
- the flush-mounted jet produces a potential core that adds stiffness and very low turbulence to the initial flow, and

- for the flush-mounted case vorticity developed in the wall boundary layer will roll up in the wake of the jet.

In addition to the velocity or concentration centrelines, Moussa *et al.* (1977) proposed "...that in addition to the jet's maximum velocity centreline, the axes of maximum vorticity joining the centres of the bound vortices be considered equally in the development of the flow." (p. 79). Although this proposal does not appear to have been widely accepted, it would provide a more complete description of a specific flow case.

2.7 Elevated Jets

Surprisingly few researchers have focussed on the case of an elevated jet in crossflow, given that it occurs so frequently in the case of a stack or chimney exhausting into the atmosphere. In addition, the work undertaken on elevated jets has largely been focussed on the wake region and little attention has been paid to the detailed structure of the flow. Moussa *et al.* (1977) and Eiff *et al.* (1995 & 1997) both provide detailed measurements of the wake characteristics of the flow. Moussa *et al.* measured the 'shedding' frequency behind both a flush-mounted (skirted) jet and an elevated jet for various velocity ratios. For the elevated case it was found that the wake shedding frequency was independent of the velocity ratio and the 'shedding' from the jet was dominated by the shedding from the outer surface of the jet pipe. However, for the skirted case, i.e. the wake from the jet pipe is separated from the jet-wake by a splitter plate, the frequency of the vortical structure in the jet-wake was a function of the velocity ratio. The question of whether the jet sheds vorticity in a manner similar to a solid cylinder, as proposed by Moussa *et al.*, is an issue that needs to be better understood. As stated by Fric & Roshko (1994), in a flow of constant density, vorticity can only be generated at the interface between a solid and a fluid and not at the interface between two fluid streams. Eiff *et al.* therefore argue that the vorticity shed by the elevated jet comes from the inside surface of the jet pipe. The question then arises as to whether the flush-mounted and elevated flow cases are fundamentally different, since it has been concluded by recent authors that the wake-like structures in the flush-mounted case evolve from wall boundary layer fluid and not from jet fluid. Eiff *et al.* suggest that there are two wake regions present downstream of the elevated jet; the pipe-wake region and the jet-wake region. The generation mechanisms of the vortical structures in each are different and they arise from different sources of vorticity, but the structures are linked; a conclusion which is also made by Moussa *et al.* Thus, for the elevated case, the outer jet pipe diameter controls the shedding frequency of both the pipe-wake and jet-wake. A wake mechanism was proposed by Eiff & Keffer (1997), based on spectral measurements taken in the jet wake, is shown in Figure 2-8. However, the details of the formation mechanism of the jet-wake structures, and why it is different to the flush-mounted case, was not resolved.

Differences in the mixing and trajectory between the elevated and flush-mounted cases have been identified by Moussa *et al.* (1977), however a detailed comparison between the two cases has not yet been reported.

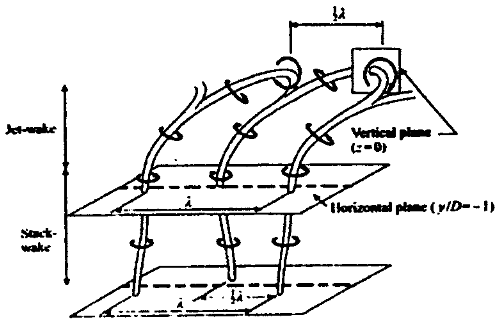

Figure 2-8 Vortex skeleton model of the elevated jet in crossflow proposed by Eiff & Keffer (1997)

2.8 Other Related Work

Given the nature of the flow and its occurrences both in nature and industrial applications, more specific flow cases have also been investigated. Other related flow cases studied include the effect of forcing (Wu *et al.* 1988, Kelso *et al.* 1995 and Diep & Sigurdson 2001), non-circular cross section jets (Wu *et al.* 1988 and Haven & Kurosaka 1997), multiple jet configurations (Toy *et al.* 1993), and swirling jets (Niederhaus *et al.* 1997).

3 Apparatus

3.1 Introduction

To extract as much information from the flows as possible the studies were undertaken in a water channel. The use of water was chosen so as to minimise the flow velocity required for the given apparatus and chosen Reynolds number.

Table 3-1 Values for the density and viscosity of water and air at standard atmospheric conditions (1 atmosphere and 20°C)

	Density (kg/m^3)	Dynamic Viscosity (μ) (Ns/m^2)	Kinematic Viscosity (ν) (m^2/s)
Air	1.2	1.8×10^{-5}	1.5×10^{-5}
Water	998	1.0×10^{-3}	1.0×10^{-6}

Given the values for the density (ρ) and dynamic viscosity (μ) of air and water, as presented in Table 3-1, the ratio of the flow velocities for equivalent flows in water and air based on the Reynolds number can be found by

$$\mathrm{Re} = \frac{\rho_a U_a d}{\mu_a} = \frac{\rho_w U_w d}{\mu_w} \tag{1}$$

where the subscripts a and w represent air and water respectfully. Equation 1 can be rearranged to yield

$$\begin{aligned} \frac{U_a}{U_w} &= \frac{\rho_w}{\rho_a} \times \frac{\mu_a}{\mu_w} \\ &= \frac{998 \times 1.8 \times 10^{-5}}{1.2 \times 1.0 \times 10^{-3}} \\ &\approx 15 \end{aligned} \tag{2}$$

Therefore, the flow velocity required in a water channel is approximately one fifteenth that of the flow in a wind tunnel for the same Reynolds number. The effective slowing of the flow in water means its visualisation is less demanding and allows a better temporal resolution to be achieved. The mechanisms of the flow consequently become far easier to visualise and resolve using conventional visualisation and recording media such as video cameras and still photography.

The experimental work was undertaken in the 0.5m × 0.5m water channel in the Laser Laboratory situated in the Department of Mechanical Engineering at the University of Adelaide. The 0.5m × 0.5m cross-section of the working section of the water channel allowed a larger jet pipe diameter to be used than in most previous investigations. A better spatial resolution is therefore possible allowing a refinement in the visualisation and interpretation relative to previous studies. In addition, by using larger flow apparatus it can be shown that there is also an improvement in the temporal resolution achieved based on the Strouhal number of the flow, given as

$$St = \frac{fd}{U}. \tag{3}$$

Substituting into Equation 3 the Reynolds number given as,

$$\mathrm{Re} = \frac{Ud}{\nu} \Rightarrow U = \frac{\nu}{d}\mathrm{Re}, \tag{4}$$

and rearranging yields,

$$St = fd \times \frac{d}{\nu\,\mathrm{Re}} \Rightarrow St \times \mathrm{Re} = \frac{f}{\nu} \times d^2. \tag{5}$$

Therefore, for a given fluid, Reynolds number and Strouhal number, then $fd^2 = \text{const}$. This implies a doubling of the geometric scaling parameter for the flow, in this case the jet diameter, provides a four times reduction of the frequency of the flow structure. A lower frequency provides a better temporal resolution.

As the water channel facility was new, and no previous work had been undertaken on jets in crossflow within the Department, it was necessary to design and manufacture all of the associated apparatus to provide the necessary flow conditions. These include the components required to produce the jet as well as the imaging equipment. Most of these components were designed and built in-house. The details of the jet apparatus and imaging equipment used in the experiments will be discussed in the following sections, along with the specifications of the water channel itself.

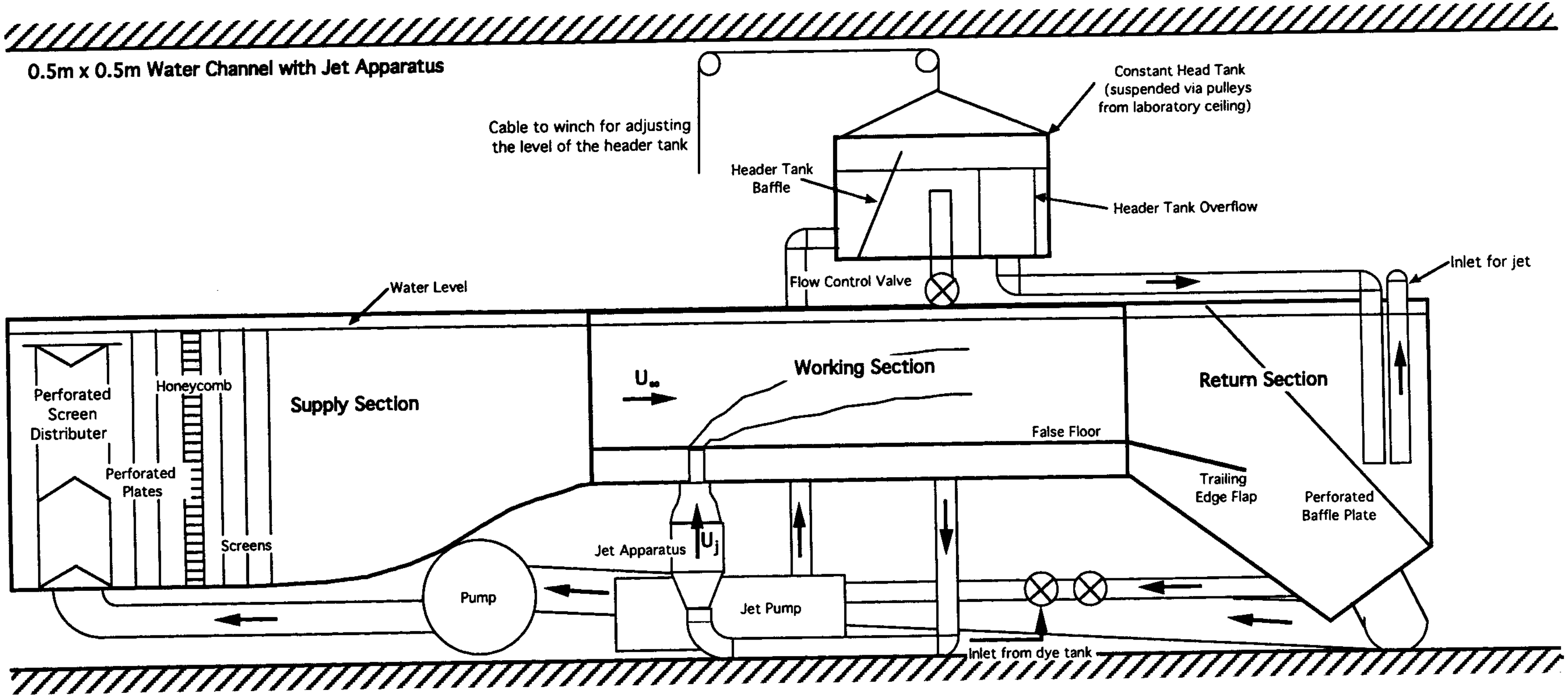

Figure 3-1 Schematic diagram of the experimental arrangement incorporated into the 0.5m x 0.5m closed circuit water channel in the Department of Mechanical Engineering at the University of Adelaide.

3.2 Water Channel

The water channel used for the experiments was a closed circuit channel incorporating a 2m long working section, 0.5m × 0.5m in cross section, shown schematically in Figure 3-1. A working section of these proportions allowed a 50mm diameter pipe to be utilised for the jet flow. A jet pipe with as large a diameter as possible was preferred for the experiments in order to provide the best possible spatial resolution. The channel working section was manufactured from Plexiglass, thus allowing the flow to be viewed from four sides or a laser to be directed through any side. A Plexiglass window was also situated at the return end of the channel to allow the jet to be viewed from a downstream location.

The velocity of the flow through the working section of the channel was controlled via a variable-frequency AC motor driving a centrifugal pump incorporated in the return leg of the flow circuit. The velocity range through the working section of the tunnel was 0m/s to 0.4m/s, allowing a maximum crossflow Reynolds number of 22,500, based on a 50mm diameter jet. For most of the experiments, the channel velocity (crossflow velocity) was fixed at 0.04m/s which allowed a range of velocity ratios up to 8 to be achieved without impingement of the jet on the water surface.

The flow from the pump entered the settling section of the channel through a perforated cylindrical chamber into which were incorporated perforated conical screens. These distributed the flow evenly into the settling section. Before entering the working section of the channel, the flow passed through two metal perforated plates, a honeycomb flow straightener, three fine nylon mesh screens (58% open area ratio), and finally a 4:1 three-dimensional contraction. These were fitted to keep the turbulence level in the working section to a minimum and ensure laminar boundary layers along the walls of the working section.

3.3 Jet Apparatus

Careful consideration was paid to the design and configuration of the jet apparatus in order to provide the best flow and visualisation conditions possible. It was therefore necessary to meet the four following requirements

- to provide a steady jet flow;

- to provide the necessary top-hat velocity profile for the jet flow;
- to allow the visual interrogation of the pipe flow; and
- to fit into the restricted space around the water channel in the laboratory.

The associated components of the jet apparatus consisted of a pump, a header tank, flow control valve and flow meter, a settling chamber, a dye port and the jet pipe, and a false floor. The arrangement of the individual items is shown in Figure 3-1. The apparatus was designed in such a way to make it as flexible as possible to allow for future work.

The jet flow was provided by an Onga Model 663 swimming pool pump that had a capacity of 470 litres per minute into a 3 metre head, and a maximum pressure of 190kPa. The pump was controlled by a three-phase variable frequency controller. The jet flow was pumped either from the return section of the water channel or from a dye storage tank, depending on the nature of the intended experiment.

3.3.1 Header Tank, Flow Control Valve and Flow Meter

In order to produce a uniform jet flow, a header tank was utilised as a reservoir for the jet (Figure 3-1). Its main function was to provide a constant pressure head in order to drive the jet flow at a uniform flow rate. The tank, however, also provided a means of isolating the jet flow from any pressure or flow fluctuations resulting from the flow passing through the pump. Any air bubbles that may have been drawn into the pipe flow system were allowed to escape from the free surface within the tank rather than passing into the jet pipe.

The tank was fabricated from welded 12mm thick PVC sheet. It was fitted with an inclined screen or baffle, shown in Figure 3-1, to reduce any irregularities in the flow into the tank, reduce any waves forming, and to trap and remove air bubbles from the system. The flow exited the header tank through a raised pipe in the bottom of the tank, which was fitted to ensure the fluid was removed in a steady condition from the centre of the tank. The pipe entry was located sufficiently far below the free surface as to avoid ventilation of air into the pipe flow. A second PVC pipe with a 150mm diameter formed an overflow wall within the tank, in order to maintain a constant head. The tank held approximately 150 litres of water.

Two methods were used to control the flow rate of the jet. The first method allowed the head of water between the top surface of the tank and the channel to be varied in order to allow a large range of jet velocities to be generated. To allow the header tank to be moved it was suspended via a winch and pulleys from the laboratory ceiling. In this way the head could be changed from approximately 30cm to 2m. The flow velocity achievable, assuming no flow losses, may be estimated by applying Bernoulli's equation between the tank and pipe exists. The standard result applies, namely

$$V = \sqrt{2g\Delta h}\,. \tag{6}$$

where Δh is the height difference between the header tank and tunnel water surfaces and g is the gravitational acceleration (9.81 m/s^2). This assumes that there is no crossflow in the water channel.

Therefore, the maximum flow velocity for the minimum and maximum heads of 0.3m and 2m respectively are 2.4m/s and 6m/s. However, flow losses in the pipe work between the header tank and jet exit will reduce the actual velocities achievable.

The second method used to control the flow rate of the jet was a 50mm gate valve, termed the flow control valve, installed downstream of the tank. This valve allowed reproducible, fine control of the flow rate into the jet pipe. Using this combined setup produced the very stable flow that was vital for undertaking work at low Reynolds numbers.

To calibrate the jet flow rate, the flow rate of water into the header tank was measured by pumping water from the dye tank through a rotameter and into the header tank. With this flow rate set to the desired value and the dye tank kept at a constant level, the flow control valve was adjusted so that a small flow of water trickled into the overflow pipe. Given the small overflow rate compared with the flow rate supplied to the header tank, the flow rate measured by the rotameter provided an excellent approximation to the jet flow rate. This procedure reduced the number of components and fittings in the flow path between the header tank and the jet exit, thus avoiding the associated unsteadiness and flow losses.

A plug could be fitted into the jet flow pipe within the header tank to stop the jet flow. This was used when the jet fluid was marked with dye to increase the number of experimental runs that could be performed without having to replace the water in the channel due to the background concentration level becoming too high. Using the plug meant the flow control valve did not have to be altered, ensuring consistent flow velocities, and it meant that dye was entering the water channel for only short periods of time when the data were being gathered.

To ensure a consistent dye concentration was achieved between experimental runs, dye was mixed in a separate dye tank. The header tank was initially empty. The plug was then fitted to the inlet of the jet pipe in the header tank and the dyed mixture pumped into the header tank to fill the tank. The pump was turned off once the header tank was full and the valve to the dye tank was closed to ensure the dyed fluid did not flow back into the dye tank. Once an experimental run was ready to be undertaken, the pump was turned on, the dye tank valve was opened and the plug was removed. This procedure ensured that the jet flow was maintained at the pre-set rate and that the dye concentration in the tank remained constant. The data were captured a few seconds later in order to allow the flow to settle down to a steady rate. As soon as the data were captured, the pump was turned off, plug inserted, and dye tank valve closed.

3.3.2 Settling Chamber

A settling chamber was necessary upstream of the jet pipe in order to control the velocity profile of the flow within the pipe. It is vital to ensure the velocity profile of the flow into the jet pipe is as uniform as possible in order to be able to investigate the effect of the crossflow on the jet. Although either a top-hat velocity profile or a fully developed pipe flow is ideal for the experiments, a true top-hat profile is hard to implement with a false floor and dye reservoirs fitted. In addition, it was reported by Andreopoulos (1983) that the influence of the crossflow on the jet flow within the pipe has been observed up to four jet diameters upstream of the jet exit. This would affect the performance of the flow conditioning devices installed within this distance. However, a pipe length of approximately 100 jet diameters, in this case 5 metres, required to achieve a fully developed laminar pipe flow, for a laminar flow, was far from practical in the space available. Therefore, the length of pipe used between the end of the contraction and the pipe exit was chosen to be approximately 5.5 jet diameters in order to fit in the space available and avoid the crossflow affecting the flow within the flow conditioning section.

The settling chamber consists of three components, the layout of which is shown in Figure 3-2. These components consist of a wide-angle expansion and a settling section followed by a contraction. The details of each component will be discussed in the following sections. The design of all of the flow components was undertaken according to the principles outlined in Mehta (1977) and Mehta & Bradshaw (1979).

The contraction used was axi-symmetric with a contraction ratio of 9 to 1, and a length three times the jet diameter. The interior profile was created using a fifth order polynomial between points at 15% and 85% of the contraction length. The plot is shown in Figure 3-3. Both the contraction and expansion were milled from Plexiglass on a CNC machine. Manufacturing these parts from Plexiglass allowed the screens and honeycomb contained within the settling section to be seen from outside in order to check for any bubbles or foreign particles.

The central section of the settling chamber, the settling section, was manufactured from standard 150mm PVC pipe into which a flow straightener, positioned 50mm from the exit, and wire mesh screen were installed. The flow straightener, consisting of 5mm diameter, 40mm long plastic drinking straws, was used to reduce any swirl from the flow due to the upstream bends in the pipes. The screen, placed at the downstream end of the section (where the settling volume and contraction join) was used to even out any variations in velocity across the chamber. The screen was made from a high porosity wire mesh, with a wire diameter of 0.315mm and approximate open area of 58%. Although it is advantageous to have more than one screen, as recommended by Mehta (1977) and Mehta & Bradshaw (1979), the problem of blockage by air bubbles negated the beneficial effect of the extra screens. A single screen could readily be cleared of air by a syphon or brush.

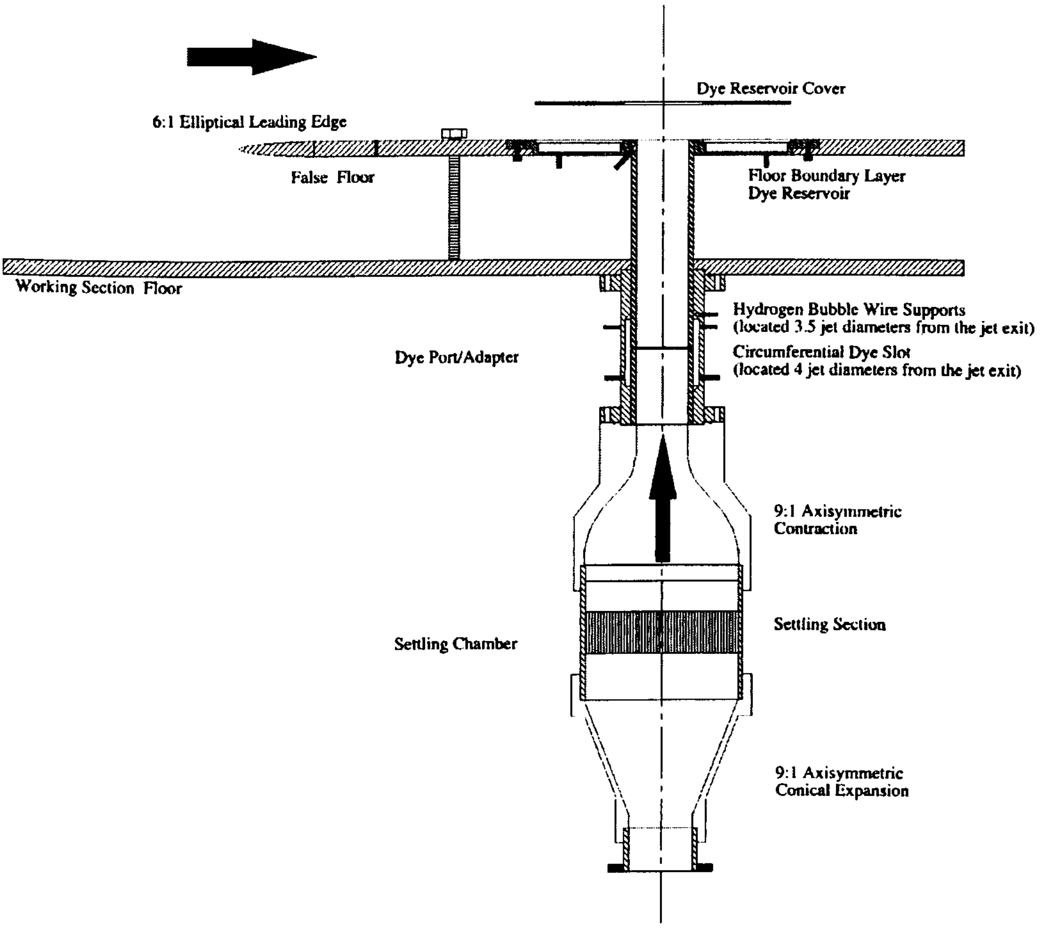

Figure 3-2 The complete layout of the jet apparatus.

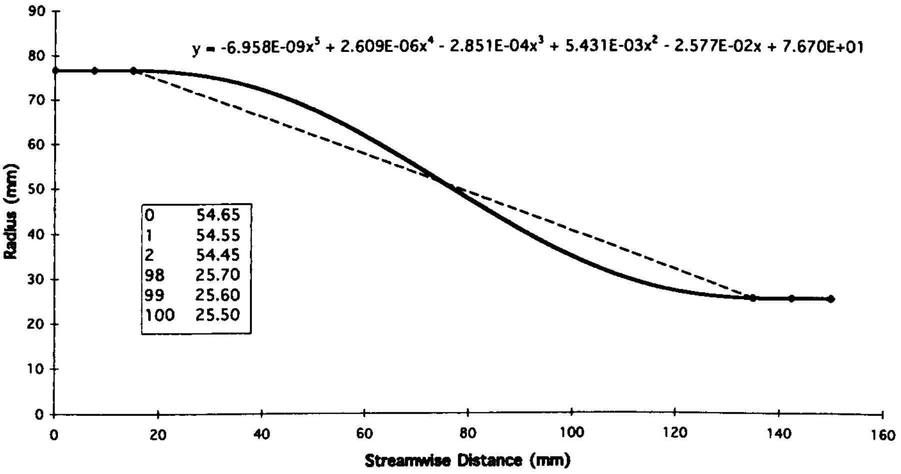

Figure 3-3 The profile used to create the contraction for the jet shown as a solid line (the dashed line is a straight line for reference).

3.3.2.1 Wide-angle Diffuser Performance

Due to the limited space into which the apparatus had to be incorporated under the working section of the water channel, a wide-angle diffuser was necessary to achieve a sufficient area ratio for the contraction. The required diffuser had a total expansion angle of 55° and an expansion ratio of 9:1. Such a diffuser requires a means of ensuring the flow within it does not separate, particularly from the first corner. The performance of the wide-angle diffuser is critical to the stability of the flow it generates.

Mehta (1977) describes several successful designs used for wide-angle diffusers in blower tunnels. The conventional method of ensuring an attached flow in a diffuser is to install a series of curved screens that are fitted perpendicular to the diffuser walls. However, this method has not been widely used with expansion angles as high as was required in this case. In addition, as mentioned previously, it is impractical to place a series of screens into a flow when water is the working fluid, since removing bubbles from the screens is a significant problem. An alternative method of preventing separation, mentioned in Mehta's paper, was used by Gibbings (1973). It involved the use of a single gauze pyramid, positioned in the diffuser with the apex pointing upstream. Gibbings used the pyramid in a wide-angle diffuser with an area ratio of 16.7 and an expansion angle of 54°; a similar configuration to the diffuser required for the current work. Since this method uses a single screen, it was thought to be an appropriate configuration for the current apparatus. The idea of a forward facing cone or pyramid, however, is a variation on the Pope and Goin perforated cone (see Mehta 1977), which is applied in several blow-down supersonic tunnels.

A conical screen with a base diameter of 150mm, the same diameter as the diffuser exit, and a height of 100mm, the same as the length of the diffuser, was therefore fabricated from wire mesh. The wire mesh had a diameter of 0.315mm and an open area ratio of 58%. The screen was fabricated from a 220° arc of wire mesh and formed into a cone with a 10° overlap. To hold the shape, the mesh was sewn together using nylon thread. In order to hold the conical screen in place within the diffuser, the base of the cone was then fastened to a high open area ratio wire-mesh screen that was fitted in the join between the diffuser and settling volume. This additional screen was made from coarse wire mesh with a wire diameter of 0.45mm, an aperture of 2mm and approximate open area of 67%.

Dye visualisation of the flow through the diffuser with and without the conical-screen in place, presented in Figure 3-4 and Figure 3-5, indicated that the conical screen was effective in removing the flow separation from the first corner of the diffuser. However, in order to quantify the effectiveness of the conical screen the velocity profiles at the exit of the settling chamber and contraction were measured with and without the screen in place. The velocity profile from the jet pipe was also determined.

It was deemed that the mean velocity data would be sufficient to determine whether the conical screen was improving the flow. A Pitot-static probe was therefore used for the experiment. The experiment was carried out using air as the working medium instead of water since working with pressure probes is far easier in air than water.

The velocity data was gathered using a 1mm diameter Pitot-static probe connected to a 1 Torr Baratron, the output of which was measured on an HP 54501A 100MHz oscilloscope. A regulated compressed air supply was connected to the inlet of the jet apparatus. The configuration of the jet apparatus for each run was identical to that used to provide the jet flow in the water channel; that is, a honeycomb upstream of the diffuser inlet, a screen fitted at the diffuser exit and the flow straighteners in the settling volume. For the measurements taken with the contraction fitted, the screen was also installed between the settling section and the contraction.

Figure 3-4 Dye visualisation of the flow through the wide-angle diffuser without the conical screen fitted. The flow appears to separate from the first corner of the diffuser as indicated by the dye and also the presence of the bubbles in the recirculation zone on the top inside surface of the diffuser.

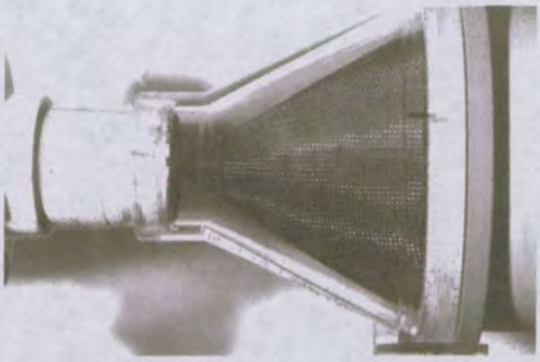

Figure 3-5 Dye visualisation of the flow through the wide-angle diffuser with the conical screen fitted. The flow appears to remain attached to the walls of the diffuser. Note that in this case no bubbles are present in the diffuser.

Each measurement was averaged over a 20 second period on the HP oscilloscope. For each run the data were corrected for the probe offset relative to the jet centreline, measurements converted from volts to velocity, and the velocity profile was integrated in order to determine the bulk velocities and therefore Reynolds number of the flow. The location of the centreline was determined by plotting the velocity data for positive and negative traverse positions on top of one another. In this way the offset of the probe relative to the centreline could be determined, especially by zooming in on the boundary layer region of the plot. A correction factor (half the offset distance) was then applied to the position data to effectively shift the centreline so that the data from the negative and positive positions fitted over one another.

In order to determine the Reynolds numbers of the flows used for each case, the bulk velocity was required. The bulk velocity is based on the flow rate and the cross-sectional area of the section of interest. Since the velocity data, U(r), was only measured along one radial line, the velocity at each data point was assumed to be constant for half the area, A(r). The flow rate was therefore determined by the integration,

$$Q = \tfrac{1}{2}\int_{r=-\frac{d}{2}}^{r=+\frac{d}{2}} U(r).2\pi r.dr.$$

The first velocity measurements, shown in Figure 3-6, were taken at the exit of the settling section (Figure 3-2) with and without the conical screen fitted within the diffuser. Note that the screen was not fitted at the exit of the settling section. The probe was traversed in one plane along the centreline of the settling section, approximately 5mm downstream of the exit. When the conical-screen was fitted, the seam was situated on the measurement plane, on the positive traverse side. The bulk velocity through the settling section was determined to be approximately 2m/s.

As can be seen from Figure 3-6, the flow is vastly improved with the conical-screen in place. Although a velocity deficit and skew still exist the profile is not skewed far to the negative side. The most likely reason for the skew is the upstream flow conditions, caused by bends in the pipes supplying the air. The seam of the screen, positioned on the positive traverse side, may also contribute to the velocity deficit.

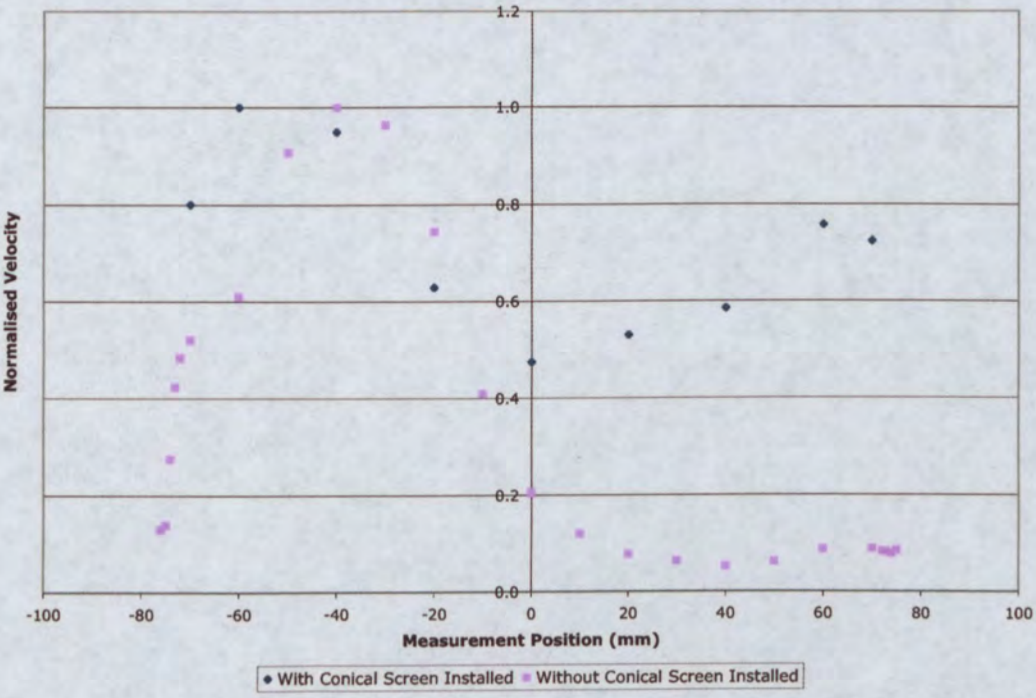

Figure 3-6 Velocity profile taken at the exit of the settling chamber.

3.3.2.2 Contraction Mean Velocity Profiles

A second velocity profile, shown in Figure 3-7, was determined for the flow at the exit plane of the contraction. The data were taken on two planes, 90° to one another, along the centreline of the contraction exit, with the probe positioned less than 5mm downstream of the exit. In order to take the measurements on the second plane, the entire jet apparatus was rotated 90°. On the first traverse, the seam of the screen was placed on the positive traverse side; and for the second, it was 90° out of the measurement plane.

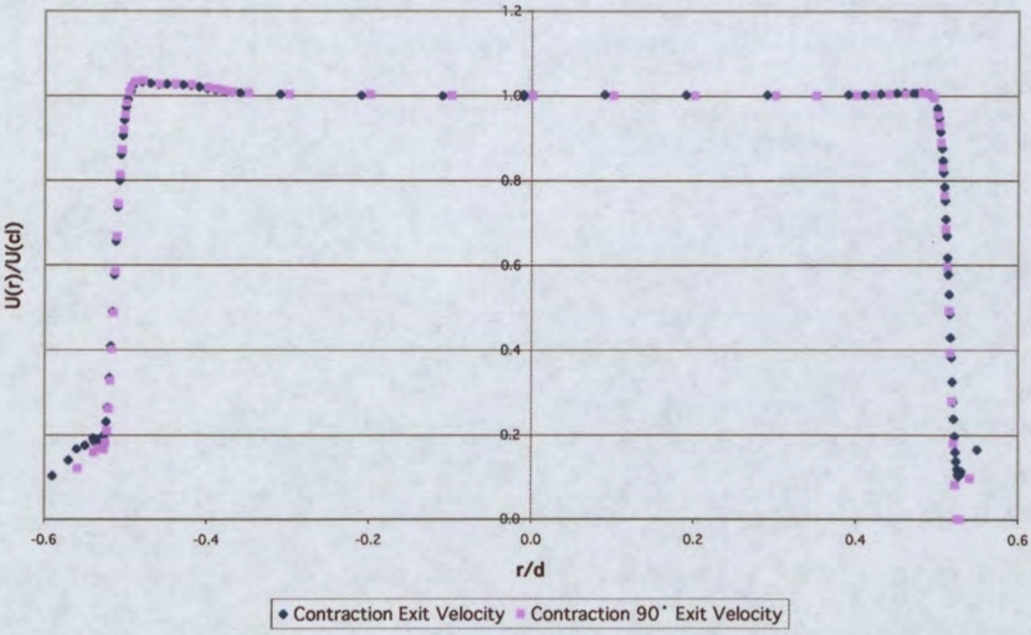

Figure 3-7 Normalised velocity profile taken from the exit of the contraction. The Reynolds number based on the bulk flow velocity and contraction exit diameter was 10,000.

The normalised velocity profile for each measurement plane is 'top-hat' in nature and nearly symmetric about the jet centreline. The data for the two different measurement planes also show extremely good agreement with one another. This implies that the flow is closely axi-symmetric. The only discrepancy between the two sides of the data appears near the jet shear layer. Since it appears in both measurement planes, it is likely to be an effect of the flow conditions upstream of the apparatus.

A third set of measurements, shown in Figure 3-8, was taken at the exit to the jet pipe. The jet pipe is 5.5 jet diameters long, and therefore a developing boundary is present. Two sets of data were taken; one at a Reynolds number of approximately 10,000 and the other at a Reynolds number of approximately 2000. For the low Reynolds number case the two sets of readings were taken on two planes at 90° to one another along the centreline of the contraction exit, with the probe positioned less than 5mm downstream.

The velocity profiles show that the flow is still developing as expected. The results taken on two transverse planes show that the profiles are symmetric about the jet centreline. This implies that the flow is axi-symmetric at the tested flow conditions.

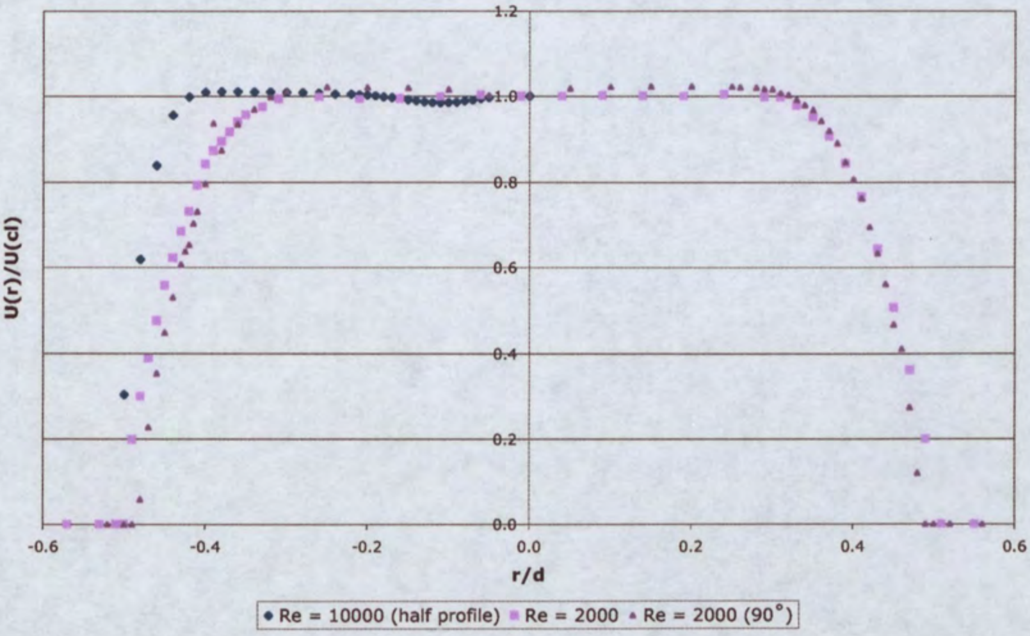

Figure 3-8 Normalised velocity profile taken from the exit to the jet pipe at two different Reynolds numbers; 10,000 and 2000

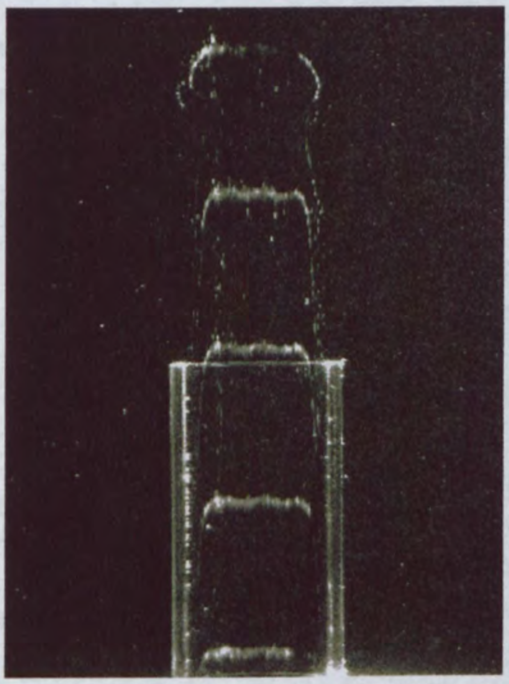

Figure 3-9 Velocity profile for a Reynolds number of 4000, based on the bulk velocity and jet diameter.

3.3.2.3 Jet Pipe Timelines

An indication of the velocity profile within the jet pipe with the jet apparatus installed on the water channel was obtained using a bubble wire, as described in Section 3.3.3. An image of the timelines generated by pulsing the wire is shown in Figure 3-9. In this case the jet velocity is 0.08m/s, which is equivalent to a Reynolds number of approximately 4000, based on the inside diameter of the pipe. The crossflow velocity in this case was zero. As can be observed, the velocity profile is symmetric and shows good agreement with the profiles obtained in air (Figure 3-8).

3.3.3 Dye Port/Adaptor and Jet Pipe

An adaptor, shown in Figure 3-2, was designed to secure the settling chamber to the underside of the working section of the channel, and also to hold and align the jet pipes. In addition, the adaptor incorporated a dye manifold and mountings for a hydrogen bubble-wire. Fabricating the jet pipes and adaptor as separate components allowed different configurations of jet pipe to be used. The adaptor was CNC-machined from Plexiglass. The jet pipes were fabricated Plexiglass tube with a nominal inside diameter of 50mm and wall thickness of 5mm. To ensure that the ends of the pipes were flat and smooth, they were machined after cutting. No machining to chamfer or round the external or internal edges was performed.

Inserting two segments of pipe into the adaptor with a narrow axial gap of no more than 0.5mm, provided a circumferential dye slot and a means of mounting the bubble-wire in the flow. The dye slot allowed the jet boundary layer to be marked, thus providing a means of observing the evolution of the jet shear layer. By changing the length of the pipe, the dye slot could be positioned up to three jet diameters upstream of the pipe exit.

Terminals and supports were incorporated in the adaptor to allow a hydrogen bubble-wire to be installed on the jet's axis of symmetry and aligned with the crossflow. The position of the wire was three and a half jet diameters upstream of the jet exit. The cathode for the bubble-wire was located within the dye manifold in order to be as close to the wire as possible, yet avoided any disturbance to the pipe flow. The bubble-wire was used to determine the effect of the crossflow on the velocity profile within the pipe, and to mark the centreline jet flow so as to visualise the separation and vortex system inside the leading edge of the pipe.

3.3.4 False Floor

A false floor was fabricated and installed in the working section of the channel for the experiments in which the flush-mounted jet case was required. The false floor was fabricated from a 10mm thick Plexiglass plate and sat approximately 115mm above the floor of the working section. The false floor was supported by threaded rods at each corner. These enabled the height of the floor to be adjusted in order to ensure it was level and fitted flush with the jet pipe exit. The jet exit was situated 8 jet diameters downstream of the leading edge of the false floor.

The use of a false floor served a number of purposes. The first of these was to control the boundary layer into which the jet entered, and to avoid interference from streamwise vortices in the boundary layer of the working section floor. The false floor incorporated a 6-to-1 semi-elliptical leading edge, originating at the exit of the channel contraction. The false floor was also fitted with an adjustable trailing edge flap. The angle of the flap was adjusted to ensure that there was no circulation around the floor. The circulation was checked using a pulsed vertical bubble-wire positioned upstream of the floor. The profiles of the timelines were observed. The angle of the flap was adjusted in order to maintain straight vertical timelines as the flow passed over the floor. If the angle of the flap was not correct, a bulge in the profile of the timelines close to the plate was observed, implying an acceleration of the flow over the floor. In addition, the timelines passing above and below the false floor could be observed to ensure there speed was the same.

Another purpose for using the false floor was to allow dye ports and boundary layer control slots to be incorporated in the crossflow wall. A circumferential dye reservoir was machined into the false floor around the jet exit, as shown in Figure 3-2. A brass cover was used to seal the dye reservoir. This allowed a variety of dye slots and ports to be machined into the brass cover, and the cover rotated such that dye could be bled from a series of locations in the floor. The slots could be sealed with tape when not in use. A dye slot across the full width of the false floor was incorporated approximately 5.5 jet diameters upstream of the jet centreline. The slot allowed the boundary layer along the plate to be marked with dye, and also provided a means of sucking the boundary layer, in order to reduce its thickness. A second boundary layer control 'slot' was positioned approximately 2 jet diameters upstream from the jet centreline, consisting of a row of 1mm diameter holes with a centre-to-centre spacing of 5mm drilled into the wall. The spanwise width of the 'slot' was 250mm, half the width of the floor. Below both the slots, channels were fitted to the underside of the false floor. The pipes used to supply the dye or suck the boundary layer were secured into the channels, and trailed beneath the floor, exiting the channel from the return section, in order to minimise any disturbance to the flow.

In addition, the use of the false floor allowed the same jet pipe to be used for both the elevated and flush-mounted jet cases. This ensured that the jet produced in either case had the same development length, which was vital for making a comparison between the two flow cases.

3.4 Laser and Imaging Apparatus

A 5 Watt Coherent INNOVA 90 Argon-Ion laser was used as the laser source for the planar laser induced fluorescence (PLIF) and volumetric visualisation studies. The laser was coupled to the optical elements used in each experiment via a fibre-optic conduit.

Most of the data captured from the experiments was imaged using a Kodak MEGAPLUS ES1.0 10-bit CCD camera. The camera features a 1 inch CCD with 1018 x 1008 pixels and can capture data at a maximum frame rate of 30 Hz. The camera requires a computer for its control and image storage. The camera was controlled by a Pentium IV based computer, with an EPIX video card installed and running EPIX XCAP V1.0.990621 software for Windows NT. The computer was fitted with 786 Mbytes of RAM, of which approximately 690 Mbytes was set aside for the camera. This allowed 330 images to be captured during each experimental run. The image data were stored as either 8 or 16-bit images with no compression. A Sony SSC-M350CE high resolution B&W analogue CCD and Sony DCRTRV900 MiniDV 3CCD camera were also used for some of the work. Still images of the dye visualisation were captured using an Olympus C-2100UZ digital camera.

The storage and processing of the data accumulated in the laboratory were carried out on a Silicon Graphics O2 workstation and a Power Macintosh G3. The O2 computer was purchased due to its ability to handle a high throughput of two channel video data directly from high-resolution cameras. The Macintosh computer was fitted with a Firewire card for easy data transfer between the Sony digital camera, and a 16 GB ultra fast SCSI hard disc for the storage of video data.

4 Experimental Techniques

4.1 Introduction

As has been highlighted in the previous chapters, the transverse jet is a highly complex flow, containing many interrelated flow structures. In the current work a variety of flow visualisation techniques were applied in order to resolve the details of the flow. The present work is purely experimental. Although there is a trend toward numerical investigations of flows at the present time, new experimental investigations can be very beneficial, especially when they utilise modern flow visualisation and image processing techniques. As Werlé (1973, p.361) stated very eloquently "All experimenters know that once a phenomenon is visualised, a large step has been taken toward understanding it and toward solving the theoretical and experimental problems involved". This statement sums up the work that has been undertaken in the current project.

A range of both qualitative and quantitative experimental techniques are available for use in flow visualisation studies. Some of these techniques and their uses are presented in Table 4-1. Two laser-based visualisation techniques were developed for this project that allow the flow structure and concentration field to be investigated in three dimensions, rather than the usual two dimensions. The first, namely the 'Volume Quantitative Time-average Scalar Field Technique', allows the time-averaged scalar field of the flow to be investigated, and provides information such as the jet trajectory, mixing rates, and location of the high concentration fluid within the jet structure. The second, the 'Quasi-instantaneous Volume Visualisation Technique', provides a means of visualising the flow, not only in two dimensions, as has previously been undertaken, but in three dimensions, plus time. Using the three-dimensional data the flow can be viewed from different angles and locations within the flow field.

Velocity and scalar field studies are both important in determining the structure of a mixing flow. However, the majority of the experimental work undertaken in the present study focuses on the scalar mixing field. By obtaining both instantaneous and time-averaged quantitative information about the jet concentration, information may be readily established such as the resulting temperature downstream from a jet, the concentration of a hazardous substance entering the crossflow from a jet, and the trajectory and physical path of the jet.

A description of each technique applied in the current work is given in the following sections of this thesis.

Table 4-1 Examples of Experimental Techniques used in Water and Wind Tunnels

Visualisation Method	Imaging Technique	Uses	Experimental Rig	
			Water Tunnel	Wind Tunnel
Liquid/Gas tracers	Ambient light	Flow structure	Dye, food colourings, milk, inks	Smoke
	Laser	Concentration	Fluorescent dyes	Acetone seeding
Solid tracers	Scattered light	Velocity	Hydrogen bubbles, solid spherical particles, wax	Smoke, titanium oxide particles, soap bubbles
	Scattered light	Velocity and shear	Solid disk shaped particles (mica flakes, aluminium flakes)	
Chemical techniques	Ambient light	Mixing	Iodine solution, indicator method	

Sources: Bradshaw (1970) and Werlé (1973)

4.2 Flow Visualisation Techniques

4.2.1 Spherical Particle Tracers

Particles such as polystyrene beads or hydrogen bubbles can be used as tracers in a flow to define particle paths, velocities or streamlines, depending on the observation time. Quantitative velocity measurements can be made using techniques such as laser speckle velocimetry (LSV), particle image velocimetry (PIV) or particle tracking velocimetry (PTV). The technique used depends on the number and density of particles seeding the flow, or being tracked. The velocity of a particle can be resolved by taking two or more successive images over very small time intervals and dividing the distance the particle travels between successive images by the time interval between the images. Instantaneous streamline patterns of the entire flow field can be determined, assuming the time intervals are sufficiently small, by determining the velocity vectors for every particle or group of particles within the flow. To ensure the particles being observed accurately follow the flow and do not follow a trajectory independent of the local flow structures, the particles must be sufficiently small. A measure of how small they need to be is provided by the Stokes number, defined as the ratio of a particle time scale to a flow time scale, given as

$$S_t \equiv \frac{\tau_p}{\tau_f},$$

The time scale for the particle is defined as,

$$\tau_p \equiv \frac{\rho_p d_p^2}{18\mu},$$

where ρ_p is the density of the particle, d_p is the diameter of the particle and μ is the viscosity of the fluid in which the particle is immersed.

The time scale for the flow is given as,

$$\tau_f = \frac{L_v}{U_v},$$

where L_v is a length scale of the flow and U_v is the velocity of the flow.

If the Stokes number is less than approximately one fiftieth, the particles can be assumed to follow the flow reasonably well (Crowe, Gore & Troutt 1985), which implies

$$d_p < 0.6 L_v \frac{\mu}{\rho_p U_v}.$$

However, determining a value for the length scale of the flow is not trivial and depends significantly on how finely the details of the flow are to be resolved.

The hydrogen bubble technique was first implemented by Geller in 1954 and involves the creation of very small hydrogen bubbles by electrolysis of an electrolytic aqueous solution, usually water (Gad-el-Hak 1989). The electrolysis process is created by placing a very fine wire, of the order of 30 microns, into the water and applying a DC voltage of the order of 30 to 100 volts. The wire acts as the cathode and another nearby electrode acts as the anode. The current may be either pulsed or constant, depending on whether bubble lines or a continuous sheet is required. A pulsed straight wire will create timelines in the flow, whereas a constant current kinked wire will provide streaklines. The particles are viewed by illuminating the plane of the flow containing the bubbles with a beam of light directed from behind the bubbles. Alternatively quantitative or semi-quantitative measurements can be made via one of the particle velocimetry methods mentioned above, or by forming an array of square particle sheets of bubbles which deform in the flow. The latter technique is achieved by coating portions of the wire with insulating paint and pulsing the wire. Measuring the size, shape and separations of the particle sheets provides information about the local velocity, angular velocity and strain in the flow. Wires placed spanwise across a flow can be used to visualise and measure velocity profiles. A spanwise or normal wire configuration is usually used on boundaries to determine the velocity profile of the boundary layer.

4.2.2 Scalar Flow Visualisation

The use of a fluidic marker, such as smoke or dye, as a means of visualising the structures of a jet in crossflow has been extensive. Recent examples of work undertaken in water include Lim *et al.* (1998), Kelso (1991), and Wu *et al.* (1988), and examples of studies undertaken in air include Smith & Mungal (1998) and Fric & Roshko (1994). Fluidic markers fall into a number of categories; those that require energy for visualisation, such as fluorescent dyes; those that use chemical reactions to show mixed regions; and those that are passive, such as food colouring, ink, milk or smoke. A dynamically passive conserved scalar quantity is one that is advected with the fluid and diffuses relative to the fluid, but which is neither created nor destroyed within the flow and which does not directly affect the flow field (Dahm, Southerland & Buch 1991).

A significant challenge of using either smoke or dye as a flow marker is introducing the substances into the flow in such a way that they do not disrupt the flow. When introducing dye into boundary layers the dye slots must be small, and the flow rate of dye must be such that it is not injected, but 'bleeds' into the flow and is then transported with the flow. Dye slots with a width of 0.5 mm, which from previous experience have been found to work well, were used during the current studies. As described by Bradshaw (1970), introducing dye into the free stream entails an additional challenge, namely the interference to the flow from the dye probe. It is necessary, as much as possible, to prevent the wake from the dye probe becoming turbulent and therefore influencing the flow field downstream. This constraint effectively confines the technique to low velocity flows, however a number of remedies are available to mediate the problem. Where possible, the smoke or dye should be emitted from short pipes located in the trailing edge of a streamlined aerofoil section. In some cases boundary layer suction can be applied to the streamlined support in order to prevent the flow separating and therefore forming a large wake. In addition, locating the probe in or ahead of the contraction of the water tunnel, where a favourable pressure gradient exists, assists in minimising the size of the disturbance. Alternatively, the probe can be placed upstream of the final screen in the settling section of the tunnel, with the dye pipes projecting through the screen, so that the velocity defect in the wake is reduced. Care also needs to be taken with the lighting when photographing smoke or dye flows to ensure shadows or reflections from the walls of the tunnels or probes do not occur.

As emphasised by Goldstein and Smits (1994) in a smoke visualisation study carried out in a wind tunnel, "one of the greatest limitations of flow visualisation studies is the uncertainty as to whether the smoke actually tags the pertinent vortical structures, and whether the smoke then follows the structures as they convect and evolve". The same concerns exist in flow studies in water tunnels where dye is assumed to be a marker of the vortical structures. Further, it is important to realise that the mixing and therefore the flow observed using dye in a water tunnel may differ from that of smoke in a wind tunnel. The discrepancy comes about due to the difference in the molecular diffusion of different fluids.

Dye introduced at places where vorticity is generated, namely at solid boundaries in the case of an incompressible fluid, will follow the vorticity if the effects of viscous diffusion are small. However, the effects of diffusion can only be neglected during the initial roll up of vortices or in the early stages of development of a jet, wake or boundary layer (Perry & Chong 1992). Morton (1995) highlights this problem by emphasising that the rate of diffusion of the dye in unsteady flows is some three orders of magnitude slower than that of the vorticity. It is important therefore that this difference is considered when interpreting dye traces in an unsteady flow field. Hence, it can be concluded that dye can be used as a means of indicating the position and geometry of vortex sheets but must be carefully introduced into the flow in order to ensure interpretation of flow is accurate.

The above effects are characterised by two parameters. The first is the molecular Schmitt number, Sc, which is defined as the ratio of the momentum diffusivity (viscosity) to the molecular species concentration (or mass) diffusivity. The second is the turbulent Schmitt number, Sc_t, defined as the ratio of the momentum diffusivity by turbulent transport to the mass diffusivity by turbulent transport (Goldstein and Smits 1994). Also of importance is the location at which the marker is introduced into the flow. A Schmidt number (molecular or turbulent) near unity, therefore, implies that the molecular diffusivity of a marker or scalar is comparable to the momentum diffusivity. In most flow cases, such as the mixing of constituents in industrial processes, however, the molecular diffusivity of the scalar is much smaller than that of the vorticity, so that the molecular $Sc >> 1$. For smoke in air the molecular Schmitt number is of the order of 1000, which implies that the vorticity diffuses at a much higher rate than the smoke (Goldstein and Smits 1994). A suggested value for the Schmidt number of fluorescein dye in water is 2075 (Dahm *et al.* 1991). It has been determined by Dahm *et al.* (1991) that for a large range of Schmidt numbers (2 to 1000), many fine scale features of a turbulent scalar field are relatively invariant.

4.2.3 Planar Laser Induced Fluorescence

Planar Laser Induced Fluorescence (PLIF) is a very powerful flow visualisation technique that allows both qualitative and quantitative information about the scalar field of a flow to be determined. The technique is non-intrusive, effectively instantaneous and can be used to gain concentration information across a complete plane within the flow. It has been used by many researchers to investigate jets in crossflow, including recent work by Smith & Mungal (1998), Kelso, Perry & Lim (1997), Haven & Kurosaka (1997) and Kelso (1991).

PLIF utilises a laser formed into a two-dimensional sheet to illuminate planes within the flow field. A fluorescent dye is injected into the flow to act as a form of molecular marker that absorbs the laser light and then radiates it at a different distinct wavelength (colour). The marked parts of the flow can then be captured using either still or video imaging techniques. The use of a molecular marker ensures that minimal disruption occurs in the flow and that a high spatial resolution can be obtained. There are many fluorescent dyes available for use in water, and more than one may be used at a time, thus allowing dyes that fluoresce with different colours to be used simultaneously.

The main requirement for selecting a dye is that it will absorb radiation at the frequency that is produced by the laser in use. It is also important for gathering concentration data that the absorption properties of the dye are known. In the case of the PLIF work undertaken in the current thesis, fluorescein is used as the scalar marker, since it provides high quantum efficiency, a highly linear response and is readily available at low cost.

Concentration information can be obtained from the image data by calibrating the image intensity information against a known intensity, and by determining and correcting for any irregularities within the laser light or the flow. The technique is significantly simplified since the intensity of the fluorescence is linearly proportional to both the concentration of the dye and the intensity of the laser sheet at the point of measurement.

4.2.4 Critical Point Theory

The visualisation of a flow is a very useful technique to give an idea of the entire development of a flow at a glance. It can be very satisfying to look at a flow and obtain an insight into it without the need for any data processing. However, the interpretation of a flow field is difficult and can lead to differing opinions, particularly for complex unsteady flows such as a jet in crossflow. One technique that was established to classify the features in a flow and minimise ambiguities is critical point theory. Critical point theory (CPT) provides a means of describing and interpreting a complex and unsteady flow field. The theory helps in understanding which features to look for in a flow and how to make sense of a flow. CPT offers an unambiguous terminology to describe complex flows and thus an appropriate means of classifying similar features in flows of widely varying configurations. A detailed description of CPT and its terminology can be found in Hornung & Perry (1982) who established a "vocabulary of well-defined terms for the description of three-dimensional steady separated flows" as an aid to prevent misconceptions with flow interpretations. Perry & Chong (1987) extend this work and demonstrate how critical point concepts can be applied to the interpretation of velocity fields. They state that critical points are "the salient features of a flow field; given a distribution of such points and their type, much of the remaining flow field and its geometry and topology can be deduced, since there is only a limited number of ways that the streamlines can be joined". In the current work, the concepts of CPT were considered in order to aid in the interpretation of the flow, and to assist in identifying flow features.

4.3 Volume Flow Visualisation Techniques

The present study involved the investigation of the near-field structure and mixing of low Reynolds number transverse jets. Due to the highly three-dimensional nature of the flow, volume visualisation techniques were developed and used during the experimental program to investigate both the mixing and structural aspects of the flow. Most present flow visualisation techniques are largely planar and therefore provide only two-dimensional information about a flow. Using dyes or other fluid markers provides a means of seeing the three-dimensionality of a flow, but capturing three-dimensional information on video is not possible. A second disadvantage is that only the external flow features can be observed. Techniques involving particle tracers or fluorescent dyes allow the interrogation of the internal features of the flow, with little or no disturbance. However, until recently such techniques have largely been limited to planar studies.

In order to achieve a more complete picture of the entire structure of the flow, two three-dimensional imaging and presentation techniques were applied. To investigate the mixing, a quantitative volume technique was used to determine the three-dimensional time-averaged concentration field. In addition, a volume visualisation technique was used to investigate the instantaneous structure of the jet in three dimensions. Details about the implementation of both techniques are discussed in the following sections.

4.3.1 Volume Quantitative Time-averaged Scalar Field Technique

4.3.1.1 Introduction

Quantitative measurements of the concentration field provide a means for determining the levels of mixing obtained in a flow or the rate of dispersion of a fluid. The information obtained is useful for any type of application in which a fluid is discharged into a secondary stream. In the case of the control of the discharge of pollutant into a body of water or the atmosphere, it is important to be able to predict the rate of dispersion of the pollutant.

In the case of the transverse jet it is difficult to get a complete understanding of the mixing mechanism, particularly in the near-field, due to the highly complex three-dimensional nature of the flow. This difficulty is primarily because of the way in which the jet fluid is drawn into the counter-rotating vortices, which are not only rapidly deflected in the direction of the crossflow, but also diverge from one another. Smith & Mungal (1998) and Smith, Lozano, Mungal & Hanson (1993) undertook a detailed investigation of the mixing of transverse jets. The research was undertaken on jets with high velocity ratios and Reynolds numbers and dealt with the far-field mixing. In addition, the work focused on the plane of symmetry between the vortices of the counter-rotating vortex pair. This work has made a significant contribution to our understanding of the flow. However, it is unclear whether measurements on the plane of symmetry give a complete picture of the global development of the JICF structure. The technique developed here sought to extend the previous studies by gathering and analysing scalar concentration data on additional sectional planes and in particular to investigate the mixing along one of the counter-rotating vortices.

The CVP is assumed to have the largest influence on the far-field mixing characteristics of the jet in crossflow and is believed to be the reason that the flow has enhanced mixing compared with a free jet. For this reason the formation, strength and trajectory of the CVP are important properties of the flow. To provide a better understanding of these it was therefore thought that the concentration profiles along the trajectories of the CVP would offer a better insight into the mixing of the flow than measurements on the plane of symmetry.

Although the counter-rotating vortices are easy to identify by experimental techniques, predicting their location and trajectory at any instant in time or for different flow cases is difficult due to the unsteady nature of the flow. It is therefore not possible to accurately align a laser sheet through the core of the CVP vortices in order to gather the data necessary to generate the required concentration plots. Therefore, a technique was established whereby the concentration profiles were determined from data gathered on a series of sectional planes within the flow. The data were combined into a three-dimensional grid and the time-averaged trajectory and concentration values determined.

4.3.1.2 Technique

The concentration profiles were obtained using PLIF as described in Section 4.2.3. By comparing the concentration profiles for the cases investigated, it was possible to establish differences in the mixing levels. As previously stated, PLIF is a very valuable technique for flow analysis as it provides a non-intrusive means of interrogating the flow structure along any plane and can also be used as a means of determining the concentration of a scalar within the flow field being visualised. The concentration profiles were determined from data gathered on a series of planes within the flow. The images at each plane were averaged, and then combined, using three-dimensional rendering software, to form a three-dimensional mean concentration plot for each flow case.

4.3.1.3 Experimental Arrangement

To measure the jet concentration, Fluorescein dye, in a concentration of 0.5mg per litre of water, was mixed with water in the dye tank. This dye concentration was found to give a good signal strength whilst minimising the contamination of the background fluid during the run time of the experiments. The water dye mix was then pumped into the header tank to provide the jet fluid. Pre-mixing the dye ensured the jet concentration was uniform, although this limited the experimental run length. Since the source of water for the crossflow and jet were different, the temperatures of the two water sources were ensured to be within 1°C of one another at the beginning of each experimental run, in order to make sure any buoyancy effects were minimised.

The Argon-Ion laser, via the fibre-optic conduit, was used as the laser source to excite the dye fluorescence. A laser sheet was formed using three optical elements that were all mounted on a traverse above the working section of the channel. The optics produced a 4mm thick light sheet in the xy-plane which could be moved in the z-direction. A wide laser sheet was used in order to effectively spatially average data in the z-direction in order to provide to better resolve the concentration between the planes. The spreading beam emerging from the fibre was collimated using a 25mm diameter achromat with an effective focal length of 42mm. A 1000mm spherical lens was then used to focus the collimated beam to a point approximately in the centre of the imaged area. A 12.5mm cylindrical lens was then used to spread the focussed beam. The spreading angle of the laser sheet was approximately 75°. A false ceiling of Plexiglass was mounted on the working section to avoid refraction effects due to surface waves on the water.

Since the data for an entire volume was being captured on separate planes, it was important to ensure the intensity levels captured on each plane were as consistent as possible. In order to ensure this consistency the entire data set for each flow case investigated was captured. In addition, enough dye was measured out for five tank-fulls of dye to be mixed in order to reduce any measurement errors and ensure the concentration used was similar for the four flow cases investigated. In order to minimise the amount of dye used during each run, and allow a sufficient number of images to be recorded, the procedure outlined in Section 3.3.1 was used.

Data were captured along 10 parallel planes, at 12mm intervals, beginning at the jet centreline (z = 0) and across 2 jet diameters to z = 108mm. Therefore, only one half of the flow was captured for each flow case. At each plane, 100 images were captured at a frame rate of 30 frames per second using the Kodak MEGAPLUS ES1.0 camera. Although a larger data set, recorded over a longer time period, would have been beneficial, a compromise was made in order to allow the data to be gathered using a single batch of dye for each flow case, as discussed above. A 12.5mm fixed focal length lens was used which provided an imaged area of approximately 1 metre square, on the jet centreline. The lens aperture was set to the lowest available f-stop of 1.4, and a filter was placed in front of the camera lens to remove any scattered laser light from the images. A laser power of 1.5 Watts (at the laser output) was used. The exposure for each image was set at 25 milliseconds. This is long exposure in terms of the flow movement (the flow not frozen) but since the data were to be averaged, achieving a good signal was thought to be of more importance than freezing the flow. A maximum pixel intensity of over 250 out of 1024 levels was able to be achieved using these configurations (comparable to an 8-bit image). The images were stored as 16-bit TIFF images with no compression.

4.3.1.4 Image Correction

In order to extract the concentration data from the images, corrections had to be made to correlate the intensity levels in each image to the concentration level of the jet. Each image was individually corrected before being averaged. All of the processing of the data was undertaken using MATLAB. The data were corrected for background dye signal, the intensity variation across an image due to the spreading of the laser sheet, and the absorption of the laser as it passes through the dyed region of the flow using the scheme,

$$C_{ij} = N \times \frac{(S_{ij} - SB_{ij})}{(L_{ij} - LB_{ij})},$$

where C_{ij} is ijth element of the corrected image, N is the factor to normalise the image by the 100% intensity level, S_{ij} is the image captured during the ijth element experiment, SB_{ij} is the ijth element of the averaged background image, taken before each experimental run,

L_{ij} is the corrected laser sheet profile and LB_{ij} is the averaged background laser profile image.

Therefore, for each data set, in addition to the flow data, a series of background images were also required to be captured before each run. Ten such background images were captured prior to each run with the laser on, the crossflow on, but the jet off. In addition, a series of images was taken of the laser sheet passing through a uniformly dyed section of the channel. This was achieved by isolating a section of the channel working section with Plexiglass plates, and adding a small quantity of dye to the isolated section. As small a quantity of dye as possible was added to attempt to produce a sheet with little absorption of the laser, but with a sufficiently strong signal. A background image for this configuration was also taken with the laser on but no dye in the section.

Before any processing was undertaken on an image, it was cropped and the intensity values converted to 32-bit floating point format. The cropped images were approximately 8 jet diameters wide by 6 jet diameters high. The background and laser profile images were also processed using the same routine and then averaged to use in the correction scheme. A laser profile image was only captured for the jet centreline image. No account was made for perspective.

An alternative processing scheme was also applied as detailed in Smith *et al.* (1993). In this scheme a modified laser sheet profile was required to be generated for each image, and used in place of the general laser sheet profile was also applied. The modified profile accounts for the absorption of the laser light as it passes through any regions of dyed fluid. However, by comparing the results from both schemes, it was found that the absorption in the data collected was negligible, and therefore the basic scheme was found to be adequate.

4.3.1.5 Volume Data Processing

In order to establish any near-field differences between the jet configurations tested, the trajectory of the jet on the plane of symmetry and the trajectory of the high concentration fluid off the plane of symmetry were used. To generate plots of concentration along both trajectories it was therefore necessary to be able to locate the high-concentration points from the concentration data. The process of determining the trajectories is complicated due to the bending of the jet that occurs in the near-field. Therefore, the data was interrogated on two orthogonal planes to locate the points of interest. Close to the jet exit (y = 0 to 0.5 Rd) where the jet remains approximately vertical (aligned with the y-axis) the data were analysed on xz-planes. As the jet progresses and becomes aligned with the crossflow (x-axis) from about x = 0.5Rd the data were analysed along yz-planes. Data were gathered on planes with a spacing of 10 pixels on both the xz- and yz-planes.

The locus of fluid with the highest intensity off the jet plane of symmetry was used to determine the location of the CVP. It has been established that in the far-field the region of high concentration marks the location of the CVP cores (Smith & Mungal 1998). Although at the jet exit the high intensity jet fluid will occur along the jet's plane of symmetry, an indication of where the CVP formation begins and how the jet fluid is transferred to the CVP can be made by determining at which stage the fluid moves away from the plane of symmetry. The trajectory of the CVP was therefore found by constructing a contour plot on each interrogation plane with a single contour line at an intensity level of 80% of the jet exit concentration. The average of all the points in the two axial directions on the plane was used to provide the coordinates of the centre of the CVP for the plane of interest. The plots in Figure 4-1 and Figure 4-2 graphically show the technique applied to the concentration data for the flush-mounted jet at a velocity ratio of 2. The plot in Figure 4-1 shows a side view of the data. The black horizontal lines show the edge view of the 80% contours on the xz-planes whereas the red vertical lines show the edge view of the 80% contours on the yz-planes. The blue asterisks indicate the location of the maximum concentration on the plane of symmetry, whereas the green asterisks indicate the centroid of the contour, used to define the location of the CVP. The vertical location of the contours fits well with the expected side profile of a JICF. The plot shown in Figure 4-2 shows the same information as that in Figure 4-1 except the data are viewed from a position upstream of the jet looking downstream toward the jet. The right hand side of the plot represents the axis of symmetry of the jet. As can be seen the data in the z-direction is rather coarse in the z-direction although the profile of the contour plots suggests that of one half of a kidney shape, as would be expected for a cross-section through one of the vortices in the CVP.

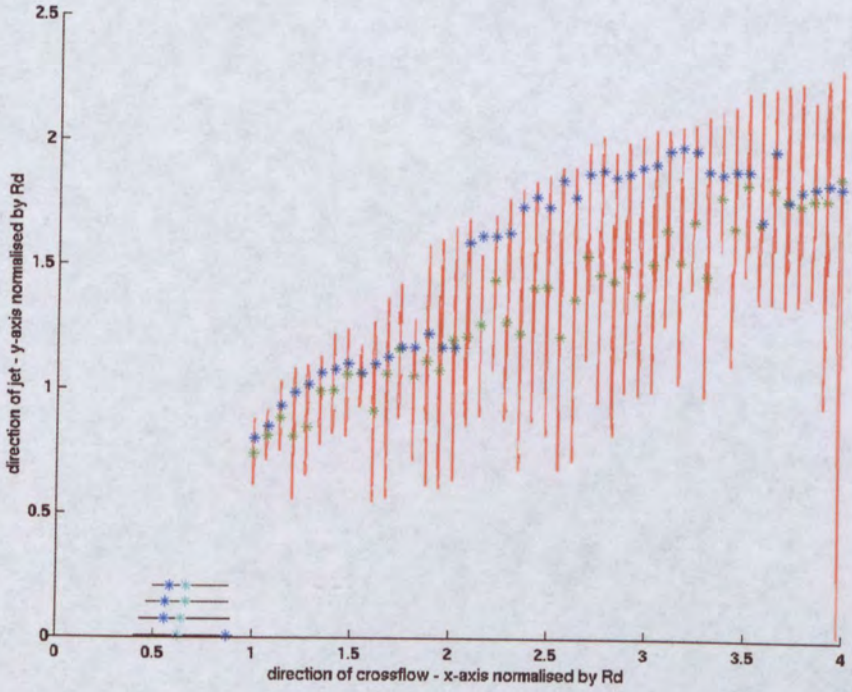

Figure 4-1 R=2, flush; side view of CVP contours and CVP & jet centreline trajectories.

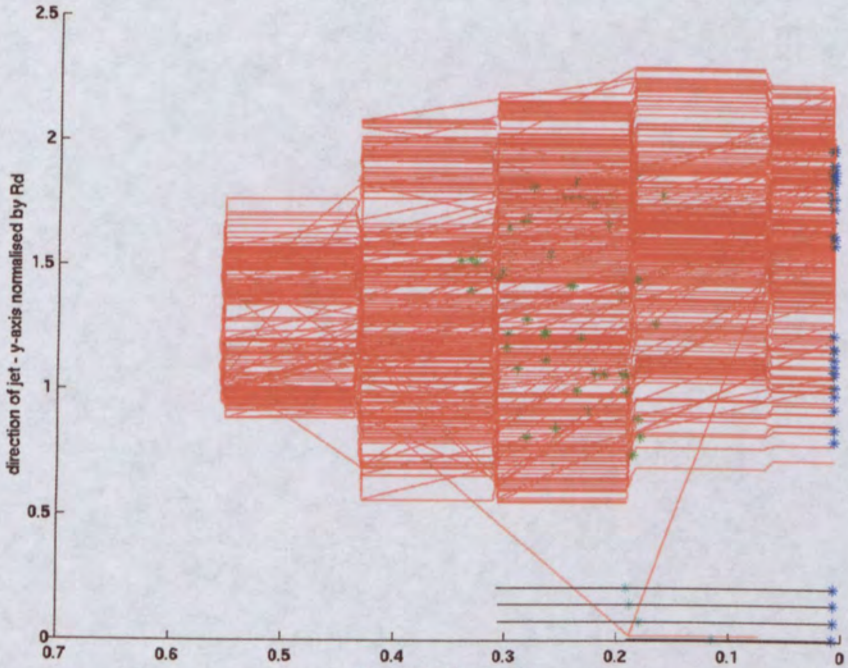

Figure 4-2 R=2, flush; front view of CVP contours and CVP & jet centreline trajectories.

4.3.2 Quasi-instantaneous Volume Visualisation Technique

4.3.2.1 Introduction

A number of authors have used techniques to capture the three-dimensional nature of a flow (Prasad & Sreenivasan 1990, Dahm *et al.* 1991, Dahm, Su & Southerland 1992 and Kelso *et al.* 1993, among others). The techniques, however, have been confined to either small areas of the flow or cover very short time intervals. Prasad & Sreenivasan (1990) performed a quantitative three-dimensional mapping of the turbulent field of a passive scalar within a jet flow. The authors were able to acquire a sequence of 16 images at a frame rate of up to 104 frames per second. Dahm *et al.* (1991) provided a technique, further refined in Dahm, Su & Southerland (1992), for capturing four-dimensional measurements of the fine scale structures a turbulent jet by imaging the scalar concentration field. The imaged area, however, was required to be very small compared with the overall length scale of the flow in order to capture the fine scale structures of the flow. Other authors including Brücker (1995), Garcfa & Hesselink (1986), Brücker & Althaus (1992) and Goldstein & Smits (1994) have developed various techniques for performing volume visualisation of different flows, but do not provide a data set with as many time steps, nor which covers as larger volume as that proposed here. The rotating drum PLIF based volume scanning technique, similar to that proposed in the current study, was implemented on a JICF by Kelso *et al.* (1993) and Delo & Smits (1997). These studies proved it a useful technique in the determination of the formation and evolution of such a flow. The current implementation of the apparatus and data processing schemes, however, has all been the current authors work.

Various experimental techniques have been applied to perform volume visualisation. However, the two main techniques make use of either oscillating mirrors or a rotating scanner. All of the techniques use PLIF in order to capture the structure of the flow. Drum scanners are particularly suited to volume studies since they provide a means of forming laser sheets on different, distinct planes.

4.3.2.2 Apparatus and Experimental Arrangement

For the volume work undertaken in the present study a rotating drum scanner was used to generate the laser planes within the flow. The design of the scanner evolved from a system developed at Princeton University by Delo, Kelso & Smits. A drum scanner, shown schematically in Figure 4-3, works on the following principle. Square reflecting surfaces, at a 45° angle to the vertical, are positioned around the circumference of a rotating cylinder or drum. A laser beam aligned parallel with the rotational axis of the drum is directed onto the surfaces from above. As the drum rotates, the reflecting surfaces reflect the beam at right angles to the incoming beam. In addition, due to the rotation of the drum, the beam is swept through an angle defined by the width and number of reflecting surfaces. By mounting the reflecting surfaces in a helical arrangement around the drum, each sweep of the laser (or 'sheet') occurs at a different height. The assembly therefore causes the laser to scan through the entire flow once for each revolution of the scanner. An example of the experimental arrangement used to capture a jet in crossflow is shown in Figure 4-4.

The advantages of a drum scanner over oscillating mirrors are numerous. First, it allows a relatively large volume to be scanned. In addition, the spacing between the sheets is variable. This means the spacing between layers can be varied over the volume depth, allowing regions of particular interest to be scanned at a higher resolution, while still capturing the overall large-scale structure. An extension of this is that by placing two adjacent mirrors close together, the system could be used for PIV. This effect may also be achieved with oscillating mirrors by varying the frame rate of the camera. Also, since the positions of the reflecting surfaces are fixed, rather than continuously moving as with the rotating mirrors, it is easier to align, and set up.

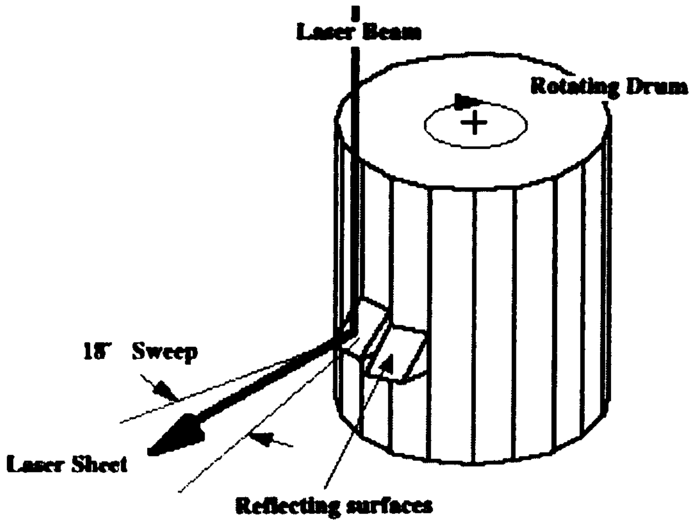

Figure 4-3 Rotating drum with reflecting surfaces to sweep the laser beam through an angle of 18° at different depths through the flow.

The major disadvantage of a drum scanner is that only a set number of sheets can be produced, given by the number of reflecting surfaces used. This results in a limitation in the spatial resolution of the scanned volume that can be achieved. Although building a drum with a large number of sides is possible, the more reflecting surfaces used the smaller the swept angle of the laser. Therefore, to image the same area the scanner must be placed further from the plane of interest which may be impractical within the space available and make alignment more difficult.

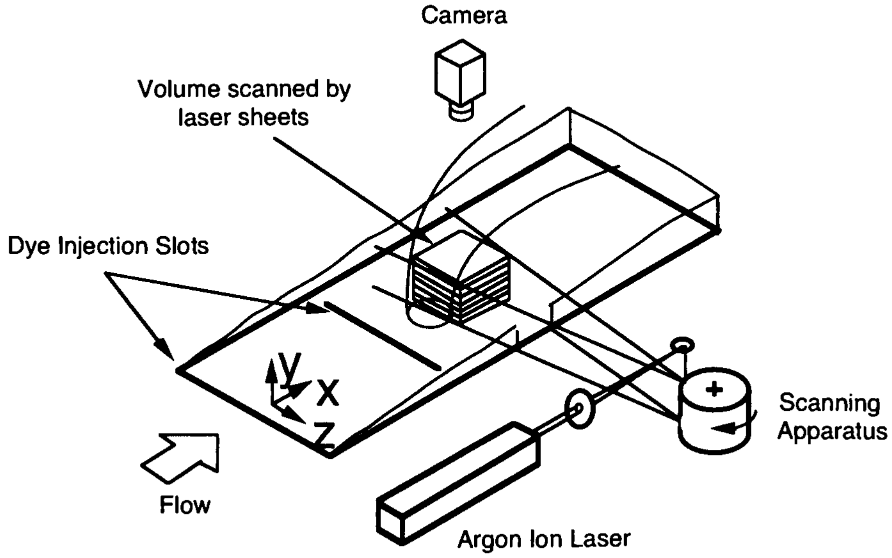

Figure 4-4 Experimental arrangement of the laser scanning equipment.

4.3.2.3 Scanner Drum Design

It was decided that for the present work, a drum with twenty sides would be the most feasible in terms of the number of laser planes generated and the ease of manufacture and general use of the system. Such a drum sweeps a laser beam through a maximum angle of 18° to produce 20 laser sheets for each rotation. In order for the scanner to be easily mounted in any orientation and installed safely above the working section of the water channel it was designed to be as compact and light as possible. The scanner drum was machined from 101.3mm outer diameter aluminium tube with a wall thickness of 6mm. The drum was 220mm in length, which allowed a volume with a depth of approximately 200mm to be scanned. Dove-tail slots were machined into each face of the tube as guides for the optical supports, which held the mirrors, and to provide both transverse and lateral restraint. A detailed cross-section of the drum is given in Figure 4-5. Spring clips, incorporated in the back of each optical support, as shown in Figure 4-7, provide additional support against vibration or movement of the optical supports.

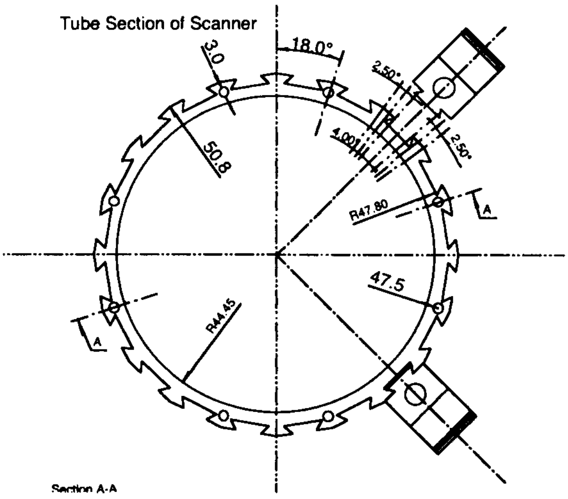

Figure 4-5 Cross-section of the drum scanner.

To build as much adjustability as possible into the scanner, each of the optical supports could be moved independently through a distance of 200mm, or approximately half the depth of the working section of the water channel with the false floor installed. The location of the optical supports was controlled via threaded shafts with a 1mm pitch that allowed precise and reproducible positioning of each laser sheet independently. The arrangement of the shafts and the drum assembly is shown in Figure 4-6. With an accuracy of 5° in the alignment of the shafts, this provided an accuracy of approximately 1/100th of a millimetre in the location of the optical supports. The spacing between the full twenty laser planes when they are evenly distributed could therefore be varied from 0mm to 10mm.

The drum scanner was supported on a central shaft mounted in two roller bearings in the drum housing, as shown in Figure 4-6. The drum housing was fabricated from 10mm thick aluminium plate in order to provide stiffness to the structure. Supporting the drum on two bearings provided additional stiffness and allowed the drum to be used in both a horizontal and vertical alignment. Both the scanner drum and drum housing were modular and bolted together to allow any modifications to be easily implemented to meet future requirements. The central shaft both supported the scanner and connected the drum to the motor. An important requirement was that the bearings must fully support the drum in the axial direction, so that no axial load was placed on the motor.

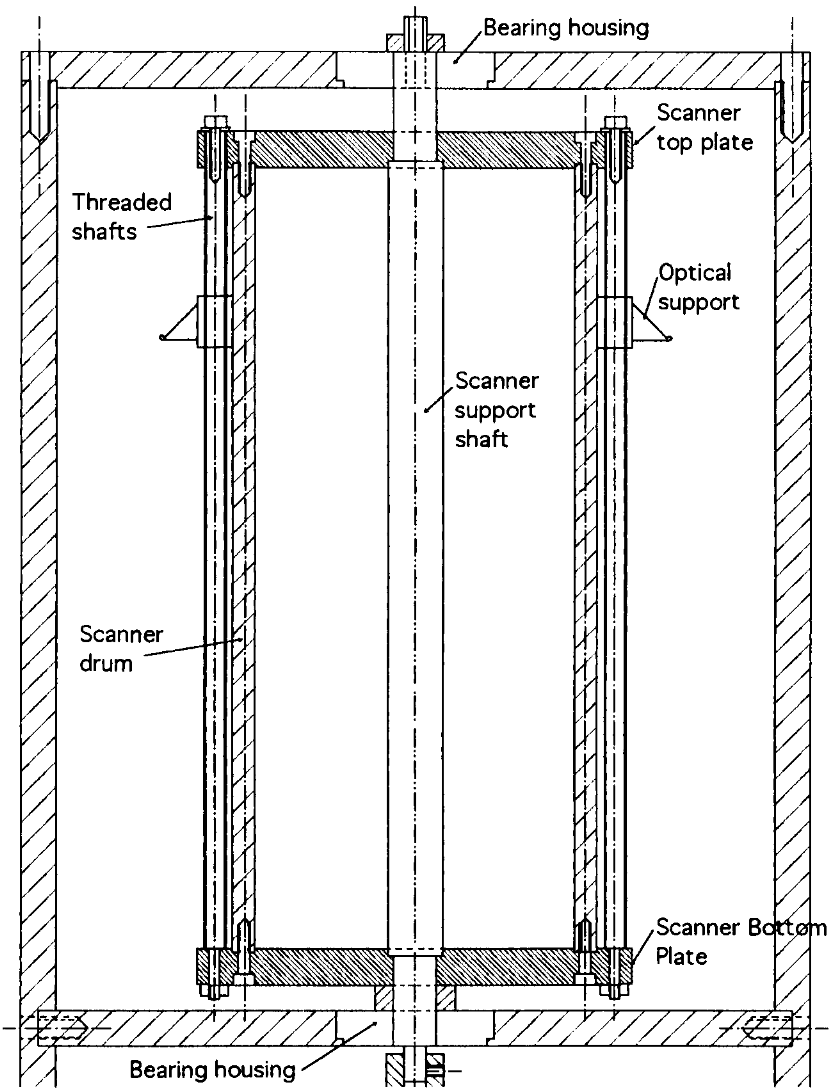

Figure 4-6 Scanner drum in support.

4.3.2.4 Reflecting Surfaces

The design of the optical support platforms that hold the mirrors is shown in Figure 4-7. The mirrors were fabricated from 1mm thick glass microscope slides cut into pieces 15mm × 7mm. The reflective surface was produced by vacuum depositing a layer of aluminium on the front surface of each piece of glass. This technique is reported to produce a reflectance of 90%, although the surface deteriorates with time. Glass was used for the reflecting surfaces rather than depositing aluminium directly on to the mirror platforms. This ensures that the reflecting surface is as flat as possible.

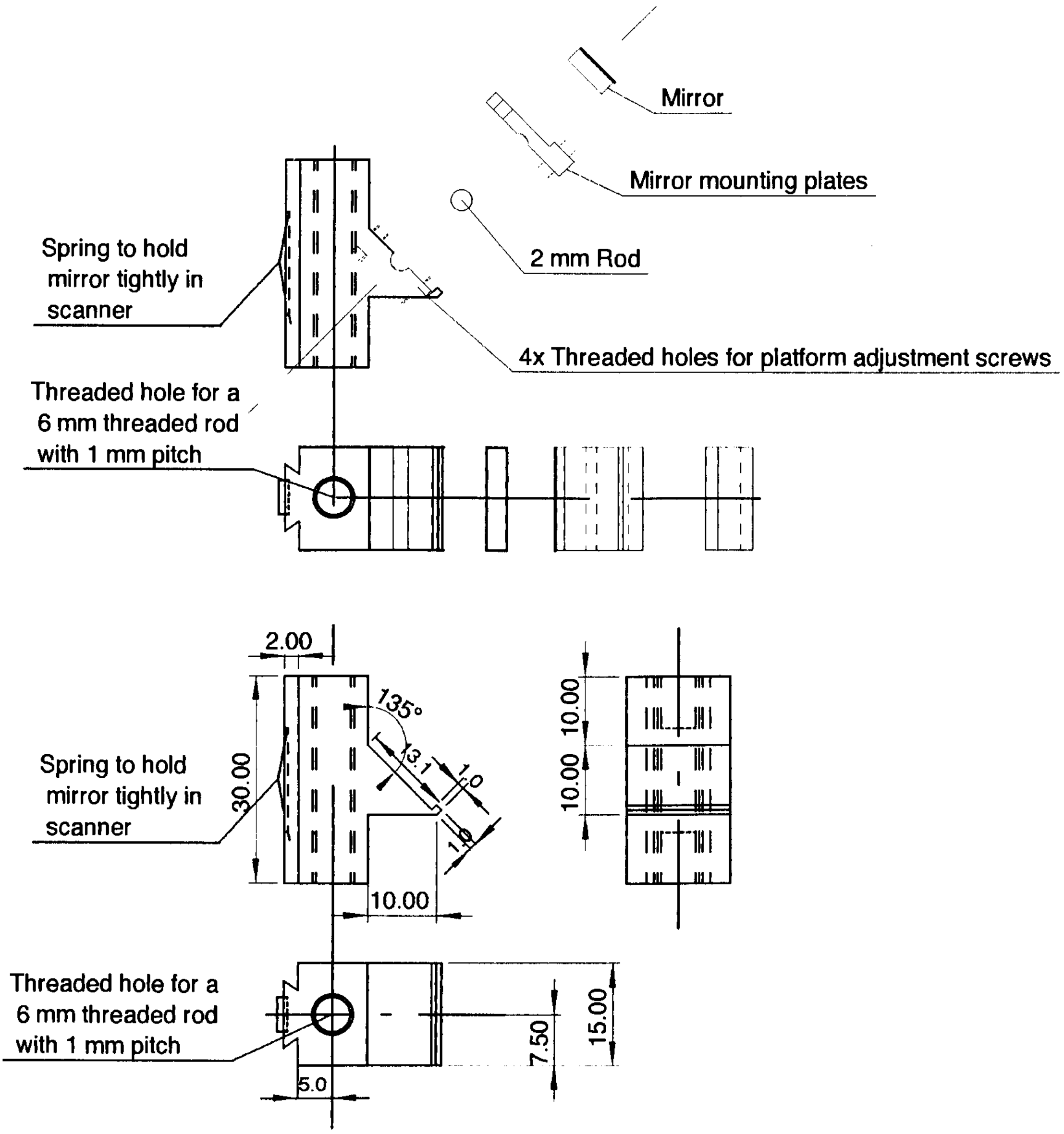

Figure 4-7 Design of the mirror support platforms.

It is vital that each mirror is at an angle of 45° to the incoming laser beam and that the laser beam is itself accurately aligned with the scanner axis, to ensure the sheets produced by the mirrors are parallel to one another. In order to ensure the incoming laser beam was aligned with the vertical axis of the scanner (parallel with the scanner support shaft) a small hole was drilled into the top of the motor platform during fabrication, directly below the hole in the top of the scanner through which the laser was aimed. By ensuring the laser passed through both holes the alignment of the laser relative to the scanner shaft could be checked. In order to allow some adjustment to be made in the angle of the mirrors, to account for machine tolerances and other misalignments, the angle of each mirror from the vertical could be adjusted independently. To achieve this, the mirrors were glued on to mirror mounting plates that were then fastened by four screws to the mirror support platforms. A metal rod was placed between the mounting plates and the platforms that allowed the angle of each mirror, from the vertical, to be changed. The alignment of each mirror was checked by passing the laser beam through a thin transparency sheet with horizontal lines marked on it, and then onto a thicker Plexiglass block. Both the mirror and transparency were fixed in a vertical position. Part of the laser beam was internally reflected in the Plexiglass block and therefore travelled back toward the oncoming beam. Ensuring both beams pass through the same level on the transparency sheet allowed the angle of the mirror to be checked and corrected.

4.3.2.5 Image Capturing

The synchronisation of the scanner to the imaging device was achieved via a slotted opto-switch triggered by a toothed disk attached to the end of the drum shaft. The twenty-toothed disc rotated between the slotted opto-switch (Radio Spares 304-560) which incorporated a Schmitt trigger and provided a TTL output signal based on the speed of rotation of the scanner. Problems were encountered, however, in obtaining a sufficiently 'clean' signal for the camera directly from the opto-switch. This was thought to be due to small irregularities with the disc from its manufacture. A purpose built signal generator was therefore constructed which used the signal from the opto-switch as the input, and generated a 'clean' TTL output signal at the same frequency as the input. The unit allowed the duty cycle and triggering edge to be selected, and incorporated a power supply for the opto-switch.

The phase delay between the camera and the sweep of the laser, governed by the position of the mirrors, could be adjusted by mounting the opto-switch on a traverse. The traverse used a threaded rod with a 1mm pitch, which provided sufficient accuracy to ensure the camera was triggered at the beginning of a laser sweep. By setting a slightly lower exposure time for the camera (< 1/frame rate) any phase jitter between the camera and the laser sweeps could be avoided.

4.3.2.6 Motor Platform Design

The scanner was designed to be operated at a variety of speeds so that it could be used with different imaging systems. This allowed the system to be used with both conventional video cameras, operating at a frame rate of 25 or 30 frames per second, and a high-speed camera with a frame rate of up to 500 frames per second. The scanner was, therefore, required to operate at speeds from 1.25 to 25 revolutions per second (75 to 1500 rpm). To accommodate this, two different motors were used. A stepper motor was utilised to drive the scanner at low speeds (up to approximately 1000 rpm) to provide accurate synchronisation of the laser sheets with the imaging device. For the higher speed a Davies Craig, model DCSL14, 130 Watt, 12V DC, electric motor was used. This motor type is used to drive a car radiator fan and is therefore very compact. A maximum speed of 3500 rpm was achieved using this motor to drive the scanner drum.

A motor support platform, shown in Figure 4-8, was designed as a separate entity from the drum scanner housing to accept the two different motors and as a platform to drive different optical scanners that may be developed in the future. The platform was fabricated from 10mm aluminium plate, bolted together, to make any future modifications as easy as possible. The stepper motor was mounted on a turntable that can be rotated up to 30°. The use of a turntable allows the phase delay between the mirrors and the camera trigger to be adjusted.

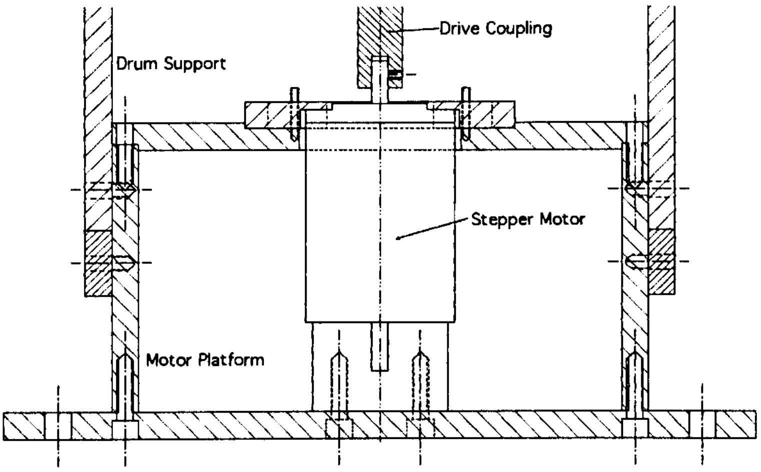

Figure 4-8 The scanner motor platform with the stepper motor and turntable fitted.

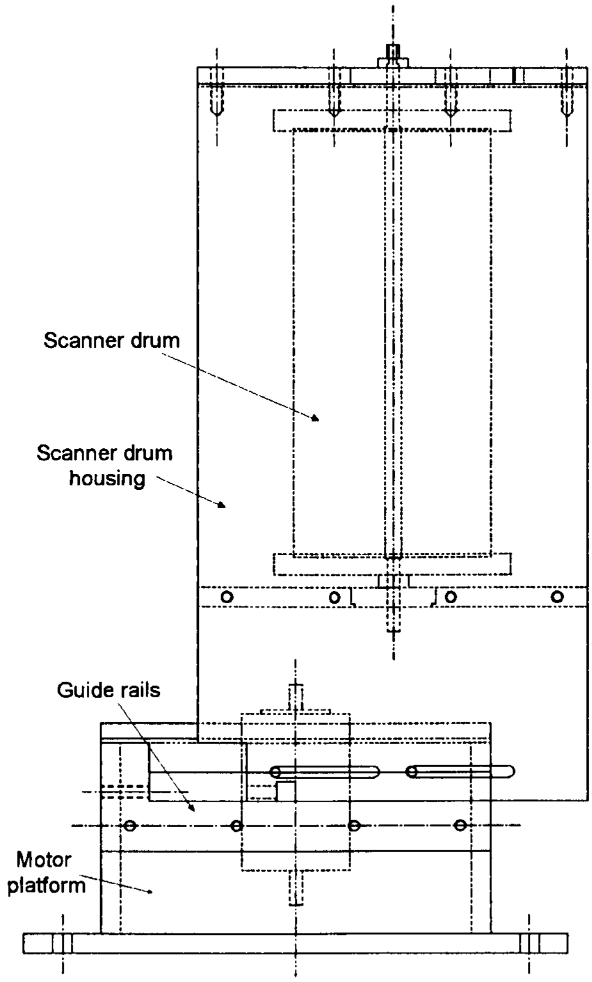

Figure 4-9 Motor platform and drum housing shown at full misalignment.

When installed on the motor platform, the scanner drum housing sat on two guide rails bolted to the side of the motor platform as shown in Figure 4-9. The guide rails made it easier to align the drum shaft and the motor during assembly. They were also incorporated into the design to allow gearing of the drum scanner to be implemented in the future. This would allow either a belt-driven or gear-driven system to be installed that would allow the scanner to be driven at a different speed to the motor.

4.3.3 Volume Experimental Limitations and Arrangement

Although volume visualisation is a powerful research tool, it does, as does any technique, have limitations and compromises that must be considered. The volume visualisation technique applied in the current work is based on capturing a series of parallel PLIF images of a flow field sufficiently fast to limit the propagation of the flow through the image volume in the time taken to completely capture a full volume. The limitations of the system predominantly relate to the speed at which the system is able to capture the data compared with the speed at which the flow moves.

Many of the compromises relate to the hardware used and limit the temporal and spatial resolutions that are achievable for the experiments. The limitations and compromises made for the current work will now be discussed along with some general considerations for the technique. Figure 4-10 is a flow diagram that shows the relationship between the hardware and the experimental conditions

For any experiment, it is necessary to consider both the limitations of the hardware, and the experimental conditions required when planning an experiment. In this case, the experimental conditions of importance are the volume size of interest (relating to spatial resolution), and the Reynolds number (relating to temporal resolution) of the flow being studied. The major hardware limitations are the maximum power of the laser, the number of laser sheets produced by the scanner, and the frame rate and sensitivity of the imaging device. The volume technique should aim to meet the requirements of a two-dimensional technique as well as the three-dimensional technique.

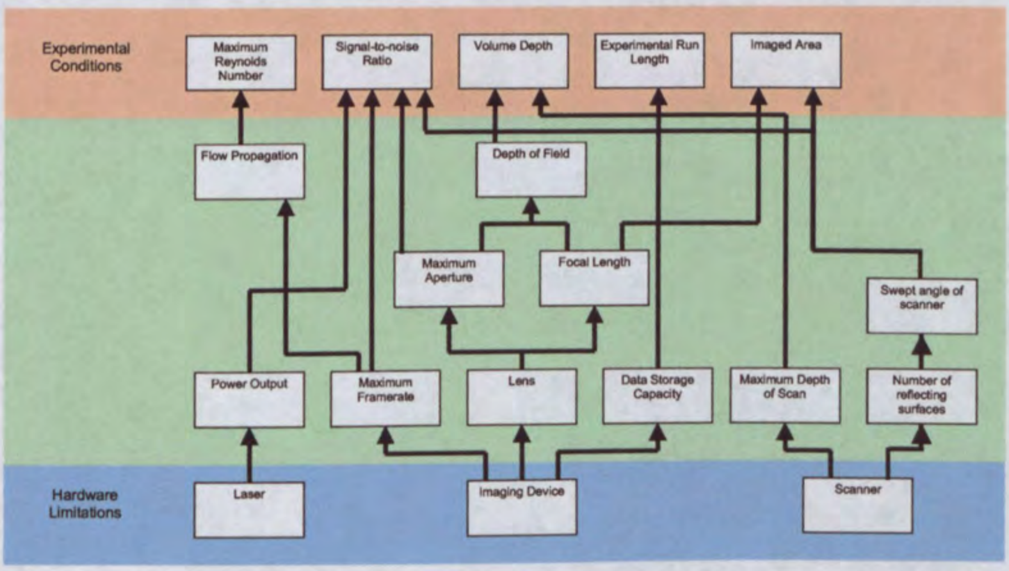

Figure 4-10 Flow diagram of system limitations.

4.3.3.1 Temporal Resolution

The maximum framing rate at which the flow may be captured is primarily dependent on the signal to noise ratio of the imaging device. This ratio is dependent on the time for which each pixel of the CCD is exposed to the fluorescence signal and on the quality of the CCD. To accurately capture the full three-dimensional flow field, it is necessary to image the flow at a sufficiently fast rate to minimise the movement of the flow during the time taken to capture each individual image. In practice, there is therefore a limit to the maximum velocity of the flow that can be accurately captured. As with standard (two-dimensional) PLIF it is necessary to limit the propagation of the flow during the time taken to capture each image. Since the imaging device requires a finite time in order to capture a sufficient signal level (the exposure time) the minimum exposure period to achieve a reasonable signal-to-noise level for each image sets the maximum flow velocity for the experiment in order to effectively freeze the flow. For a set frame rate, the exposure time period in two-dimensional PLIF is set either by the laser pulse duration (for a pulsed laser), or by the camera exposure time (for a continuous wave laser). In the case of the drum scanner, however, sweeping the beam through the flow generates each laser sheet. This requires the camera shutter to be open for the full time taken to capture each frame, that is, the exposure must be set close to the inverse of the frame rate. This implies that the frame rate (rather than the shutter exposure) sets the timing for each image. Depending on the imaging hardware available this can be a major limitation of volume visualisation. This situation is made worse by the fact that to capture the entire volume, an additional number of images need to be captured with little movement of the flow. This requirement sets an experimental limit on the flow velocities, based on the hardware available.

As with PLIF, the signal strength for a given exposure is set by the laser power, dye concentration and magnification of the imaging system. Increasing the laser power and/or using a higher dye concentration will increase the signal-to-noise ratio. The dye concentration, however, has a maximum limit, such that there is not a significant drop-off in the signal strength as the laser passes from one side of a region of dye to the other, due to absorption of the laser. This absorption results in a difference in the captured intensity level from one side of a dyed region to the other for the same dye concentration, and is difficult to accurately correct for in post-processing. It is therefore good experimental practice to use as high a laser power and as low a dye concentration as possible. Since the laser power is limited by the hardware available it is important to ensure good optics are used to limit any losses both in the delivery of the laser to the scanner, and in the reflecting surfaces used on the scanner itself. In the current set up, a fibre-optic conduit was used to deliver the laser beam to the scanner. The maximum power that could be carried by the fibre-optic conduit was 1.5 Watts, compared with the laser power of 7 Watts. Although this results in a significant loss in available laser power, it makes the system far more flexible, allowing the scanner to be used in different positions and orientations without having to realign the laser to the scanner each time it is moved.

Three time scales exist for the swept volume laser based system used in the current work. The smallest, is the illumination time for each pixel. For a given CCD and optical magnification, this time is set by the speed at which the laser moves across each imaged plane and must be sufficiently long to achieve a reasonable signal to noise level. The faster the laser is moved across the imaged plane the shorter the time for the CCD to capture the signal and therefore the lower the intensity. Note, however, that this time is different for each location of the imaged plane due to differences in the linear velocity of the laser as it is swept. This means the intensity will be less on one side of the imaged plane than on the other, although this effect will generally be small. The second time scale is the time taken to capture each plane. This time is set by the frame rate of the imaging device. The third time scale is the time taken to capture a complete volume and this is proportional to the number of planes used to capture the complete volume.

4.3.3.2 Spatial Resolution

The major limiting spatial resolution for the volume technique is the spacing between the planes on which each image is captured. In the case of the drum scanner, the spacing of the image planes is dependent on the number of reflecting surfaces installed and on the overall depth of the volume of interest. The number of image planes has an impact both on the spatial requirements of the system and on the temporal requirements. In terms of the spatial requirements, the number of reflecting surfaces used defines the number of laser sheets produced. This in turn defines the swept angle of the laser, which is in the optimum case 360° divided by the number of surfaces. Therefore, if the number of reflecting surfaces is increased, the angle swept by the laser is reduced. This implies that to achieve a similar swept area for a larger number of planes, the scanner must be placed further from the interrogation area. This may be impractical due to space limitations, and makes correct alignment more critical. In terms of the temporal requirements, the greater the number of slices in each volume, the longer the time period required to capture a complete volume. This has two consequences. First, the flow will have moved a greater distance (for the same frame rate) during the time taken to capture the images, and second, the smaller the number of time-steps that can be captured due to the memory requirements of the imaging system. It is necessary, however, to have a sufficient number of reflecting surfaces to enable a plane spacing which, based on the geometry of the flow studied, allows a good range of the large and small scale structures to be captured.

A significant limitation on the maximum spacing between image planes, and on the overall depth of the volume, is the depth of field of the imaging system used. To achieve well defined data it is necessary to ensure the image captured on each plane is adequately in focus. Capturing well defined (sharp) images makes the edges of the marked structures much easier to resolve during processing and therefore makes the final flow renderings more accurate. The depth of field of an imaging system is defined by

$$DOF = 4\lambda\left(1+\frac{1}{M}\right)^2\left(f^{\#}\right)^2, \tag{1}$$

where λ is the wavelength of the light imaged, $f^{\#}$ is the f-number of the lens used and M is the magnification of the image given as

$$M=\frac{f}{(S_0-f)}, \tag{2}$$

where S_0 is the distance from the image plane to the focal plane and f is the focal length of the lens used.

It is important to note that the depth of field of a lens does not extend equally in front of, and behind the point of focus plane. Rather, as a general rule, the depth of field produced by a particular lens will extend approximately one third in front of the point of focus and two thirds behind. The points in the near-field and far-field that will be in focus can be calculated using the expressions

$$S_{o,near}=\frac{h.S_o}{h+(S_o-f)} \tag{3}$$

and

$$S_{o,far} = \frac{h.S_o}{h-(S_o-f)} \tag{4}$$

where h is the hyperfocal distance for the lens given as

$$h = \frac{f^2}{c.f^{\#}} \tag{5}$$

where c is the circle of confusion for the imaging system and $f^{\#}$ is the f-number of the lens. The circle of confusion is the smallest resolvable region on the image plane; in the case of a CCD it is equal to the size of a single pixel.

The above equations imply that the positioning of the camera and the lens is very important as it dictates the minimum scale of the structures that can be resolved in each slice, given by the magnification, as well as the overall depth of field in which the images will be in focus. Equation 1 implies that for lenses of higher focal lengths, or using lower f-number, the depth of field decreases. In addition, it implies that for a large magnification, which may be used to resolve the fine scale features of the flow, the depth of field is very small. From the above details, it is evident that to achieve a good depth of field it is necessary to use a lens that incorporates a large aperture. In many instances, there will be restrictions on where the camera can be positioned and this will impact on the choice of lens. Although a short focal length lens is beneficial in terms of the depth of field, the further the camera is placed away from the image plane the smaller the region of interest (in this case the dyed region of the flow) becomes relative to the area of the captured image, see Table 4-2. This means a large portion of the image will be wasted as it will only contain background data and the details of the region of interest will not be well resolved.

Equation 2 implies an additional issue in relation to volume visualisation, which is that since each image in a volume is at a different distance from the imaging device, the magnification of each image is different. This has the effect of enlarging the images closest to the imaging device. A correction for this is applied in the image pre-processing which applies a scaling factor to each image to reduce the effect. This process is discussed in Section 4.3.4.14.

Since the depth of field also decreases for lower values of f-number, it is important that the imaging system receives a good signal strength from the dye to achieve a good signal-to–noise ratio. This means the optical arrangement used should be as efficient as possible, and use the minimum number of components to reduce any losses in laser power. In order to use a higher f-stop value to achieve the required depth of field it may also be necessary to reduce the framing rate which will also increase the signal strength.

Table 4-2 C-Mount Lens Chart for Horizontal Angular Field of View in Degrees

C-Mount Lens Focal Length	CCD Sensor Size (Diagonal Inches)		
(mm)	1/2"	2/3"	1"
4.2	88		
6.5	52	72	99
8.0	44	59	
12.5	29	39	55
25	14.5	20	28
50	7.3	10	14.5
75	5	7	10

Source: Web site http://www.vision1.com/chart.shtml

4.3.3.3 Maximum Experimental Run Length

One of the major drawbacks of undertaking volume visualisation is the amount of data that must be recorded and stored. The MEGAPLUS camera used in the current work stores data in a digital form directly to a dedicated portion of RAM situated on the computer controlling the camera. The computer used for the current work had 786 Mbytes of RAM installed, of which 690 MB was dedicated to the camera. Therefore, 330 images at 1008 x 1018 pixels, 10-bit resolution were able to be captured in a single experimental run. This has two implications. First, the number of images captured by the system limits the number of time steps that are available to be rendered for each experimental run. Second, the duration of each experimental run is limited. For a flow that shows any periodicity, such as the jet in crossflow, the experimental run length may not be sufficient to capture the full motion of the flow.

4.3.4 Volume Image Processing

4.3.4.1 Introduction

The goal of the image processing was to produce accurate three-dimensional renderings of the flow from the two-dimensional cross-sections captured experimentally. The impetus behind this was two-fold. First, it was necessary to visualise and display the entire structure of the jet, and second, the presentation needed to show the connections and interactions between the flow structures. The image processing, in its simplest form, serves to extract the raw data from each image file and store the data in a format that can be imported into the volume rendering software. A commercial rendering package was utilised to produce three-dimensional renderings of the jet, from which anaglyphs (red-blue stereo images) were generated. A sequence of such anaglyphs could then be concatenated into a movie allowing both the complete structure and temporal evolution of the structure to be presented in three dimensions. The following section details the process used and provides some background on the image processing techniques applied to achieve the most realistic representation of the flow possible.

4.3.4.2 Software Selection

The first requirement was to select the software that would carry out the rendering and decide on the best way of presenting the data, both in print and on computer. A number of different options were considered to generate and display the three-dimensional renderings of the flow. The first step was to decide between using an existing package, or developing specialised software for the task. Since it was established that numerous packages, both public domain and commercial, could be used to import sets of two-dimensional data and display them in three dimensions, it was decided it was unnecessary to write any new software to perform the task for the present work. A significant amount of the software available is orientated toward medical imaging for presentation of scanning data. It is, however, very expensive.

The package selected to generate the volume renderings of the flow was T3D a commercial volume rendering package developed by Fortner Research LLC, now owned by Research Systems. Version 1.1.3 was used, running under Windows 95 and Windows NT. The software allowed the renderings of the flow to be rotated in real time, and produce cut-aways and slices from the volumes produced. To convert the TIFF image data captured during the experiments into the correct raw binary data format for the software, MATLAB was used since it incorporates image-processing routines that made converting the data easier than writing code from scratch. Version 5.3.0.10183 (R11) of MATLAB was run on the Silicon Graphics workstation. In addition, MATLAB was used to perform some image processing on the data. The routines used for both the conversion of the data and the processing are outlined in the following section.

Following the rendering of the data, a number of techniques were applied to present the data for print and on computer. The techniques include 3-Box-Views, volume renderings and cut-aways, stereo anaglyphs, QuickTime Movies and QuickTime VR movies. Stereoscopic or three-dimensional images that allow the flow to be viewed from different angles could then be produced. By combining the three-dimensional images into a time-series the data could be presented as a movie. Such a presentation allowed the evolution and mixing of the flow features to be viewed. Additionally, data could be re-processed to produce cross-sections in planes other than those sampled, albeit at a much reduced resolution.

4.3.4.3 Image Processing Requirements

Before importing the data into the visualisation packages some processing of the original image data was performed. The processing served three functions. The first was to convert the experimental data into a format that could be used with the volume rendering packages. Second each image was normalised relative to the highest dye intensity in order to increase the contrast.

The final function of the processing was the crucial step of calculating the threshold intensity value for the data set. This value defines the intensity level that separates the data representing the dyed region of the flow from the background fluid. As emphasised by Yoda & Hesselink (1989), selecting the threshold value is a challenge when the optimum detail of the flow is to be retained. The fine scale structures occur in the low contrast region surrounding the main dyed structures. In addition, as the threshold value defines the boundary of the unmarked and marked fluids, it is important to determine its value as accurately as possible, since this boundary region represents the interface where molecular mixing of fluids takes place.

Much of the processing was based on being able to determine the intensity values of the dyed flow and background. Since the intensity values may vary between the images, a method of being able to automatically determine the values was necessary. To do this the image histogram was used. Therefore, before discussing the processing of the data in depth, the image histogram will be discussed.

4.3.4.4 The Image Histogram

Each image captured using the PLIF technique contains two regions; an object region (a lighter coloured region that corresponds to the fluorescence captured by the camera) against a dark or black background region. Such an image has a bi-modal grey-level histogram. An example of such a histogram divided into 256-intensity levels and corresponding to the PLIF image displayed alongside is given in Figure 4-11. The two peaks, one at low intensity values (on the left), and the other at higher intensity values (on the right), correspond to the relatively large number of pixels within the background and object regions respectively.

In addition to using the image histogram at the processing stage, it is also a valuable tool to use while undertaking the experiments since it provides a quick visual reference to the quality of the data being captured. To achieve the best data, the grey levels in an image should be spread across the entire range of available levels. This ensures the optimum contrast is achieved between the dyed and undyed regions. It is vital, however, that a large number of pixels are not located at the highest intensity level. This situation would imply saturation or blooming of the camera CCD. For the work undertaken during the current experiments the range of grey-scales captured was determined by the dye concentration, laser power and lens aperture. A balance between these variables was therefore required. To complicate matters these variable are also dependent on other factors. The lens aperture is also dependent on the depth of field required to keep each of the image planes in focus. The laser power was limited by the throughput of the fibre-optic system in use. The concentration of dye must be sufficient to ensure as many of the fine scale structures are visible but without being too high to cause problems due to the absorption of the laser as it passes through the dyed region. The general rule was therefore followed such that, to ensure the best contrast, one should use as low a dye concentration as necessary and the highest laser power, with the largest lens aperture to ensure sufficient depth of field.

In order to make use of the image histogram during the processing it was necessary to determine the intensity levels at which the peaks in the histogram occur. The location of the first peak, which corresponds to the intensity level of the background fluid, was generally easy to determine. The peak corresponds to only a narrow band of intensity levels, and contains a large number of pixels, since most of each image shows the region of undyed fluid. The peak on the histogram was therefore narrow and tall, and was determined by simply finding the intensity level containing the greatest number of pixels.

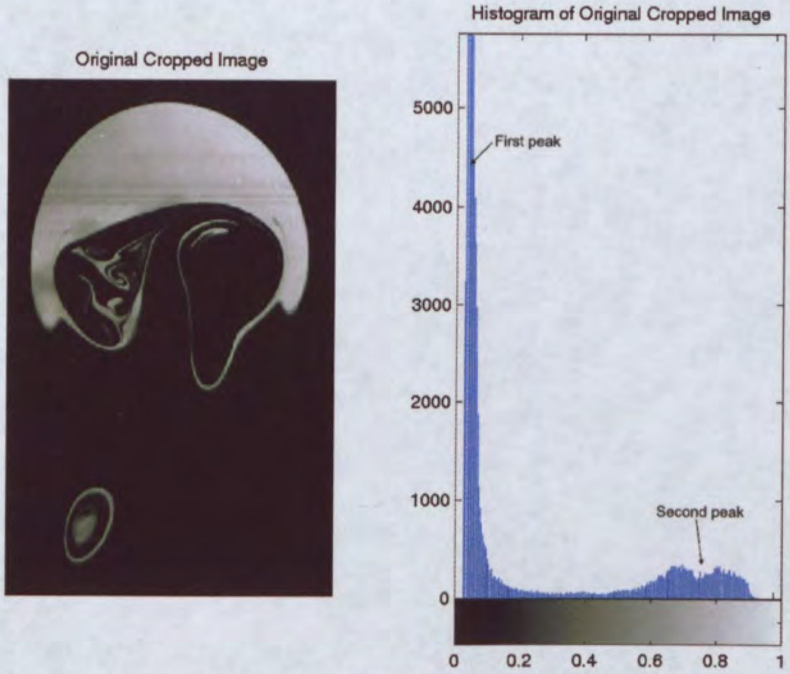

Figure 4-11 A sample PLIF image and corresponding grey level histogram. The histogram contains two main peaks; the first peak is the tall slender peak on the left corresponding to the narrow range of 'dark' grey levels in the background, and the second peak the short, broad peak on the right corresponding to the large number of grey levels in the dyed (jet) region.

However, locating the intensity level of the peak corresponding to the dyed region was more complicated. As can be seen in the histogram, in Figure 4-11, the second peak is very broad. This is mainly due to the drop-off in intensity due to absorption of the laser light by the dye as the laser passes through the dyed fluid. Therefore, the intensity value of the dyed fluid is higher on the side of the image from which it is illuminated. This implies that the intensity value for 100% jet fluid changes across the image. The effect of the absorption, and therefore the width of the peak, can be reduced during the experiments by using a low dye concentration and high laser power, however it is difficult to totally remove it. In addition, there is rarely a clearly-defined boundary between the marked and un-marked fluid. This is due to a number of reasons including imperfections of the mirrors and lenses, the imperfect focus of the camera lens, and of more importance, the diffusion of the dye into the surrounding un-marked fluid. Two methods were applied to determine the location of the second peak depending on the shape of the image histogram.

In the case where the histogram contained two distinct peaks, as shown in the Figure 4-11, a third order polynomial curve fit was applied to the histogram. It is then easy to determine the location of the second peak of the polynomial function. An example of how this worked is shown in Figure 4-12 in which the polynomial curve fit is superimposed over the plot of the image histogram. Once the location of the second peak had been determined the threshold intensity level was then set at the intensity level mid-way between the two peaks.

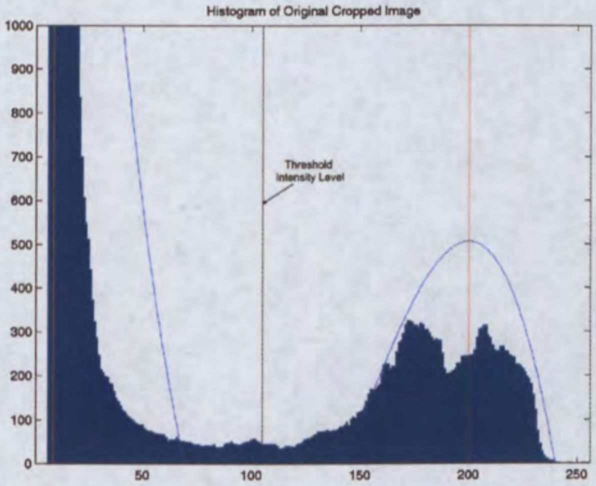

Figure 4-12 Histogram of the sample PLIF image in Figure 4-11, with a third-order polynomial curve fit superimposed. The left hand red-line is positioned at the intensity level with the maximum pixel count, which defines the background intensity level. The second red-line is positioned at the crest of the second peak of the polynomial, which corresponds well with the position of the second peak of the histogram. The black line is positioned at the intensity level mid-way between the two peaks, used as the dividing intensity level between dyed and undyed fluid.

One other value that was extracted from the image histogram was the highest intensity level on the second peak. This intensity level is assumed to correspond to the highest intensity level of the dyed fluid in the image and therefore is used to define an estimated intensity level corresponding to 100% jet fluid. The value was found by consecutively scanning each intensity level and storing the last intensity level containing a number of pixels above a minimum pixel count. The minimum pixel count was set to discount any intensity levels (with high intensity values) that may contain a low number of pixels due to noise or scattering of the laser light. The minimum pixel count was set independently for each image at the minimum pixel count between the two peaks of the image histogram as shown in Figure 4-13.

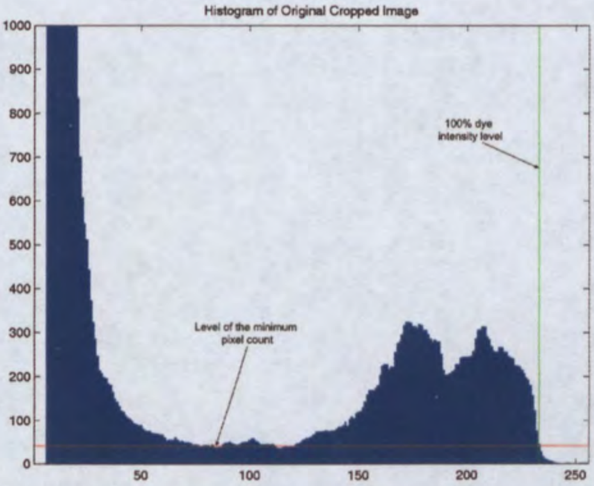

Figure 4-13 Histogram of the sample PLIF image in Figure 4-11. The horizontal red-line is located at the minimum pixel count level for the image, and the vertical green line is at the intensity level defined highest intensity level with a number of counts above the minimum pixel count level. The position of the green line shows the intensity level assumed to correspond with 100% dye.

4.3.4.5 Processing Sequence

All of the images acquired during the experiments were captured using the Kodak MEGAPLUS ES1.0 digital camera and stored as either 8-bit or 16-bit TIFF files with no compression. An example of a single image as captured by the camera is shown in Figure 4-14. An outline of the sequence in which each data set was processed was;

- Extract raw data from TIFF images
- Pre-process
    - Crop image
    - Convert data to type float
- Process
    - Subtract background
    - Normalise image relative to 100% jet value
    - Determine the threshold of the image
- Store the data in the required format
    - Shift intensity values in each image to match the intensity threshold value across a complete data set
- Apply an interpolation loop to generate additional data levels between the captured data planes (if required).

Figure 4-14 A sample PLIF image captured using the Kodak MEGAPLUS ES1.0 10-bit camera. The image is 1018 by 1008 pixels. The camera was positioned directly above the jet exit, with the jet flow coming out of the page and the crossflow going from the top of the page to the bottom. The red lines define a region of area 285 by 475 pixels which was used for processing.

4.3.4.6 Cropping

In order to minimise any perspective effects the camera's axis was always aligned normal to the plane to be imaged. When the flow was imaged from above the jet exit, the camera was aligned with the axis of the jet, and when viewed from the side, the centre of the camera's image plane was aligned with the jet exit. In addition, in order to achieve a sufficient depth of field and field of view, as discussed above, it was required to position the camera a reasonable distance away form the image plane. These requirements meant a significant area of each image contained only the background region of the flow. Therefore, the images were cropped to remove most of this background region. This reduced the memory and computational requirements of the processing but did not result in any losses of data in the region of interest. Each image in a data set was cropped to the same region. The region was determined by examining the top and bottom image in each volume set and manually selecting the boundaries within which the dyed region is located. Figure 4-15, shows the image given in Figure 4-14, cropped to 285 x 475 pixels.

normalise each image, the highest intensity value on the second peak on the image histogram was used.

As an example, the intensity value for each pixel in the original cropped image, Figure 4-15, was normalised by the highest jet intensity value from the image histogram of the cropped image, to generate the normalised image, shown in Figure 4-16.

Figure 4-16 Normalised image of the cropped region shown in Figure 4-15.

4.3.4.9 Image Threshold

Once an image had been corrected for the differences in intensity, the images were ready to be imported into the volume rendering packages. However, an important parameter that is required so that the flows can be correctly rendered to show the 'surface' or 'boundary' of the jet fluid, is the intensity level or threshold that distinguishes the background region from the dyed region. This requirement was emphasised by Yoda and Hesselink (1989 & 1990) during their work. A value for the threshold that is too large will mean some of the marked features will be eliminated. Alternatively, a low value will allow background noise to be included with the jet.

As discussed earlier, the method used to determine the threshold value was based on an optimal threshold technique that makes use of the image histogram. The dip in between the peaks corresponds to the pixels around the edge of the marked region, in which diffusion and other image imperfections mentioned previously are captured. Placing the threshold within the region of the dip on the image histogram (where relatively few pixels are counted) minimises the sensitivity in the size of the region of interest to small errors in the threshold value. Since the images for PLIF data are typically noisy, the exact location of the 'dip' between the peaks is hard to determine. Therefore, a better method is to place the threshold at a point that is defined relative to the two peaks. In this case, the threshold for each image was set at the midpoint between the two peaks. The location of the peaks were determined using the method outlined previously in Section 4.3.4.4.

In order to determine whether the technique used to find the threshold intensity level gives a reasonable value, an image was generated using the data from the normalised image, in which pixels with values above the threshold were set to a value of 1. The resulting image is shown superimposed on the corrected image for comparison in Figure 4-17

4.3.4.10 Threshold Shift

Once every image in a data set had been processed, the intensity values of the pixels in each image were adjusted to ensure the threshold value is the same for each image within a data set. This is carried out by first determining the maximum threshold value for the entire data set, following which each processed image is re-opened and the intensity values for each pixel shifted by the difference between the maximum threshold value and the threshold value for the current image. The routine ensures that the same intensity value will define the boundary for the dyed and undyed fluid when the individual images are combined in the volume rendering.

4.3.4.11 Interpolation

The final processing step applies a three-dimensional interpolation to the data in order to generate additional data planes that allow a smoother profile to be generated with the renderings. In the future it is also planned to use the interpolation loop to generate evenly spaced planes from unevenly spaced data. This is necessary since the rendering packages require the data to be on equally spaced parallel planes. Due to the large difference in the size of the structures, some experimenters may choose to take data at unequally spaced planes to try to capture the smaller scales with a finer resolution. The interpolation would then be required to fill in the addition planes necessary to render the full data set. The present interpolation is undertaken in MATLAB using the *interp3* function. MATLAB provides three different interpolation methods with this function; linear, cubic and nearest interpolation. In this case, the cubic method was used, which appeared to produce the smoothest profile, although is very processor intensive.

Figure 4-17 An image generated by changing the values of all the pixels with an intensity level equal to or above the threshold level calculated for the image to 1 (displayed as white).

4.3.4.12 Processing Code

A summary of the MATLAB code used during the processing, and each of the files of code used is given in Appendix A.

4.3.4.13 Binary Formats

The final processing step involved storing the processed image data in the correct format to be imported into T3D. In this case each image was stored as a separate 32-byte binary file. Each file was numbered sequentially in order for T3D to be able to import the data in the correct sequence.

4.3.4.14 Correction for Perspective

In the case of volume visualisation, the image plane for each slice occurs at a different distance form the imaging device. Therefore, the area viewed in each image is different due to the perspective. This effectively causes a difference in the size of one side of the flow structure to the other. To reduce this effect, each image was scaled during the pre-processing to match the size of elements within each image. The required scaling was calculated manually for each experimental set up, using the following method. A target with a grid of known dimensions printed on it was placed in the water channel (with water) and imaged at three or more locations; centre focal plane, farthest and nearest image planes. The magnification of each image was then determined by measuring a known distance on the grid, and determining the number of pixels/mm for each image. A plot was then generated of the image scale (pixels/mm) versus the location of each image plane in the z-direction. A linear line of best fit was constructed between the three (or more) measured points, from which the slope and intercept values were determined. The slope and intercept, along with the location of the first image in the z-direction and the spacing between image planes (in millimetres), were entered into a 'macro' written for NIH Image. NIH Image then calculated the scaling factor for each image in the data set, and applied the scaling using a bilinear scaling function.

Examples of a portion of the target, both scaled and unscaled, are shown in Figure 4-18. In this case the image farthest from the camera was kept at the original size and the images in front were scaled to match. An averaged image of both the scaled and unscaled images is also shown to highlight the improvement made by scaling. Although the horizontal alignment has been fixed, the vertical alignment is affected slightly due to the portion of the template shown being below the axis of the camera.

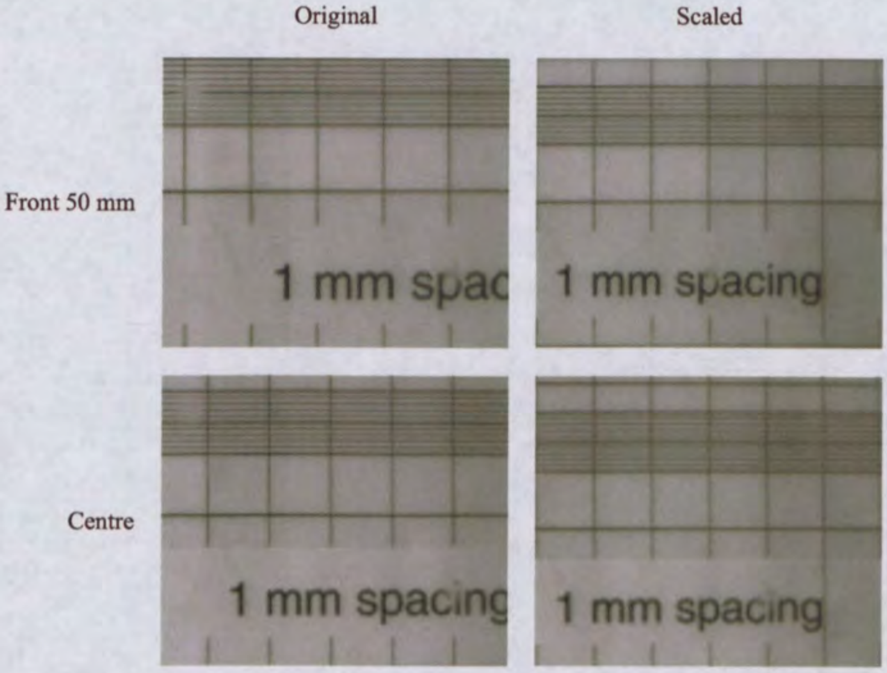

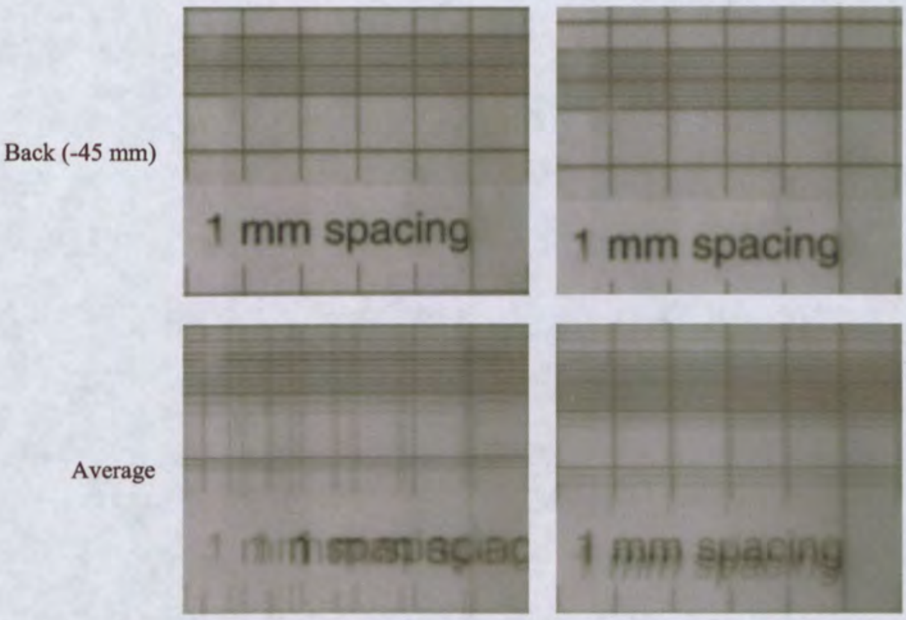

Figure 4-18 Example of image scaling to correct for magnification

4.3.4.15 Producing Anaglyphs – Red-blue 3D Images

In order to obtain a better realisation of the flow structure the volume renderings were converted to anaglyphs, which are red-blue stereo images. In order to view the anaglyphs, glasses with red and blue lenses are required. To view the anaglyphs produced in the current work the glasses must have a red lens on the left and blue lens on the right. Alternative techniques for displaying data in three dimensions are stereo pairs or holograms. However, anaglyphs are generally easier for people to visualise (providing they have the glasses) and are preferable for displaying on a computer screen or to multiple viewers. (If glasses are not available, red and blue cellophane or acrylic plastic can be used to construct home-made glasses.)

In order to generate a single anaglyph image, two separate images of the same object are used, each of which represents the view of the object from each eye of the viewer. Since the eyes are horizontally offset from the each other, each eye sees a slightly different view of an object. Therefore, after a volume rendering is generated in T3D, two additional images are generated by rotating the rendering by a small amount in both directions from the original central view to generate the views that each eye would see on its own. The two rotated images (not the cental image) are opened in an image software application that is able to separate the image into RGB (red/blue/green) layers. In this case the application NIH Image was used. In order to generate an image which is viewed with a pair of glasses with a red lens covering the left eye, and a blue lens covering the right eye the red layer on the right image (image that the left eye would see) is first removed from the image. The red layer from the left image (image that the left eye would see) is then copied and pasted to the red layer of the right image. The resulting image is then saved and when viewed with the glasses appears three-dimensional. The effect works because the glasses filter out the part of the image with the different colour to the lens. Therefore, the right eye sees only the right image and the left eye the left image.

4.3.4.16 Sample Results

An example of the volume renderings, converted to stereo anaglyphs using the technique detailed in Section 4.3.4.15 are shown in Figure 4-19. The renderings displayed show a jet in crossflow in which the crossflow is from left to right and in the top image the jet flow is into the page, whereas the bottom image shows the jet flow coming out of the page. Both images were generated from 39 slices, 20 slices from captured image data, and 19 slices producing by interpolating the captured data. Displaying the data in the form of anaglyphs, and viewing it with red-blue glasses, provides a great insight for the overall shape of the structure of the flow.

Figure 4-20 shows a volume rendering of the same data as in Figure 4-19, but the rendering was carried out using an interpolation and over-sampling routine in T3D. In the authors opinion, however, the overall shape of the images in Figure 4-19, are easier to resolve where the 'stepped' appearance improves depth perception. A similar finding was made by Yoda & Hesselink (1989) in their renderings of jets.

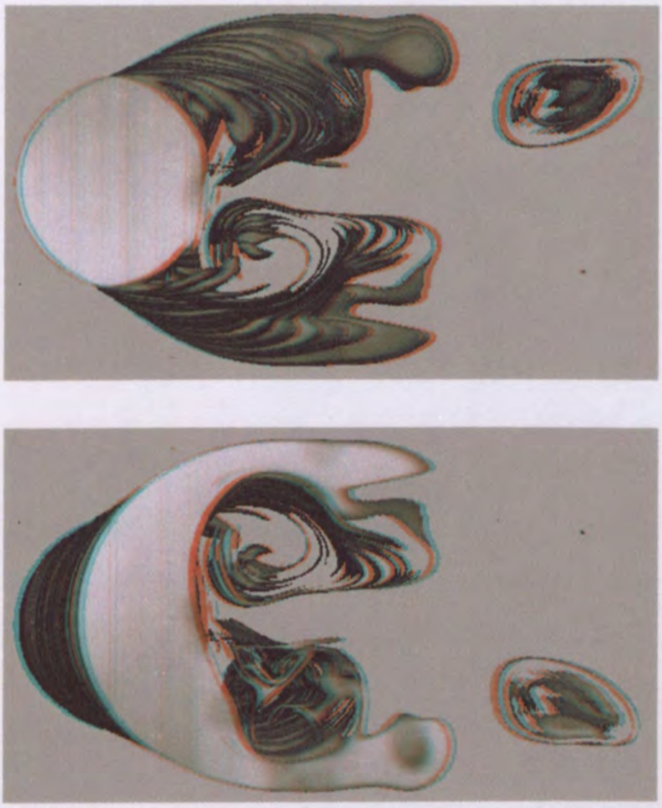

Figure 4-19 Red-blue stereo anaglyphs, generated from volume renderings produced by T3D. The renderings show a jet in crossflow (crossflow left to right, jet into page in top image, and out off page in bottom image). Thirty nine data planes were used to create the renderings, twenty of which were from images captured during the experiments, and 19 were produced during the processing of the data by interpolating the experimental data.

Figure 4-20 Red-blue stereo anaglyph, generated from volume renderings produced by T3D. This rendering was generated using an interpolation and over-sampling routine included in T3D. The renderings show a jet in crossflow (crossflow left to right, jet into page in top image, and out off page in bottom image). Thirty nine data planes were used to create the renderings, twenty of which were from images captured during the experiments, and 19 were produced during the processing of the data by interpolating the experimental data.

5 Time-averaged Trajectories and Mixing

5.1 Introduction

As a means of developing a better understanding of the structure of a jet in crossflow, a direct comparison between the cases of a flush-mounted jet and an elevated jet was undertaken using both the volumetric time-averaged scalar field and volumetric rendering techniques discussed in the previous chapter. The work was carried out in order to provide an understanding of the effect of the presence of the wall and its associated boundary layer on the mixing and structure of the jets. In addition, only a small amount of work has been undertaken on elevated jets, principally that of Eiff, Kawall & Keffer (1995) and Eiff & Keffer (1997), compared with the amount undertaken on flush-mounted jets. However, Moussa *et al.* (1977) made mention of the differences between the jet trajectories of various authors work stating "... jet rise resulting from a hole in a wall shows considerable disagreement with that resulting from a pipe discharge ..." (p.63). Nevertheless, a study that directly compares the two flow cases using the same experimental apparatus does not appear to have been undertaken.

Three reasons were presented by Moussa *et al.* (1977) for the differences between the two flow cases reported in their work. The first was the difference in the momentum distribution (shape factor) of the jet at the jet exit. The second was the presence of a potential core in the case of the flush-mounted jet. Third was the roll-up of the boundary layer vorticity in the flush-mounted case into the wake of the jet. Although these reasons were given, they do not seem to have been verified. The findings from the work presented in this thesis will indeed show that there are substantial differences between the two flow cases and by using a number of different flow visualisation techniques some explanations for the differences found will be presented which differ from those of Moussa *et al.* (1977).

Velocity ratios of 2 and 4 were chosen to make comparisons between the two flow cases. It was decided to use relatively weak jets (low velocity ratios) so that any differences in the jet structure would be more clearly defined. Firstly, comparisons of the structure of the jet on the jet's plane of symmetry are presented for the flush-mounted and elevated cases. Second, volumetric mean scalar field data are presented, to show the three-dimensional mean concentration for the two flow cases. In the following chapter, volumetric renderings of the jet structure are presented which clearly demonstrate differences between the two flow cases.

5.2 Experimental Conditions

All of the results presented in this chapter are from experiments conducted in the 0.5m × 0.5m water channel as described in Chapter 3, making use of the 50mm inside diameter jet pipe. In order to change between the flush-mounted and elevated jet flow cases, the false floor, discussed in Section 3.3.4, was placed in the working section of the channel. This arrangement allowed the same jet pipe to be used for both cases, ensuring the pipe-flow development length was constant for all experiments, being approximately 5 jet diameters from the contraction to the jet exit. The circulation around the false floor was controlled via the adjustable rear spoiler. The jet exit was located 8 jet diameters downstream from the leading edge of the false floor, such that the boundary layer thickness at the jet exit was less than half the jet diameter. This is confirmed in the following section.

The crossflow velocity was fixed at 0.04m/s for all the flow cases studied, which implies a crossflow Reynolds number of 2000, based on the crossflow velocity and internal jet pipe diameter.

5.3 Initial Conditions

As a first step, it was considered important to determine the near-field jet velocity profiles, both upstream and downstream of the jet exit, for both the elevated and flush-mounted cases in order to establish the jet's initial conditions for both cases. This requirement was considered important as Moussa *et al.* (1977) had partly attributed the wide variation of experimental jet trajectories in the literature to the flow conditions at the jet exit. To provide an indication of the profiles of the jet exit conditions in both the flush and elevated jet cases, timelines were generated by pulsing the hydrogen bubble-wire situated within the jet pipe. The resulting velocity profiles for the flow condition with R=2 are shown in Figure 5-1 for the flush-mounted and elevated jet cases.

The timelines indicate the velocity profiles greater than one jet diameter upstream of the jet exit are similar in both cases and approximately symmetric about the jet centreline. Close to the jet exit, the timelines remain similar to one another in terms of their slope and the indicated size of the separation within the pipe. This implies that the initial jet conditions (within the jet pipe) are not substantially different between the two cases. It is important to remember that the jet pipes are the same length for both cases and that using different jet pipe lengths would cause a difference due to the variation in boundary layer development lengths.

Outside the jet exit, however, the development of the timelines changes substantially, particularly in the region of the upstream side of the shear layer. In the case of the flush-mounted jet, the leading edge shear layer rolls-up in a periodic ring-like manner very close to the jet exit plane. By contrast, the leading edge shear layer in the case of the elevated jet does not roll up until at least two jet diameters downstream of the jet exit and appears to do so by a Kelvin-Helmholtz mechanism.

The crossflow boundary layer profile was estimated by positioning a vertical hydrogen bubble wire at the leading edge of the jet pipe, with the jet pipe exit covered. The resulting timelines for a crossflow velocity of 0.04m/s are presented in Figure 5-2. An image of a ruler has been superimposed to allow the boundary layer thickness to be estimated. The bubble-wire is visible as a vertical line to the right of the ruler. The jet exit is marked with a white line in the figure as a reference. From Figure 5-2, the approximate boundary layer thickness can be determined to be 15mm, or 0.3d. The timelines also indicate that the boundary layer appears laminar at the location of the jet exit.

The fact that the boundary layer is laminar is supported by considering that the Reynolds number at the centre of the jet exit, Re_x, is approximately 20,000 for the crossflow velocity and jet location used in these experiments. This value is one order of magnitude below the transition Reynolds number for a flat plate. Assuming a Blasius boundary layer profile, the boundary layer thickness would be 16mm or 0.31d, which is in close agreement with the experimental measurement.

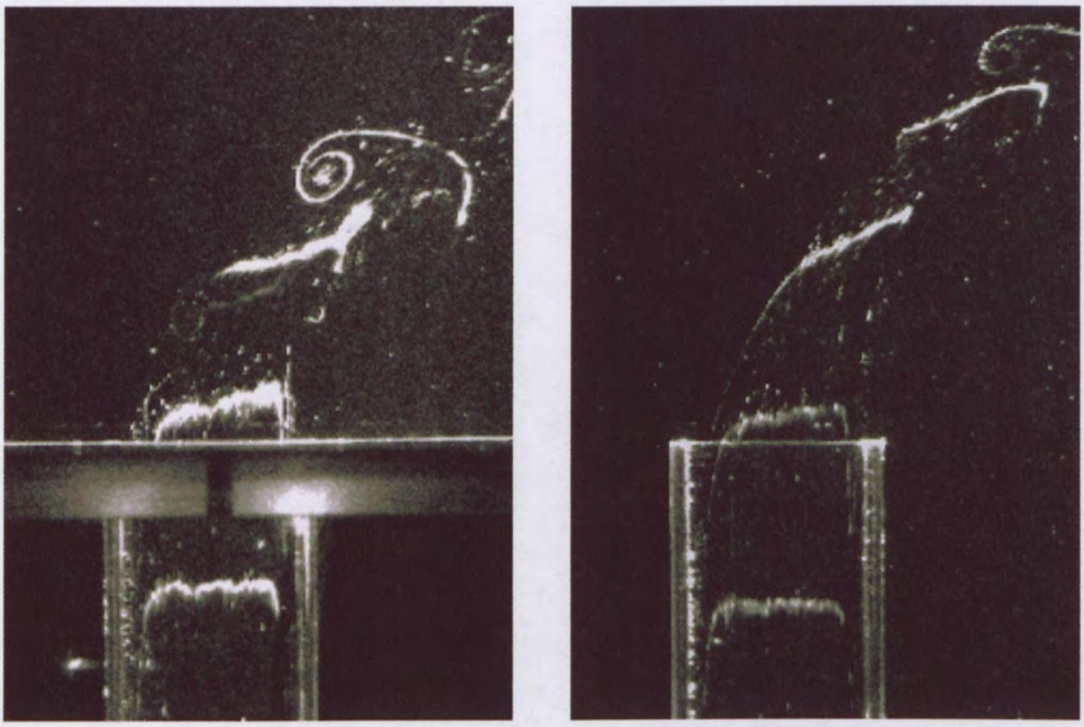

Flush-mounted jet **Elevated jet**

Figure 5-1 Time lines generated in the jet pipe for the flush-mounted and elevated jets. In both cases the velocity ratio was 2 and the jet Reynolds number 4000. The profiles were generated with a bubble-wire positioned 3 jet diameters upstream from the jet exit.

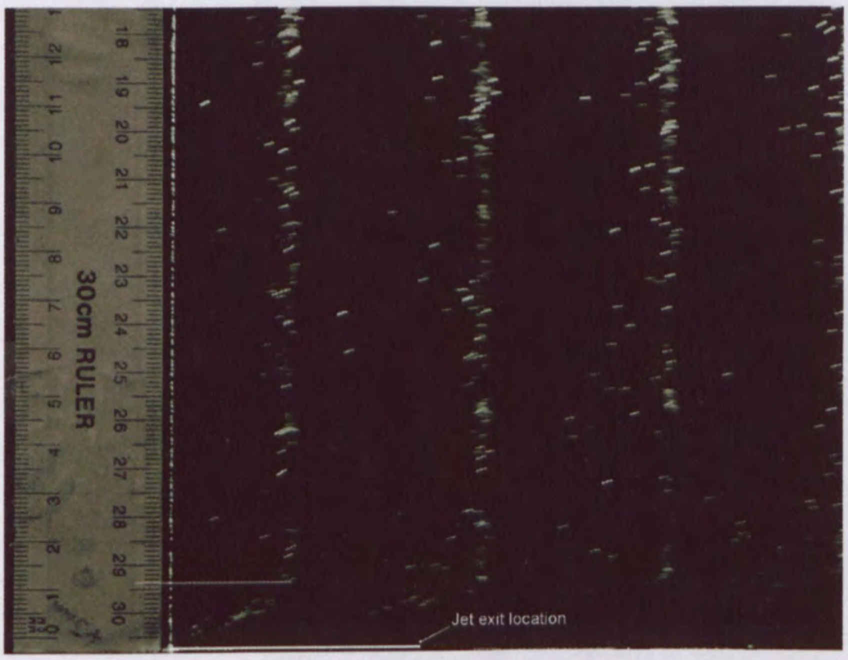

Figure 5-2 The crossflow boundary layer profile at the leading edge of the jet pipe for a crossflow velocity of 0.04m/s. An image of a ruler has been superimposed to allow the boundary layer thickness to be estimated.

5.4 Time-averaged Trajectories and Mixing

5.4.1 Introduction

Using the volumetric quantitative time-averaged scalar field technique described in Chapter 3, comparisons were made between the mixing and trajectory of the flush and elevated jets at velocity ratios of R=2 and R=4. In these experiments the jet fluid was uniformly marked with fluorescent dye and the flow was imaged using the PLIF technique. The time-averaged data were averaged over 100 images.

The obtained data allow;

- a comparison between the jet centreline trajectories for the different jet conditions investigated and the effect of scaling using R and Rd;
- a comparison between the jet centreline concentration profiles along the plane of symmetry for the two velocity ratios and for both the flush and elevated jets;
- a comparison between the jet centreline concentration along the plane of symmetry and the concentration of the high concentration fluid off the jet plane of symmetry for each of the cases investigated;
- a comparison between the trajectories of the jet both on the centreline and in the three-dimensional flow based on the locus of highest concentration.

5.4.2 Time-averaged Jet Centreline Trajectory

Instantaneous cross-sections of the jet along the jet's plane of symmetry, obtained by planar laser fluorescence, are shown for the two flow cases and two velocity ratios, R=2 and R=4, in Figure 5-3 and Figure 5-4 respectively. By comparing the top and bottom images in each figure it can be observed that there are differences in the trajectory of the entire jet, in the roll-up of the shear layer and possibly in the structure of the wake. The corresponding time-averaged images are shown in Figure 5-5 and Figure 5-6.

As mentioned in the Chapter 2, the jet centreline can be defined by either the locus of the maximum velocity (Moussa *et al.* 1977) or concentration measured on planes normal to the jet trajectory on the jet plane of symmetry (Smith & Mungal 1998). In the present case, the maximum concentration will be used to define the jet centreline. This will also allow a direct comparison to be made with the findings of Smith & Mungal.

In order to extract the jet centreline trajectory from the data collected, the points in each interrogation plane, defined in Section 4.3.1.3, were found which had the highest intensity level. If more than one point had the same value, a point halfway between the first and last point was used to define the trajectory. Plots showing the location of the resulting points representing the jet centreline are presented in Figure 5-7 to Figure 5-10. These are superimposed on contour plots representing the mean jet concentration on the jet plane of symmetry. Together these show where the jet centreline occurs relative to the jet structure.

As may be observed from the contour plots in Figure 5-7 to Figure 5-10, although corrections were made during the processing for the variations in the laser sheet intensity, imperfections in the Plexiglass panel through which the laser passed have caused vertical streaks to be present in the concentration plots. In addition, due to reflections from residual dyed fluid in the jet pipe present when the background images were captured, the intensity levels peak at the leading edge of the jet, close to the jet exit, whereas the highest intensity should be recorded across the entire jet exit. However, the overall results are still valid away from the immediate vicinity of the jet exit.

In Figure 5-11 and Figure 5-12 the jet centreline trajectories for each case are plotted, allowing a comparison to be made between them. Two conclusions may be made from the plot in Figure 5-11 which shows the jet centreline trajectory normalised by the jet diameter. The first is that the centreline trajectory of the jets with a velocity ratio of 4 penetrated further into the flow than the corresponding jets with a velocity ratio of 2. This finding is expected and is consistent with that of Smith & Mungal (1998) and others. Second, for both the velocity ratios tested, the centreline of the elevated jet penetrated further into the crossflow than the flush-mounted jet. Although a difference in jet trajectory was anticipated given the findings of Moussa *et al.* (1977), the reasons for the differences have not been adequately resolved. It can therefore be concluded from the results presented so far that for the flow cases investigated the jet from an elevated pipe penetrates further into the crossflow than the jet from the same pipe with a wall fitted flush with the jet exit. The plot shown in Figure 5-12 shows the jet centreline data for each case normalised by the product of the velocity ratio and jet diameter (Rd). As can be seen, the data are found to follow much more similar profiles, suggesting an Rd dependence, as was shown by Smith & Mungal (1998), Pratte & Baines (1967) and others. For comparison, the jet centreline data plotted in Figure 5-12 is reproduced in Figure 5-13 superimposed with trajectories formulated by Pratte & Baines, calculated for R=5 to 35 and Smith & Mungal, calculated for R=5 to 25. The trajectories of Pratte & Baines and Smith & Mungal are curve fits of experimental data extending into the far-field. The jet used by Pratte & Baines was elevated, whereas that used by Smith & Mungal was flush-mounted. As can be seen, the trajectories of the jets obtained in the current research show a reasonable agreement with the trajectories found by others, given that there is a large range of velocity ratios, Reynolds numbers and other flow conditions used to obtain the trajectories.

Flush-mounted jet

Elevated jet

Figure 5-3 Instantaneous cross-section of the jet through the jet's plane of symmetry for R=2. The jet Reynolds number was 4000 and crossflow Reynolds number 2000.

Flush-mounted jet

Elevated jet

Figure 5-4 Instantaneous cross-section of the jet through the jet's plane of symmetry for R=4. The jet Reynolds number was 8000 and crossflow Reynolds number 2000.

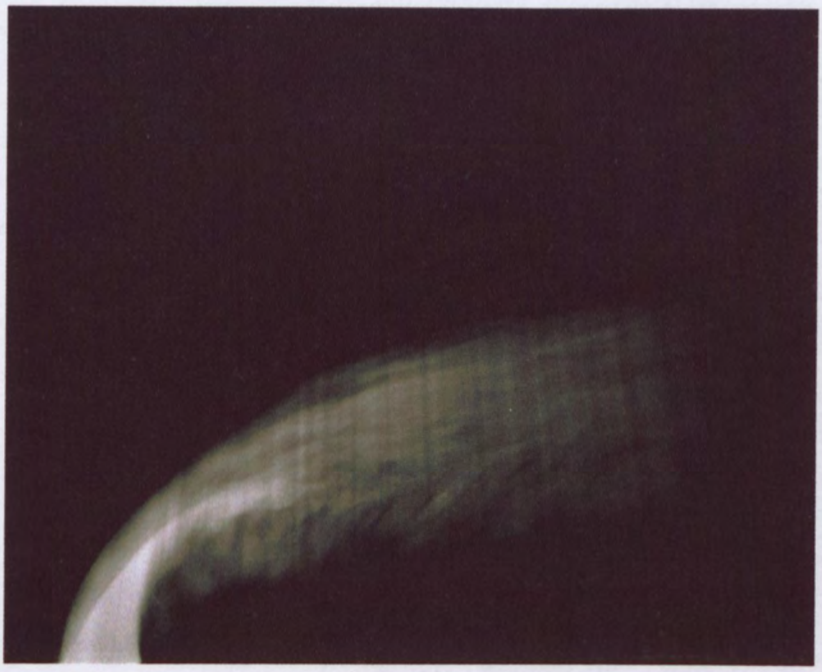

Flush-mounted jet

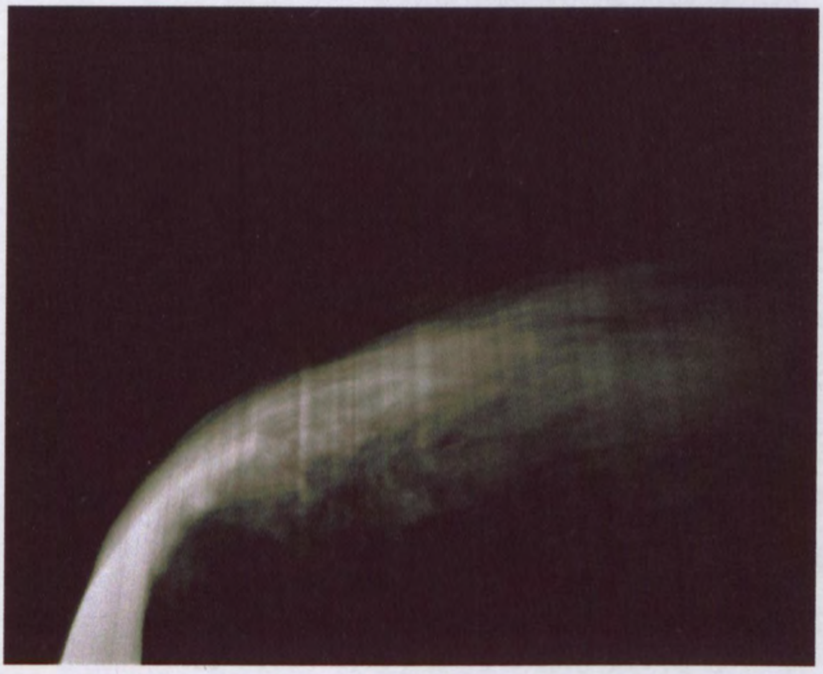

Elevated

Figure 5-5 Time-averaged cross-section of the jet through the jet's plane of symmetry for R=2. The jet Reynolds number was 4000 and crossflow Reynolds number 2000.

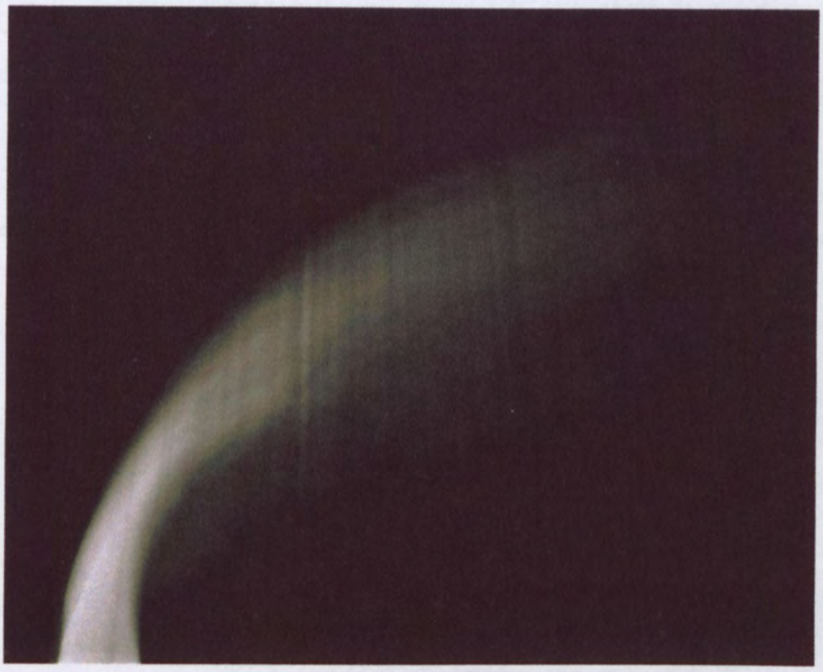

Flush-mounted jet

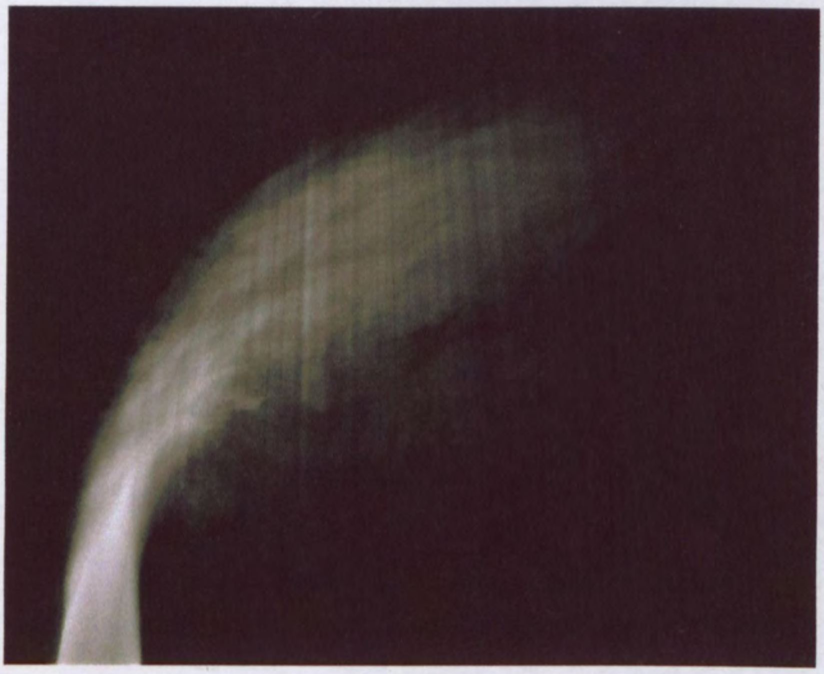

Elevated jet

Figure 5-6 Time-averaged cross-section of the jet through the jet's plane of symmetry for R=4. The jet Reynolds number was 8000 and crossflow Reynolds number 2000.

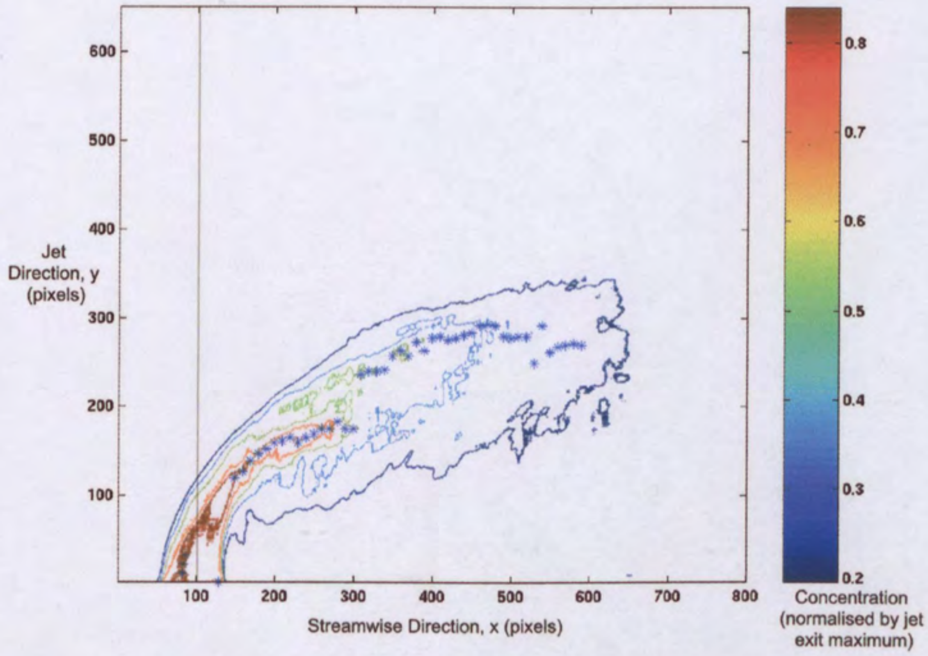

Figure 5-7 Concentration contour plot of the jet plane of symmetry for the R=2 flush-mounted jet with the resolved jet centreline trajectory shown as blue asterisk.

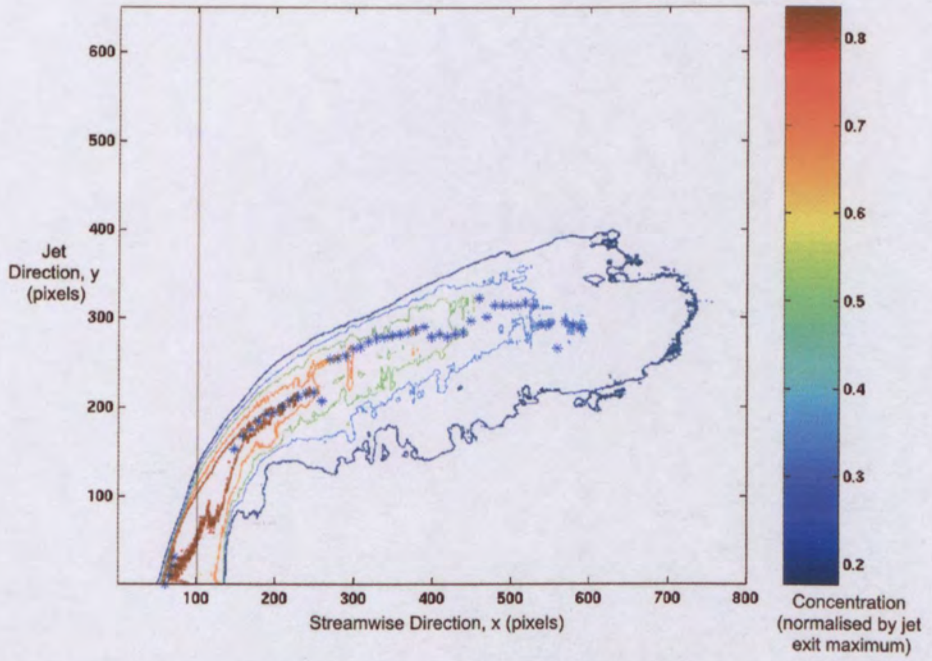

Figure 5-8 Concentration contour plot of the jet plane of symmetry for the R=2 elevated jet with the resolved jet centreline trajectory shown as blue asterisk.

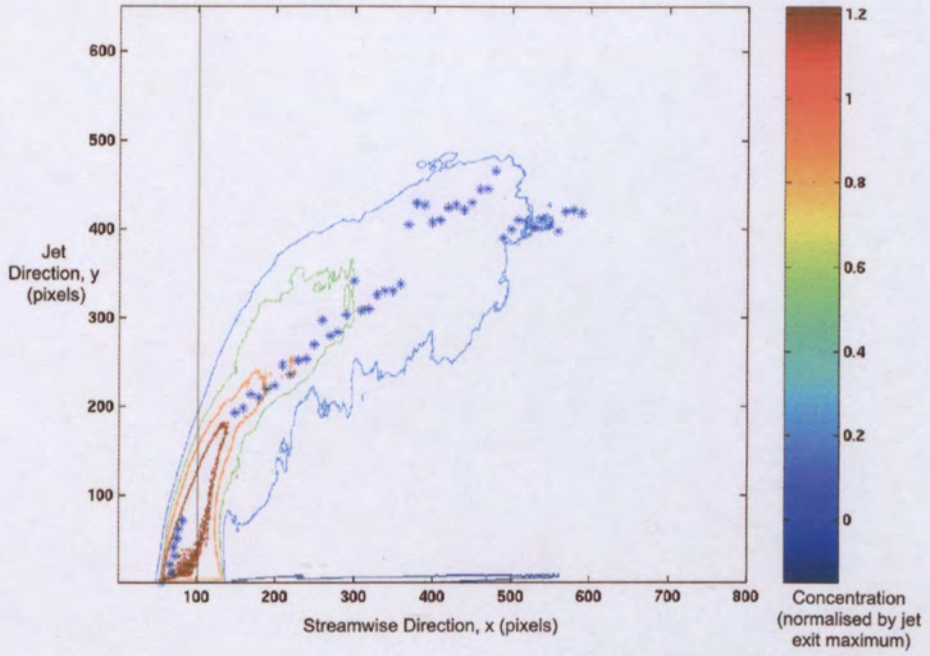

Figure 5-9 Concentration contour plot of the jet plane of symmetry for the R=4 flush-mounted jet with the resolved jet centreline trajectory shown as blue asterisk.

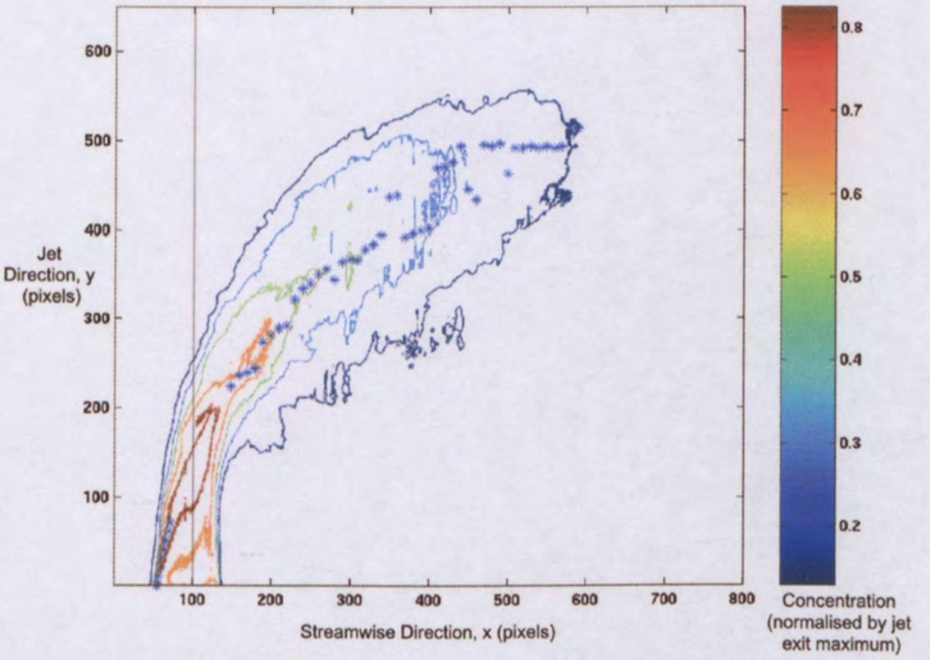

Figure 5-10 Concentration contour plot of the jet plane of symmetry for the R=4 elevated jet with the resolved jet centreline trajectory shown as blue asterisk.

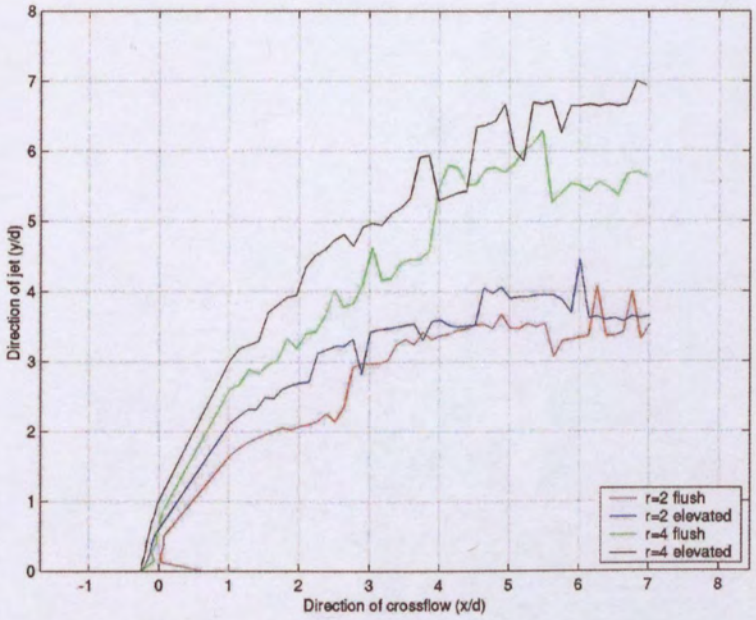

Figure 5-11 Jet centreline trajectory for each flow case normalised by the jet diameter (d).

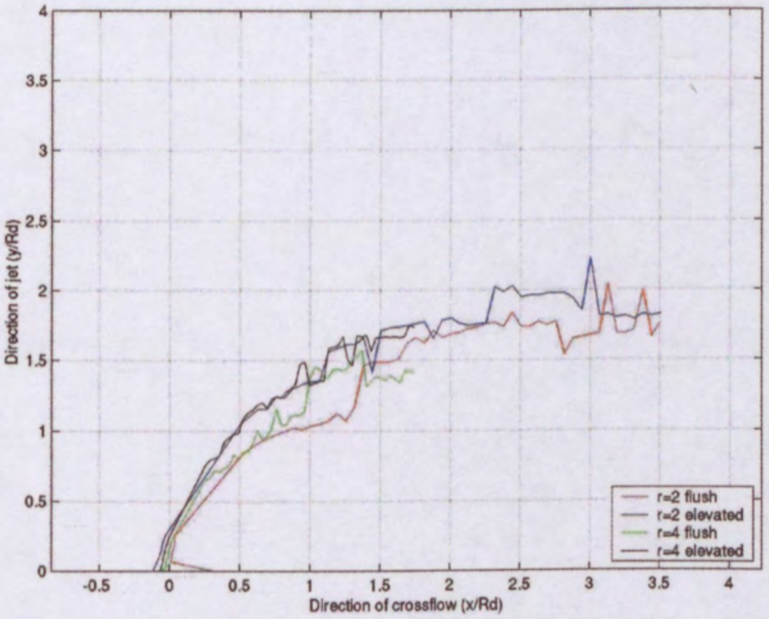

Figure 5-12 Jet centreline trajectory for each flow case normalised by the product of the velocity ratio and jet diameter (Rd).

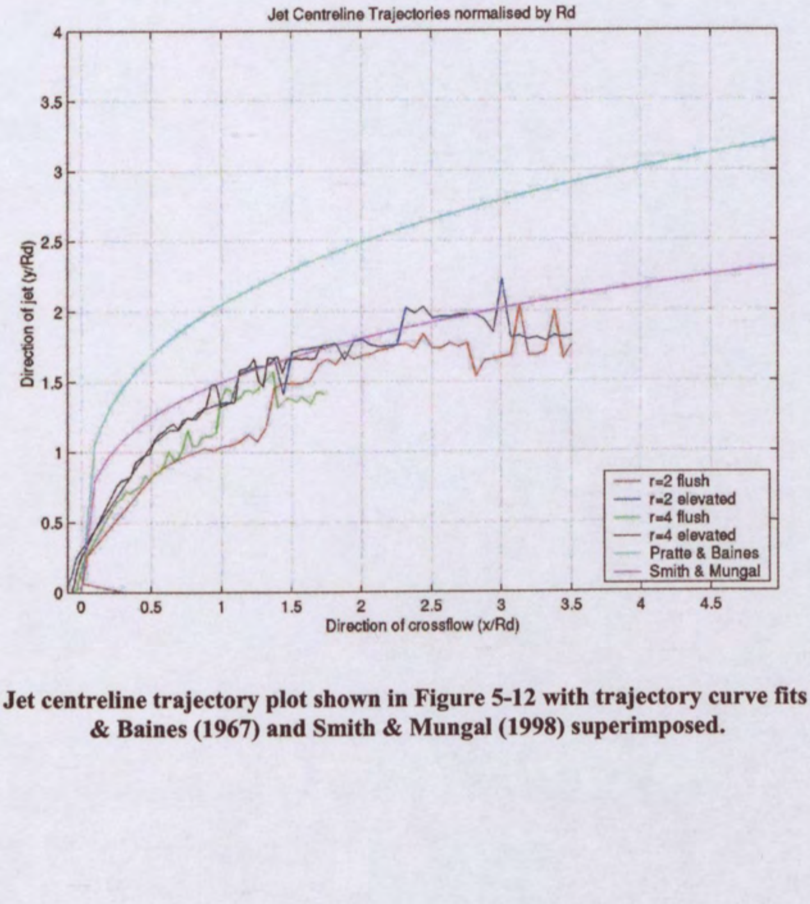

Figure 5-13 Jet centreline trajectory plot shown in Figure 5-12 with trajectory curve fits from Pratte & Baines (1967) and Smith & Mungal (1998) superimposed.

5.4.3 Time-averaged Jet Centreline Trajectory versus CVP Trajectory

By rendering only the portion of the dye-marked fluid at and above a particular concentration level, it is possible to show the three-dimensional trajectory of the fluid with the highest concentration. It is therefore possible to investigate the three-dimensional development of the CVP as the jet is deformed from its original circular cross-section at the jet exit to a kidney shape, and then as the position of the maximum local concentration moves off the plane of symmetry (Smith & Mungal 1998). Indeed, Smith & Mungal (1998) concluded that the maximum concentration of jet fluid resides in the core of the CVP. This is also in accord with the author's visual observations. Therefore, in the following discussion it will be assumed that the locus of maximum concentration in the three-dimensional flow field resides at the core of the CVP, and further, that this locus defines the trajectory of the CVP.

The volumetric renderings in Figure 5-14 to Figure 5-21 have been generated by normalising the concentration in each of the x-z planes by the maximum concentration in each plane, and rendering the intensity levels at and above a concentration level of 80% of the jet exit concentration. They are therefore not a true representation of the jet concentration, but do show the trajectory of the fluid with the highest concentration. It is important to note that the flow was captured on one side of the plane of symmetry only and so the renderings only represent one half of the structure of the jet. Although the results of Smith & Mungal (1998) show that there may be an asymmetry in the concentration profiles of cross-sections of the CVP, presumably due to small imperfections in the initial conditions, the asymmetries are small compared with the scale of the jet. Therefore the results shown here can be assumed representative of the complete flow structure. In Figure 5-14 to Figure 5-21 the renderings are shown against a background of the normalised concentration fields on the plane of symmetry and on the plane of the jet exit. These provide a reference for the trajectory of the high concentration fluid. The concentration values shown on these planes are normalised by the same method as that for the high concentration data, described above. As noted previously, a drop-out in the intensity signal occurred on the downstream side of the jet, close to the jet exit. The effect of this is present in Figure 5-14 to Figure 5-21, and therefore the rendered structures appear to emerge from the leading edge of the jet, although the intensity should be the same across the entire exit plane.

As may be observed there are substantial differences between the flush-mounted and elevated jet cases. Apart from the difference in trajectory, as noted previously, the lateral spreading of the high concentration jet fluid is also different. The lateral spreading of the high concentration fluid in the elevated jet is small, as the fluid remains close to the jet centreline, whereas the flush-mounted jet expands more and the high concentration fluid moves laterally away from the jet centreline, especially in the R=4 case. This can be seen more clearly in Figure 5-18 and Figure 5-21 in which the same renderings are shown as those in Figure 5-14 and Figure 5-17 respectively, but from a view above the jet exit, looking down at the jet coming out of the page.

The plots shown in Figure 5-22 and Figure 5-23 allow the trajectory of the CVP to be compared for a flush-mounted jet and an elevated jet, for the two velocity ratios investigated. The top image in both figures is a three-dimensional perspective view of the data, looking from a position upstream of the jet with the jet shown moving into the page. The lower left hand and right hand plots provide a side view and top view, respectively, of the upper plot. It is evident that for the R = 2 case the trajectory and lateral spreading of the CVP is similar for both the elevated and flush-mounted jets. However, for the R = 4 case there is a substantial difference in both the trajectory and lateral spreading of the CVP between the flush-mounted and elevated flow cases. This finding is supported by the volumetric renderings of the jet which show a substantial increase in the lateral spreading of the flush-mounted jet compared with the elevated jet for the higher velocity ratio. The spurious points which appear in Figure 5-22 (and also later in Figure 5-24) are a result of the data processing technique not correctly locating points in the data representing the location of the CVP.

The plots shown in Figure 5-24 and Figure 5-25 allow a comparison between the trajectories of the CVP and the jet centreline for the two velocity ratios to be made for the flush and elevated flow cases respectively. In the flush-mounted jet case the increase in velocity ratio from 2 to 4 causes an increase in the lateral spreading of the CVP. In the elevated jet case, however, the lateral spreading is does not change significantly as R is increased from 2 to 4.

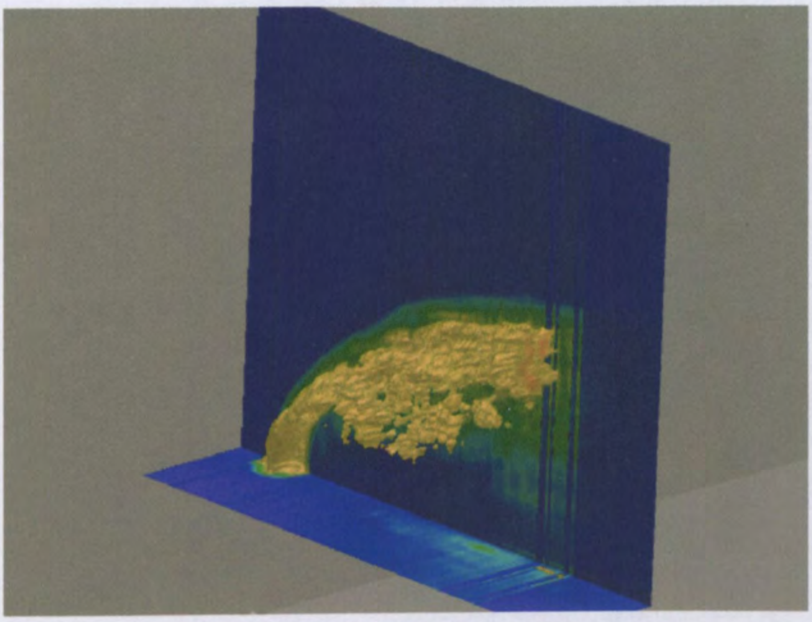

R=2, Re=2000 Flush-mounted

Figure 5-14 Volume rendering of the high concentration flow structures (in yellow) shown against the normalised mean concentration on the jet plane of symmetry and jet exit plane for a flush-mounted jet with a velocity ratio of 2.

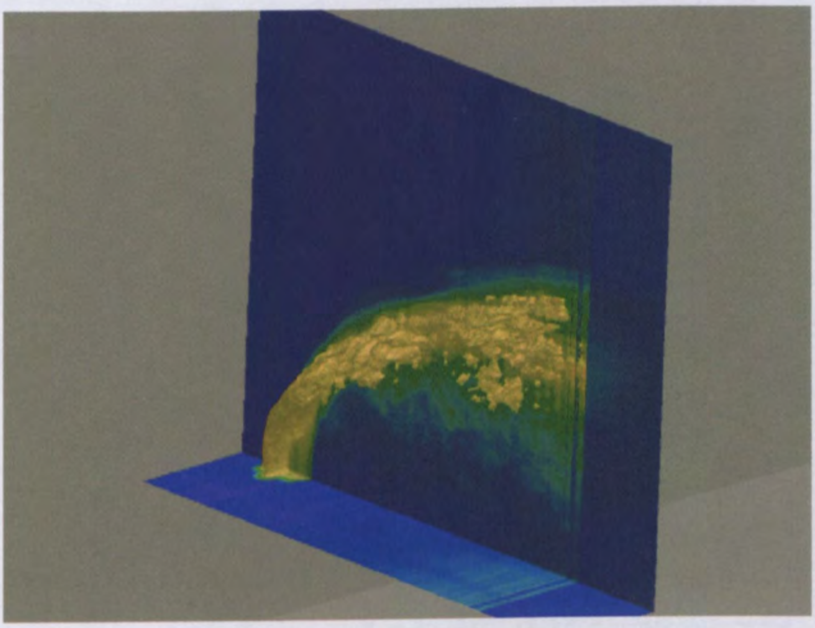

R=2, Re=2000 Elevated

Figure 5-15 Volume rendering of the high concentration flow structures (in yellow) shown against the normalised mean concentration on the jet plane of symmetry and jet exit plane for an elevated jet with a velocity ratio of 2.

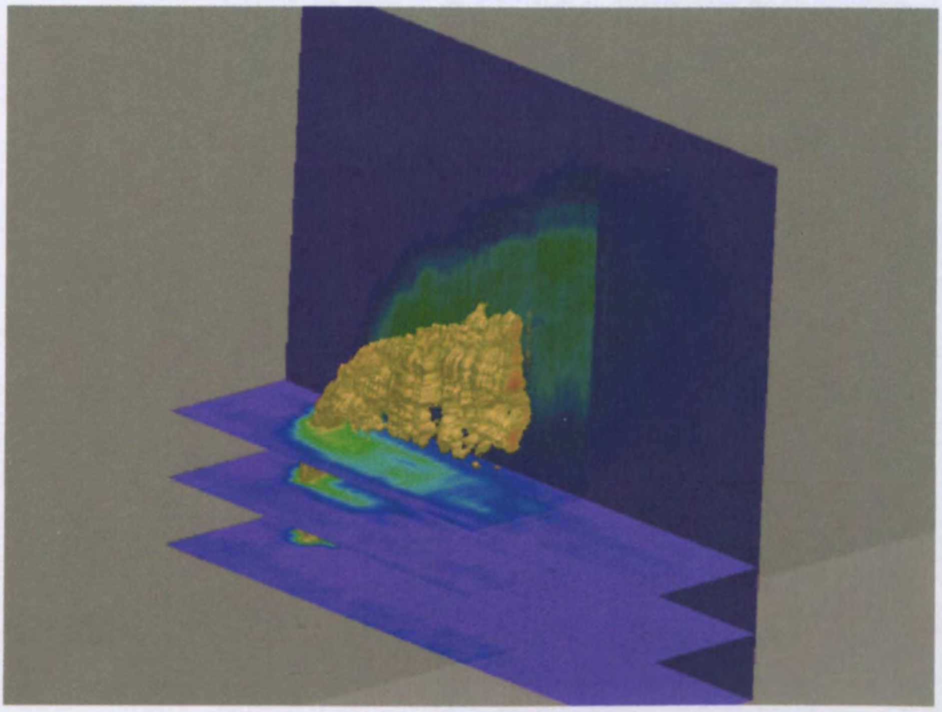

R=4, Re=2000 Flush-mounted

Figure 5-16 Volume rendering of the high concentration flow structures (in yellow) shown against the normalised mean concentration on the jet plane of symmetry and jet exit plane for a flush-mounted jet with a velocity ratio of 4.

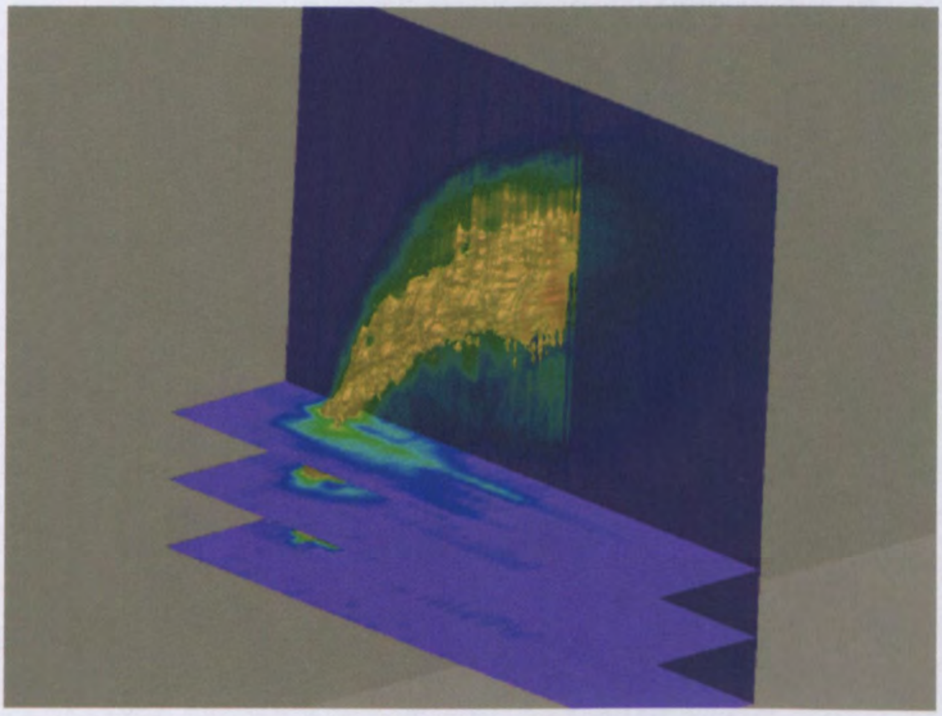

R=4, Re=2000 Elevated

Figure 5-17 Volume rendering of the high concentration flow structures (in yellow) shown against the normalised mean concentration on the jet plane of symmetry and jet exit plane for an elevated jet with a velocity ratio of 4.

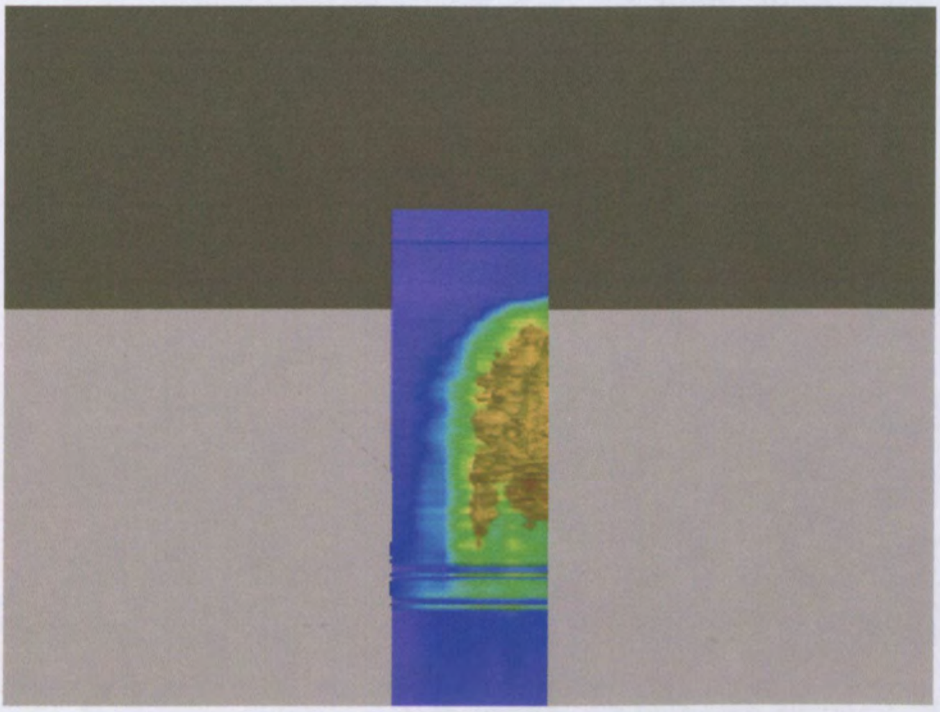
R=2, Re=2000   Flush-mounted

Figure 5-18 Volume rendering for a flush-mounted jet at a velocity ratio of 2, as in Figure 5-14, but viewed from a position above and downstream of the jet exit. The scale of the rendering is the same as in Figure 5-14.

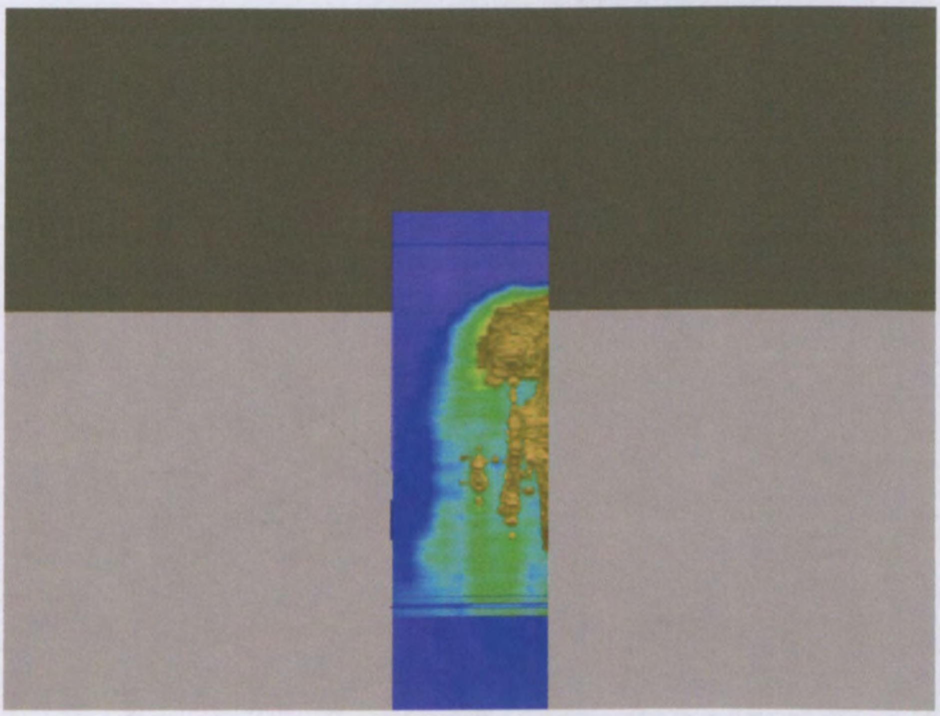
R=2, Re=2000   Elevated

Figure 5-19 Volume rendering for an elevated jet at a velocity ratio of 2, as in Figure 5-15, but viewed from a position above and downstream of the jet exit. The scale of the rendering is the same as in Figure 5-15.

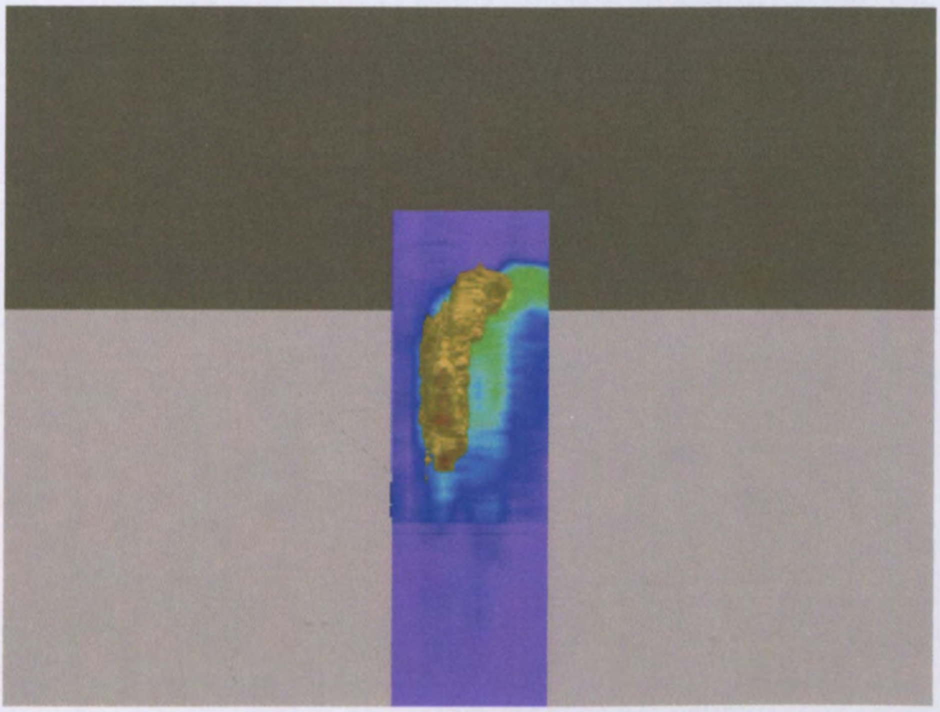

R=4, Re=2000 Flush-mounted

Figure 5-20 Volume rendering for a flush-mounted jet at a velocity ratio of 4, as in Figure 5-16, but viewed from a position above and downstream of the jet exit. The scale of the rendering is the same as in Figure 5-16.

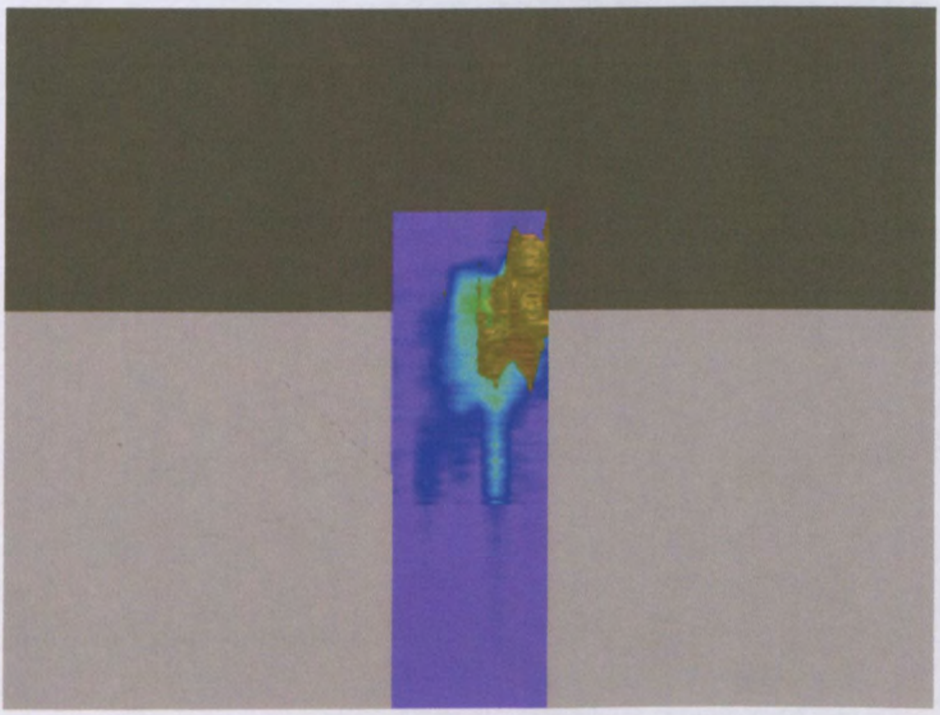

R=4, Re=2000 Elevated

Figure 5-21 Volume rendering for an elevated jet at a velocity ratio of 4, as in Figure 5-17, but viewed from a position above and downstream of the jet exit. The scale of the rendering is the same as in Figure 5-17.

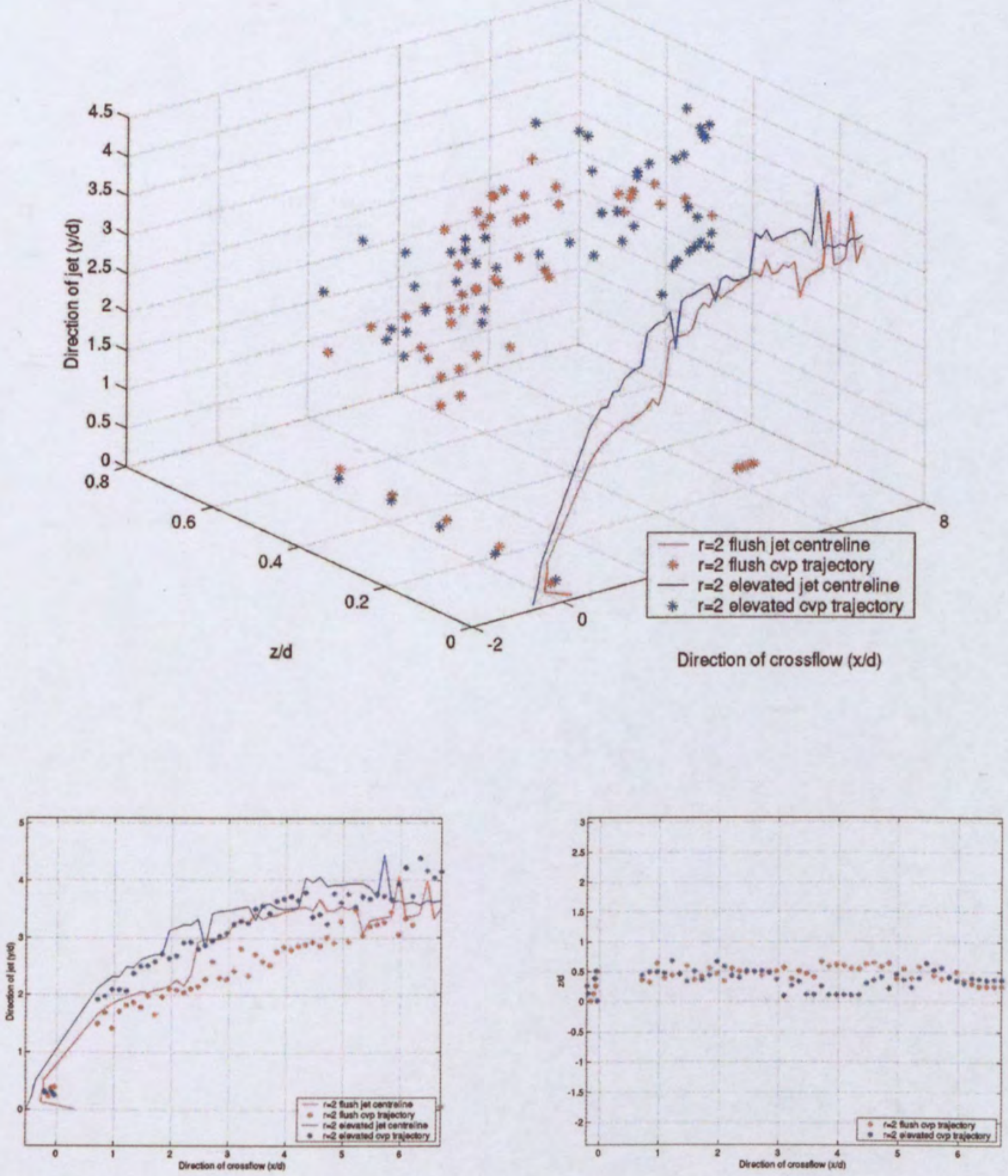

Figure 5-22 R=2 flush versus elevated jet centreline and CVP trajectories.

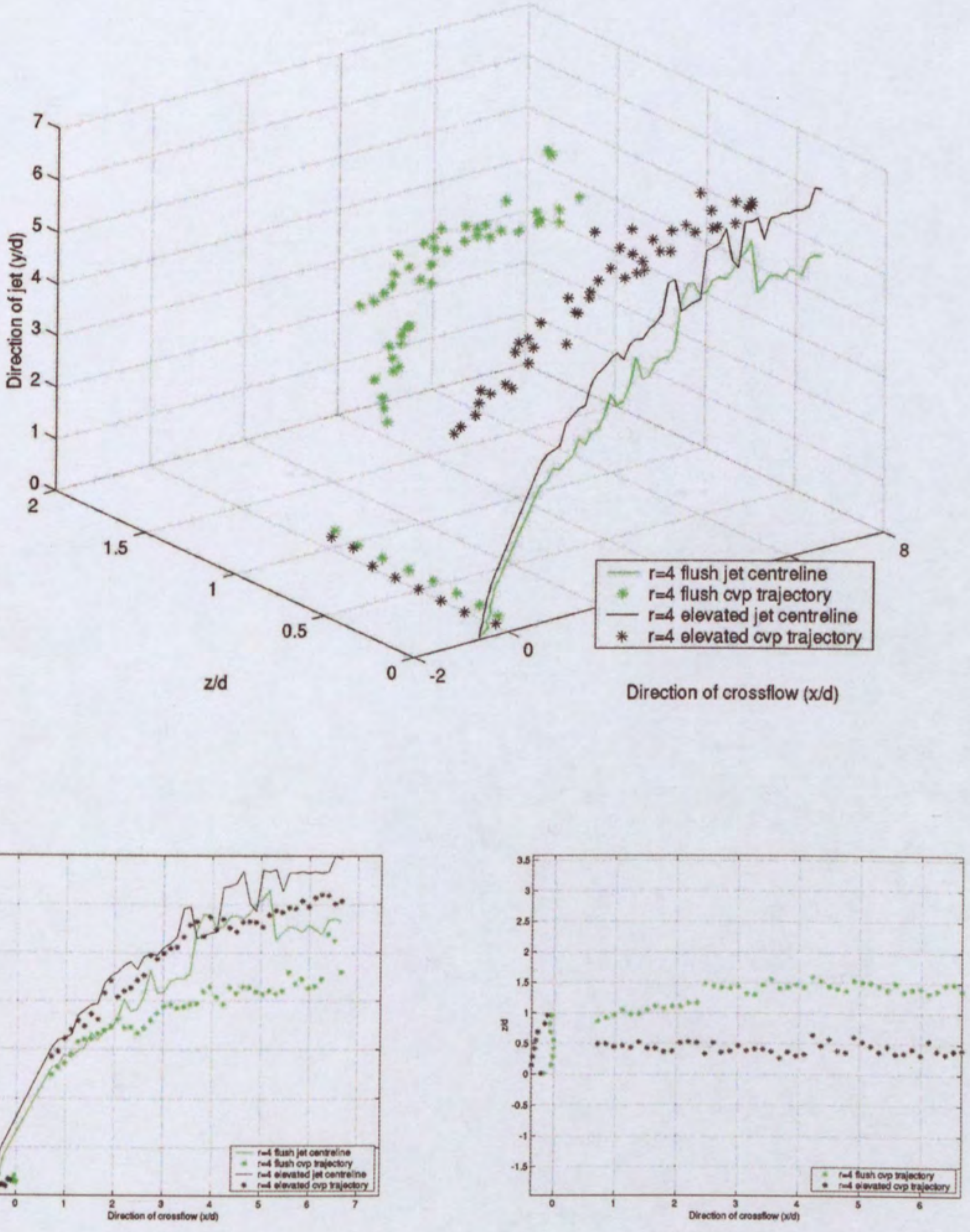

Figure 5-23 R=4 flush versus elevated jet centreline and CVP trajectories.

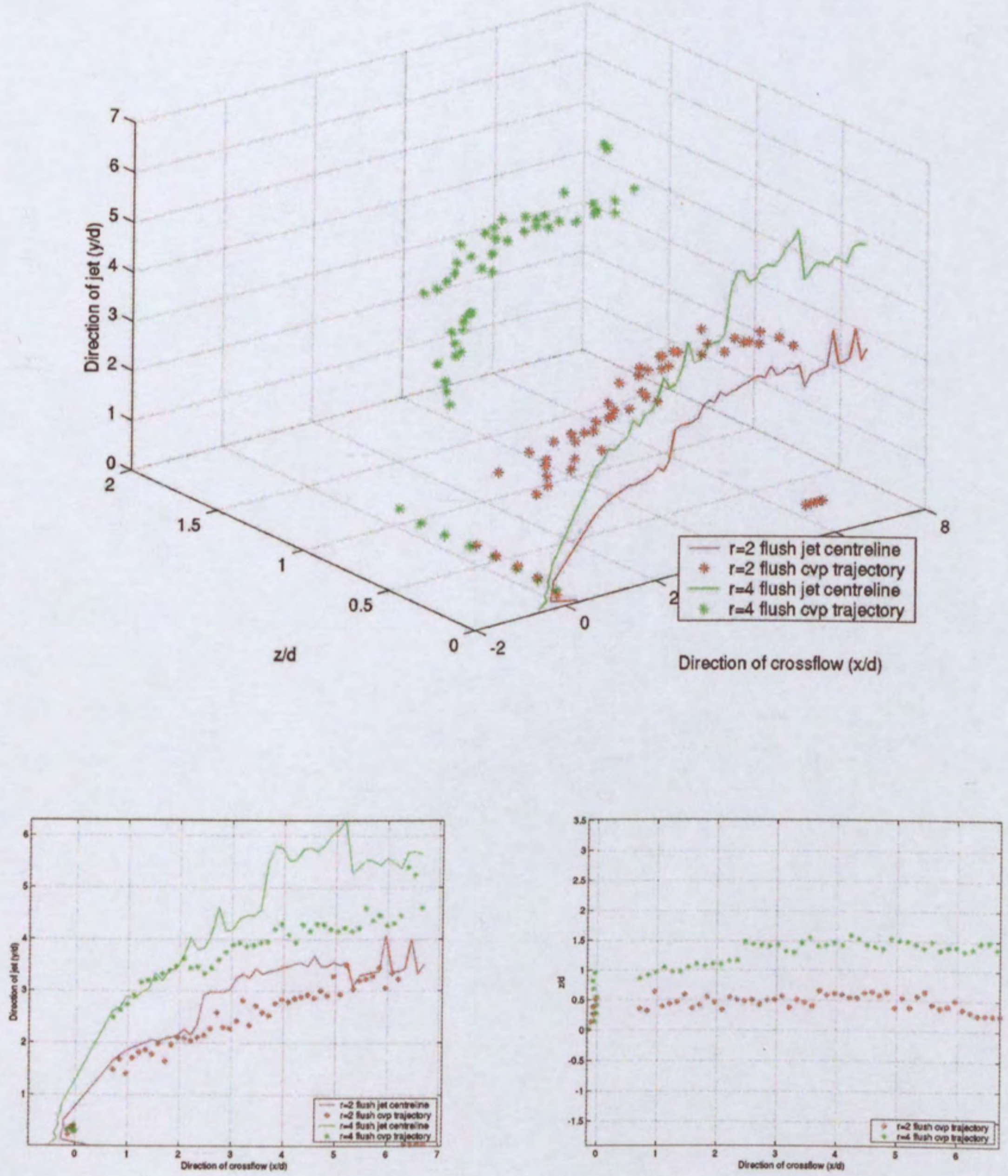

Figure 5-24 R=2 flush jet centreline and CVP trajectories versus R=4 flush jet centreline and CVP trajectories.

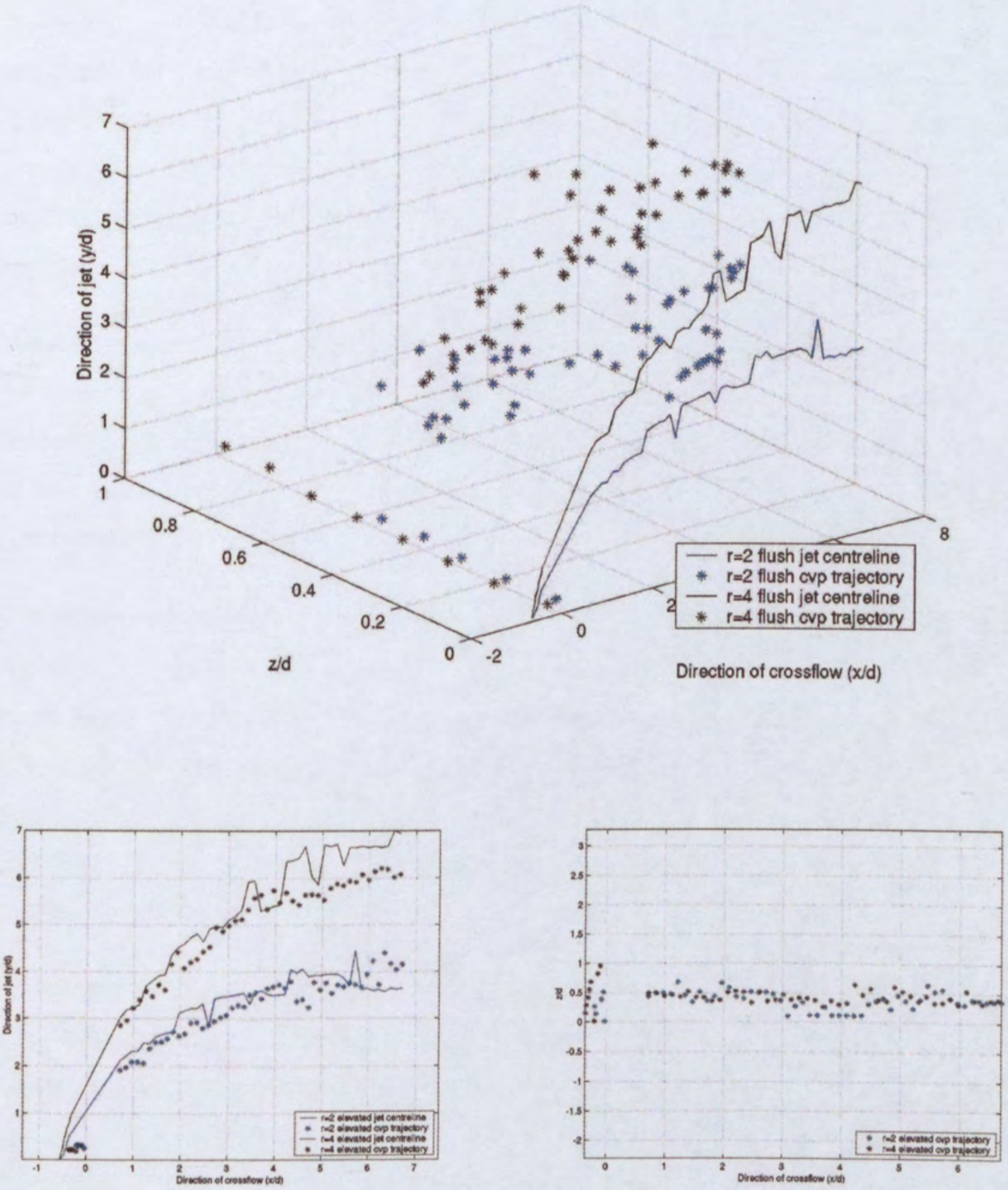

Figure 5-25 R=2 elevated jet centreline and CVP trajectories versus R=4 elevated jet centreline and CVP trajectories.

5.4.4 Time-averaged Jet Mixing

In the previous section the trajectories of the various jets were investigated based on the scalar concentration field. In this section, the same data are used to investigate differences in the time-averaged scalar concentration between the different flow cases. The results presented are based on the normalised concentration values relative to the jet exit concentration, rather than the locally normalised concentration values used in the previous section.

The renderings in Figure 5-26 to Figure 5-29 show the concentration in the flow relative to the jet exit concentration on various planes within the flow for the four flow cases. In each rendering, the back plane is the plane of symmetry and the lowest horizontal plane is the jet exit plane. The fluid with the highest concentration is shown in red, and the lowest concentration fluid is purple.

A number of important observations can be made from these results. First, the jet penetration is again shown to be increased for the elevated jet compared with the flush-mounted jet. Second, there is a difference in the location of the high concentration fluid (CVP) between the flush and elevated cases, as demonstrated in Section 5.4.3. The CVP occurs away from the jet centreline for the flush-mounted jet, but stays close to the centreline for the elevated jet. Therefore, based on the concentration data, the flush-mounted jet shows a lower trajectory and a more rapid lateral spreading.

Plots of the normalised concentration at the points used to define the jet centreline (on the plane of symmetry) versus the normalised streamwise distance were produced in order to investigate the centreline concentration decay for the different flow conditions investigated. In Figure 5-30 and Figure 5-31 plots of the maximum normalised concentration on the jet centreline for velocity ratios of 2 and 4 are shown for the flush and elevated jets respectively. The values at the centre of the jet exit have been adjusted to a normalised concentration of 1 to remove the spurious results discussed earlier. In addition, it is apparent that the data are noisy. Since the trends in the data are clear even with these artefacts, no corrections or smoothing of the data was applied. As can be seen, for both the flush and elevated cases the jet centreline concentration decay is higher for the higher velocity ratio flow.

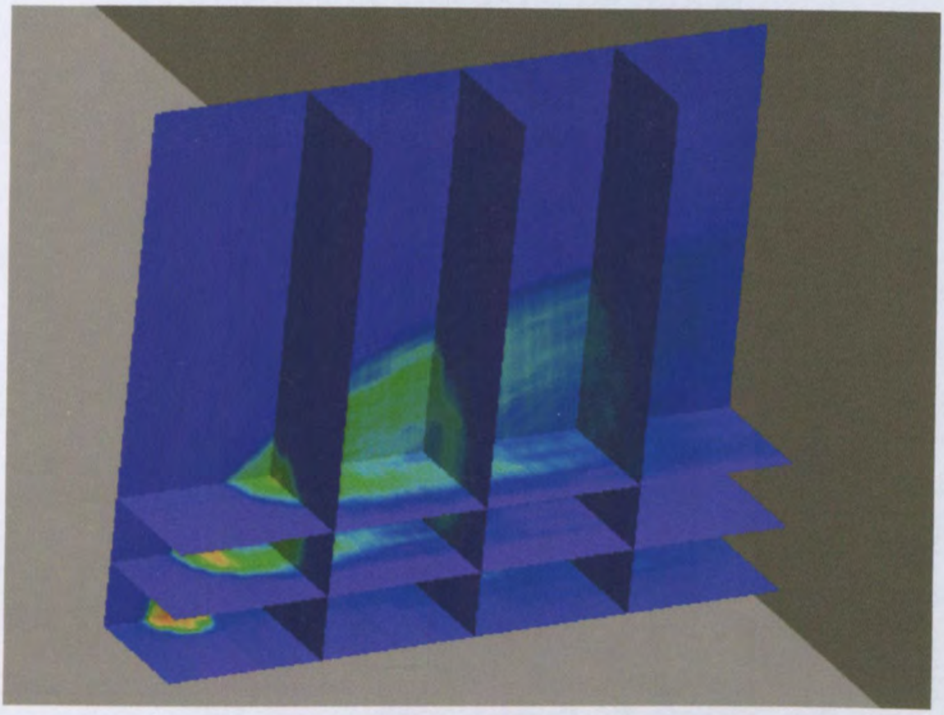

R=2, Re=2000 Flush-mounted

Figure 5-26 The jet concentration field for a flush-mounted jet with a velocity ratio of 2. The vertical slice at the back is the jet centreline plane. The lower horizontal slice is the positioned at the jet exit plane. The regions of highest concentration are shown in red, and lowest in purple.

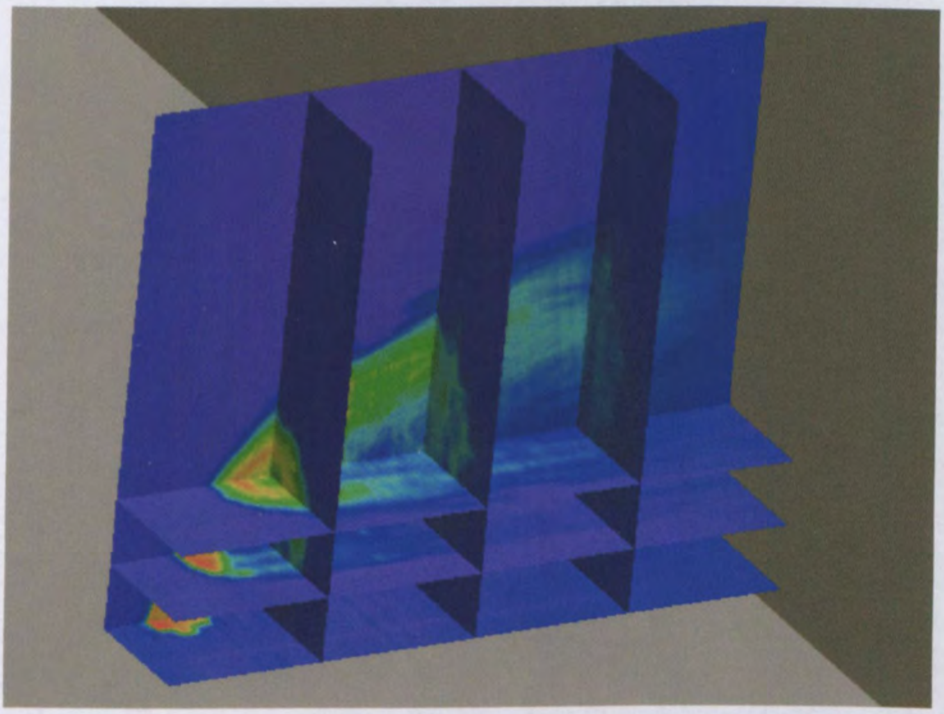

R=2, Re=2000 Elevated

Figure 5-27 The jet concentration field for an elevated jet with a velocity ratio of 2. The vertical slice at the back is the jet centreline plane. The lower horizontal slice is the positioned at the jet exit plane. The regions of highest concentration are shown in red, and lowest in purple.

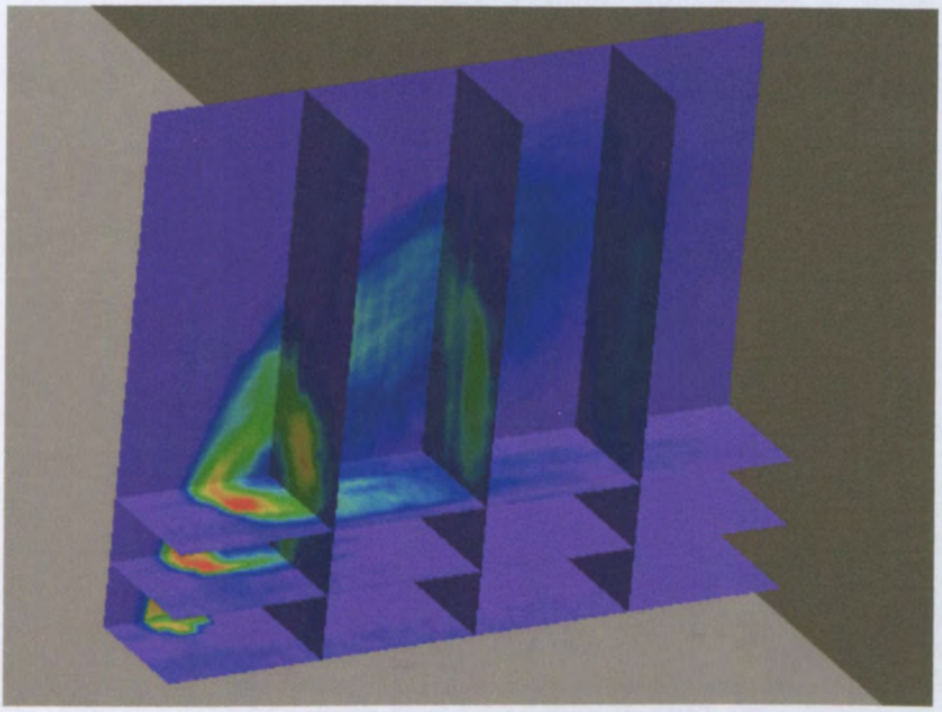

R=4, Re=2000 Flush-mounted

Figure 5-28 The jet concentration field for the flush-mounted jet with a velocity ratio of 4. The vertical slice at the back is the jet centreline plane. The lower horizontal slice is the positioned at the jet exit plane. The regions of highest concentration are shown in red, and lowest in purple.

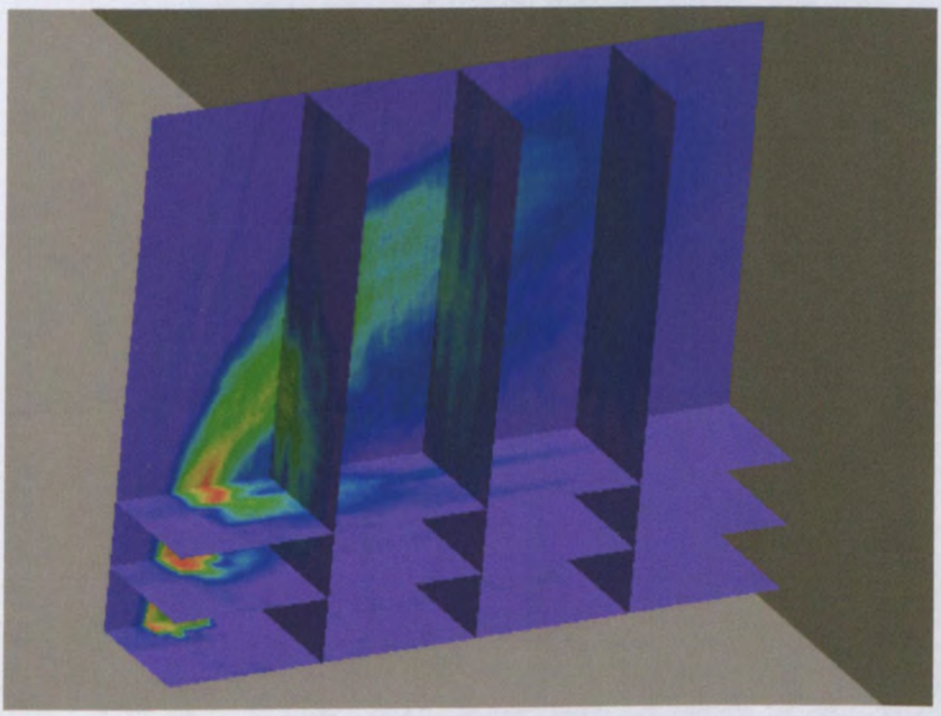

R=4, Re=2000 Elevated

Figure 5-29 The jet concentration field for an elevated jet with a velocity ratio of 4. The vertical slice at the back is the jet centreline plane. The lower horizontal slice is the positioned at the jet exit plane. The regions of highest concentration are shown in red, and lowest in purple.

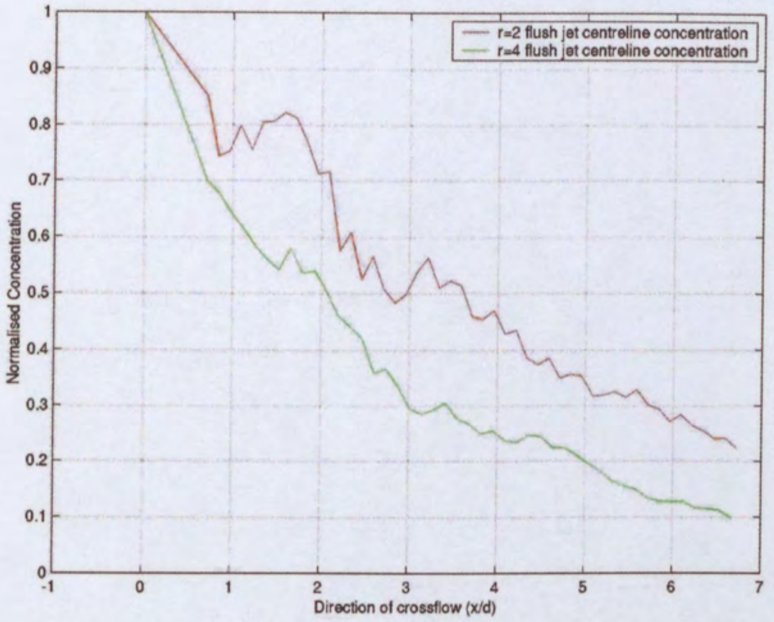

Figure 5-30 Concentration along the jet centreline trajectory normalised against the jet exit concentration for the flush-mounted jet at R=2 and R=4, Re=2000.

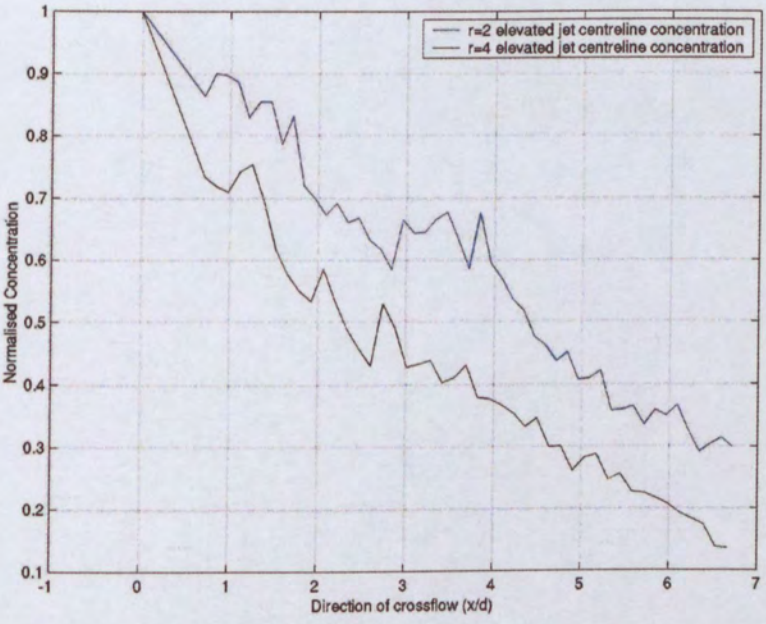

Figure 5-31 Concentration along the jet centreline trajectory normalised against the jet exit concentration for the elevated jet at R=2 and R=4, Re=2000.

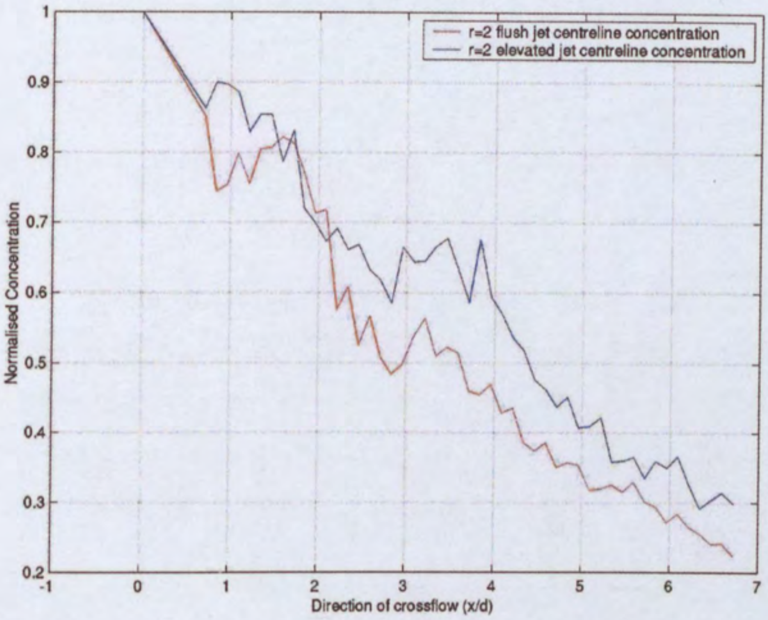

Figure 5-32 Concentration along the jet centreline trajectory normalised against the jet exit concentration for the flush-mounted and elevated jets at R=2, Re=2000.

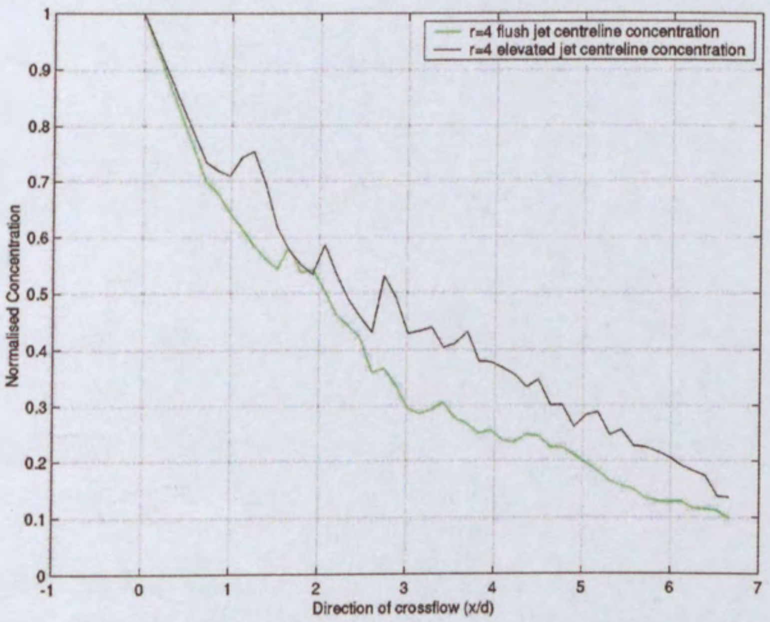

Figure 5-33 Concentration along the jet centreline trajectory normalised against the jet exit concentration for the flush-mounted and elevated jets at R=4, Re=2000.

The plots in Figure 5-32 and Figure 5-33 show a comparison of the normalised concentration along the jet centreline trajectory for the flush versus elevated jets at R=2 and 4 respectively. It can be seen that the concentration on the jet centreline tends to decrease more rapidly for the flush-mounted jet than for the elevated jet. This effect correlates well with the lower trajectories observed for the flush-mounted jets.

Plots of the concentration on the jet centreline trajectory versus the concentration through the locus of the CVP for each of the cases investigated are shown in Figure 5-34 to Figure 5-37. These plots show that, apart from the case of the flush-mounted jet at R=4, the difference in concentration between the jet centreline and the CVP is not significant, and is within the scatter of the data. Excellent correspondence exists for the elevated jet at R=4.

The findings from the plots of the normalised concentration may therefore be summarised:

- For R=2 (elevated and flush) and R=4 (elevated) the CVP remains close to the plane of symmetry and therefore the concentrations in the CVP and on the plane of symmetry are similar.
- For the R=4 flush-mounted jet the concentration within the CVP is higher than the maximum concentration on the plane of symmetry at any given streamwise location. Initially the decay rate is less rapid along the CVP, leading to the difference in the magnitude of concentration downstream. Between $1 \leq x/d \leq 5$ the decay rate is similar on the basis of the streamwise coordinate. This contrasts with results for the elevated jet where the plane of symmetry and CVP concentration curves are very similar.

Comparisons between Figure 5-32, and Figure 5-34 & Figure 5-35 for R=2 also show that in the elevated jet the decay rate along the CVP is smaller than in the flush-mounted jet. However, comparisons between Figure 5-33 and Figure 5-36 & Figure 5-37, show the opposite trend for R=4.

These findings suggest a difference in the underlying flow structure between the flush-mounted and elevated jets and between the flush-mounted jets at the two velocity ratios. These differences are small for the R=2 case.

In an attempt to determine the concentration decay rates both on the jet centreline and along the CVP, the concentration decay was plotted against the jet-wise distances, s, normalised by Rd on a log-log scale for all the jet cases in Figure 5-38. The jet-wise distance was calculated by summing the linear distance between consecutive points along the trajectories. As can be seen the jet concentration remains close to 100% to begin with, which defines the potential core region, and then decays as the core fluid becomes mixed with the ambient fluid. The reference lines included on the plot indicate decay rates of $s^{-2/3}$, s^{-1} and $s^{-1.3}$. The $s^{-2/3}$ line approximates the far-field decay rate of $x^{-2/3}$ predicted by Broadwell & Breidenthal (1984). Note that all the data shown here are near-field data. As is evident from the plot, the near-field decay rate found in this case is substantially greater than $s^{-2/3}$, added to the fact that in the near-field the difference between x and s will be large compared with the far-field. The results suggest that the decay rate for the flush-mounted jet at a velocity ratio of 4 approximates the $s^{-1.3}$ decay which was the near-field jet centreline decay rate found by Smith & Mungal (1998) for flush-mounted jets with velocity ratios greater than 5. The decay rate along the jet centreline in the near-field region is therefore higher than the s^{-1} decay rate of a free jet for this case. The other flow cases show lower decay rates than $s^{-1.3}$.

The plot shown in Figure 5-39 includes the jet centreline data shown in Figure 5-38, this time as dashed lines, along with the normalised concentration decay along the locus of the CVP, (i.e. the points of maximum concentration off the plane of symmetry). The decay rate along the CVP shows significant scatter, but the trend shows a collapse of the concentration decay data and a mean decay rate close to s^{-1} in each case. Curve fitting of the data suggests a decay rate of $s^{-1\pm20\%}$. This suggests a decay rate close to that of a free jet. The result suggests that the regions of high concentration fluid, that is the CVP cores, may decay in the near-field in a similar manner to that of a free jet. In the far-field this decay rate may be expected to decrease to the Broadwell & Breidenthal value of $s^{-2/3}$, but this is yet to be determined.

Considering these observations, it appears that in the elevated jet cases the CVP remains close to the plane of symmetry, and so the high concentration jet fluid remains close to the plane of symmetry. Thus, the CVP and centre plane concentration profiles are similar in each case. The same conclusion can be drawn for the flush-mounted R=2 jet where the CVP is relatively weak and therefore remains close to the plane of symmetry. However, in the case of the flush-mounted R=4 jet, the CVP rapidly diverges from the plane of symmetry and transports high concentration jet fluid away from the plane of symmetry. Thus, the CVP's core fluid concentration is substantially higher than the centre plane concentration, in contrast to the other flow cases. However, in all of the cases analysed the concentration decay rate along the core of the CVP appears to be similar to the decay rate of a simple jet.

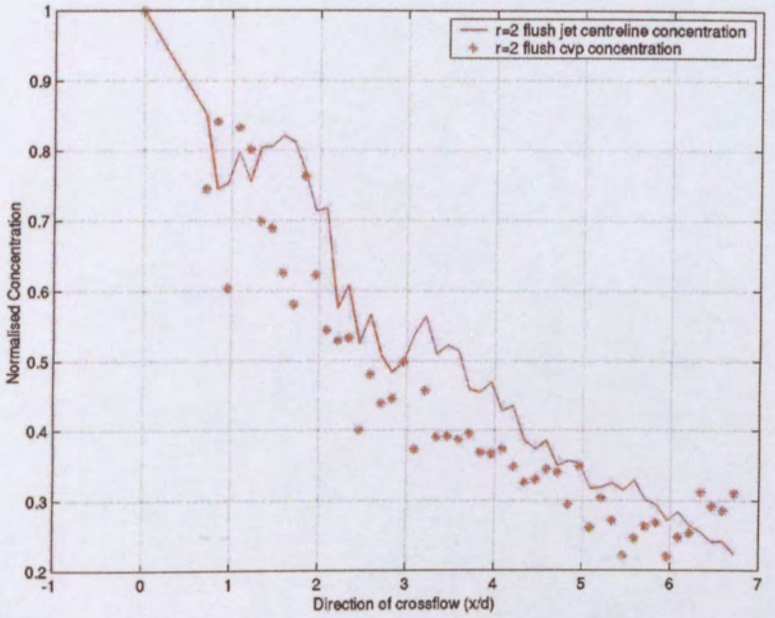

Figure 5-34 Concentration along the jet centreline and CVP trajectories normalised against the jet exit concentration for the flush-mounted jet at R=2.

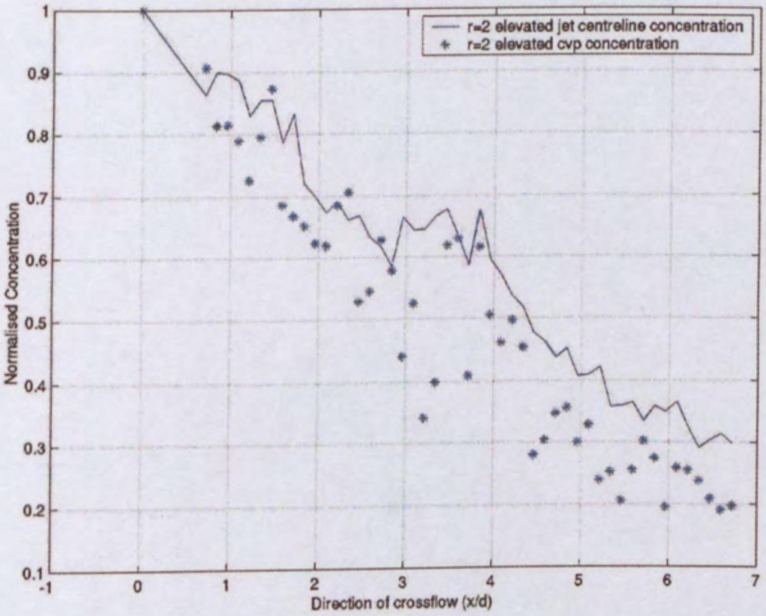

Figure 5-35 Concentration along the jet centreline and CVP trajectories normalised against the jet exit concentration for the elevated jet at R=2.

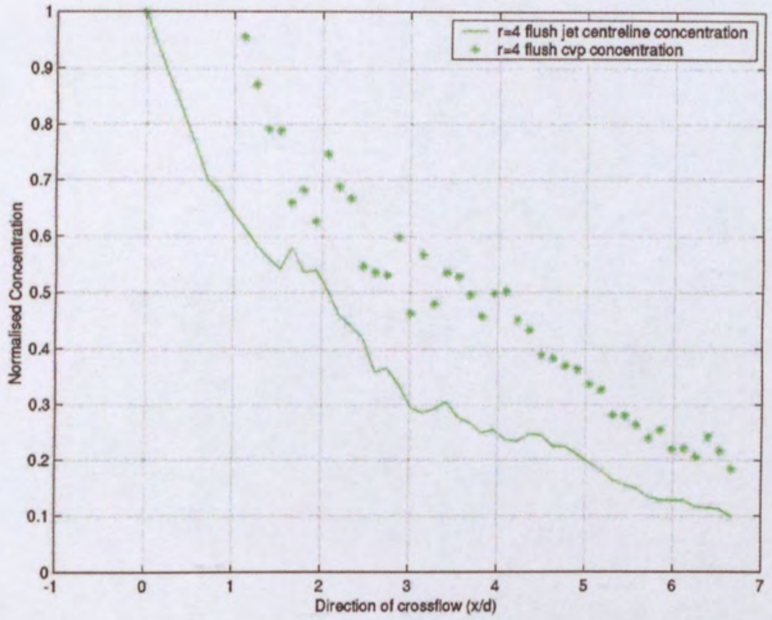

Figure 5-36 Concentration along the jet centreline and CVP trajectories normalised against the jet exit concentration for the flush-mounted jet at R=4.

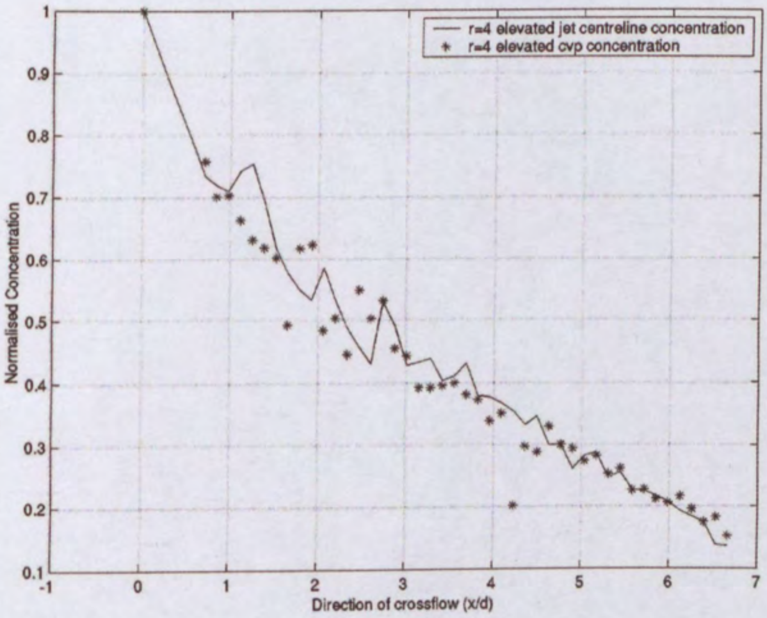

Figure 5-37 Concentration along the jet centreline and CVP trajectories normalised against the jet exit concentration for the elevated jet at R=4.

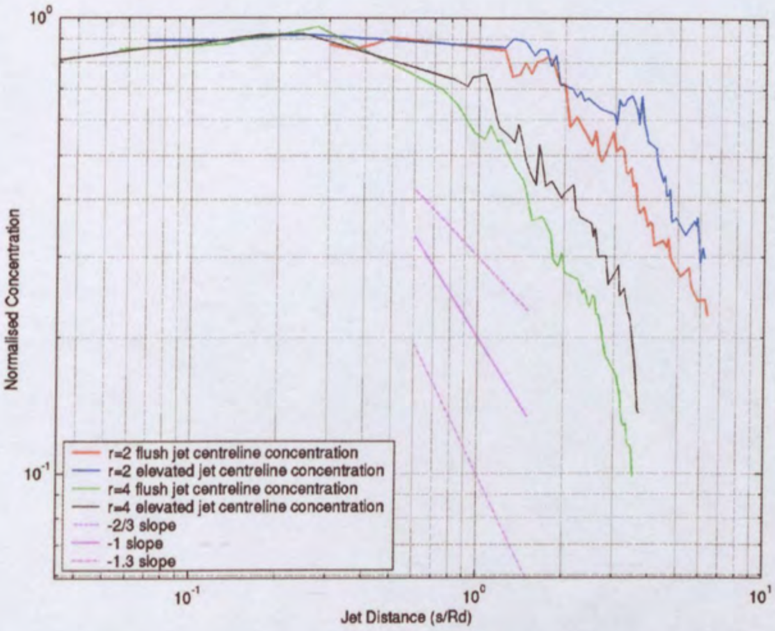

Figure 5-38 Log-log plot of the normalised jet centreline concentration data plotted against the jet-wise distance normalised by Rd.

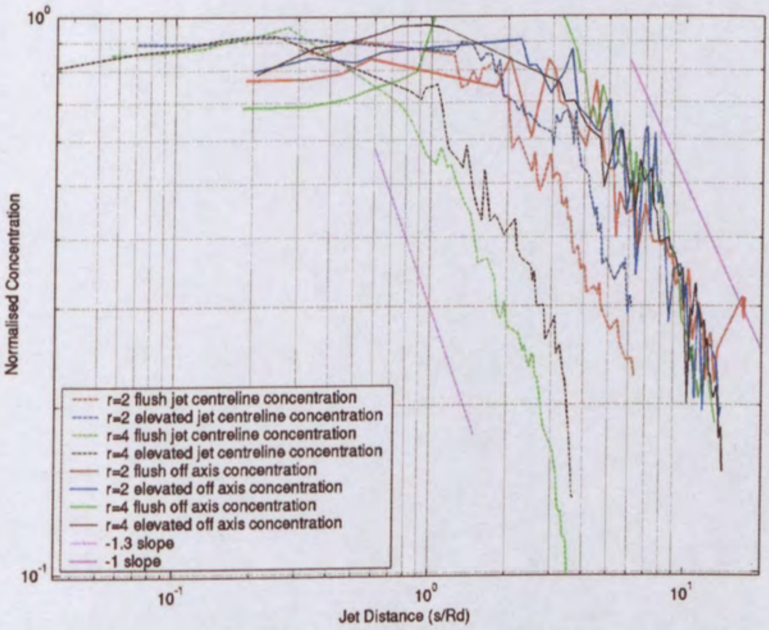

Figure 5-39 Log-log plot of the normalised jet centreline concentration data combined with the concentration for the points along the CVP trajectory.

5.4.5 Global Concentration

A comparison between the global mixing of each flow case can be made by comparing the cross-sectional area of the jet in each case at a location downstream of the jet exit. In order to visualise the difference in the area, volumetric renderings of the jets were produced from the concentration data. The renderings are shown in Figure 5-40 and show the rendered flow as seen by a viewer looking upstream. The rendered structures show the fluid with a normalised concentration compared with the jet exit above 10% (or 0.1). The viewing angle means the jet appears to be coming out of the page, and the right hand side of each structure corresponds to the plane of symmetry of the jet. The downstream plane that is shown is at a location of x/d=4 in each image. The scale of the rendering in each case is the same, so a direct comparison can be made between them.

These images once again illustrate how the dye is distributed in the various flow cases. The location of the high concentration fluid at the core of the CVP in the R=4 flush-mounted case is particularly evident. Whereas the R=2 cases shown are similar in appearance, the R=4 cases are substantially different. The R=4 elevated jet, in particular, shows a distinct vertical alignment in its structure.

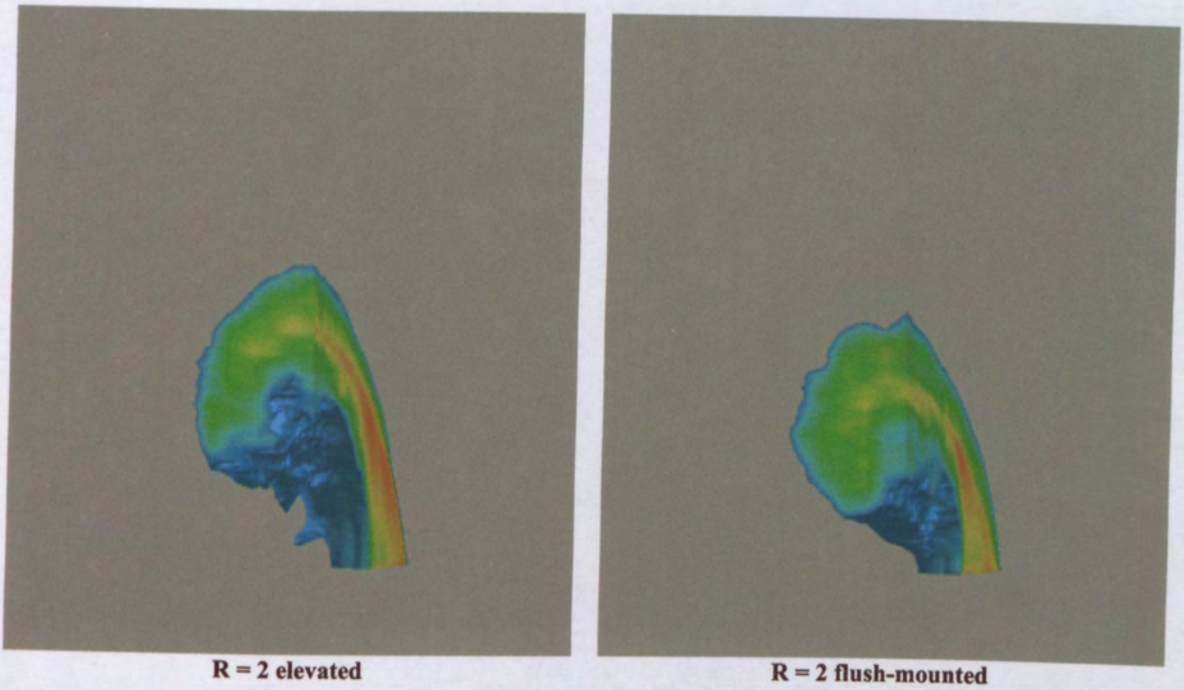

R = 2 elevated **R = 2 flush-mounted**

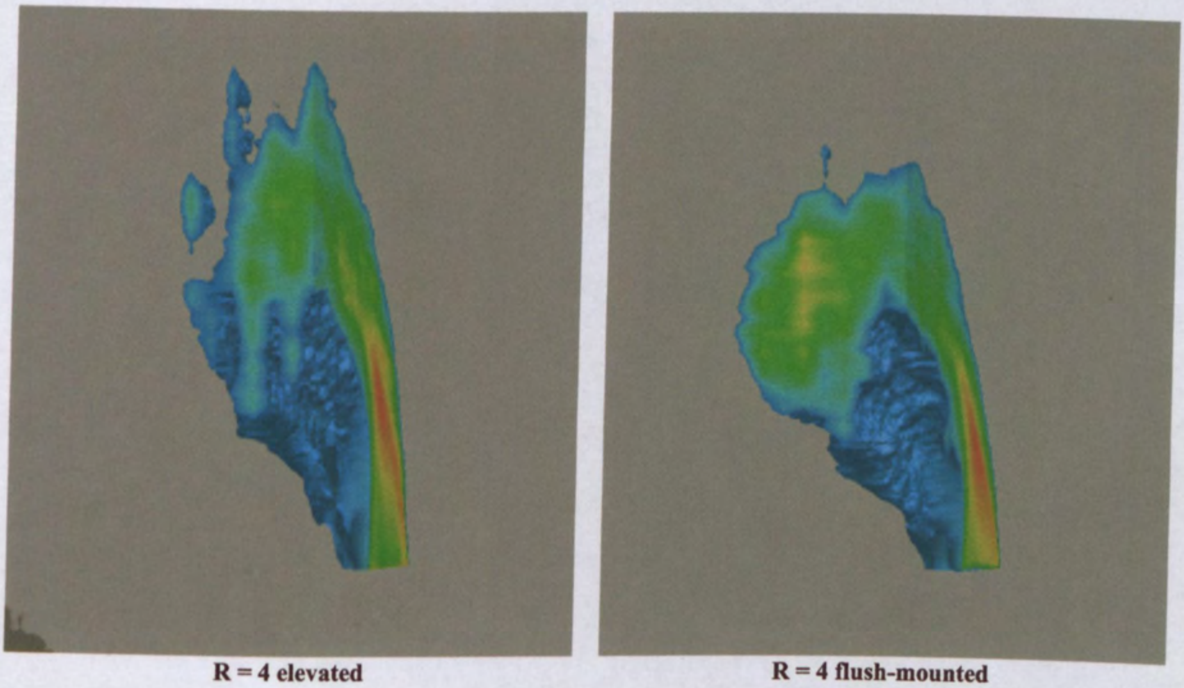

R = 4 elevated **R = 4 flush-mounted**

Figure 5-40 Volumetric renderings of the jet normalised concentration as seen by an observer located downstream and to one side of the jet, looking upstream.

6 Quasi-Instantaneous Volume Structure

6.1 Introduction

In order to investigate the differences in the volume structure of the flow observed in the time averaged concentration field, the volume visualisation technique outlined in Chapter 3 was applied to a number of different flow cases. Since the flush-mounted jet at a velocity ratio of 4 appears to be different from the other flow cases, it will be the main focus of this section. However, in order to compare the structure with other cases a variety of velocity ratios were used for both the flush and elevated flow cases. The flows investigated are summarised in Table 6-1.

Table 6-1 Flow Conditions Investigated Using the Volume Visualisation Technique

Velocity Ratio	Flush	Elevated
0.5	√	√
1.0	√	
2.0	√	
4.0	√	√
8.0	√	

6.2 Flush-mounted Jet Volume Renderings

Volume renderings, shown as red-blue anaglyphs, of the flush-mounted jet at the velocity ratios of 0.5, 1, 2, 4 and 8 are shown in Figure 6-1 to Figure 6-5, respectively. More information about the techniques used to generate the images, and how to view them, is included in Section 4.4. In each figure, the jet is moving upwards from the bottom of the image and the crossflow is from right to left. The location of the jet pipe can be seen in some of the figures below the jet exit plane. The change in velocity ratio, between the flows at R=0.5, 1, 2 and 4 was achieved by keeping the crossflow velocity constant and changing the jet velocity. The crossflow Reynolds number in each of these cases was 2000. The flow at R=8 was captured at a lower Reynolds number in order to reduce the distortion of the flow due to the propagation of the jet during the time taken to capture the individual planes used to generate the rendering. In this case the crossflow Reynolds number was 1000.

Each rendering was generated from 20 PLIF images captured on vertical planes aligned with the crossflow. The planes were spaced at 5mm intervals which enabled a span-wise distance of 95mm, nearly 2d, to be captured. The position of the planes and their relative magnification with respect to the jet plane of symmetry are shown in Figure 6-6. The data were captured with the camera positioned approximately 1m from the jet plane of symmetry, using a 12.5 mm lens, at an f-number of 1.4. This arrangement provided a depth of field extending from approximately 800mm to 1350mm from the camera lens. In addition, it allowed a sufficient field of view to be achieved such that the camera could be aligned with the jet exit and still view the entire area of interest above the jet exit plane.

Each of the separate PLIF images was captured at a rate of 30Hz. Therefore, the time interval over which the planes in each rendering were captured was 2/3 of a second. The propagation of the jet during the time taken to capture each of the planes in a volume may be seen by the spanwise tilt in the leading-edge shear layer roll-ups, for the R=4 and R=8 flow cases shown in Figure 6-4 and Figure 6-5 respectively.

As can be seen, the structure of the jet changes substantially depending on the velocity ratio. It is difficult to resolve details of the formation of the CVP due to the poor spanwise (z) spatial resolution of the images. However, the reconstructions are sufficient to resolve features on the lateral edges of the jet in the R=4 and R=8 cases. These features appear similar to the 'hanging vortices' found in the LES simulations undertaken by Yuan *et al.* (1998), who suggested they were involved with the formation of the CVP. The shear layer vortices, which are aligned into the page, are much better resolved.

A time series of volume renderings of the flush-mounted jet at a velocity ratio of 4 is shown in Figure 6-7. The left hand image in each time step is the PLIF image captured on the jet plane of symmetry. From the volume renderings (the right hand image in each time step), the large-scale roll up of the jet shear layer around the front and sides of the jet is clearly evident. Note also that the trailing edge roll-up is intermittent whereas the leading edge shear layer roll-up is highly periodic.

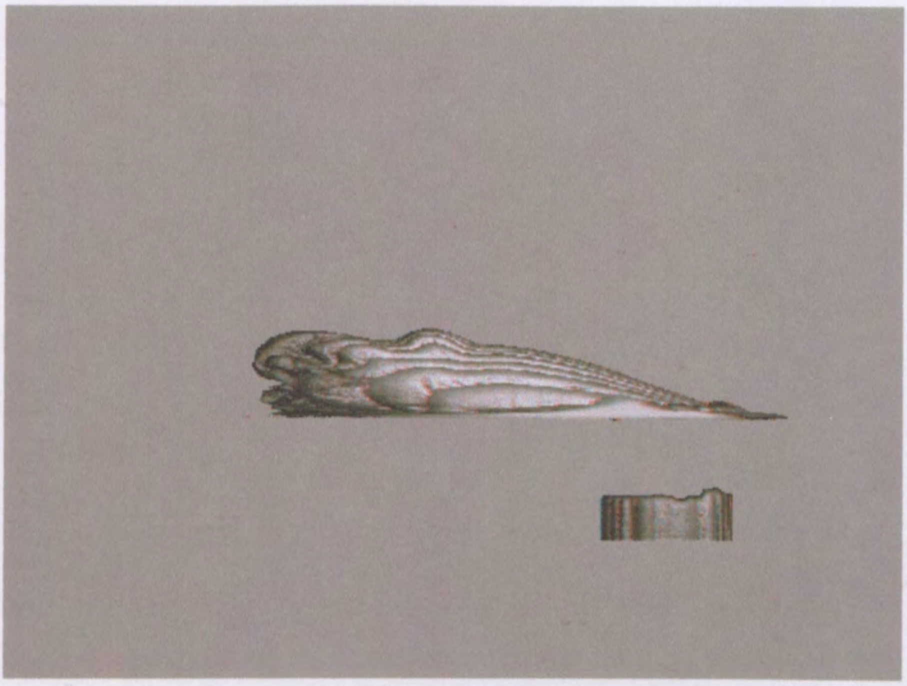

Figure 6-1 Volume rendering, shown as a red-blue anaglyph, of the side view of a flush-mounted JICF at a velocity ratio of 0.5. Re=2000, Re_j=1000, δ/D=0.3

Figure 6-2 Volume rendering, shown as a red-blue anaglyph, of the side view of a flush-mounted JICF at a velocity ratio of 1.0. Re=2000, Re_j=2000, δ/D=0.3

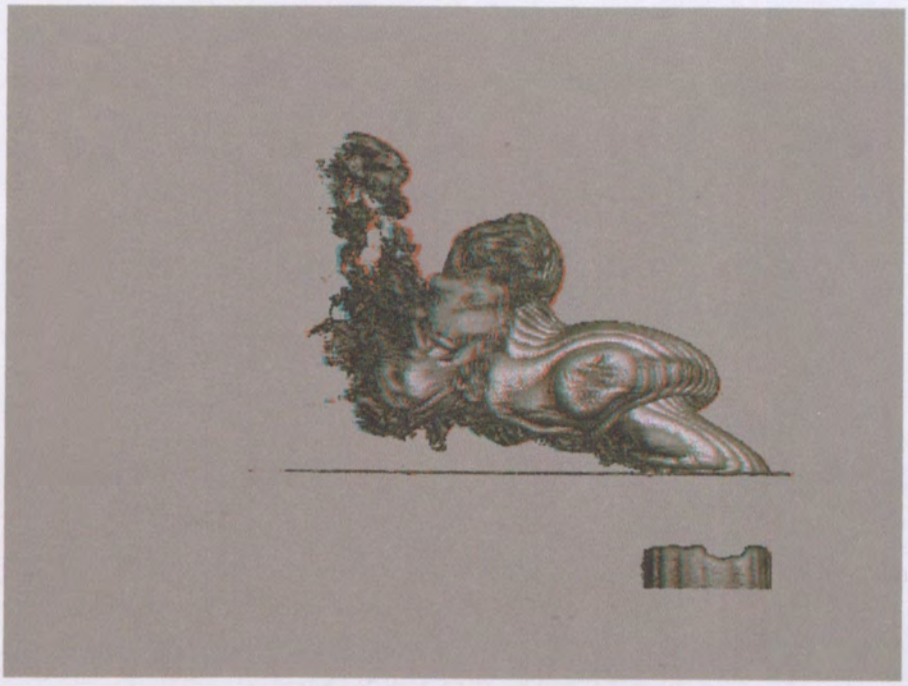

Figure 6-3 Volume rendering, shown as a red-blue anaglyph, of the side view of a flush-mounted JICF at a velocity ratio of 2.0. Re=2000, Re_j=4000, δ/D=0.3

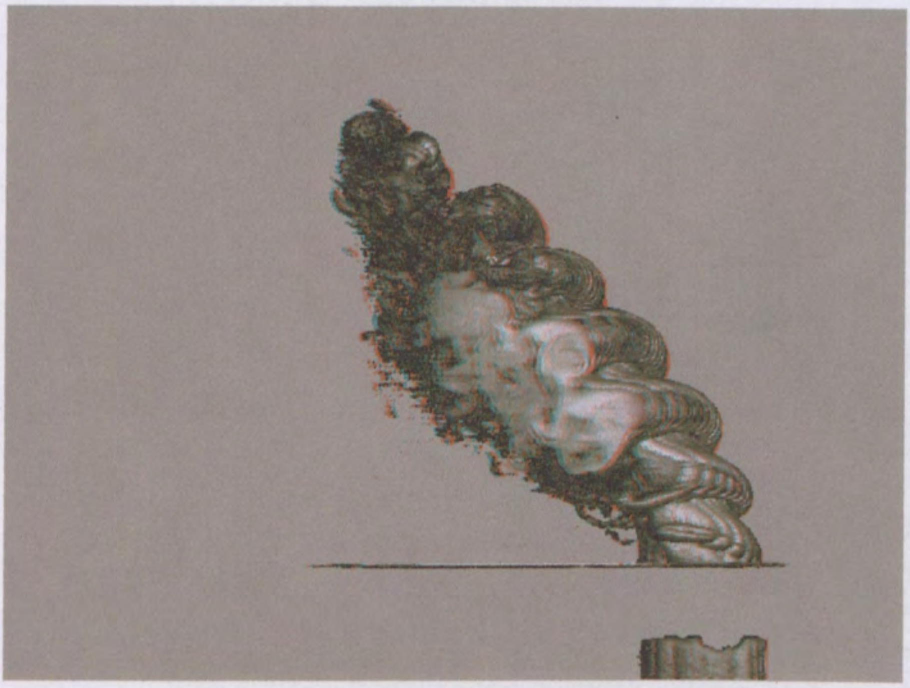

Figure 6-4 Volume rendering, shown as a red-blue anaglyph, of the side view of a flush-mounted JICF at a velocity ratio of 4.0. Re=2000, Re_j=8000, δ/D=0.3

Figure 6-5 Volume rendering, shown as a red-blue anaglyph, of the side view of a flush-mounted JICF at a velocity ratio of 8.0. Re=1000, Re_j=8000

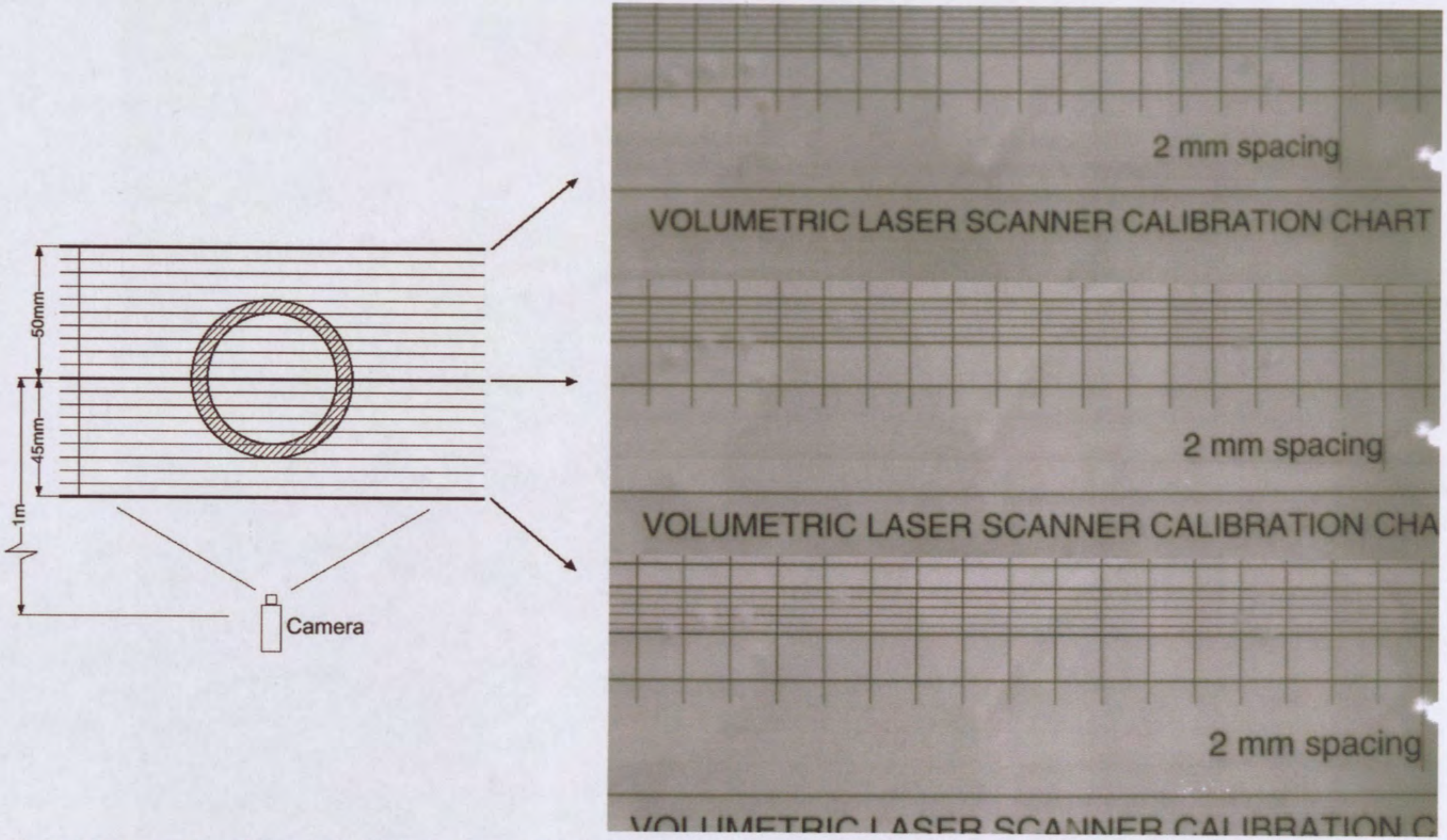

Figure 6-6 Figure to show the position of the laser sheets relative to the jet pipe, as viewed from above (on left). The camera is positioned closest to the bottom of the figure. Images of a template positioned at the closest and furthest image planes from the camera, as well as the centre plane are also presented (on right). The camera is positioned approximately 1m from the centre image plane. A 12.5 mm lens is used with an f-stop of 1.4.

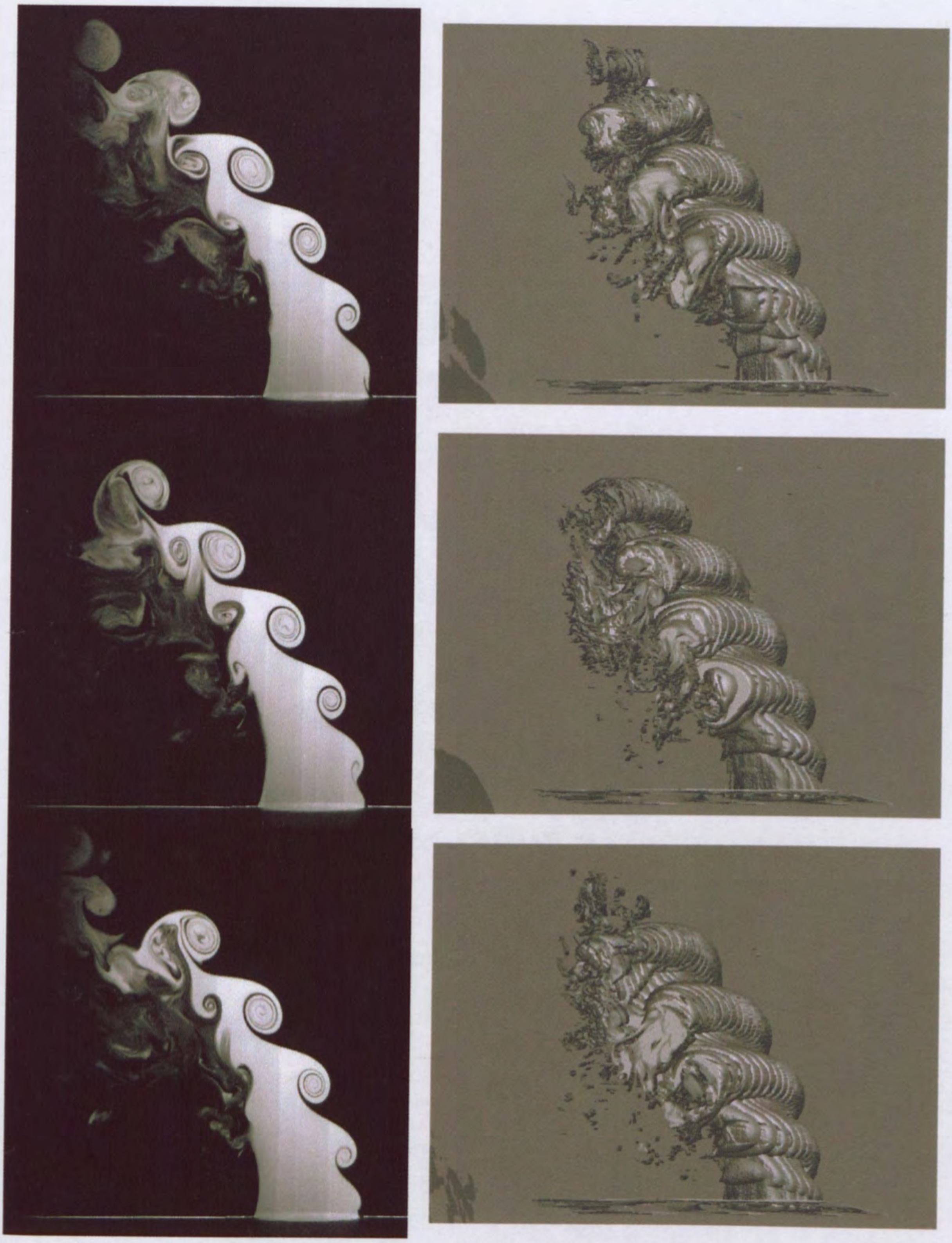

Figure 6-7 Time series of volume renderings of the side view of a flush-mounted JICF at a velocity ratio of 4. Re=2000, Re_j=8000, δ/D=0.3

6.2.1 Formation and Structure of the CVP

In order to investigate the structure of the CVP, volume renderings were produced from PLIF images aligned parallel with the jet exit plane for a flush-mounted jet. A time series of seven such renderings is shown in Figure 6-8. The renderings highlight one of the advantages of the volume scanning technique, as they show a view of the jet structure from a position within the jet itself, upstream of the exit plane. Such a position is ordinarily not available in the laboratory. In each of the renderings the jet is flowing into the page and the crossflow is from left to right. Each rendering is generated from twenty PLIF images with a spacing of 8mm and the lowest sheet positioned just above the jet exit plane. The renderings are separated in time by 2/3 of a second.

In order to minimise the effect of the propagation of the jet during the time taken to record each time step, lower flow velocities were used than elsewhere in this thesis. Due to the orientation of the laser sheets and the jet, the problem of the propagation of the jet was very significant in this case, since the jet was continuously moving out of the image plane between successive images. The individual PLIF images were captured at a frame rate of 30Hz. Therefore a complete volume of the twenty slices was captured every 2/3 of a second. The framing rate of the camera and the separation between the laser sheets dictate the maximum velocity of the flow such that the propagation of the flow between successive images is small compared with the sheet spacing. In this case, a mean jet velocity of 0.05m/s was used. Based on this velocity the distance travelled by a particle in the middle of the jet would be 1.7mm, or approximately 20% of the spacing between laser sheets. Away from the exit and in the shear layer, the propagation distance will be significantly less. Although this propagation will cause a mild distortion of the reconstructed flow pattern, it is not sufficient to alter the topology of the significant flow features. The jet Reynolds number was therefore 2500. Although the velocity ratio of the flow was thought to be 4, later re-calibration of the water channel, indicated the velocity ratio was 3.6.

The camera was positioned 0.6m from and directly above the jet exit. A 12.5mm lens was used which allowed sufficient depth of field to capture all of the imaged planes. No corrections were made for perspective. The images were cropped to remove superfluous boundary data. After cropping the volume was approximately 160mm wide by 180mm long and 152mm high (415 x 470 x 389 pixels).

The time series of Figure 6-8 is of interest as it shows the occurrence of a large-scale roll-up of the leading edge shear layer. In Figure 6-9, frames 1 and 7 from the time series in Figure 6-8, are enlarged to highlight different stages of the flow evolution. The top image shows the counter-rotating vortices forming in the shear layer adjacent to the pipe exit. The complexity of the flow structure in the breaking-down CVP is strongly evident from these images. The lower image shows the sides of the leading edge shear layer roll-up. The roll-up can be seen around lateral edges of the pipe, and appears to merge with the CVP. Four slices of the data used to produce the rendering shown in image 7 of Figure 6-8 are shown in Figure 6-10 to Figure 6-13. The planes are those located 34 mm (0.7d), 74mm (1.5d), 98mm (2d) and 130mm (2.6d) above the jet exit plane. The flour images demonstrate the rapid distortion of the jet cross-section and the rapid spreading of the jet fluid. Note that the effect of perspective will be to increase the apparent size of the images further from the wall. The image in Figure 6-10 shows the initial folding of the jet shear layer on the lateral edges of the jet to form the hanging vortices. In Figure 6-11 the presence of the leading edge shear layer roll-up can be seen on the sides of the jet. The roll-up appears to wrap around the entire jet and merge with the turbulent CVP region on the lee side of the jet.

Figure 6-10 to Figure 6-13 show the details of the spatial evolution of the trailing edge shear layer, obtained at essentially the same instant in time. It is clear from these images that the CVP roll-up begins with the folding of the lateral edges of the shear layer (Figure 6-10, 0.7d). However, further from the jet exit there appear to be numerous vortical motions in the trailing edge shear layer between the CVP vortices. In particular, the reader's attention is drawn to roll-ups identified by arrows in Figure 6-12 and Figure 6-13. These clearly represent a pair of vertically-orientated counter-rotating vortices whose directions of circulation match the neighbouring CVP vortices. The spacing between these vertically-orientated vortices appears to decrease with distance from the jet exit. These vortices will henceforth be called the 'trailing edge vortex pair'. It should be emphasised that these cross-sectional views were captured at essentially the same instant in time, and the features identified are clearly connected to a large-scale vortical feature of the flow. In Figure 6-14 frames 1 and 7 are shown but this time viewed from above the jet. It can be seen that the 'trailing edge vortex pair' occur at both times indicating the persistent features.

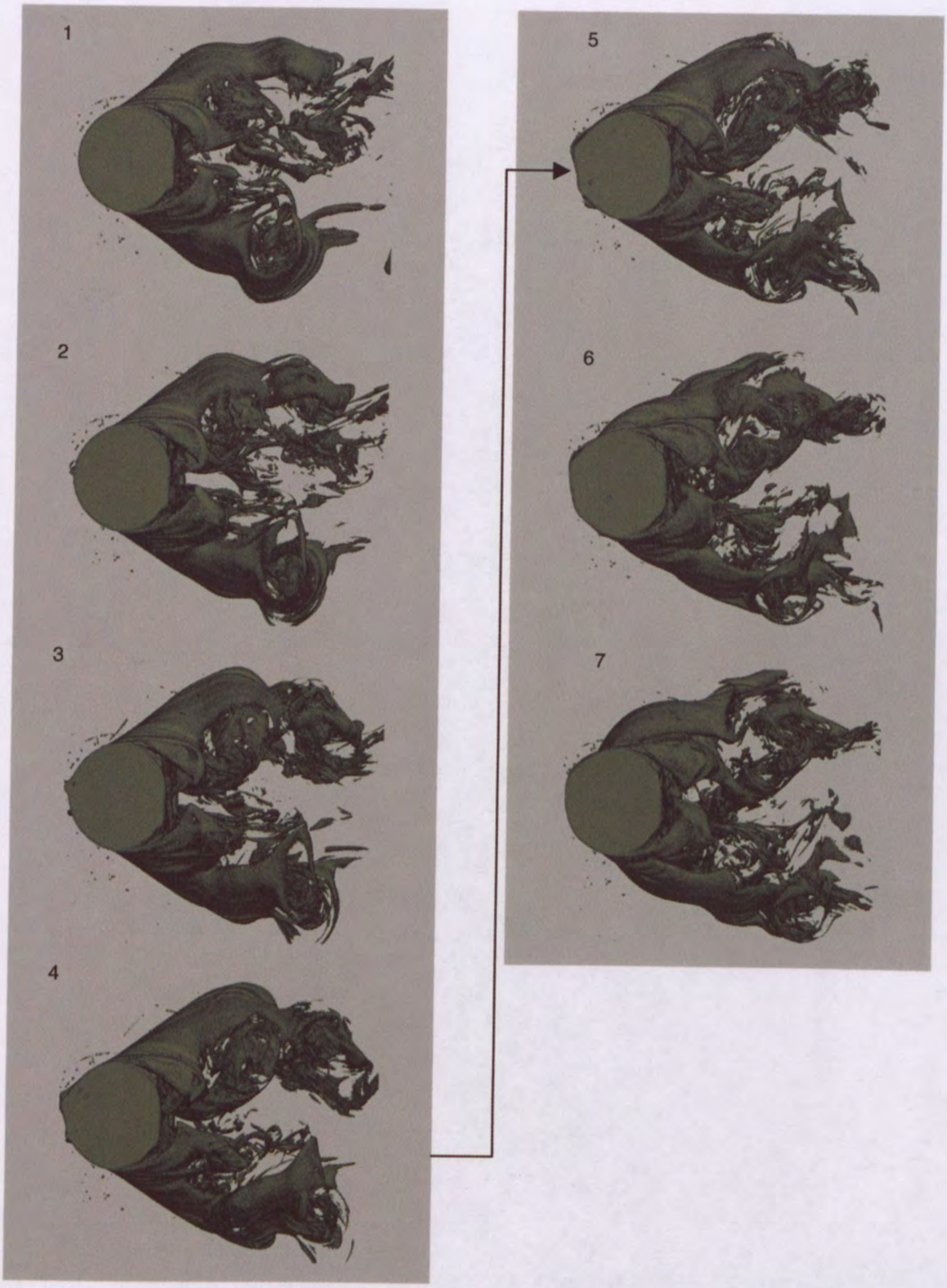

Figure 6-8 Time series of volume renderings of a JICF viewed from within the jet pipe. In each rendering the jet is flowing into the page and the crossflow is from left to right. Each frame is separated by a time interval of 2/3 of a second and is generated from 20 slices. The jet velocity ratio is 3.6, the jet Reynolds number is 2500 and the crossflow Reynolds number is 700.

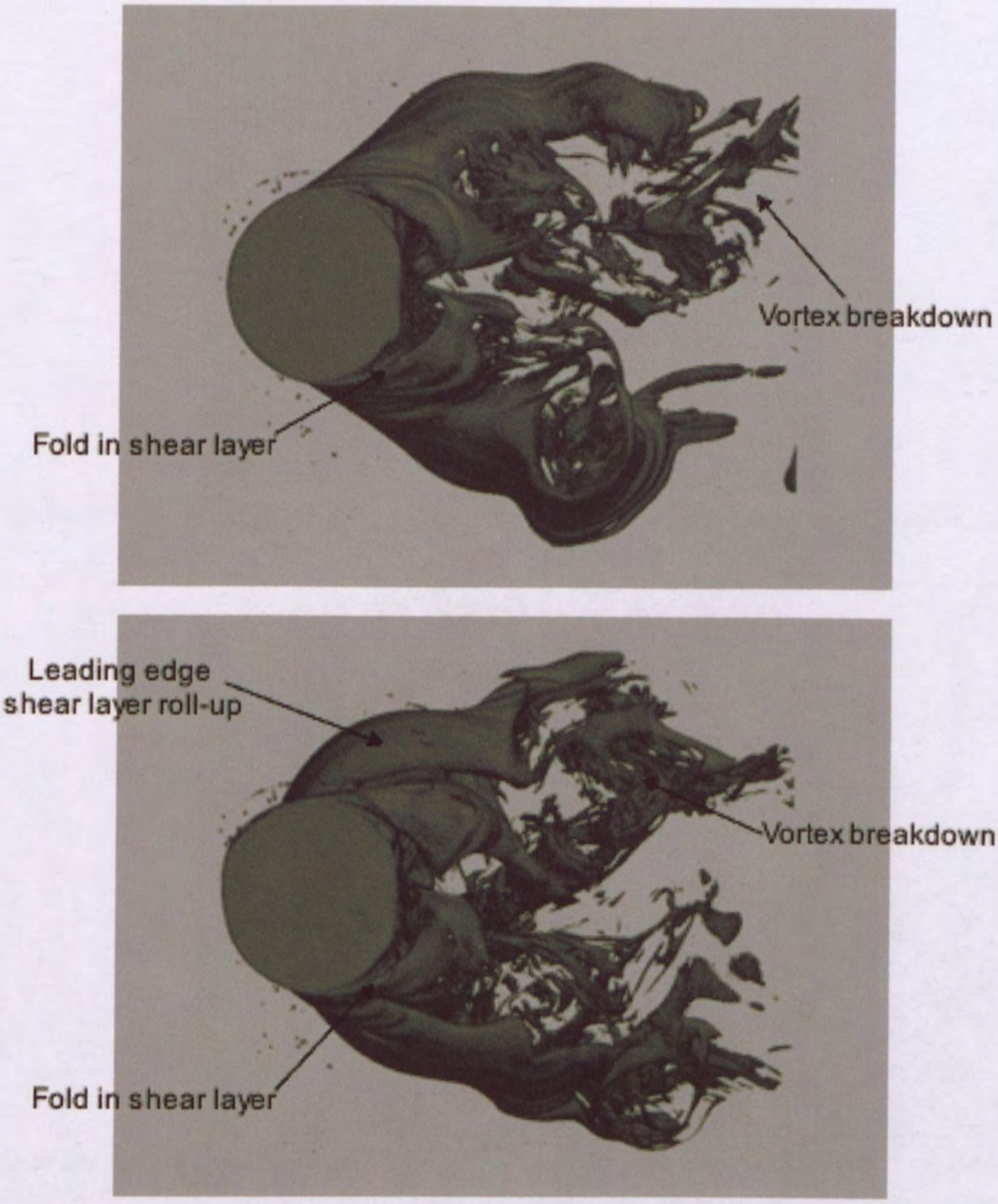

Figure 6-9 Enlargements of frames 1 and 7 from the time series in Figure 6-8. The two images are separated by a time interval of 4 seconds and are re-produced to highlight different stages of the flow evolution. The jet is flowing into the page and the crossflow is from left to right.

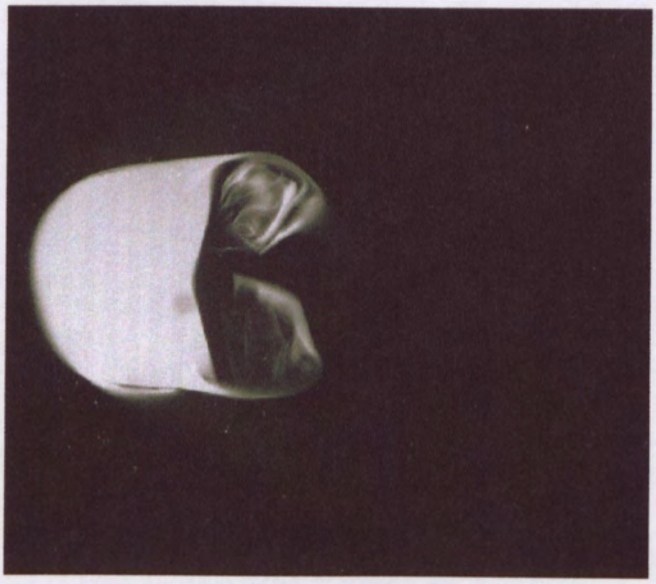

Figure 6-10 Single image slice from frame 7 of Figure 6-8 located 34mm (0.7d) above the jet exit plane.

Figure 6-11 Single image slice from frame 7 of Figure 6-8 located 74mm (1.5d) above the jet exit plane.

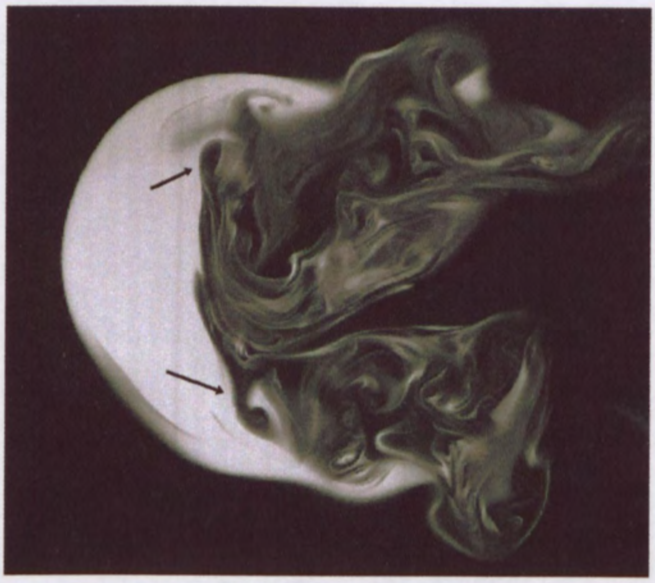

Figure 6-12 Single image slice from frame 7 of Figure 6-8 located 98mm (2d) above the jet exit plane.

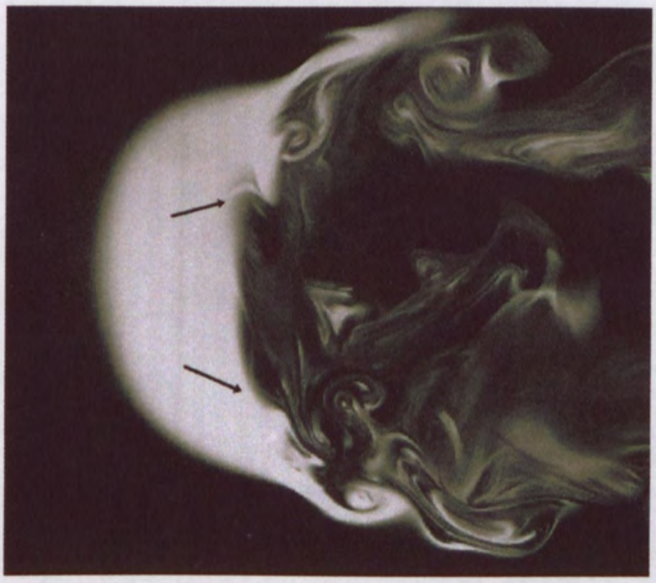

Figure 6-13 Single image slice from frame 7 of Figure 6-8 located 130mm (2.6d) above the jet exit plane.

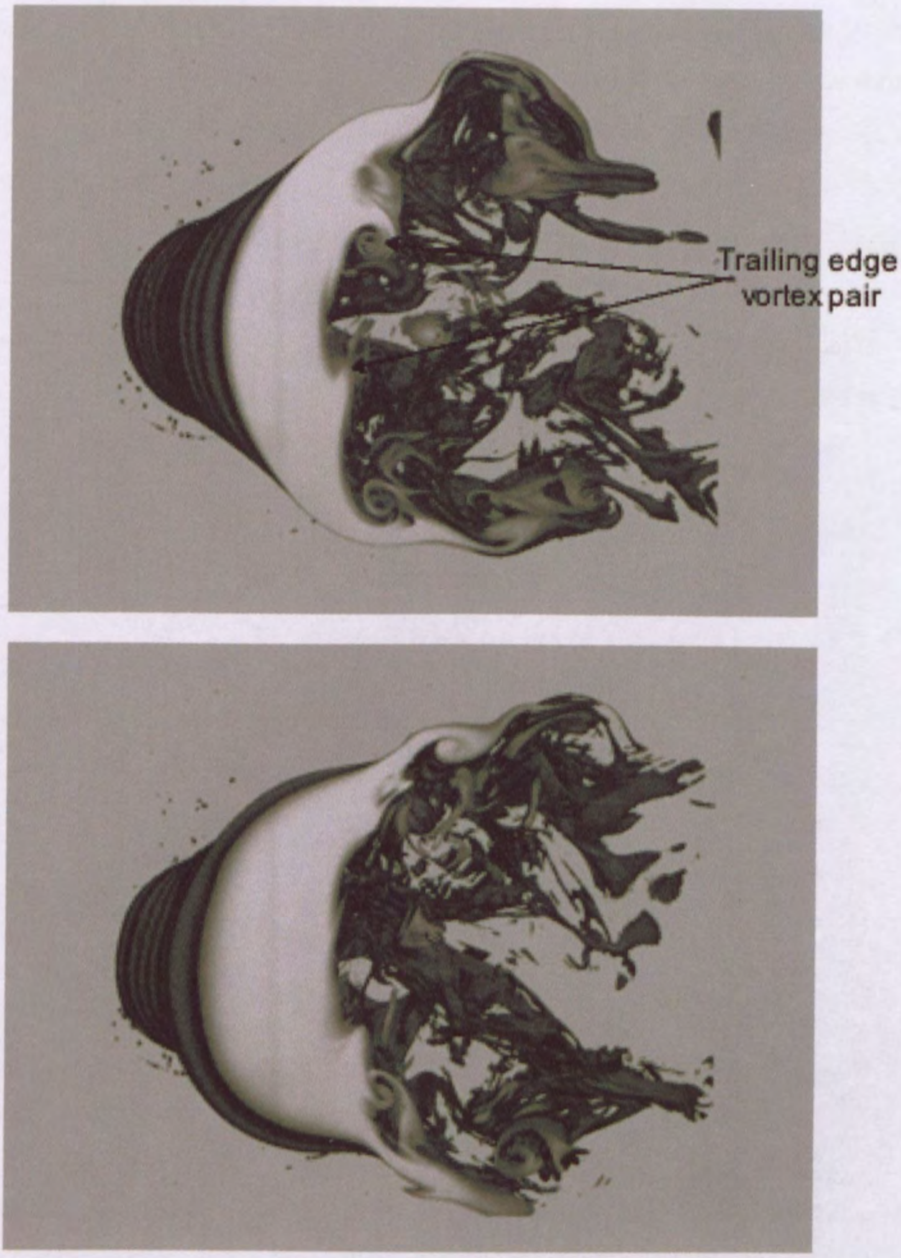

Figure 6-14 Frames 1 and 7 from the time series in Figure 6-8 as viewed from above the jet. The jet is flowing out of the page and the crossflow is from left to right. The two images are separated by a time interval of 4 seconds.

6.3 R=4 Flush versus Elevated Volume Renderings

In Figure 6-15 the volume rendering shown previously for the flush-mounted case of a jet with a velocity ratio of 4 is reproduced for comparison with the elevated jet case shown in Figure 6-16. As has been discussed previously, three major differences between the two cases can be observed: the trajectory of the flush-mounted jet is lower, the lateral spreading of the flush-mounted jet is larger, and the large scale roll up of the flush-mounted jet shear layer occurs earlier than for the elevated jet. The roll-up of the leading edge jet shear layer in the flush-mounted case occurs very close to the jet exit, and forms large periodic structures, whereas the formation of the leading edge shear layer in the elevated case starts further from the jet exit and appears to grow from a Kelvin-Helmholtz type instability.

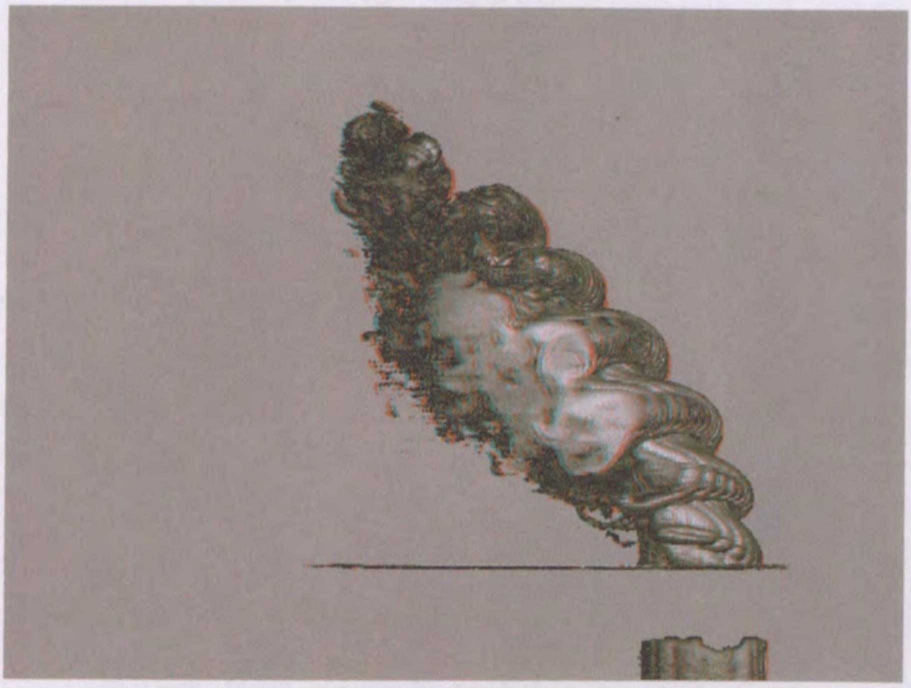

Figure 6-15 Volume rendering of the side view of a flush-mounted JICF for a velocity ratio of 4.0. Re=2000, Re_j=8000, δ/D=0.3

Figure 6-16 Volume rendering of the side view of an elevated JICF for a velocity ratio of 4.0. Re=2000, Re_j=8000

6.4 R = 0.5 Flush versus Elevated Volume Renderings

A comparison was also made between the instantaneous structures of the flush and elevated jets for a velocity ratio of 0.5. Cross-sections on the plane of symmetry are shown for the flush-mounted jet and for the elevated jet in Figure 6-17 and Figure 6-18 respectively. The corresponding volume renderings are presented in Figure 6-19 and Figure 6-20. Both flows exhibit wake-like characteristics with eddies 'pointing downstream', as is expected for a velocity ratio less than 1. However, as is the case for the higher velocity ratio flows, the flow structures also show significant differences.

The elevated jet exhibits a large-scale periodic roll-up of the upstream shear layer, whereas the flush-mounted jet does not. This may be partially explained by the presence of the flat wall boundary layer, whereby in the region of the exit, the jet velocity will be similar to the local velocity within the boundary layer. Hence, a smaller velocity gradient will exist across the shear layer than would occur if the boundary layer was infinitesimally thin.

The trajectory of the elevated jet is higher than the flush-mounted jet. This is consistent with trends in all other experiments at higher velocity ratios (R=2 to 6) but those trends also correlate higher trajectories with a delayed roll-up of the shear layer, due to a Kelvin-Helmholtz roll-up. In the present case, the higher trajectory is associated with a larger-scale wake-like roll-up.

The elevated jet shows some interesting features below the main body of the jet. These appear to be streamwise vortices that originate from the top of the jet exit. These renderings may also show some evidence of upright vortices in the wake region of the elevated jet.

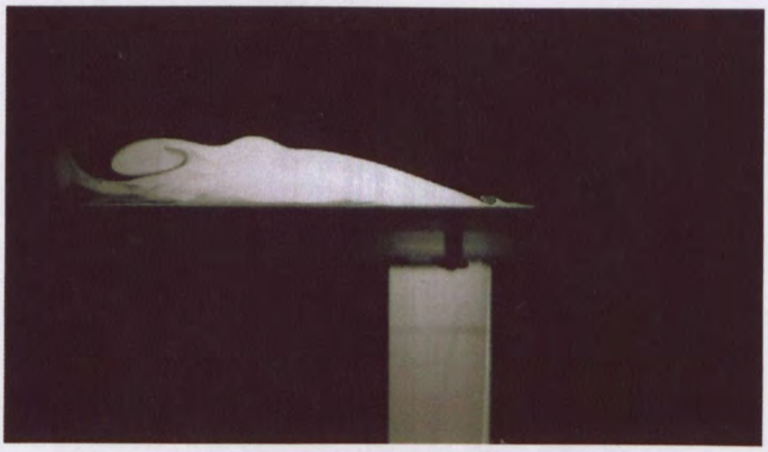

Figure 6-17 Instantaneous cross-section through the plane of symmetry of a flush-mounted JICF et at a velocity ratio of 0.5. Re=2000, Re_j=1000, δ/D=0.3

Figure 6-18 Instantaneous cross-section through the plane of symmetry of an elevated JICF at a velocity ratio of 0.5. Re=2000, Re_j=1000

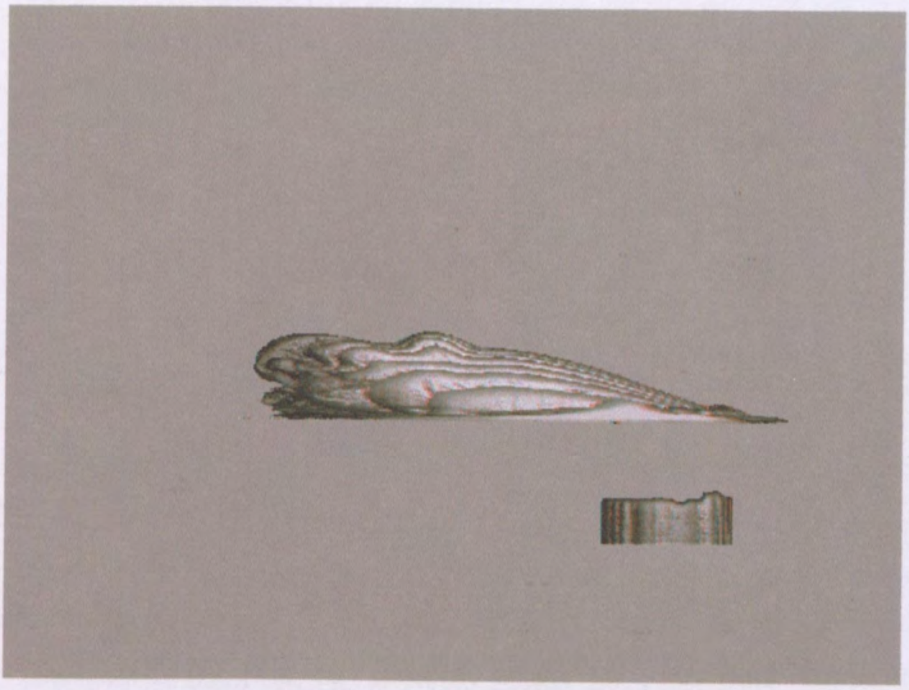

Figure 6-19 Volume rendering of the side view of a flush-mounted JICF for a velocity ratio of 0.5. Re=2000, Re_j=1000, δ/D=0.3

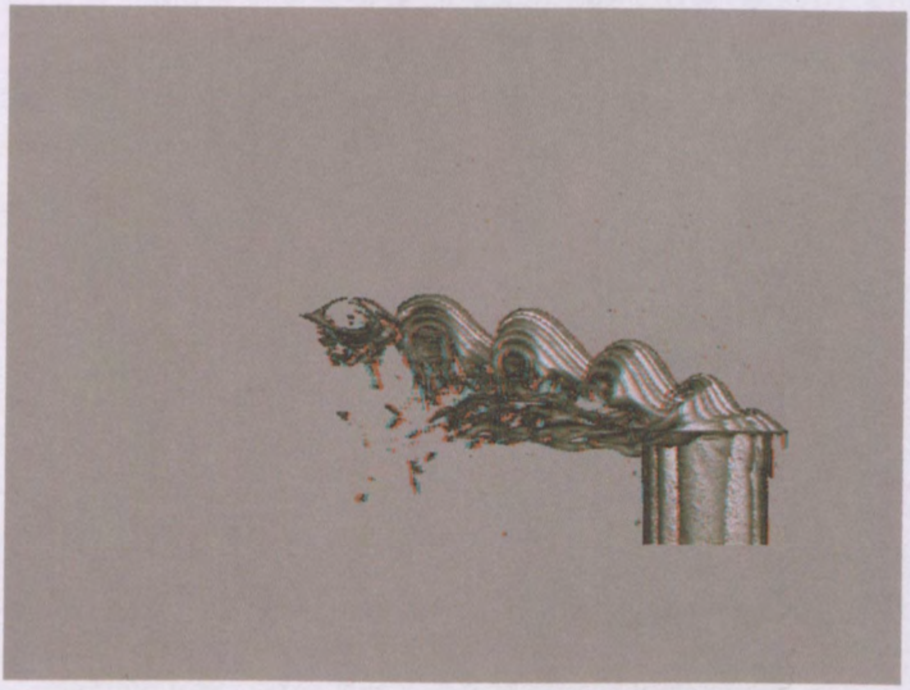

Figure 6-20 Volume rendering of the side view of an elevated JICF for a velocity ratio of 0.5. Re=2000, Re_j=1000

7 The Structure of Flush and Elevated Transverse Jets

7.1 Introduction

As a way of establishing why differences exist in the structure and mixing between the flush-mounted and elevated cases of the transverse jets investigated, a flow visualisation study was undertaken. The features of both flows were examined and comparisons were made between them. To build up a clearer picture of the flow the discussion will begin with the makeup of a free jet, that is, an elevated jet with no crossflow present. The parts of the elevated jet structure will then be examined in detail, and comparisons made to the flush-mounted jet. Building up the structure of the flow as a sequence of steps allows a better interpretation of the various elements of the flow to be established. The investigation focussed on two specific flow conditions. That is, jets with velocity ratios of 2 and 4 at a crossflow Reynolds number of 2000. The influences of the velocity ratio and Reynolds number were also investigated to show how the present limited data set applies over a broader range of flow conditions.

7.2 Free jet

When a jet flow exhausts into a still atmosphere the axi-symmetric cylindrical vortex sheet emanating from the jet pipe rolls up by a Kelvin-Helmholtz instability mechanism. An example of the flow for a jet Reynolds number of 4000 is shown in Figure 7-1. The classical vortex-ring structures are formed and the jet spreads due to the entrainment of the ambient fluid, principally within the vortex rings. The important parameters that define a particular flow case are the jet Reynolds number (based on the jet bulk velocity and jet diameter) and the jet exit velocity profile (which in turn may be defined by the jet pipe development length or jet pipe boundary layer condition). Also, the density and viscosity ratios between the jet and ambient fluids, must be specified.

Figure 7-1 Jet shear layer development for a jet with zero crossflow at a jet Reynolds number of 4000.

7.3 Adding a Crossflow (Elevated JICF)

The flow structure generated for the same jet in the presence of a crossflow is substantially different from that of the free jet. As an example, the images shown in Figure 7-2 and Figure 7-3 show the development of the jet shear layer of an elevated jet in crossflow for velocity ratios of 2 and 4 respectively. As can be observed the structure of the flow is asymmetric and far more complex than that of a free jet. The parameters that are required to define a particular flow case are the crossflow velocity and fluid properties, in addition to the jet velocity and properties, from which the momentum ratio between the jet and crossflow, and the jet and crossflow Reynolds numbers are defined. The major differences between the free jet and the jet in crossflow are the deflection of the jet and the reorientation of the jet vorticity into the various vortical features.

For the case of a free jet, the jet centreline, defined as the line joining the points of either maximum velocity or concentration at each streamwise coordinate, remains aligned with the jet pipe axis. However, in the presence of a crossflow, the jet is deflected in the direction of the crossflow until the jet asymptotes to the direction of the crossflow in the far-field. The deflection of the jet has been shown by many researchers to be the result of entrainment of crossflow fluid. The correlation between the concentration decay and the jet deflection was also shown in Chapter 5. The higher centreline concentration decay of the flush-mounted jet correlated with the larger lateral spreading of the jet and a lower trajectory than for an elevated jet at the same flow conditions. The concentration decay in the CVP itself agreed with this trend, except for the R=4 flush-mounted jet where there were clear structural differences. This chapter describes an investigation into the reasons for mixing rate differences between elevated and flush-mounted jets in crossflow.

Based on previous research (Kelso 1991, Kelso *et al.* 1996, Yuan *et al.* 1998, Lim *et al.* 2001 and others) the following effects of the crossflow on the jet have been found:

- The most significant feature is the roll-up of the sides of the shear layer, the formation of the hanging vortices and the CVP.
- Upstream of the CVP there is a shear layer roll-up. This can be a Kelvin-Helmholtz roll-up or it can be a large-scale periodic roll-up close to or within the exit of the jet pipe.
- Downstream of the CVP the shear layer exists. This shear layer has been found to roll up at some conditions and not at others.
- The orientation (direction of circulation), existence and characteristics of the roll-ups on upstream and downstream side depend primarily of the velocity ratio.

Figure 7-2 and Figure 7-3 show the development of the jet shear layer of an elevated jet in crossflow for velocity ratios of 2 and 4, respectively. The figures show the effect of marking the jet boundary layer with dye from the circumferential dye slot in the jet pipe. Introducing dye into the jet in this way allows the flow to be marked where the vorticity is greatest. In the near-field stage of the development of the jet, as shown in the images, the dye marks the shear layer vorticity. The crossflow velocity in each case is 0.04m/s yielding a crossflow Reynolds number of 2000 based on the jet diameter, or 2400 based on the external jet pipe diameter. Therefore, the only difference between the flow in each case is the jet velocity which is increased from 0.08m/s to 0.16m/s, corresponding to jet Reynolds numbers of 4000 and 8000 respectively, based on the jet velocity and jet diameter.

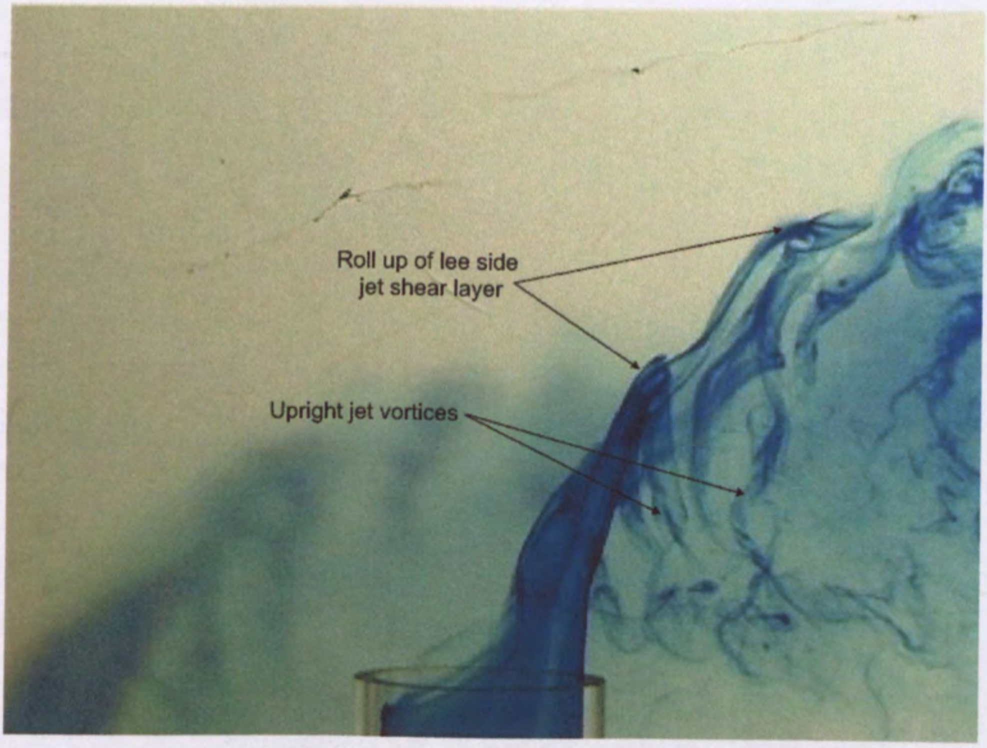

Figure 7-2 Jet shear layer as viewed from the side of an elevated jet at a velocity ratio of 2, and jet Reynolds number of 4000. The shear layer has been marked with dye from the circumferential dye slot located within the jet pipe.

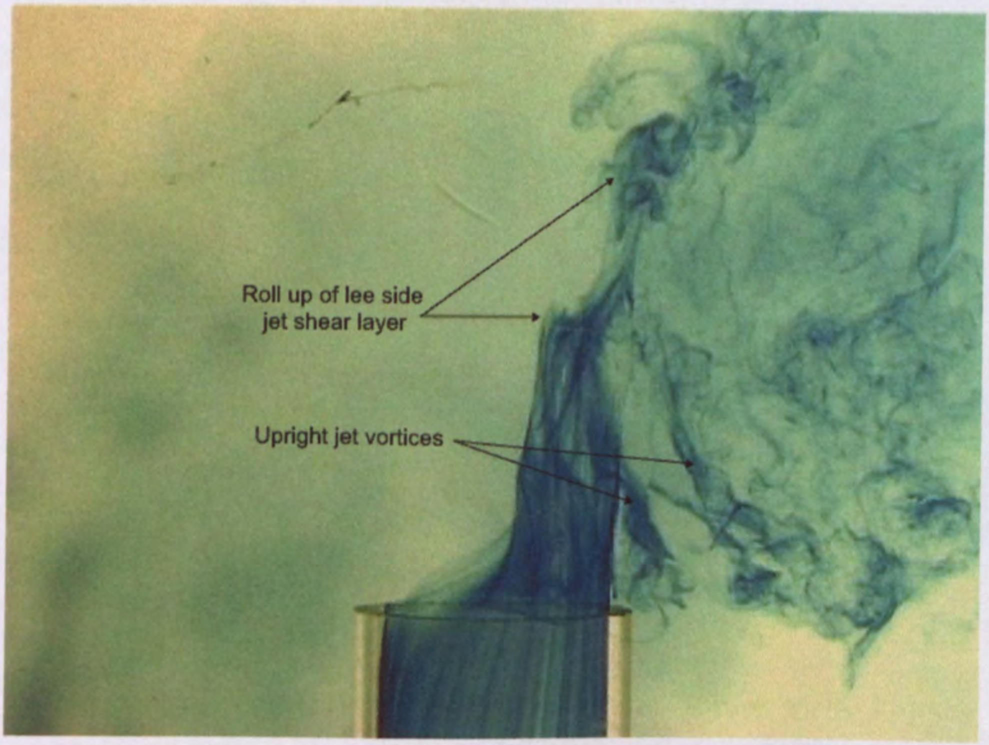

Figure 7-3 Jet shear layer as viewed from the side of an elevated jet at a velocity ratio of 4, and jet Reynolds number of 8000. The shear layer has been marked with dye from the circumferential dye slot located within the jet pipe.

7.3.1 Leading Edge Development

In the flows shown in the previous figures the boundary layer separates from the leading edge of the jet pipe upstream of the jet exit. A close-up view of the details in the very near-field of the jet exit is shown in Figure 7-4 for the case of a velocity ratio of 2. Downstream of the separation line a steady vortex is clearly seen. The vortex has the same sense of rotation as the jet vorticity. The core of this vortex curves up and around the sides of the jet. This vortex appears to be very similar to a vortex observed by Kelso (1991) and Kelso *et al.* (1996) in the leading edge of a flush-mounted jet. Kelso *et al.* named the vortex the 'hovering vortex', a name that is also adopted in the current thesis. As will be shown in subsequent sections, this vortex can be either steady or unsteady depending on the velocity ratio and Reynolds number of the flow. A similar effect was found by Kelso (1991) and Kelso *et al.* (1996) in which the hovering vortex was found to become unstable for flows at higher Reynolds numbers. In addition, as the velocity ratio increases, the position of the hovering vortex moves toward the jet exit and then it emerges from the jet pipe to hover above the jet exit.

The separation of the flow from the leading edge of the jet pipe means that although the dye is introduced evenly into the boundary layer around the entire internal circumference of the jet pipe, most of the dye is swept to the lee side of the jet. A similar process was observed by Kelso (1991) and Kelso *et al.* (1996) for the flush-mounted jet.

Above the hovering vortex seen in Figure 7-4 there is evidence of a second steady vortical feature. The upstream side of this feature lies at the exit plane of the jet pipe. The feature is marked by very little dye from the pipe boundary layer, which makes it very indistinct. In order to investigate this feature and other features of the flow at the pipe exit, dye was introduced into the crossflow fluid from a probe located upstream of the jet. To reduce any effects the probe may have had on the flow, the probe was located over 300 probe diameters upstream of the jet in the contraction section of the water channel. The probe was also inclined diagonally across the channel in order to minimise the amount of probe-wake fluid entrained into the upstream side of the jet. Figure 7-5 to Figure 7-10 show the trajectory of the dye trace produced from the dye probe located at different heights relative to the jet exit plane. The probe was situated on the jet's plane of symmetry. In each figure the velocity ratio was 2, and the jet Reynolds number was 4000. Since the dye was introduced into the crossflow, the vortices observed in the figures are those entraining crossflow fluid. Although the images and discussion presented focus on the R=2 case, the basic flow structure was found to be similar for the flow at R=4.

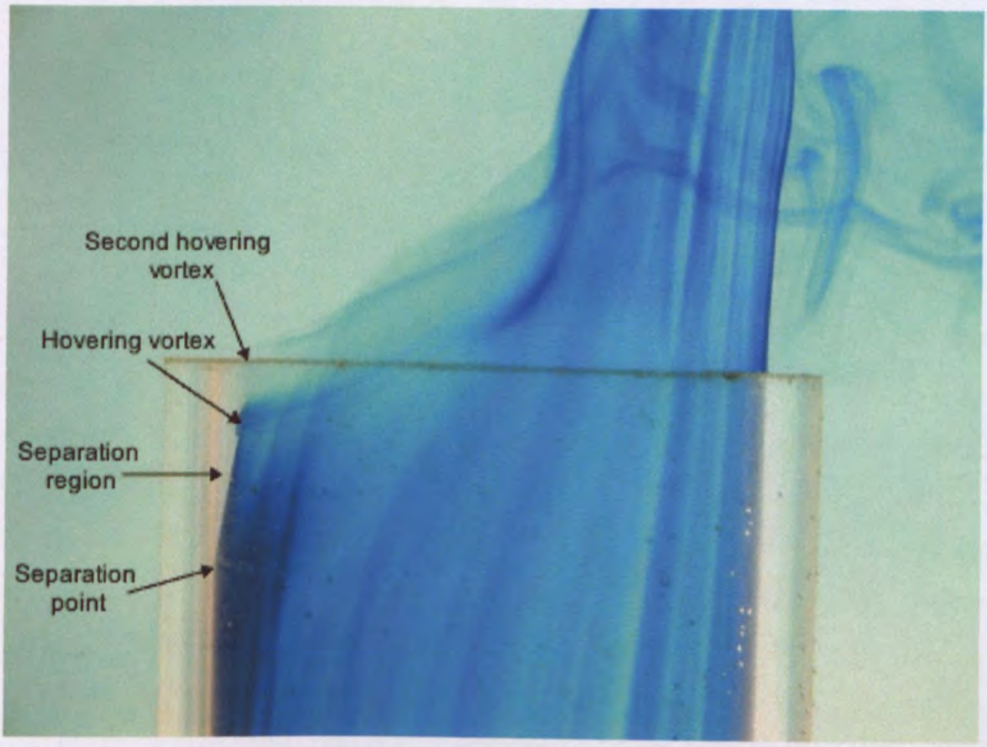

Figure 7-4 Close-up view of the jet shear layer development in the very near-field of the jet exit for a velocity ratio of 2 and jet Reynolds number of 4000.

In Figure 7-5 the dye trace rises over the jet shear layer. The steadiness of the streakline near the jet exit indicates that no large-scale rolling-up of the jet shear layer is occurring. Further from the jet exit the distortion of the dye streak indicates that the shear layer rolls up by a Kelvin-Helmholtz mechanism approximately 2 jet diameters from the jet exit.

Figure 7-6 and Figure 7-7 confirm the existence of a second steady vortex adjacent to the jet exit. This vortex exhibits the same direction of circulation as the hovering vortex immediately below and indeed the boundary layer within the pipe. The presence of this vortex indicates that a series or 'necklace' of such hovering vortices may exist for some flow conditions. Figure 7-7 shows the jet shear layer marked with blue dye and the red dye streak together to indicate the relative positions of the vortices at the flow conditions presented. It was observed that for the R=4 flow case, only two hovering vortices exist. It should be emphasised that the hovering vortices are steady flow features at the flow conditions considered in this chapter.

In Figure 7-8 dye originating from a lower position within the crossflow than in Figure 7-6 and Figure 7-7 is seen to pass between the jet pipe wall and the hovering vortex, and then accumulate within the separation region in the leading edge of the jet pipe. This image shows that crossflow fluid is induced deep into the jet pipe. The dye is then transported laterally, indicating the possible presence of another small hovering vortex within the pipe. This feature seems to be associated with the folding of the shear layer on the lateral edges of the pipe. Dye is then seen accumulating in unsteady upright vortical structures generated by the jet. These will be discussed in the following section.

The above observations indicate that the flow within the upstream region of the pipe exit contains one or more hovering vortices. There is evidence to suggest that the first (lowest) of these triggers the folding of the shear layer at the sides of the emerging jet. The folding of the shear layer appears to be the dominant feature contributing to the formation of the CVP. The other hovering vortices reside above the first and appear to merge with the folding shear layer above the pipe exit. The hovering vortices and the associated folding process together appear to constitute the inception of the hanging vortices (Yuan *et al.* 1999) and the eventual evolution of the CVP. These details are clarified in Figure 7-12.

An additional steady vortex is evident in Figure 7-9 and Figure 7-10. This vortex is analogous to the horseshoe vortex system that occurs in the flush-mounted jet case. It has a sense of rotation opposite to that of the jet shear layer and forms due to the separation of the crossflow fluid as it is drawn up the leading edge of the outer surface of the jet pipe by the jet. The core of this vortex travels along the upper surface of the jet pipe, and then down the outside of the pipe and into the pipe-wake region.

Figure 7-10 shows both of the features discussed separately in Figure 7-8 and Figure 7-9. As can be seen, the dye from the horseshoe vortex and from within the pipe both cross into and out of the pipe at very similar locations around the side of the jet pipe. As a means of comparison, a false colour composite image is given in Figure 7-11. It is composed from six separate images showing streaks of dye introduced into the crossflow from different levels relative to the jet exit plane at R=4. The inferred flow topology within the jet's near-field is shown in Figure 7-12 and Figure 7-13 for velocity ratios of 2 and 4 respectively. The topology is inferred from both of the images presented and numerous observations of the flow's behaviour.

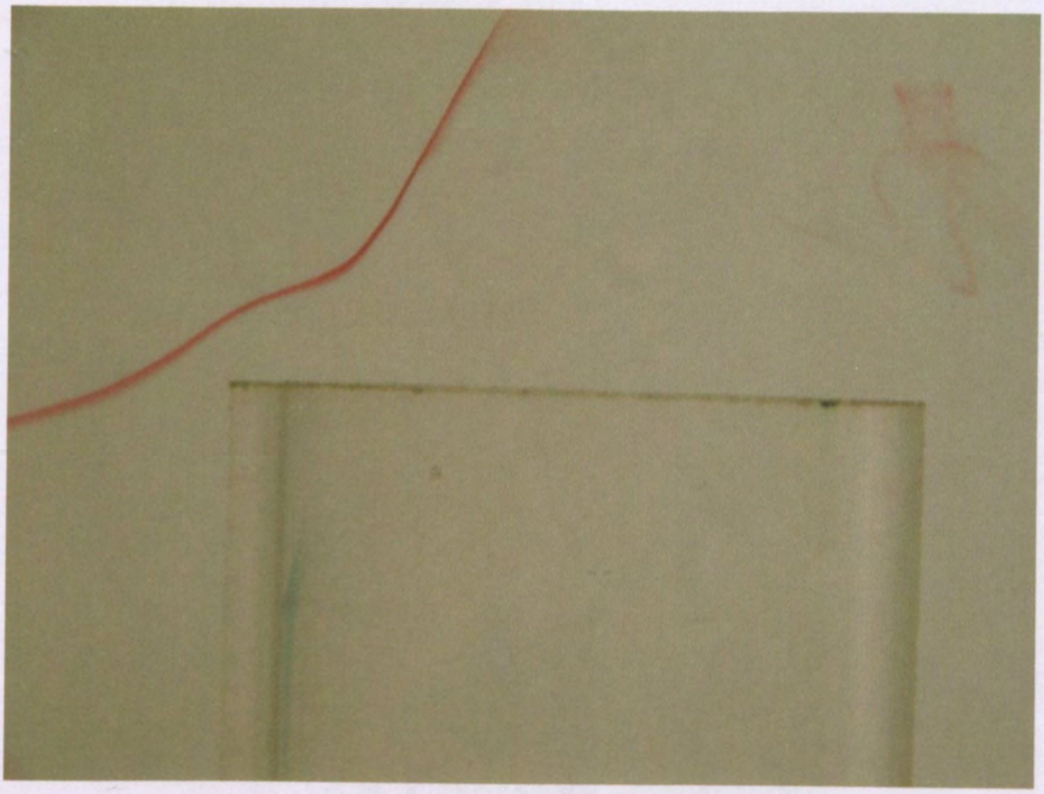

Figure 7-5 A dye trace originating from upstream of an elevated jet in crossflow marking the jet shear layer. Re=2000, Re_j=4000, R=2

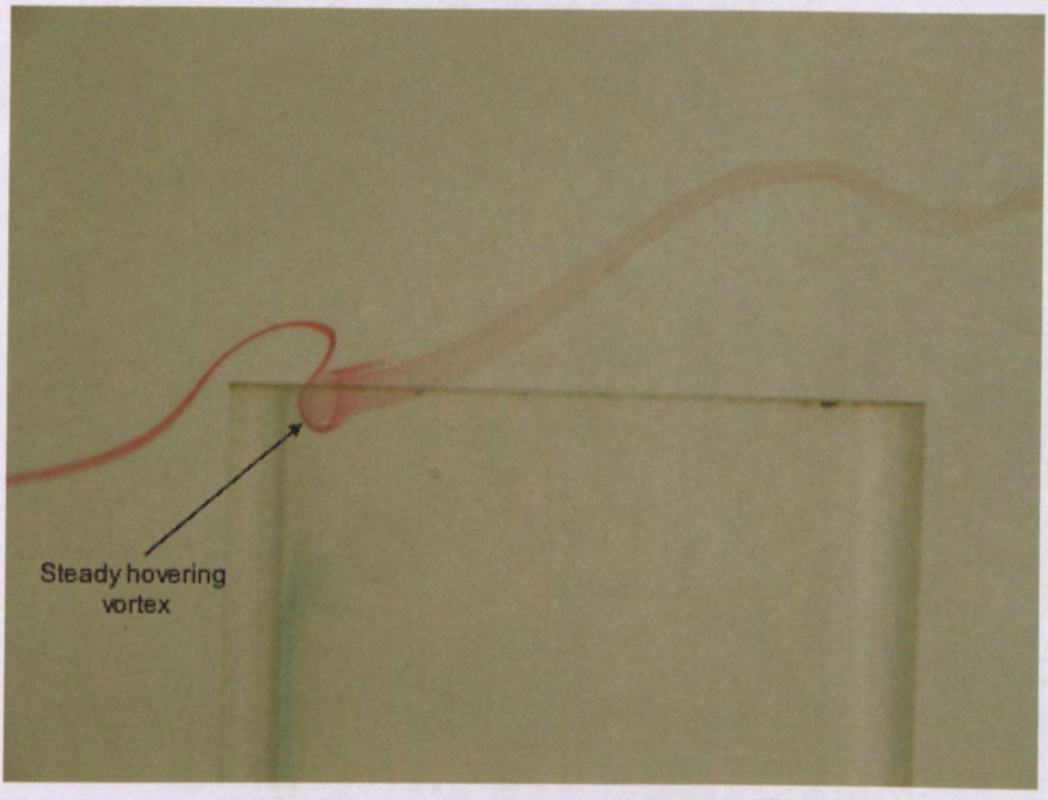

Figure 7-6 A dye trace originating from upstream of an elevated jet in crossflow marking a steady hovering vortex. Re=2000, Re_j=4000, R=2

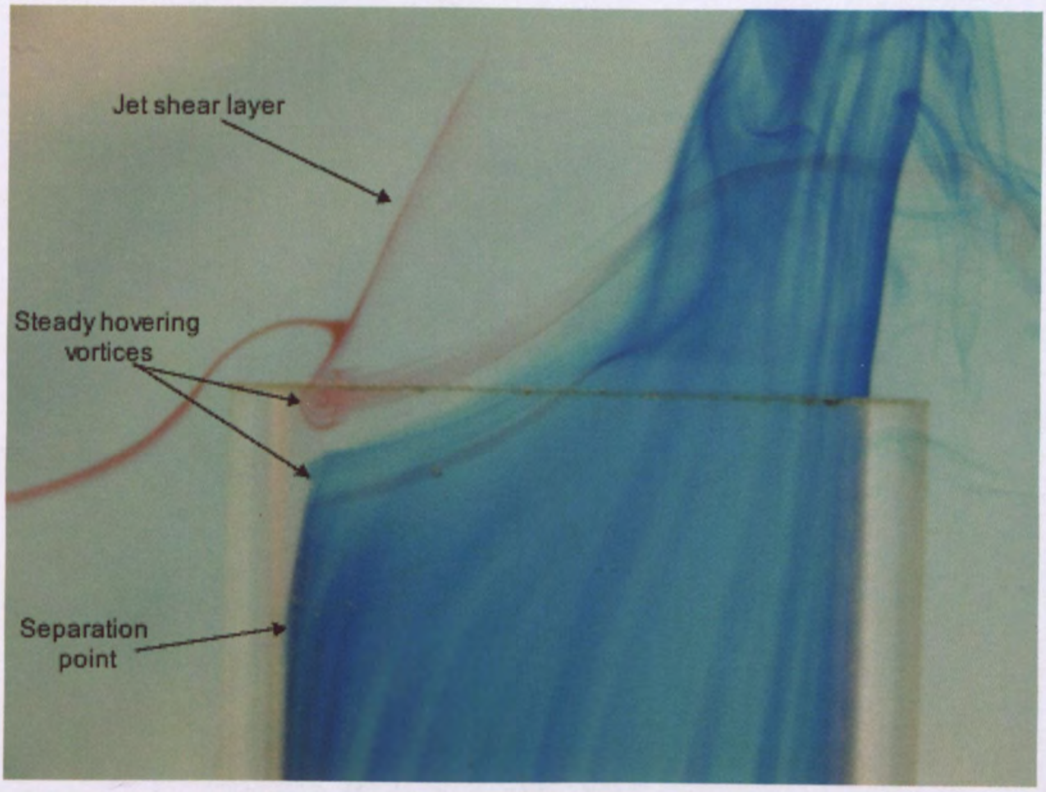

Figure 7-7 Elevated jet in crossflow, with a velocity ratio of 2. The red dye streak is marking a hovering vortex and the leading edge jet shear layer and blue dye marking the jet shear layer. Re=2000, Re_j=4000, R=2

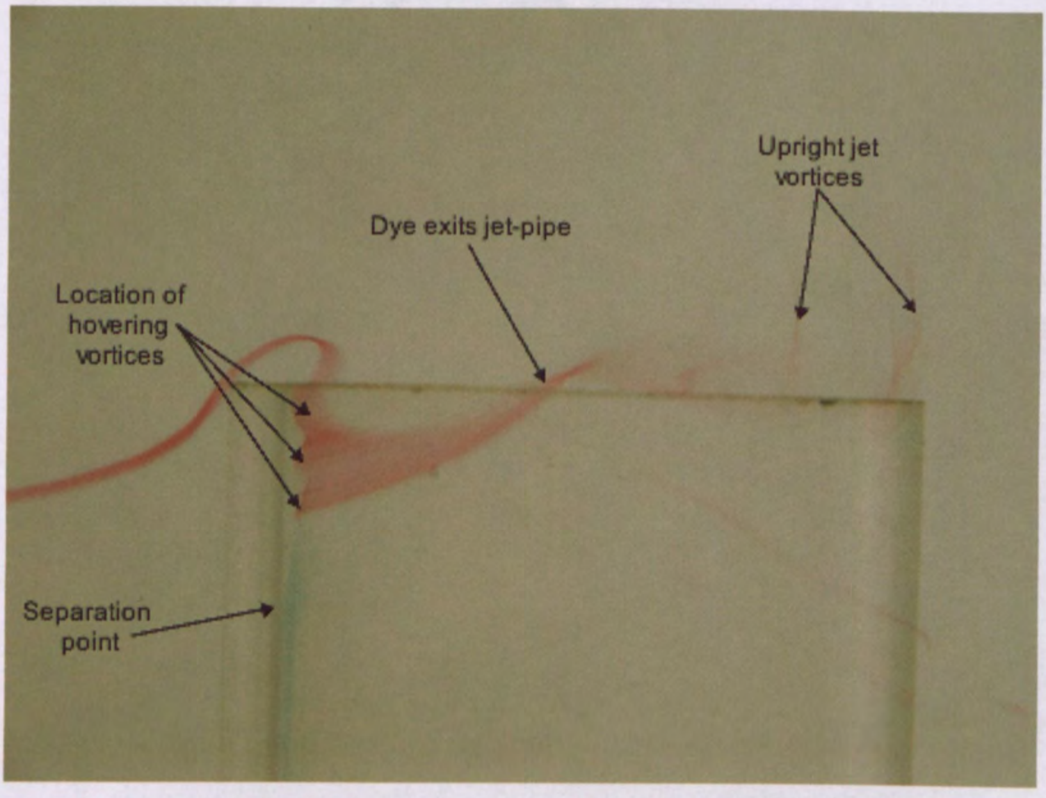

Figure 7-8 A dye trace originating from upstream of an elevated jet in crossflow marking the crossflow fluid induced into the leading edge of the jet pipe. Re=2000, Re_j=4000, R=2

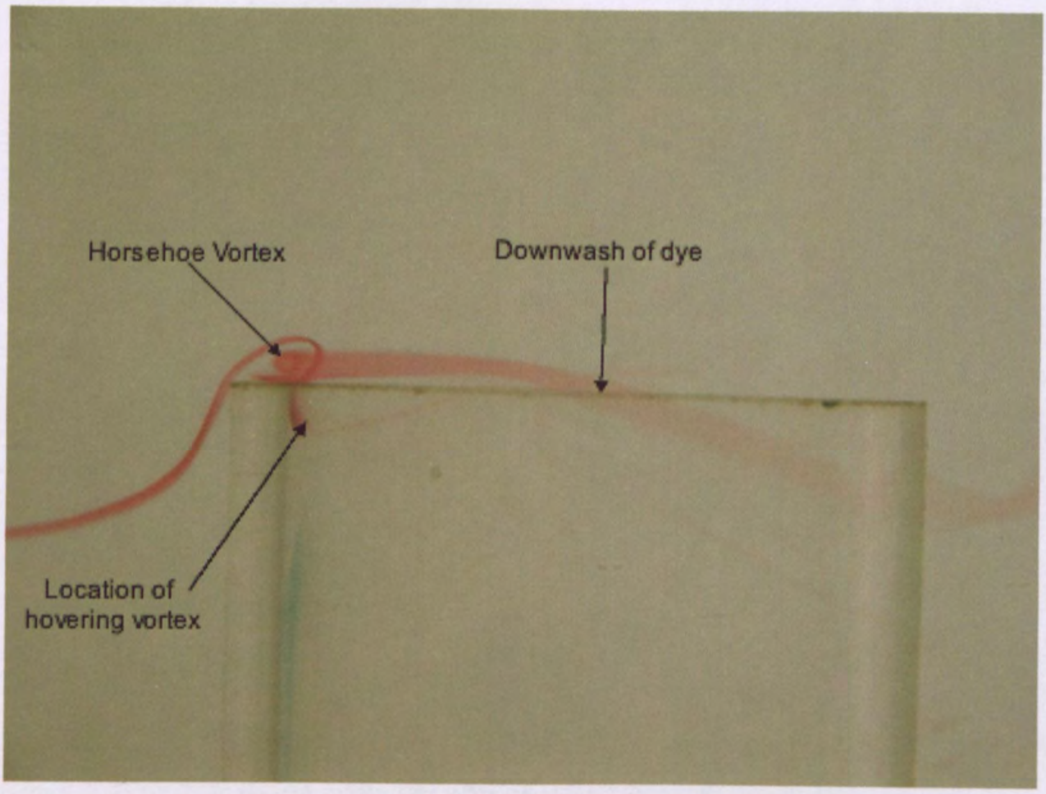

Figure 7-9 A dye trace originating from upstream of an elevated jet in crossflow marking the horseshoe vortex. Re=2000, Re_j=4000, R=2

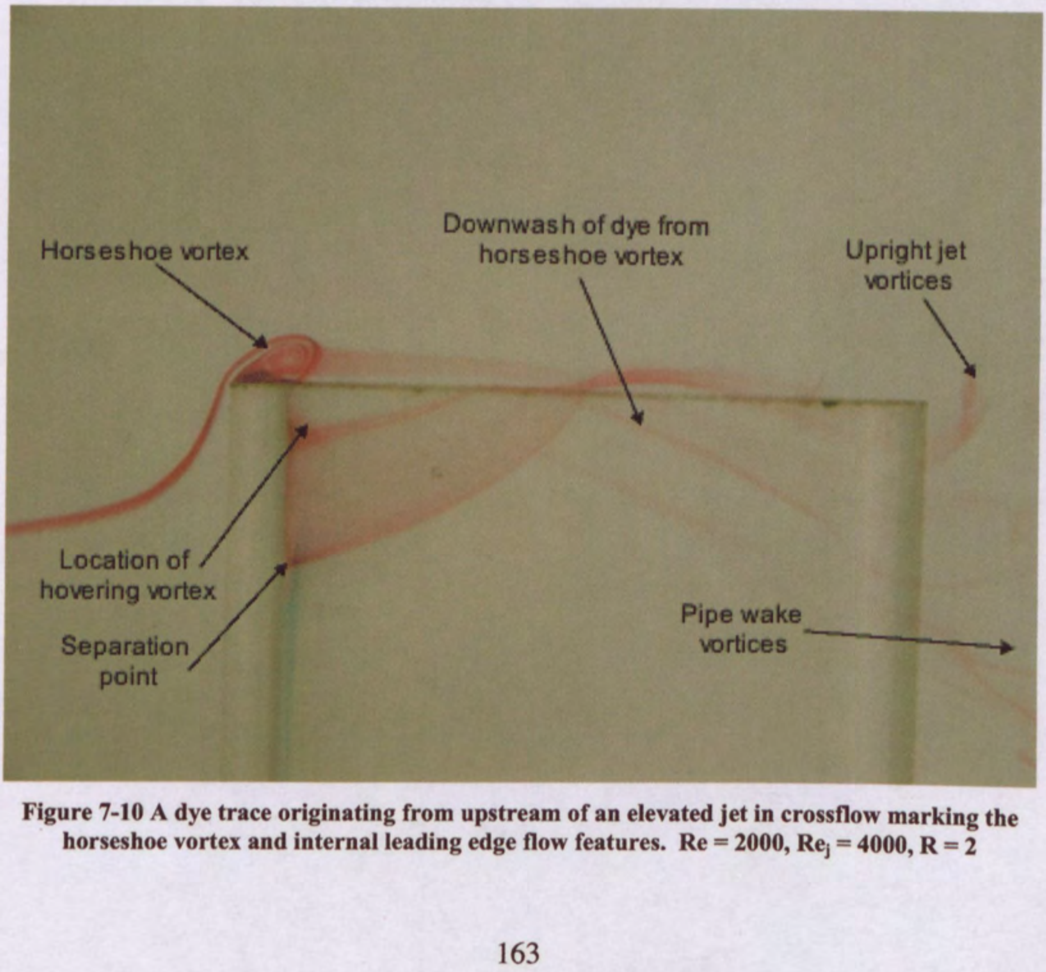

Figure 7-10 A dye trace originating from upstream of an elevated jet in crossflow marking the horseshoe vortex and internal leading edge flow features. Re = 2000, Re_j = 4000, R = 2

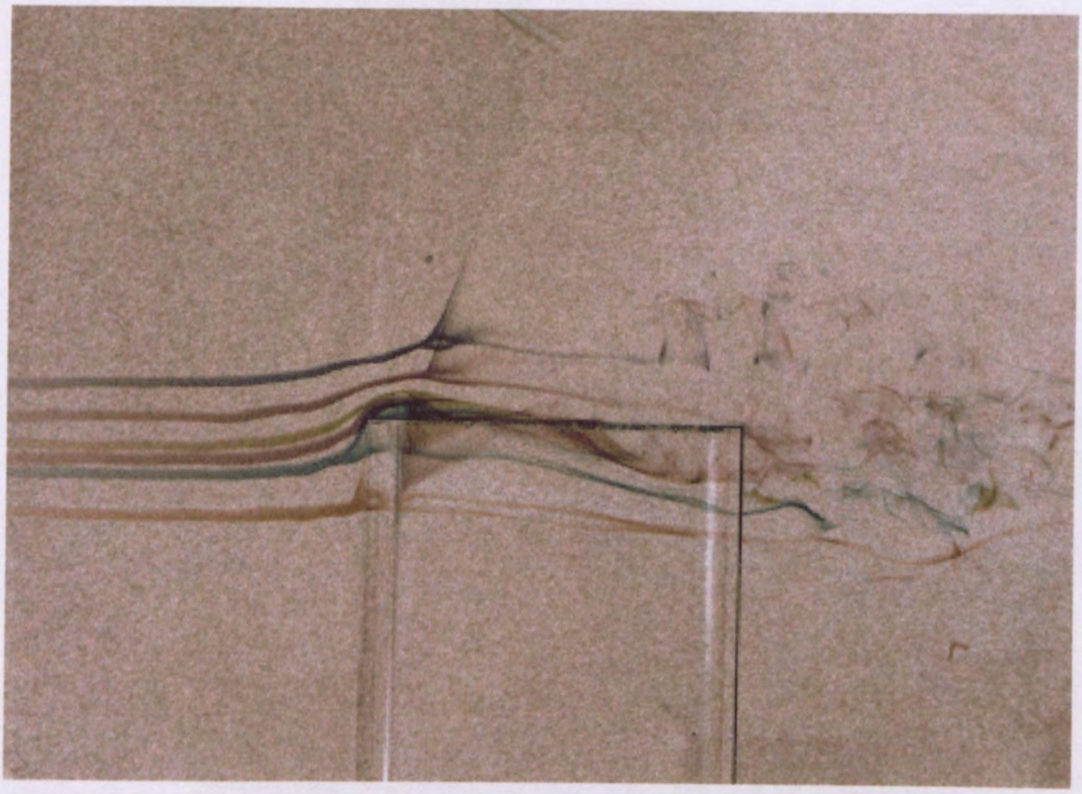

Figure 7-11 A false colour composite image composed from six separate images showing the path of dye introduced from different levels in the crossflow relative to the jet exit plane. Re=2000, Re_j=8000, R=4

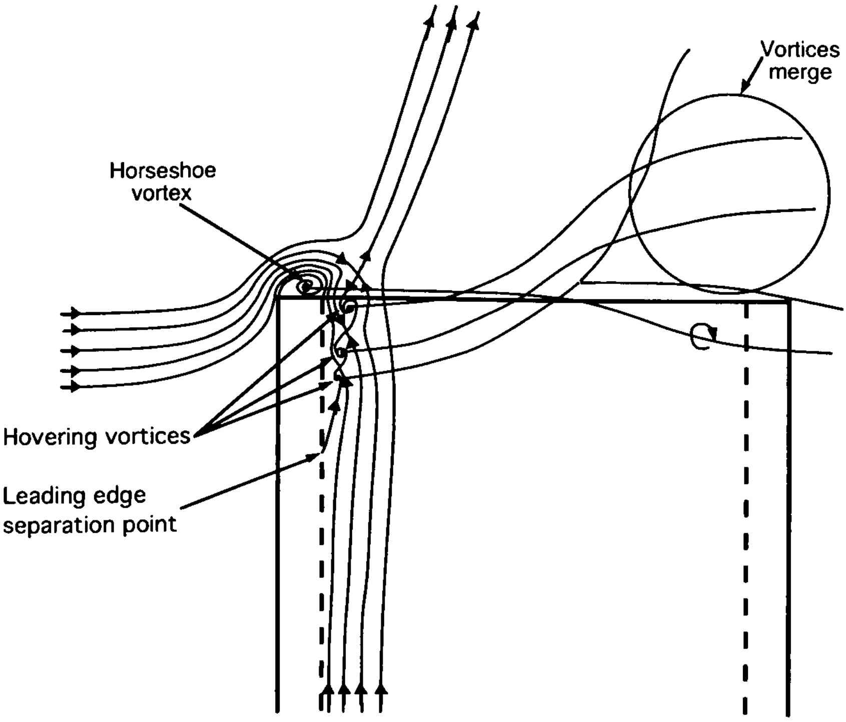

Figure 7-12 Interpretation of the shear layer structure for an elevated jet with R=2 and a Reynolds number of 2000.

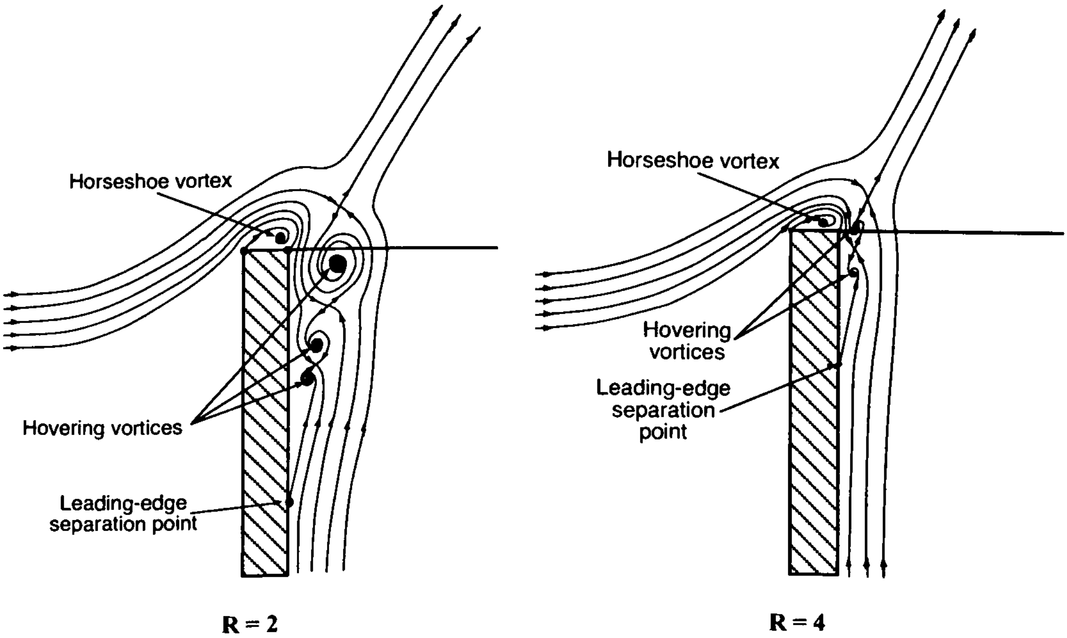

Figure 7-13 Close up details of the shear layer structure in the leading edge of an elevated JICF at velocity ratios of 2 and 4 for a Reynolds number of 2000.

7.3.2 Overall Flow Structure for $R \leq 4$

As discussed in Section 6.3.1, the shear layer of the emerging jet rolls up to produce the CVP. The shear layers on the upstream and downstream sides of the jet are essentially connected or 'joined' to the CVP but the details of this connection are unresolved. The following section will focus on the connection between the various shear layer roll-ups of the elevated jet, including the upstream, and downstream shear-layer roll-ups and the hanging vortices (and CVP).

Figure 7-14 shows a perspective view of the flow described in Figure 7-2, for R=2 and Re_j=4000. It has been shown that the upstream side of the shear layer rolls up to form two steady hovering vortices at the pipe exit and a Kelvin-Helmholtz instability approximately 2 jet diameters from the exit. In Figure 7-14 the perspective view reveals a periodic roll-up of the shear layer on the downstream side of the jet. The vortices consist of a series of loops spanning the downstream side of the jet shear layer. These loops initially, within one pipe diameter, appear to form immediately behind the CVP and then propagate downstream. The vertically-aligned sides of these loops bear a striking resemblance to the 'upright vortices' observed downstream of flush-mounted jets. The vertical sides of these loops also bear striking similarity to the 'trailing edge vortex pair' observed in the flush-mounted jet case reported in Section 6.2.1. Although the shear layer roll-up shows a strong periodicity, it must be remembered that no forcing of the flow is applied. Furthermore, no such periodicity was evident on the upstream shear layer which rolled up by a Kelvin-Helmholtz mechanism. The connection between the bottom of the vortices and the jet is shown in the following sections.

An additional feature of the flow is a large recirculation zone that is formed downstream of the jet and bounded on the sides by the upright vortices. This zone extend down to the level of the jet exit plane. From observations made during the visualisation of the flow the recirculation zone extended approximately five jet diameters downstream of the jet exit. The fluid within the recirculation zone was found to move very slowly compared with the surrounding flow. This single large recirculation zone contrasts with the observations of small recirculation zones in the breaking down CVP vortices in flush-mounted jets.

The formation of the upright vortices along the side of the jet is quite complex. In Figure 7-15, where R=4 and Re_j=4000, the vortices appear to form in two parts. The top parts of the vortices appear to be larger and are connected to the roll-up of the lee side shear layer. The bottom section of the upright vortices forms with a smaller wavelength than that of the top part. For the present case the wavelength of the lower vortices was half that of the upper vortices. The lower vortices are initially connected to the upper vortices, and as the jet progresses downstream pairing of the two lower vortices occurs to form continuous upright vortices of constant wavelength. The pairing process can be seen in Figure 7-16. The line of discontinuity between the upper and lower parts of the upright vortices corresponds closely to the location at which the upper hovering vortex meets the fold in the shear layer (marked by the edge of the dye). This is illustrated in Figure 7-16 and can be confirmed by reference to Figure 7-7. The upright vortices are also evident in Figure 7-18 in which case the structures are marked by a dye trace originating from a dye probe located in the crossflow. The entire process is extremely complex but occurs with a strong periodicity.

The visualisation of these upright vortices is significant as, although such structures have been found in spectral measurements of the flow, they have not previously been shown by flow visualisation in the elevated jet case. Eiff *et al.* (1995) found that two vortical systems are present downstream of the elevated jet, each with different sources of vorticity. One system is located in the 'jet-wake' and the other is in the pipe-wake. The two systems were found to synchronise with one another giving the appearance of continuous vortices extending from the pipe-wake into the jet-wake. Eiff *et al.* (1995) found that the source of vorticity for the vortices occurring in the 'jet-wake' was the inside surface of the jet pipe. This agrees with the present observations.

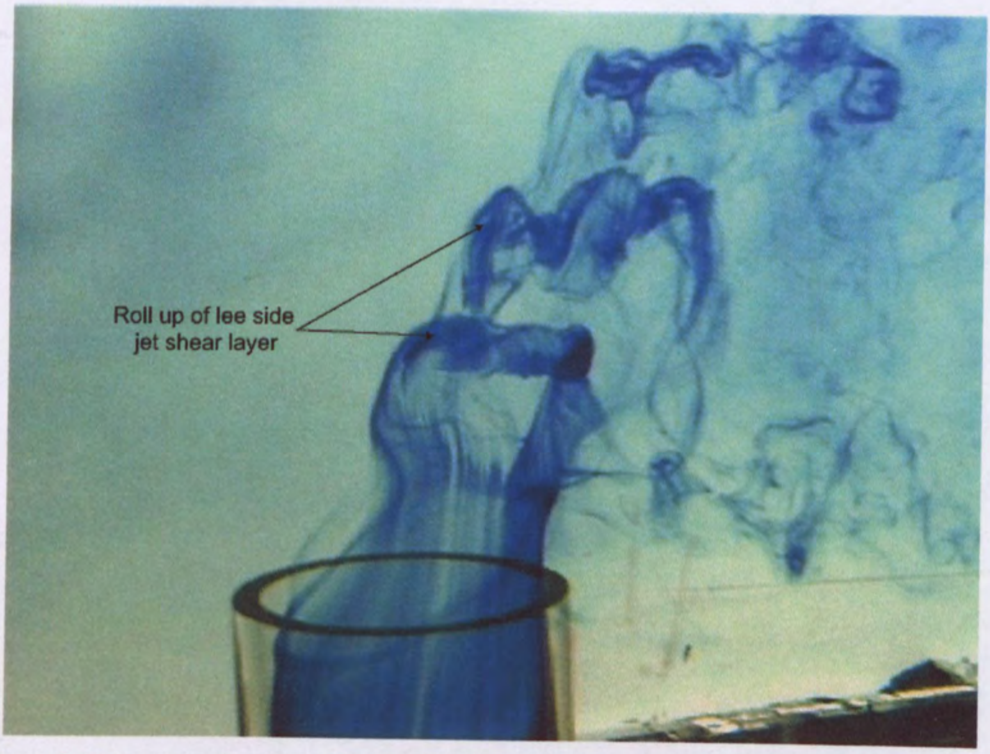

Figure 7-14 A perspective view of the jet shear layer shown in Figure 7-2 viewed from a position upstream of the jet. The connection between the upright jet vortices and the roll-up of the lee side jet shear layer is evident. Re=2000, Re_j=4000, R=2

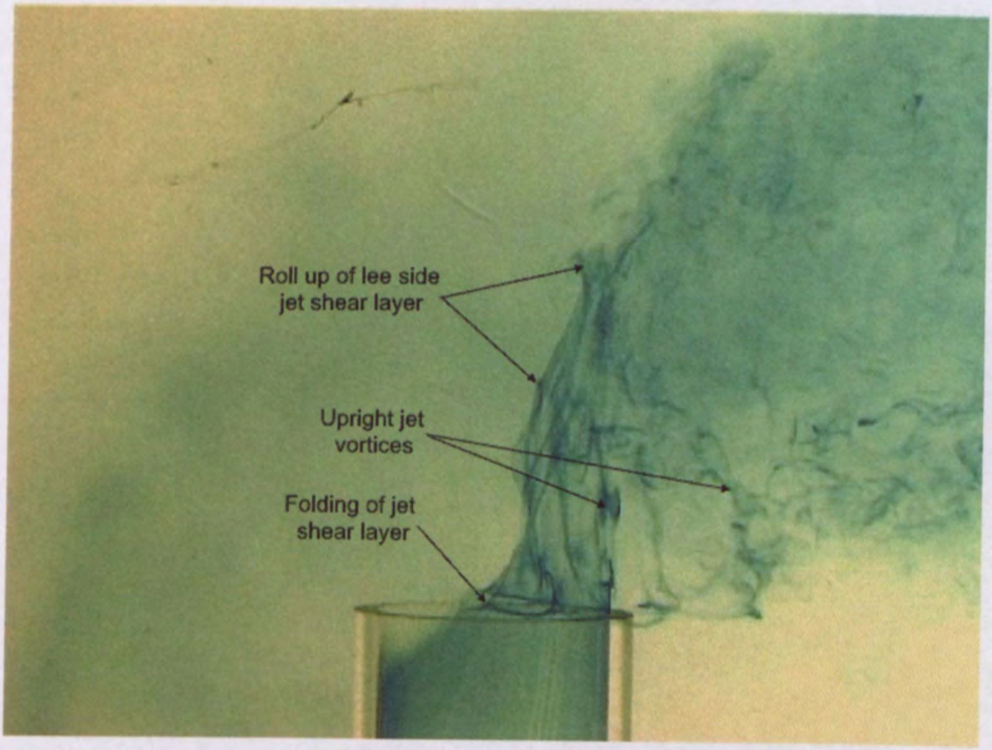

Figure 7-15 The jet shear layer for the conditions as in Figure 7-3 but with less dye marking the jet shear layer. Re=2000, Re_j=8000, R=4

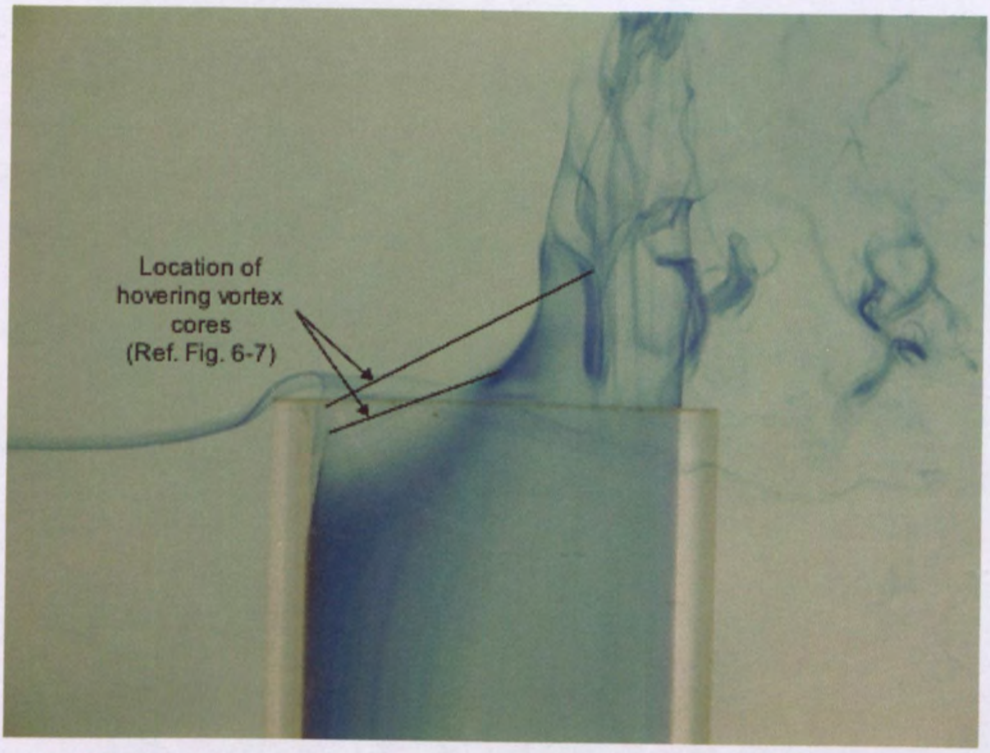

Figure 7-16 Pairing of the upright vortical structures shown for an elevated jet in crossflow at R=2 and Re_j=4000. Dye was added from the circumferential dye slot, and an upstream probe. The dye added from the slot has been turned off before the image was taken in order to show the flow features with the highest concentration of dye.

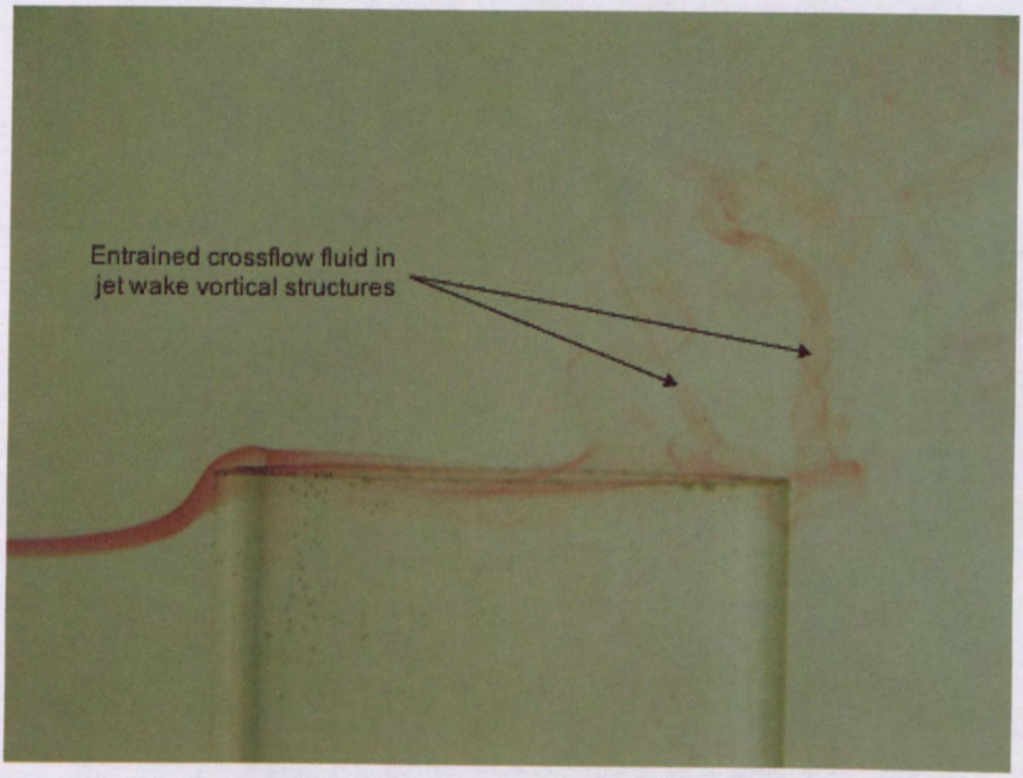

Figure 7-17 A dye trace originating from upstream of an elevated jet in crossflow with a velocity ratio of 2 marking the upright vortical structures. Re=2000, Re_j=8000, R=4

The present findings suggest the upright vortices observed in the shear layer flow from an elevated jet are the 'jet-wake' vortices discussed in Eiff *et al.* (1995). The flows reported by Eiff *et al.* were for velocity ratio of 3 but at much higher Reynolds numbers, Re_j = 41,000. The linking of the vortices in the jet-wake to those formed in the pipe-wake was not observed in the present work because classical large-scale vortex shedding from the cylinder did not occur. This is probably due to the relatively small length-to-diameter ratio of the cylinder protruding from the wall.

The conclusions of Fric & Roshko, that the vorticity cannot be generated away from a solid surface in a homogenous fluid must still hold true for the elevated jet case. Therefore, although the upright vortices give the appearance of being 'shed' from the jet, they cannot be formed by a classical 'cylinder' shedding mechanism, as it would require new vorticity to be generated within the flow. The vortices therefore must form due to the realignment of vorticity already contained within the jet.

Although it is not possible to visualise vorticity directly, some numerical simulations (eg. Rudman 1995) have shown successful visualisation of vortex lines using timelines introduced in the regions of high vorticity. Therefore, to simulate the evolution of vortex lines in the cylindrical shear layer of the pipe, pulsed hydrogen bubble visualisation was attempted. In order to produce timelines within the jet flow, a hydrogen bubble-wire was formed into a ring and inserted into the jet pipe approximately 1.5 jet diameters upstream of the jet exit. The wire was supported by three posts so that it was held approximately 2mm from the pipe wall. The arrangement is shown in Figure 7-18 producing a continuous sheet of bubbles. The wakes of the wire supports can be seen in the bubble sheet. The first attempt at this technique used a thicker wire that required only one support. This provided consistent rings of bubbles that were free of distortion from the wakes of the supports. However, the thicker wire produced larger bubbles and significantly less visual contrast. Thus, although it was possible to visualise and interpret with the naked eye, it was not possible to record clear images. The image that follow were obtained from later experiments which were unfortunately distorted by the wakes of the supports. However, the interpretations of the results are based on observations from the undistorted results.

The flow patterns produced in the pipe are shown in Figure 7-19 and Figure 7-20 for velocity ratios of 2 and 4 respectively. For comparison, the flush-mounted jet case is shown in Figure 7-21. The pattern for the flush-mounted case shows the lines within the pipe, but the lines close to the jet exit are not clear due to the presence of the floor. Although the patterns are influenced by the wake from the wire support posts (the effect is particularly evident from the near side post) conclusions can still be drawn from the bubble lines on either side of the wake disturbance. Figure 7-22 to Figure 7-24 show the images of Figure 7-19 to Figure 7-21 with lines superimposed to depict the observed evolution of the timelines in absence of any distortion. In each case the initially horizontal timelines tilt progressively with relatively little distortion until they reach the plane of the hovering vortices adjacent to the pipe exit (for comparison see Figure 7-4 and Figure 7-7 for R=2 case and Figure 7-3 and Figure 7-15 for R=4 case). At this plane the timelines undergo a rapid stretching process whereby the downstream side of the timeline ring is advected downstream by the flow, yet the upstream side remains virtually stationary. If such a timeline gives an accurate representation of a vortex line (at this radius), the results imply that the over-riding processes in the shear layer are tilting within the pipe followed by stretching outside.

Had a hydrogen bubble wire ring of smaller diameter been used, it is possible that the timelines would have shown a different deformation process. It is clear from the earlier dye visualisation results that fluid and vortex lines in the 'free' shear layer above the jet exit originated in the outer regions of the pipe boundary layer (i.e. smaller radius) on the upstream side. A timeline or a vortex line at such a radius must undergo a different deformation process in the upstream side at least. A possible interpretation is given in Figure 7-25. This interpretation is consistent with the present timeline studies and the associated dye visualisation studies for velocity ratios of 2 and 4. The interpretation suggests that the deformation process leads to a significant concentration of vortex lines on either side of the jet, thus forming the CVP. The *vortex lines* on the upstream and downstream sides are distributed initially evenly, but roll up to form independent span-wise concentrations – hence vortex loops – on the leading and trailing sides of the shear layer.

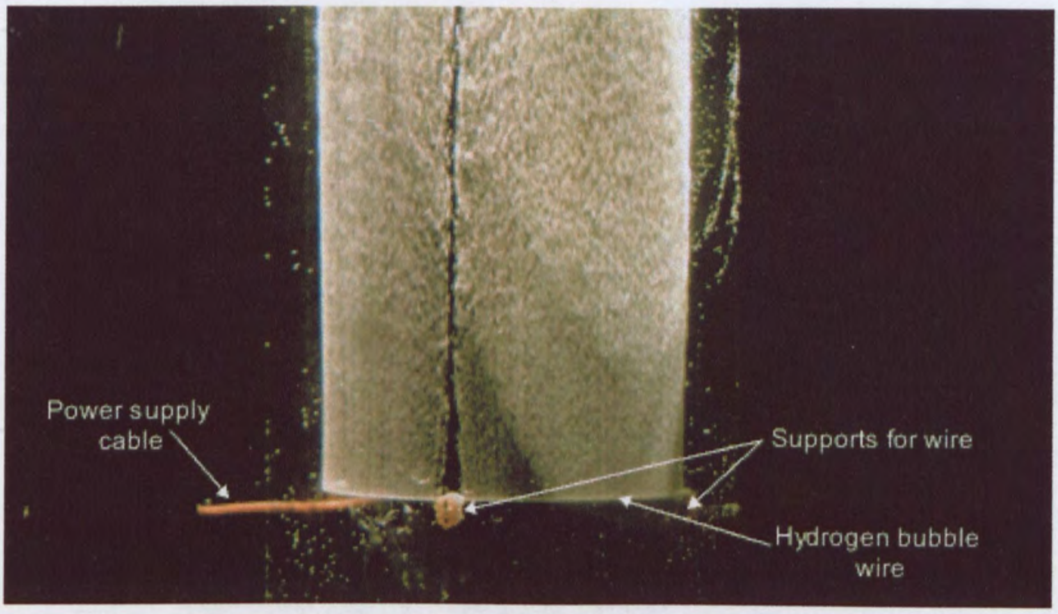

Figure 7-18 Circumferential bubble wire positioned in the jet pipe in order to mark ring of jet fluid.

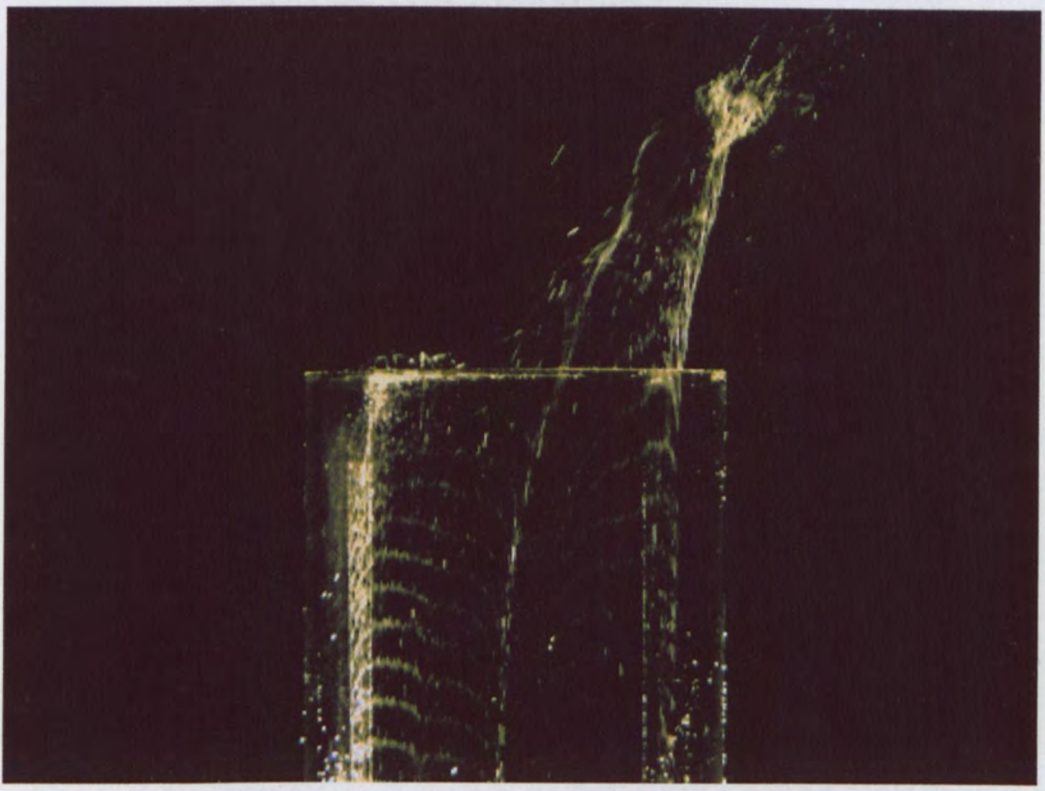

Figure 7-19 Bubble pattern produced by the circumferential bubble wire for an elevated jet at a velocity ratio of 2. The bubbles were produced at a frequency of 4.7 Hz and a duty cycle of 17%.

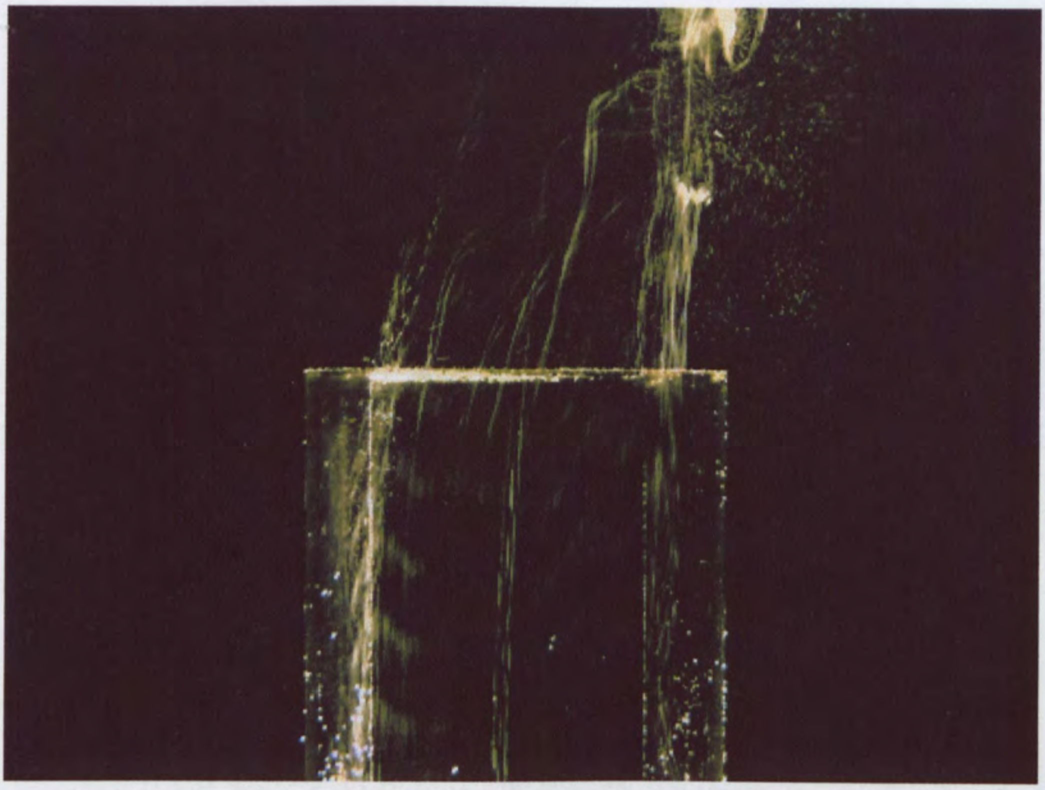

Figure 7-20 Bubble pattern produced by the circumferential bubble wire for an elevated jet at a velocity ratio of 4. The bubbles were produced at a frequency of 4.7 Hz and a duty cycle of 17%.

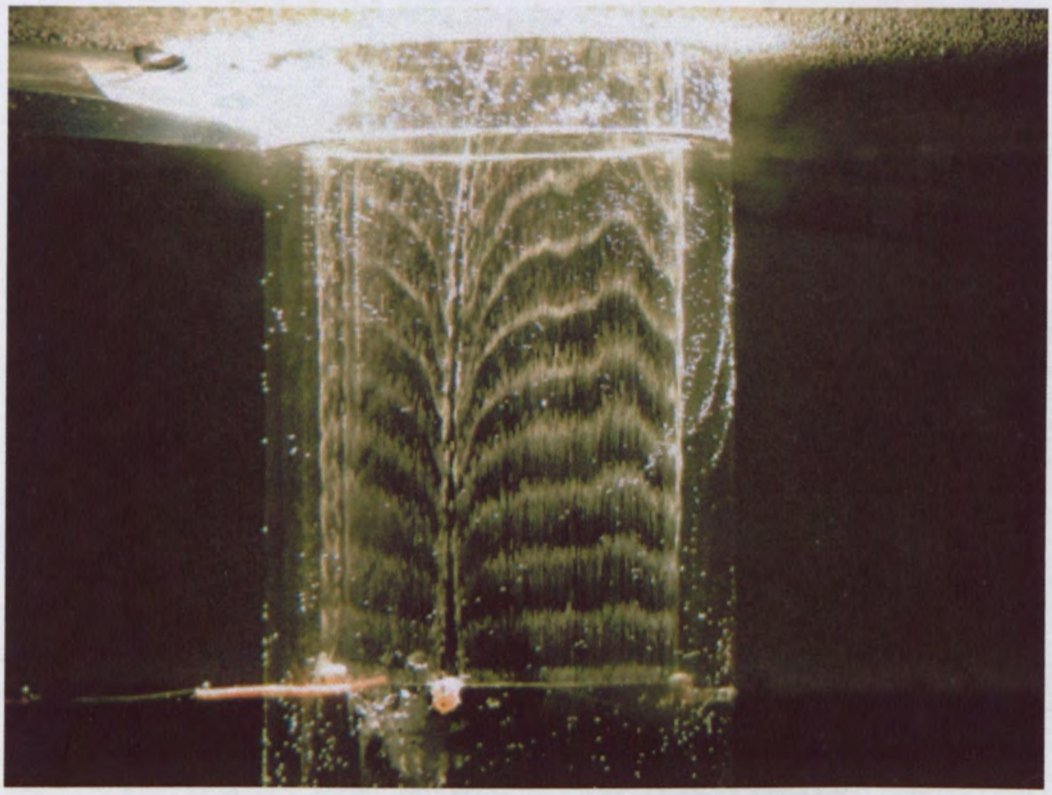

Figure 7-21 Bubble pattern produced by the circumferential bubble wire for a flush-mounted jet at a velocity ratio of 2. The bubbles were produced at a frequency of 4.7 Hz and a duty cycle of 17%.

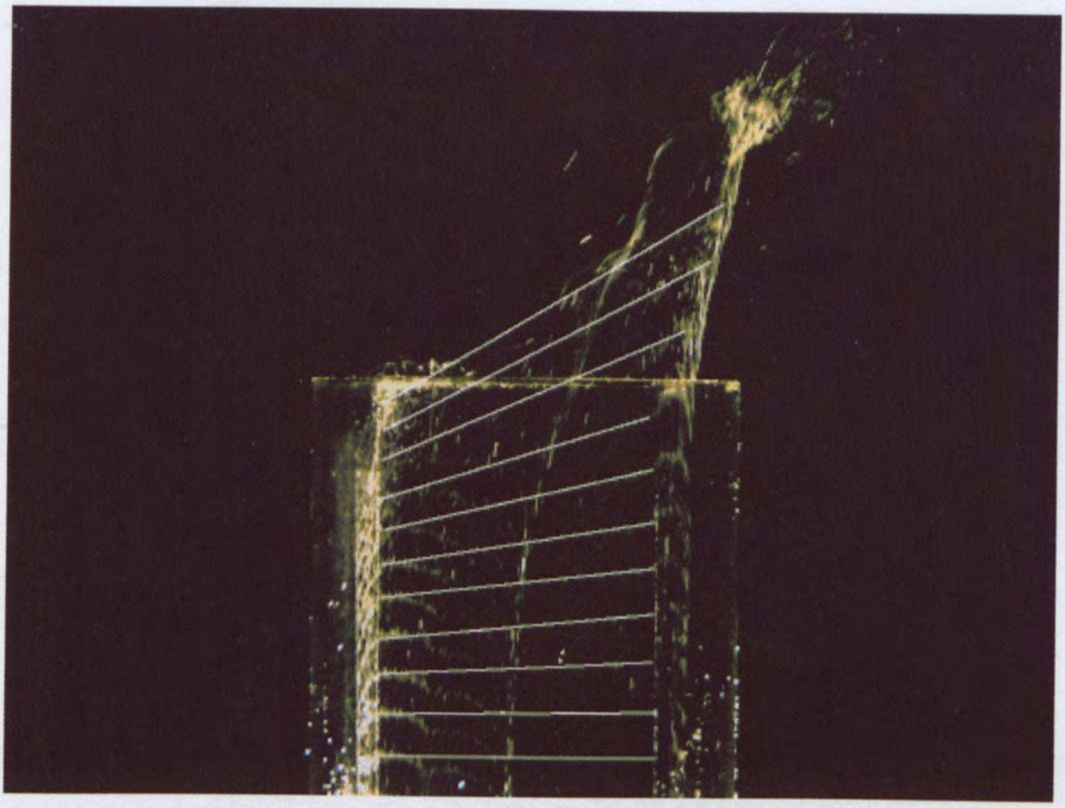

Figure 7-22 The same bubble lines as shown in Figure 7-19 but with lines superimposed to highlight the orientation of the bubble lines.

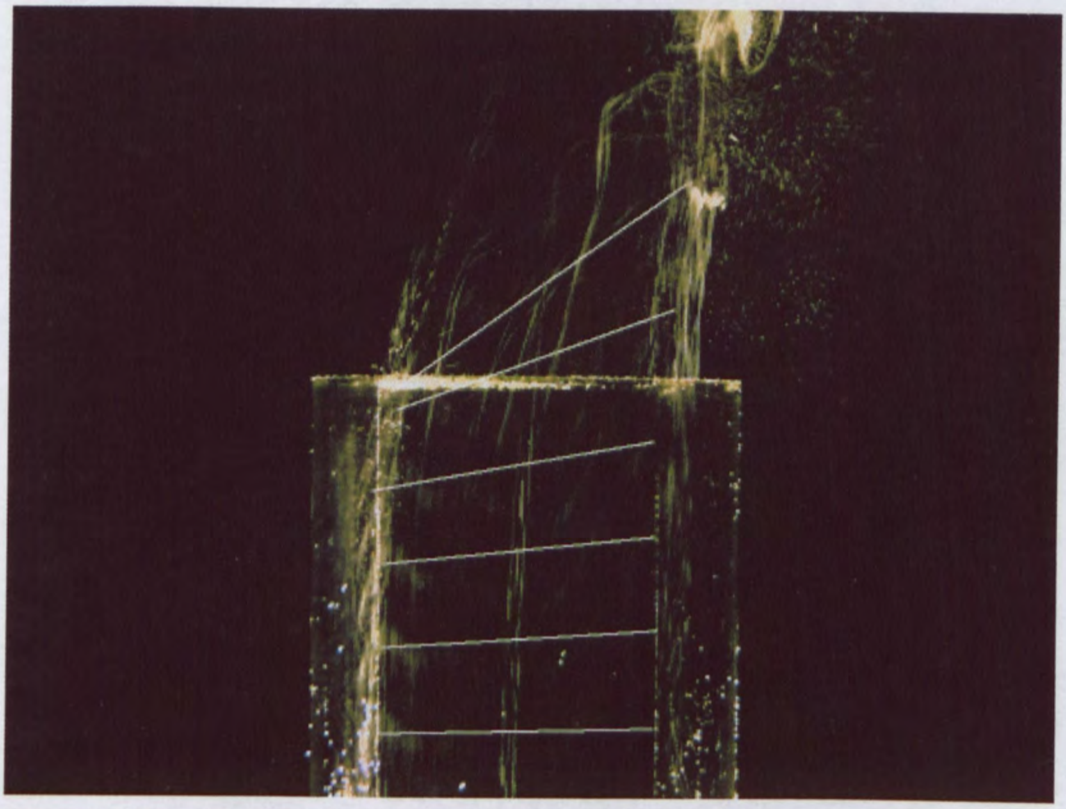

Figure 7-23 The same bubble lines as shown in Figure 7-20 but with lines superimposed to highlight the orientation of the bubble lines.

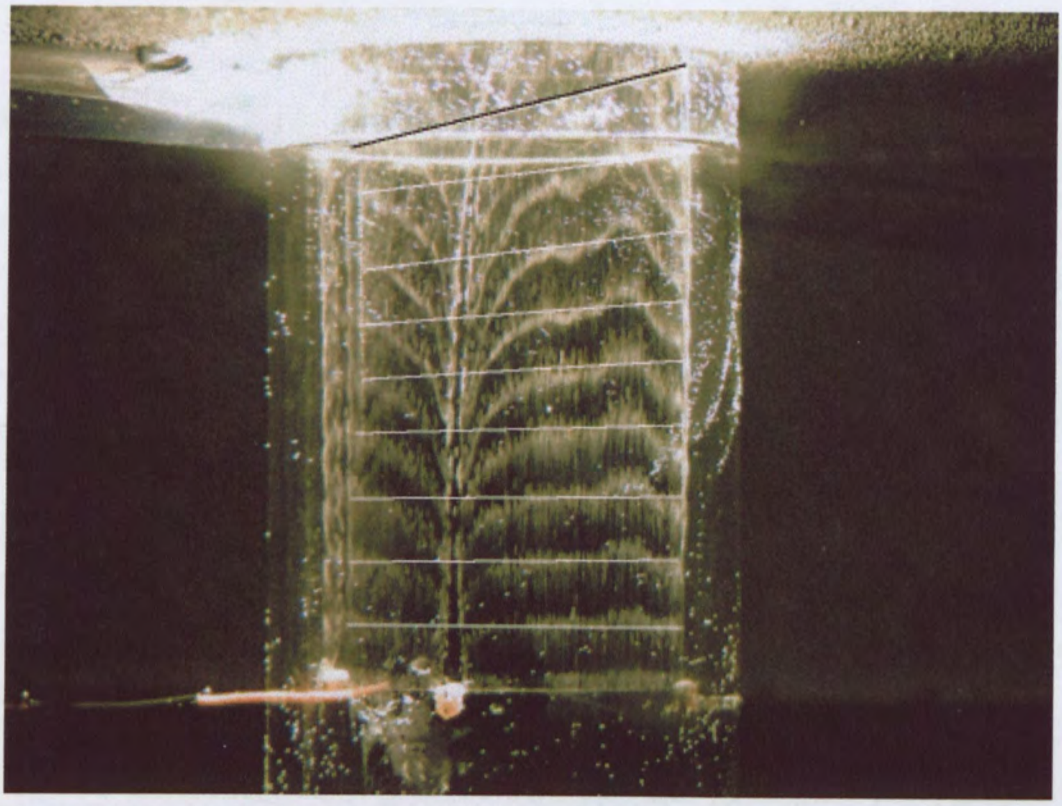

Figure 7-24 The same bubble lines as shown in Figure 7-21 but with lines superimposed to highlight the orientation of the bubble lines.

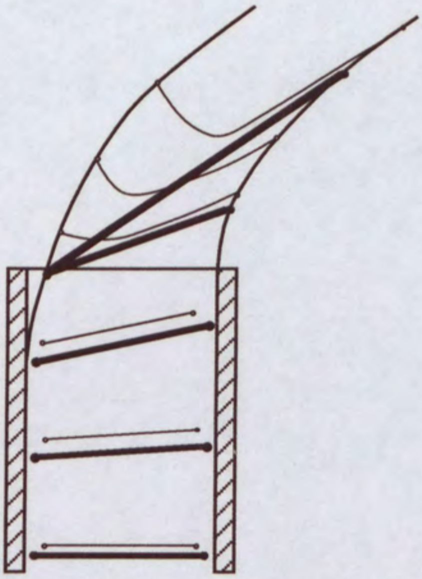

Figure 7-25 Possible interpretation of vortex line deformation. Thick solid lines represent larger radius vortex lines that become bound in the hovering vortex on upstream side. Thin solid lines represent smaller radius vortex lines that are incorporated into the shear layer on the upstream side of the jet. These vortex lines do not represent ring vortices – their spacing is arbitrary.

7.3.3 Overall Flow Structure for R > 4

In comparison with the shear layer development of the flows at velocity ratios of 2 and 4 (Figure 7-2 and Figure 7-3), the flow at a velocity ratio of 6 shown in Figure 7-26 looks distinctly different. In this case, the upright vortices formed on the side of the jet are not evident. Instead, the shear layer undergoes two folding processes. On the sides of the jet the shear layer is folded into two steady vortices similar in appearance to the hanging vortices that initiate the formation of the CVP in the flush-mounted jet case. In this case, the separation region within the jet pipe is very small and a hovering vortex can be seen to occur outside the jet pipe. In addition, the hovering vortex sheds vorticity into the leading edge shear layer. Thus, in this case, the large-scale periodic rolling-up of the leading edge shear layer occurs very close to the jet exit. For the lower velocity ratio cases the leading edge shear layer rolls up by a Kelvin-Helmholtz-like instability mechanism downstream from the jet exit.

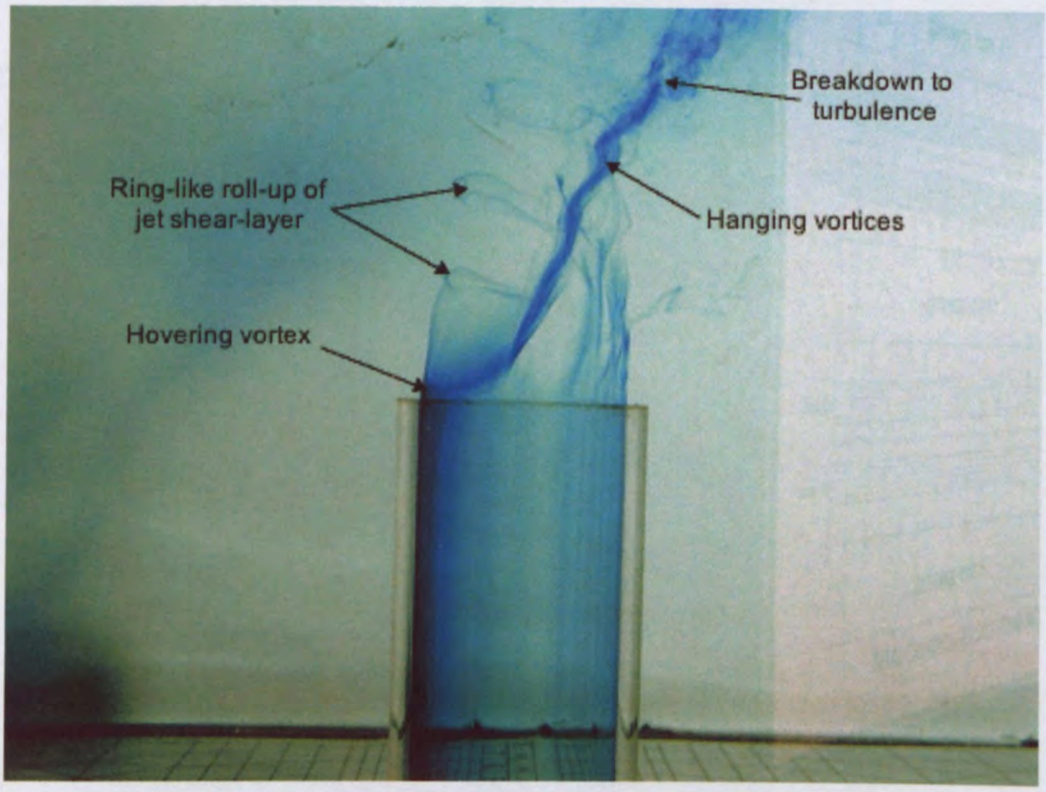

Figure 7-26 Jet shear layer as viewed from the side of an elevated jet at a velocity ratio of 6, and jet Reynolds number of 12000. The shear layer has been marked with dye from a circumferential dye slot located within the jet pipe.

The fact that at different velocity ratios the elevated jet in crossflow appears to be so different is of great interest and does not seem to have been previously acknowledged. Given that the jets at velocity ratios of 4 and 6 have different characteristics from one another suggests that there is a transition from one flow pattern to the other at an intermediate velocity ratio. This 'structural transition' is shown for the current flow conditions in Figure 7-27 to Figure 7-29. The transition occurs at velocity ratio slightly above four. In Figure 7-27 the characteristic features of the low velocity ratio elevated jet are visible within the development of the jet shear layer. However, in Figure 7-29 the shear layer resembles that of the flow at a velocity ratio of 6. The flow shown in Figure 7-28 shows an intermediate stage, in which the jet has characteristics of both the high and low velocity ratio cases. Close-up images of the leading edge of the jet are shown in Figure 7-30 and Figure 7-31 for the lower and higher velocity cases respectively. One feature evident from these images, which may be of significance, is that in this case the transition occurs when the hovering vortex is very close to the jet exit. An interpretation of the flow at the lower and higher velocity ratios is shown in Figure 7-32 and Figure 7-33 respectively.

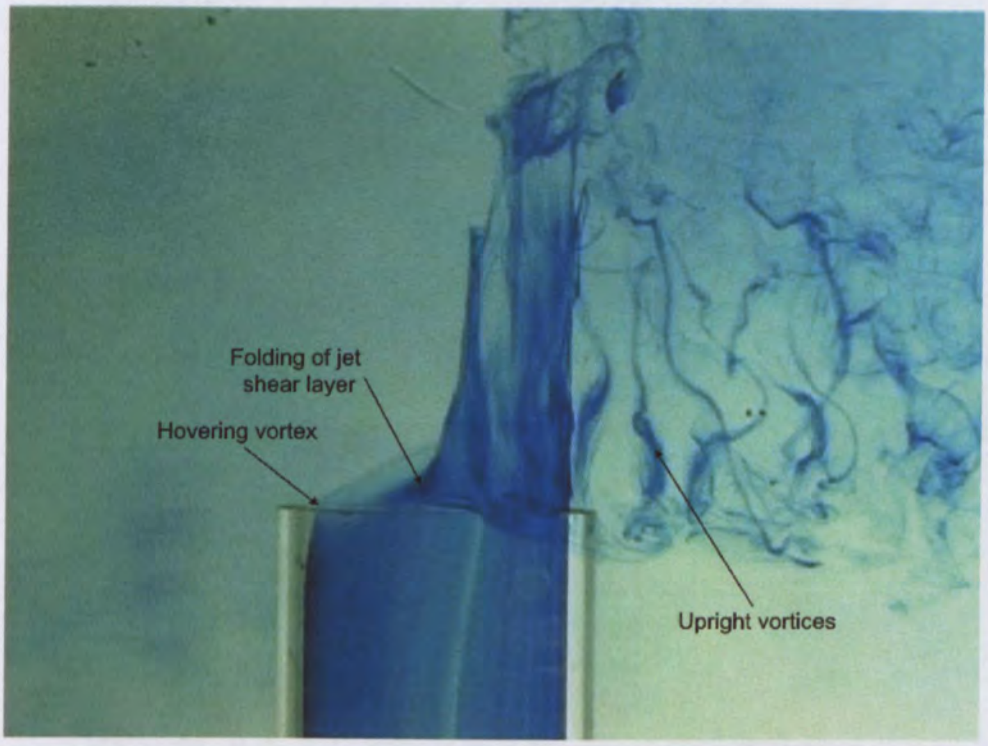

Figure 7-27 Dye visualisation of the jet shear layer of an elevated JICF obtained by injecting dye from the circumferential dye slot in the jet pipe. The pattern shows the typical characteristics of a low velocity ratio elevated jet. Re=2000, Re_j=8000, R=4

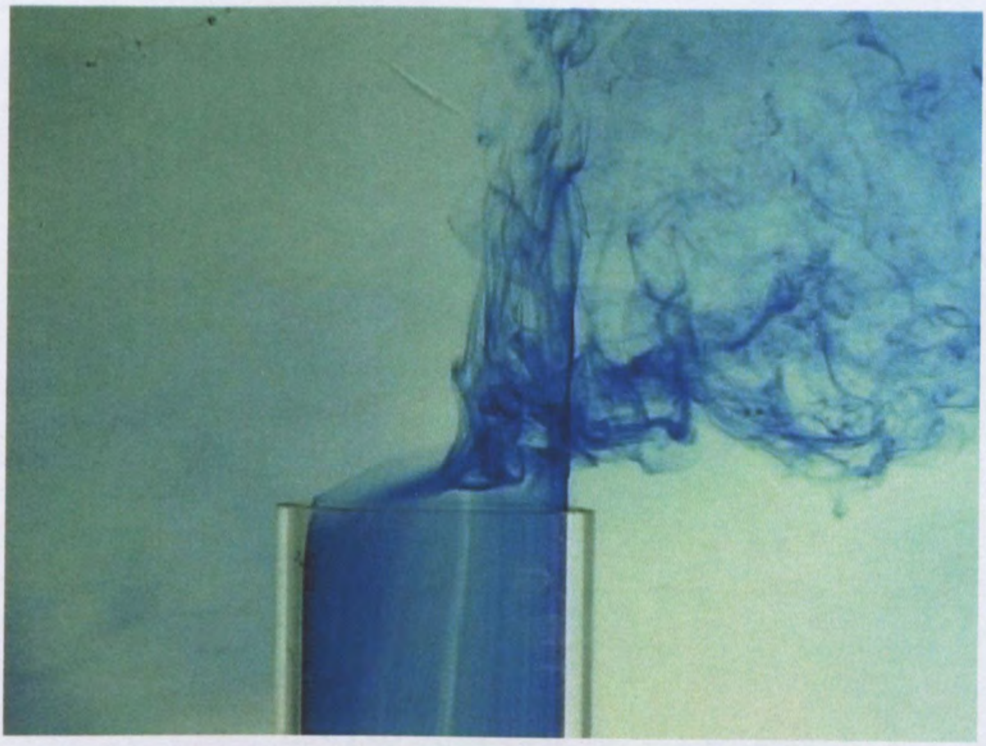

Figure 7-28 Dye visualisation of the jet shear layer of an elevated JICF obtained by injecting dye from the circumferential dye slot in the jet pipe. Jet velocity is slightly increased from Figure 7-27. The pattern shows the transition between the elevated and flush-mounted jet structure. Re=2000, R≈4.2

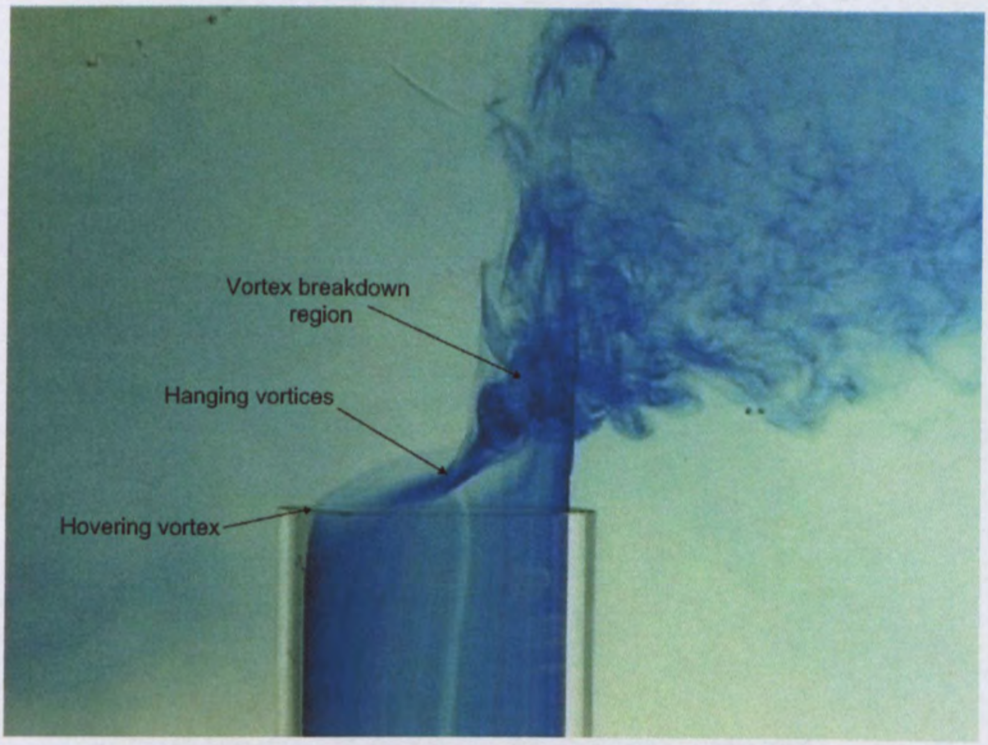

Figure 7-29 Dye visualisation of the jet shear layer of an elevated JICF obtained by injecting dye from the circumferential dye slot in the jet pipe. Jet velocity is slightly increased from Figure 7-28. The pattern shows characteristics similar to a flush-mounted jet. Re=2000, R≈4.5

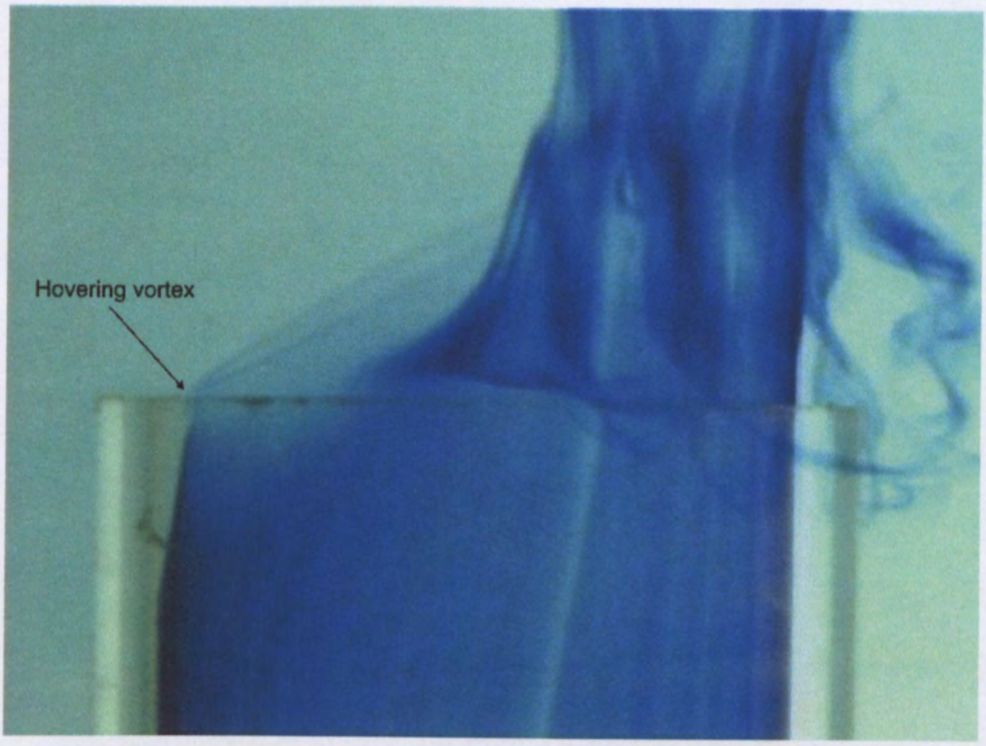

Figure 7-30 Close up view of the jet shear layer shown in Figure 7-27. Re=2000, R=4

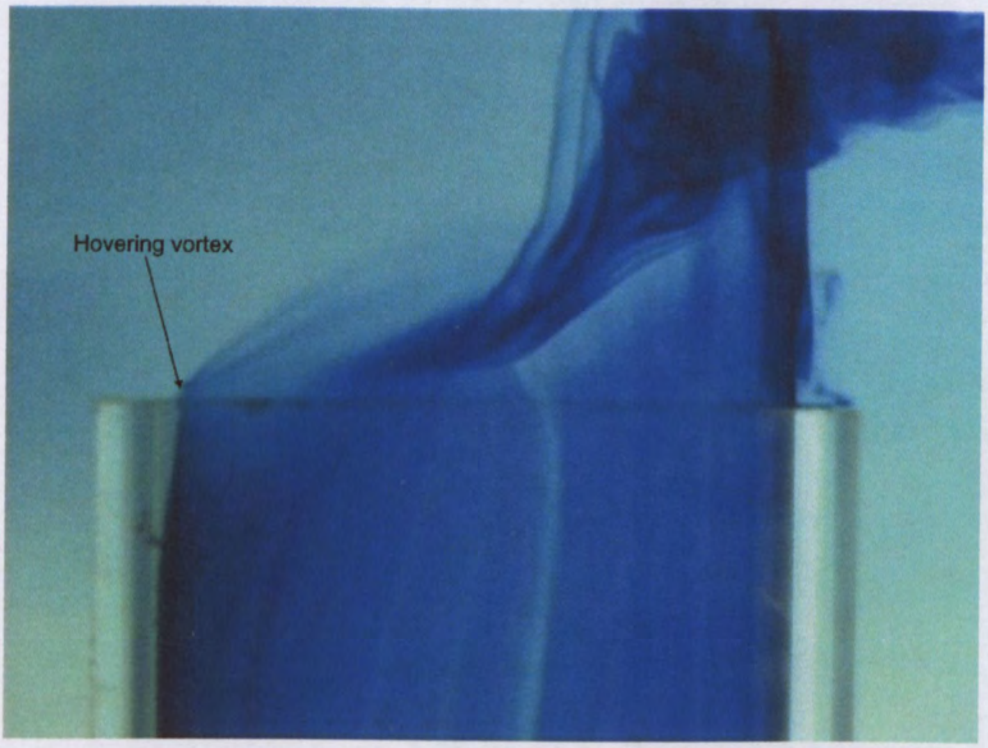

Figure 7-31 Close up view of the jet shear layer shown in Figure 7-29. Re=2000, R≈4.5

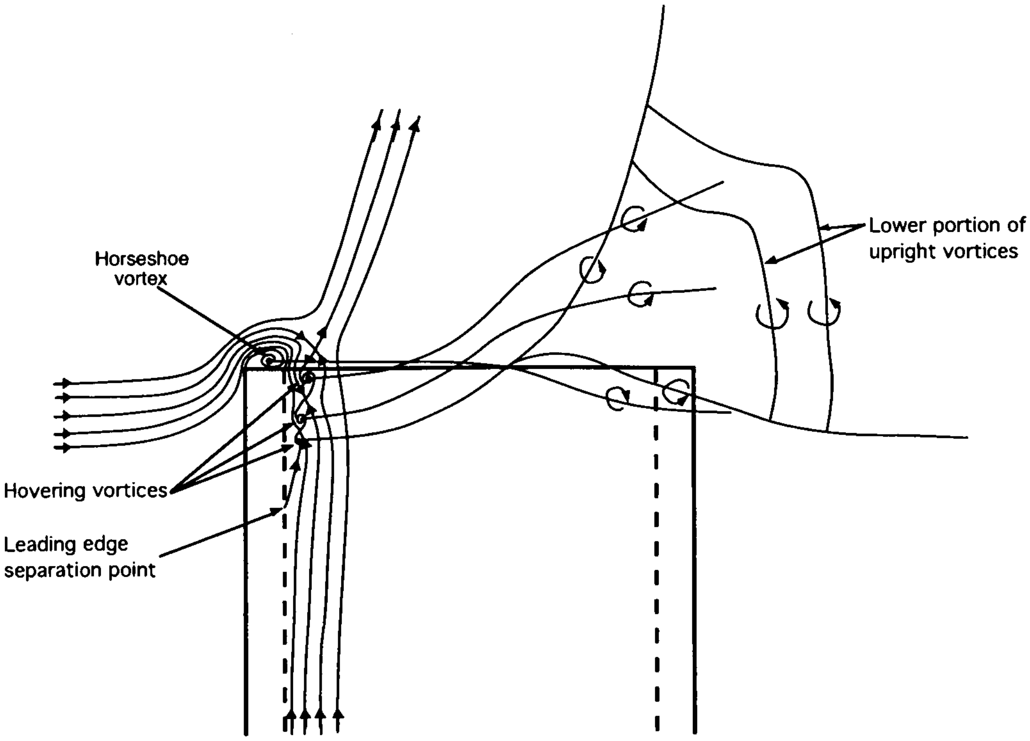

Figure 7-32 Interpretation of the shear layer structure for an elevated jet with a velocity ratio of 2 showing the characteristics of a low velocity ratio elevated jet

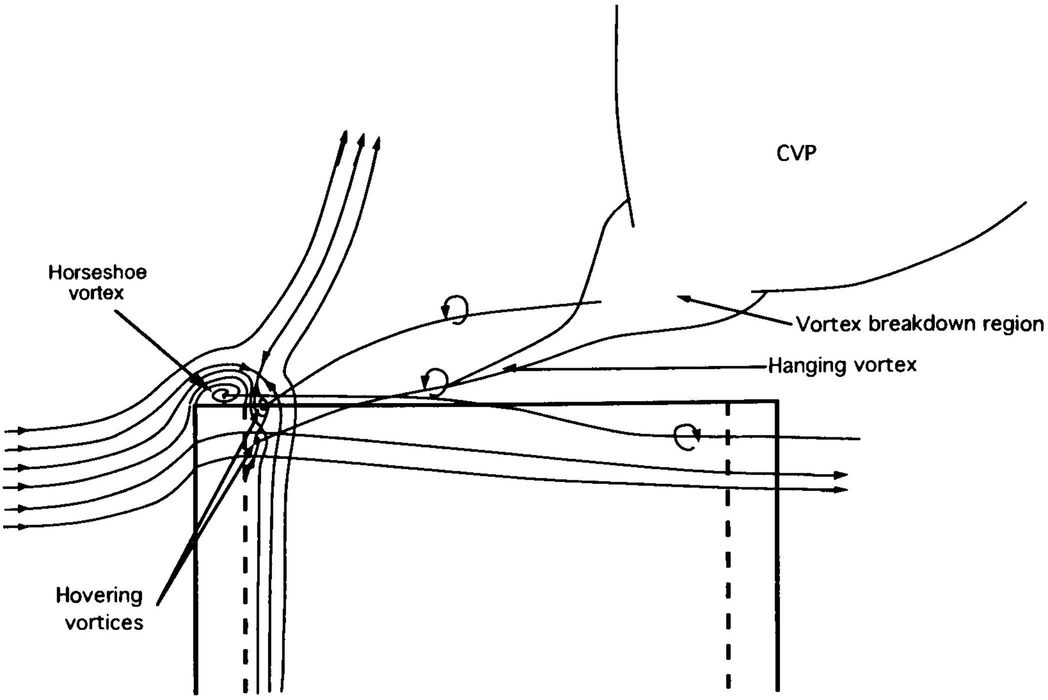

Figure 7-33 Interpretation of the shear layer structure for an elevated jet with a velocity ratio of above 4 showing characteristics similar to a flush-mounted jet.

7.3.4 Effect of Reynolds Number

For the case of a flush-mounted jet it has been established that the structure of the flow is dependent on both the Reynolds number and velocity ratio. Kelso (1991) and Kelso *et al.* (1996) show changes in the jet-wake and shear layer instability for flows with different crossflow Reynolds numbers for the same velocity ratio. As it has now been established that the structure of the elevated jet in crossflow is dependent on the velocity ratio, it is important to establish whether a Reynolds number dependence also exists.

The images in Figure 7-34 show the development of the jet shear layer for elevated jets at a velocity ratio of 2 for increasing Reynolds numbers. As the Reynolds number increases, the flow structure remains broadly similar. The upright vortices occur in each case, although they are harder to distinguish for the highest Reynolds number case. What is of interest is that for the highest Reynolds number case, periodic shedding of shear layer vortices occurs from the hovering vortex. This parallels with the flush-mounted case, although the Reynolds number above which the shedding occurs is substantially higher in the elevated case ($Re_{cf} = 5000$) than the value of 1600 reported by Kelso (1991) and Kelso *et al.* (1996) for the flush-mounted case.

For the cases of velocity ratios of 4 and 6, shown in Figure 7-35 and Figure 7-36 respectively, a definite transition between two different flow structures can be observed. At the lower Reynolds numbers the flow takes on the structure that has been found to be associated with lower velocity ratios, however as the Reynolds number is increased, the flows tend to take on the appearance of the high velocity ratio flow case. The transition for the velocity ratio 4 case occurs between the Reynolds number (based on the crossflow velocity) of 5000 and 6000. For a velocity ratio of 6 the transition occurs between Reynolds number of 667 and 1667. In addition, periodic shedding from the hovering vortex becomes more prominent as the Reynolds number is increased, again following the trend shown in the flush-mounted jet case.

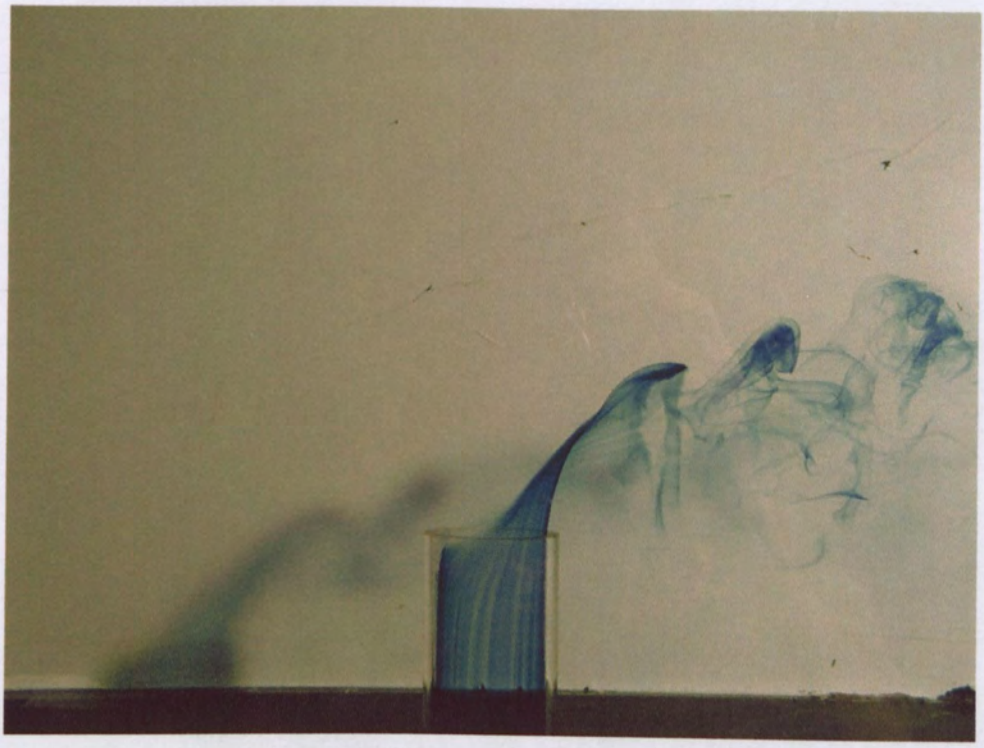

R = 2 $V_j = 0.04m/s$ $Re_j = 2000$ Re = 1000

R = 2 $V_j = 0.08m/s$ $Re_j = 4000$ Re = 2000

For caption, see following page.

R = 2 $V_j = 0.2m/s$ $Re_j = 10000$ Re = 5000

Figure 7-34 Comparison of the jet shear layer development at different Reynolds numbers for elevated jets at a velocity ratio of 2.

R = 4 V$_j$ = 0.04m/s Re$_j$ = 2000 Re = 500

R = 4 V$_j$ = 0.08m/s Re$_j$ = 4000 Re = 1000

For caption, see following page.

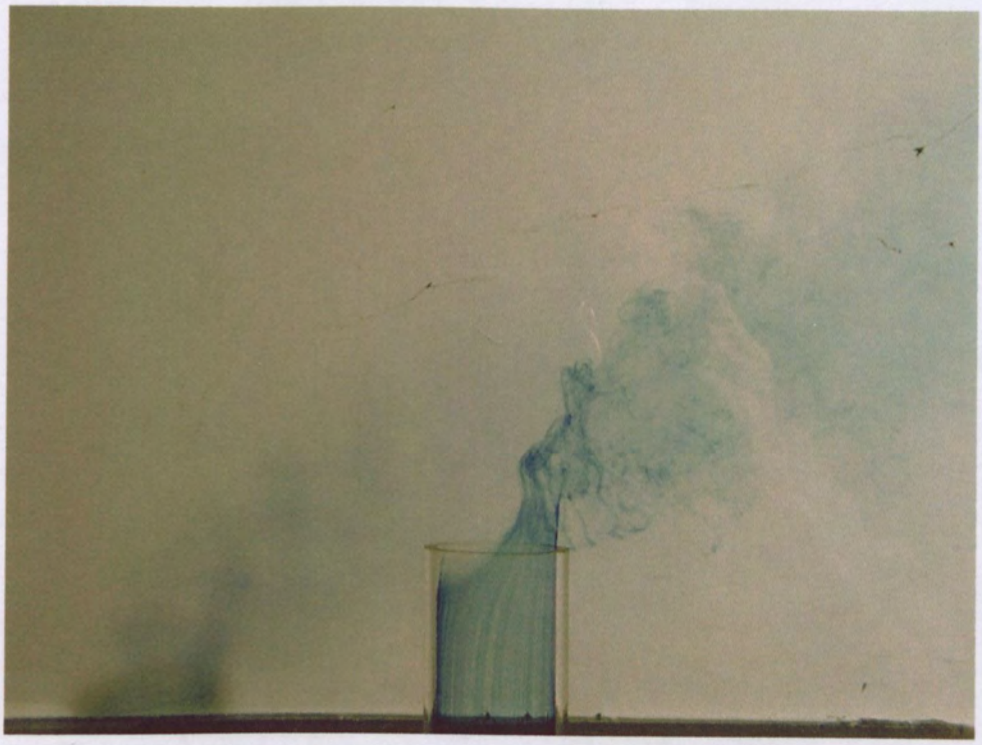

R = 4 V_j = 0.2m/s Re_j = 10000   Re = 5000

R = 4 V_j = 0.5m/s Re_j = 25000   Re = 6250

Figure 7-35 Comparison of the jet shear layer development at different Reynolds numbers for elevated jets at a velocity ratio of 4.

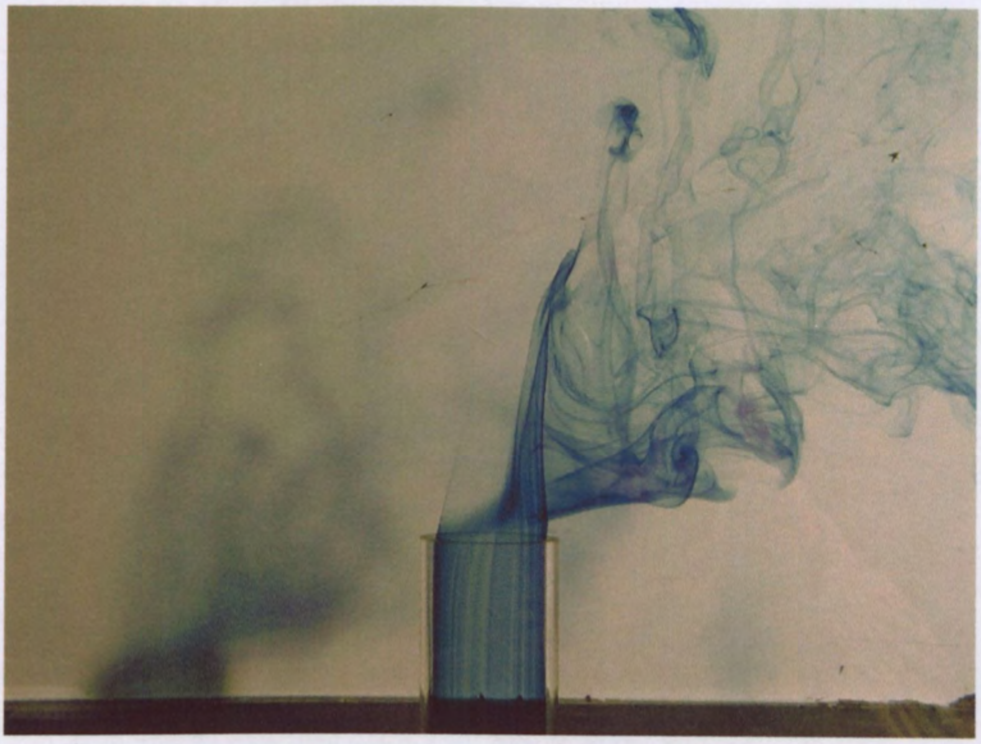

R = 6 V_j = 0.04m/s Re_j = 2000 Re = 333

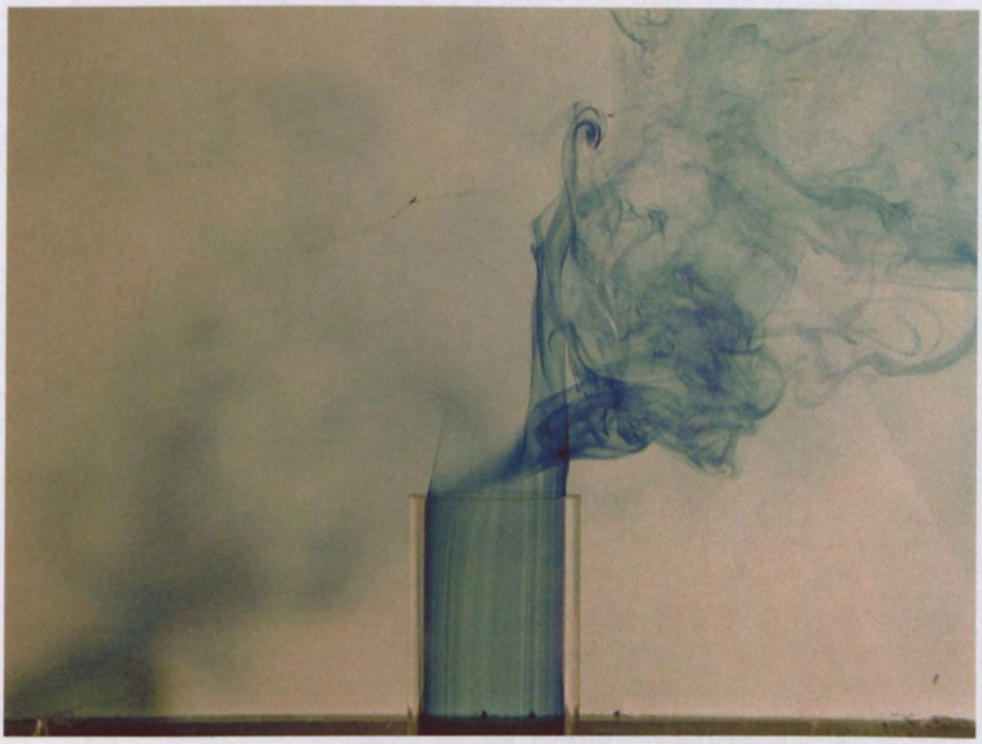

R = 6 V_j = 0.08m/s Re_j = 4000 Re = 667

For caption, see following page.

R = 6 $V_j = 0.2$m/s $Re_j = 10000$ Re = 1667

R = 6 $V_j = 0.5$m/s $Re_j = 25000$ Re = 4167

Figure 7-36 Comparison of the jet shear layer development at different Reynolds numbers for elevated jets at a velocity ratio of 6.

7.4 Flush-mounted JICF

The presence of a flat wall at the jet exit plane has a number of effects on the flow when compared with the elevated case. First, it isolates the external crossflow around the jet pipe from the jet flow, thus eliminating the external pipe boundary as a source of vorticity for the jet flow. However, an additional vorticity source is added; that of the surface of the wall itself. It is therefore necessary to specify the condition of the wall boundary layer in order to completely specify a flow case.

Examples of flush-mounted jets in crossflow at velocity ratios of 2 and 4 are shown in Figure 7-37 and Figure 7-38, respectively. In both cases the shear layer can be seen to undergo two rolling up processes. The shear layer folds along the sides of the jet forming the vortices that initiate the CVP. In addition, the large-scale self-excited roll-up of the leading edge shear layer is visible. The details of this flow have been discussed in depth by Kelso (1991), Kelso *et al.* (1996) and others.

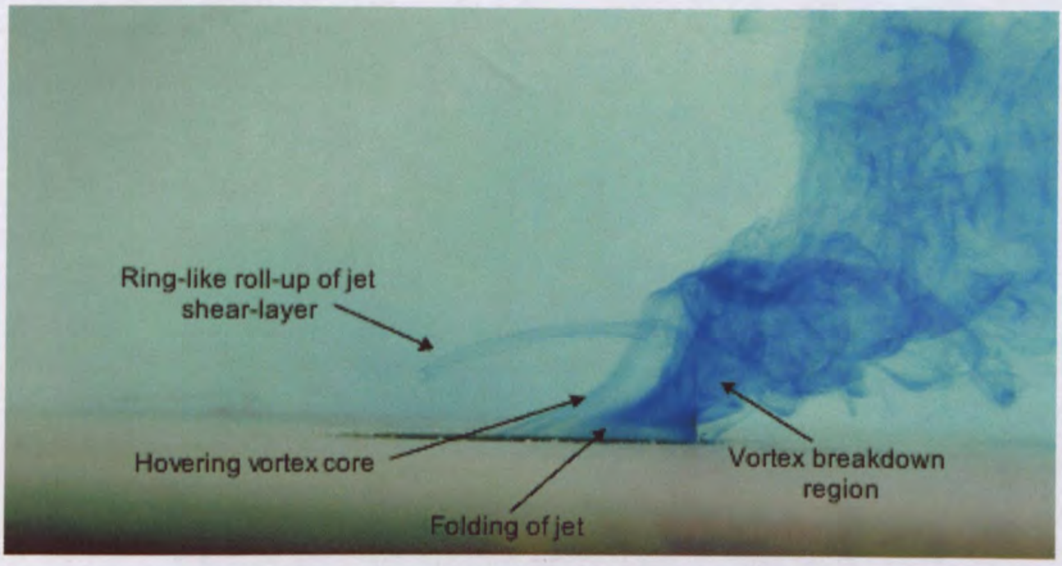

Figure 7-37 Shear layer marked by blue dye for a flush-mounted jet with a velocity ratio of 2. Re = 2000, Re_j = 4000

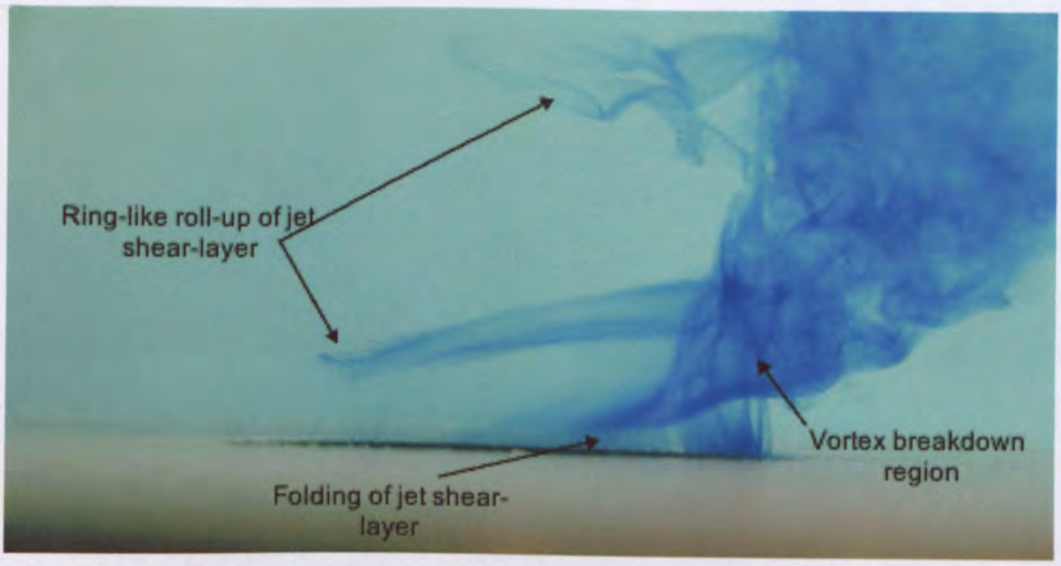

Figure 7-38 Shear layer marked by blue dye for a flush-mounted jet with a velocity ratio of 4. Re = 2000, Re_j = 8000

7.4.1 Horseshoe Vortex System

The dye trace in Figure 7-39 shows a streak of dye from an upstream dye probe that impinges on the upstream corner of the pipe exit. Some of this dye is then swept around the inside of the pipe to mark the hanging vortex on the far side of the jet. Streaklines displaced spanwise to either side of the centreline show similar behaviour. The implications of this observation are the confirmation of the existence of a separation region within the leading edge of the jet pipe, and that some of the crossflow boundary layer fluid is *not* entrained into the jet. For the case shown, R=4 and Re=2000, the wall boundary layer thickness, δ/d, was determined in Section 5.3 to be 0.3 and matched a Blasius profile. Upstream from the jet exit, the streakline shown in Figure 7-39 was located approximately 0.17d above the floor. The proportion of boundary layer circulation was therefore determined using the Blasius profile values in Table 7.1 of White (1994, p. 397). Therefore, for the current flow conditions, it was established that approximately 80% of the boundary layer circulation resides below the streakline. This result implies that the majority of the flat wall boundary layer vorticity does not interact with the upstream side of the jet, in contrast to the suggestion of Morton (1995). Instead, the circulation contributes to the horseshoe vortices or is convected around the side of the jet. Therefore, Morton's mechanism does not appear to be a significant contributor to the development of the transverse jet at this condition.

The details of the wall boundary layer flow as it approaches the jet may be seen in Figure 7-40 in which a red dye trace is injected from an upstream dye probe which is positioned closer to the wall than in Figure 7-39. As indicated in Figure 7-40 a set of steady horseshoe vortices is present upstream of the jet on the flat wall. The fluid in the horseshoe vortices is seen to convect around the jet before being drawn into the wake region of the jet. The image shown in Figure 7-41 is a composite image made up from three separate flow patterns taken at different times. The image shows the streaks of the dye introduced from different heights above the wall. These streaks are all steady ahead of the jet. An interpretation of the flow patterns in the leading edge shear layer of a flush-mounted jet is shown in Figure 7-42.

Figure 7-39 Image showing the path of dye introduced from an upstream location that impinges on the upstream corner of the jet pipe. Some dye then emerges bundled up with one of the counter-rotating vortices. R=4, Re=2000, δ/d=0.3

Figure 7-40 Dye visualisation showing the horseshoe vortex system shown with red dye. The jet shear layer is shown marked with blue dye. R=4, Re=2000, δ/d=0.3

Figure 7-41 A false colour composite image composed from three separate images showing the path of dye introduced from different heights above the floor. R=4, Re=2000, δ/d=0.3

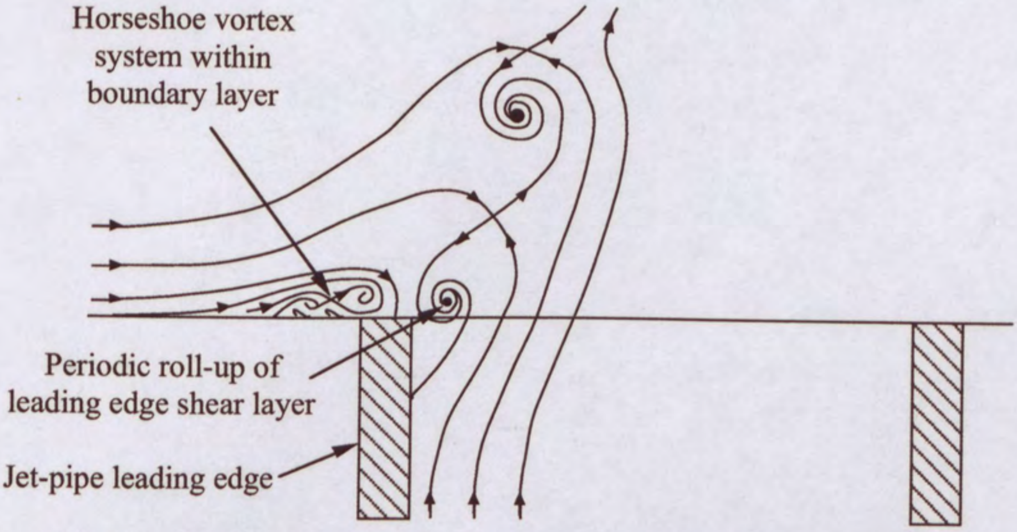

Figure 7-42 Generalised interpretation of the shear layer structure for a flush-mounted jet a the flow conditions investigated.

7.5 Comparison of the Flush and Elevated Jet Flow Cases

The images in Figure 7-43 allow a comparison to be made between the shear layer development of the elevated and flush-mounted cases. The images on the left hand side show the elevated jet cases, whereas the corresponding images on the right show the flush-mounted jets at the same flow conditions. A reference line has been added to each image to indicate the exit plane of the jet. In each case the crossflow Reynolds number was 2000 and the jet velocity was changed to produce the different velocity ratios. The images allow a comparison to be made both between the elevated and flush-mounted jets and the variation of each case for different velocity ratios at a single crossflow Reynolds number. The images presented for the flush-mounted cases show strong agreement with the similar flow patterns published in Figure 5 and Figure 6 of Kelso *et al.* (1996) for jets with a Reynolds number (based on the crossflow velocity) of 1600 at velocity ratios of 2.2, 4.0 and 5.5.

Comparing the two flow cases for the three velocity ratios presented indicates that for the two lower velocity ratio flows, R=2 and R=4, there is a substantial difference in the jet shear layer development between the flush and elevated flow cases. The difference in the flow structure would suggest a reason for the differences in the mixing rates and trajectories observed in the results in Chapter 5. For the flush-mounted case the large-scale self-excited roll-up of the leading edge jet shear layer and the formation of hanging vortices on the side of the jet are evident. However, in the elevated case neither of these flow features are evident. Instead, the shear layer is folded into the large recirculation zone discussed previously and the leading edge shear layer rolls up by a Kelvin-Helmholtz instability.

As discussed previously, the development of the shear layer of the elevated jet with a velocity ratio of 6 is different to the lower velocity ratio cases. However, what is now apparent from Figure 7-43, is the similarity between the shear layer development of the flush and elevated cases at this velocity ratio and Reynolds number. The flow looks distinctly different from the lower velocity ratio elevated cases and, instead, has the appearance of a flush-mounted jet.

R=2 elevated

R=2 flush

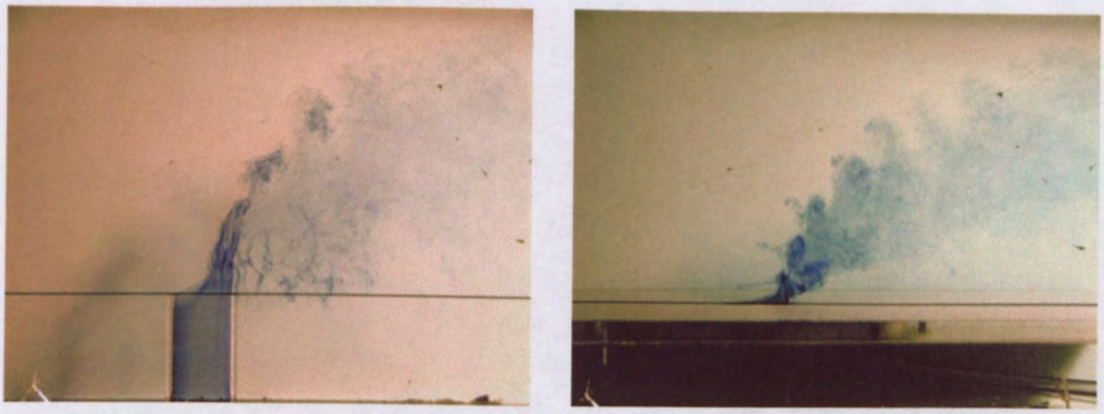

R=4 elevated

R=4 flush

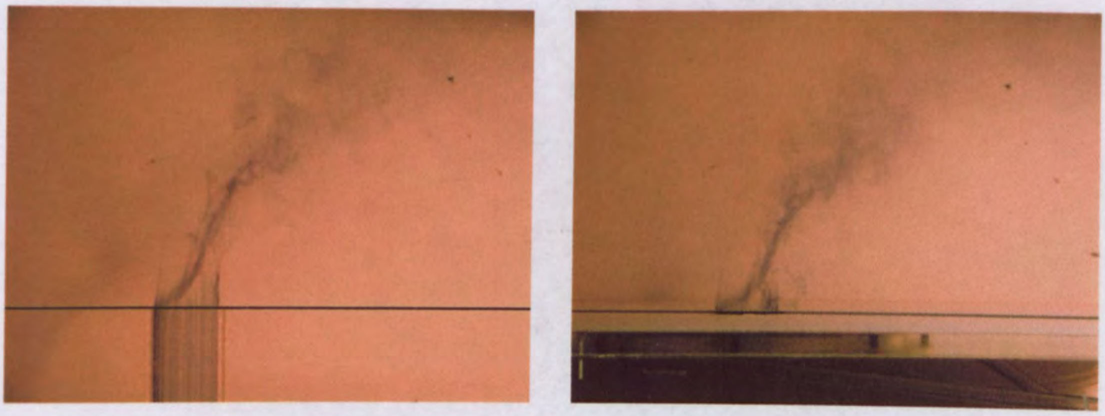

R=6 elevated

R=6 flush

Figure 7-43 Dye visualisation of the jet shear layer. Dye was bled into the jet shear layer from the circumferential dye slot positioned 4 jet diameters upstream of the jet exit. The images on the left correspond to the elevated jet case, and the images on the right to the flush-mounted case. Re=2000, Re_j = 4000, 8000 & 12000 for R = 2, 4 & 6 respectively

The differences in the leading edge shear layer structure and trajectory of the jets may, in part, be attributed to the differences in trajectory of the crossflow fluid approaching the jet. To show this difference a hydrogen bubble wire was positioned on the jet plane of symmetry upstream from the jet exit. The resulting bubble sheet patterns are shown in Figure 7-44 and Figure 7-45 for the elevated and flush-mounted jet cases, respectfully. As can be seen in the elevated jet case, the presence of the jet causes the approaching crossflow to rise in the direction of the jet. The rising flow is also evident in Figure 7-46 which shows a close-up view of the flow near to the jet exit. This may lead to the occurrence of the large-scale ring-like roll-up of the shear layer being delayed compared with the flush-mounted case. The elevated jet shear-layer appears to roll-up by a Kelvin-Helmholtz mechanism, beginning with a small instability near the jet exit and growing to large-scale eddies approximately 3 diameters from the exit. By contrast, the flush-mounted jet has a horizontal approaching stream and the shear layer in this case appears to roll-up within the pipe exit.

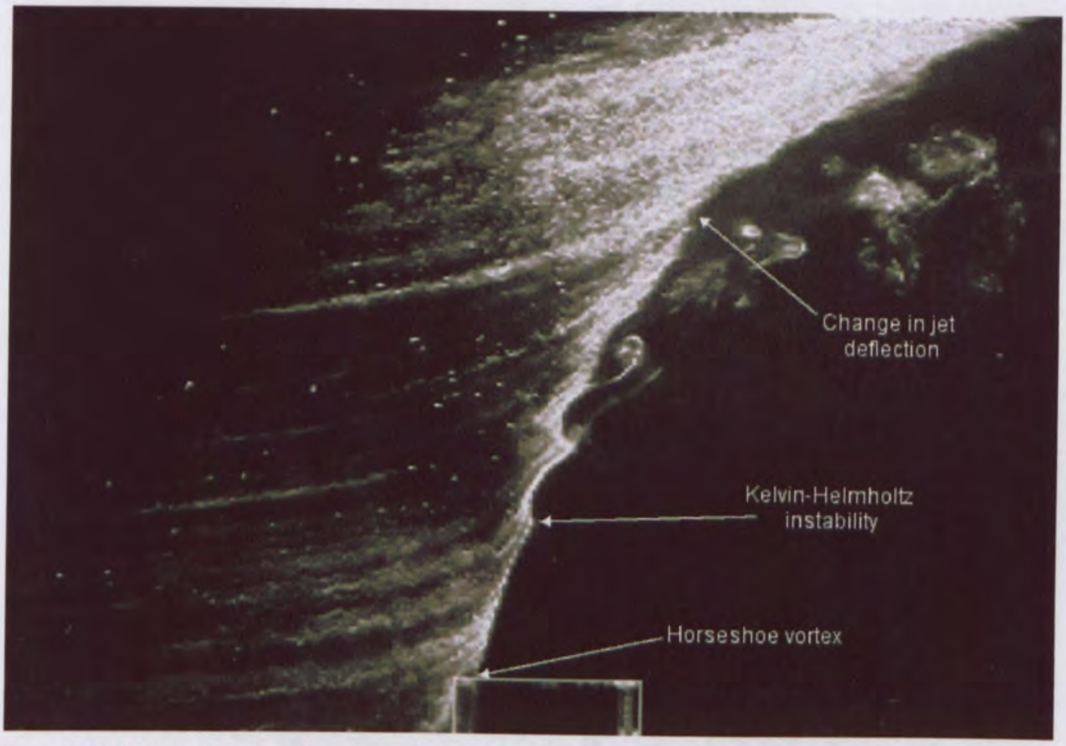

Figure 7-44 Bubble sheet produced from a vertical bubble wire mounted on the jet plane of symmetry for an elevated jet. Re=2000, Re_j=4000, R=2.

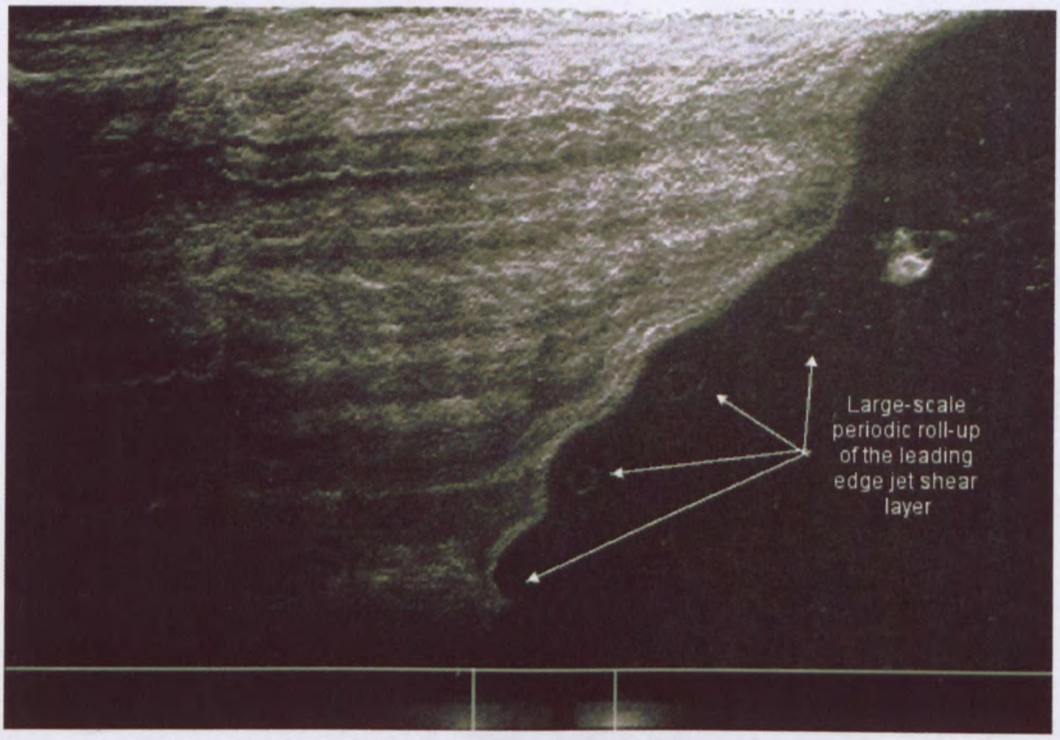

Figure 7-45 Bubble sheet produced from a vertical bubble wire mounted on the jet plane of symmetry for a flush-mounted jet. Re=2000, Re_j=4000, R=2.

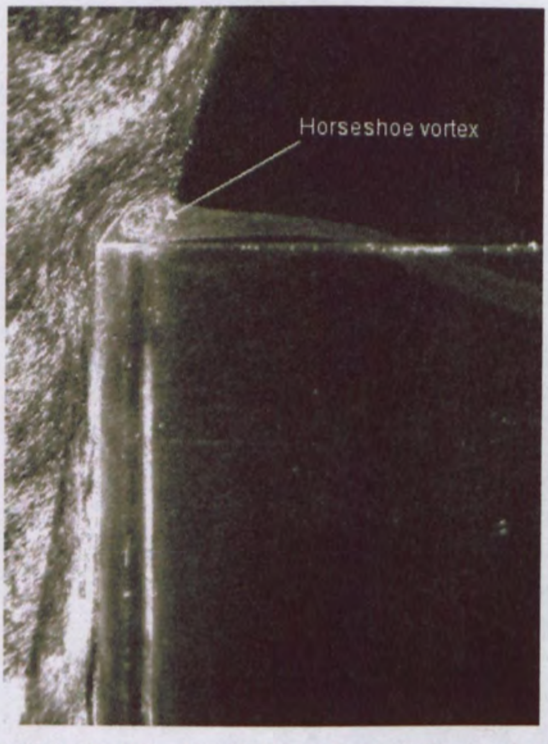

Figure 7-46 Close-up view of the leading edge of the jet pipe focusing on the leading edge vortex. The image was produced using a hydrogen bubble wire upstream of the jet pipe on the jet centreline.

In Figure 7-47 the same flow cases as in Figure 7-43 are shown but viewed from above the jet exit. Here the jet is marked by dye introduced from the circumferential slot. As noted earlier, the dye is swept to the downstream side of the jet. The location where the shear layer folds to initiate the hanging vortices is indicated by the location where the dye appears to emerge from the sides of the jet exit. From this view it is also evident that the structure of the flow is different for the two lower velocity ratio cases but similar for the higher velocity ratio case. For the elevated jet at a velocity ratio of 2 and 4 the upright vortices on either side of the jet are visible. The rolling up of the lee side jet shear layer linking the upright vortices is also clearly evident for the flow at a velocity ratio of two.

Although the details of the flow within the jet pipe are not visible due to the darkness of the jet hole, it is possible to see the position at which the hanging vortices begin to roll-up on the sides of the jet. In the flush-mounted jet case the azimuthal location on the jet exit plane at which this occurs moves from positions toward the downstream side of the jet closer to the lateral edges of the jet for increasing velocity ratios. This is in agreement with observations by Kelso *et al.* (1996). For the elevated jet, however, the hanging vortices appear to emerge from the jet pipe at a similar location for every velocity ratio. It should also be noted that although the elevated and flush jet flow structures at R=6 appear very similar when viewed from the side (Figure 7-43), the location where the hanging vortices emerge when viewed from above (Figure 7-47) is actually slightly different.

Another comparison between the shear layer development of the flush and elevated flow cases is shown in Figure 7-48. The top images in the figure compare the elevated and flush-mounted jets for a velocity ratio of 4. In this case the elevated jet displays the features previously observed for the elevated flow case. At this flow condition the elevated and flush-mounted jets are quite different in appearance. The two bottom images show the two flow cases at a slightly higher velocity ratio of approximately 4.5 and here the elevated jet is very similar in appearance to the flush-mounted jet.

In Figure 7-49 the same flow conditions as in Figure 7-48 are shown but the entire jet has been marked with red dye. The jet shear layer is again marked with blue dye (except in the R=4 flush case) as a reference to the flow shown in Figure 7-48. Again the appearance of the flows at the lower velocity ratio is different for the flush and elevated cases. The main difference in the jet structure is in the leading edge shear layer development. A large-scale roll up of the leading edge jet shear layer occurs close to the jet exit for the flush-mounted case. For the elevated case, the leading edge shear layer roll-up occurs by a Kelvin-Helmholtz type instability further downstream from the jet exit. The flow structure in these two cases is in agreement with the flow structure observed in the mixing and structural studies undertaken in Chapter 5. At the higher velocity ratio, the development of the leading edge shear layer is similar for both the flush and elevated cases (although this is not clearly shown in the images). The fact that, for the elevated jet case, changes in the leading edge of the jet coincide with the difference in the development of the jet shear structure adds further evidence to a connection between the two.

Note that (as shown in Figure 7-49) the R=4 elevated jet has a higher trajectory than the flush-mounted jet. This implies that the elevated jet has a lower overall mixing rate than the flush-mounted jet. By contrast, for R≈4.5 the two jets have similar trajectories. This implies similar overall mixing rates. Further this suggests that the R=4 to R≈4.5 structural transition causes an increase in mixing.

The flow structures shown in Figure 7-49 are shown again in Figure 7-50, this time viewed from above the jet exit. From this view, differences are apparent between the elevated and flush-mounted flow cases for both velocity ratios. For the flush-mounted jet cases, the region of marked fluid appears be separated into two halves either side of the jet's plane of symmetry. This may provide another indication of the jet fluid being entrained into concentrated CVP vortices. This is more obvious in the higher velocity ratio case, where a region with a low concentration of dye can be observed on the jet plane of symmetry. For the elevated jet case the jet (orange) fluid envelope is similar in both cases. However, even though the spreading of the jet is similar, the shear layer fluid (blue) shows markedly different behaviour.

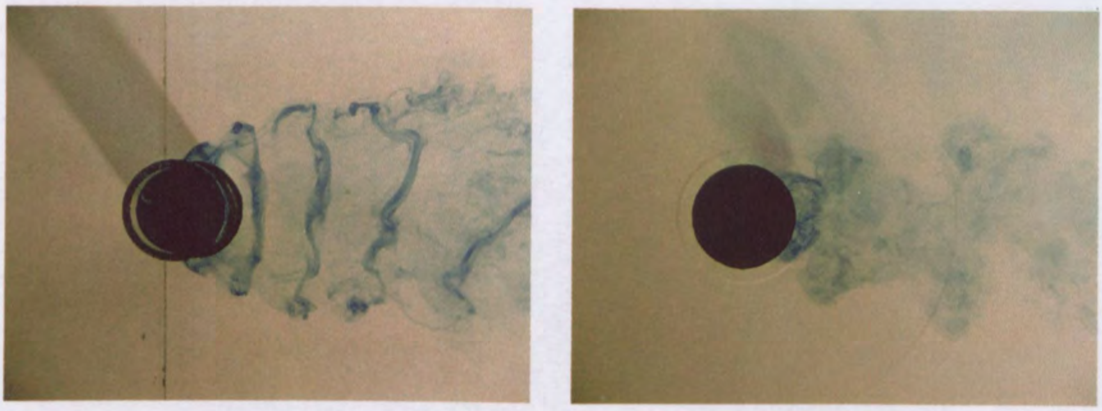

R=2 elevated

R=2 flush

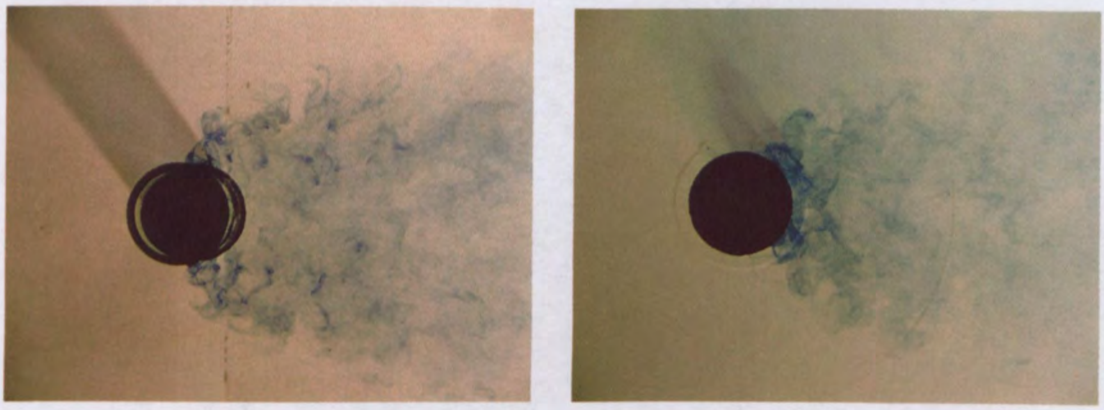

R=4 elevated

R=4 flush

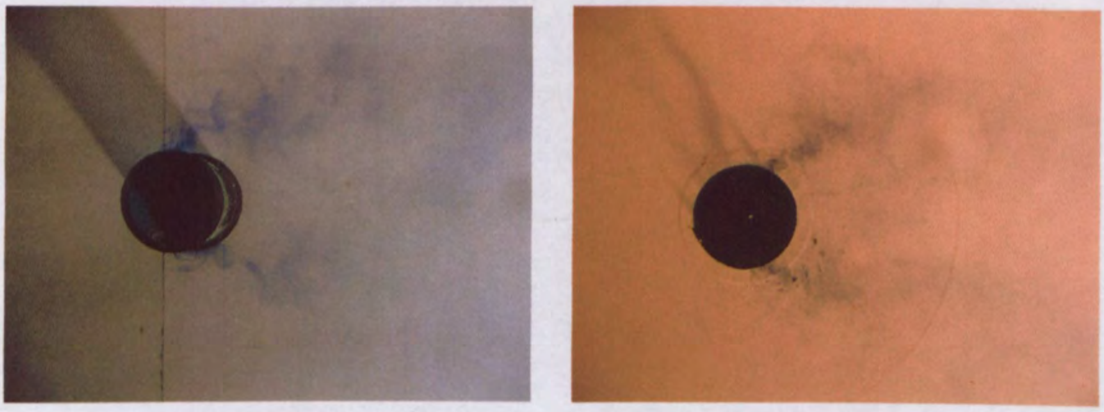

R=6 elevated

R=6 flush

Figure 7-47 Dye visualisation of the jet shear layer, as in Figure 7-43 except the flow is viewed from above the jet exit. Dye was bled into the jet shear layer from the circumferential dye slot upstream of the jet exit. The images on the left correspond to the elevated jet case, and the images on the right to the flush-mounted case. Re=2000, Re_j = 4000, 8000 & 12000 for R = 2, 4 & 6 respectively

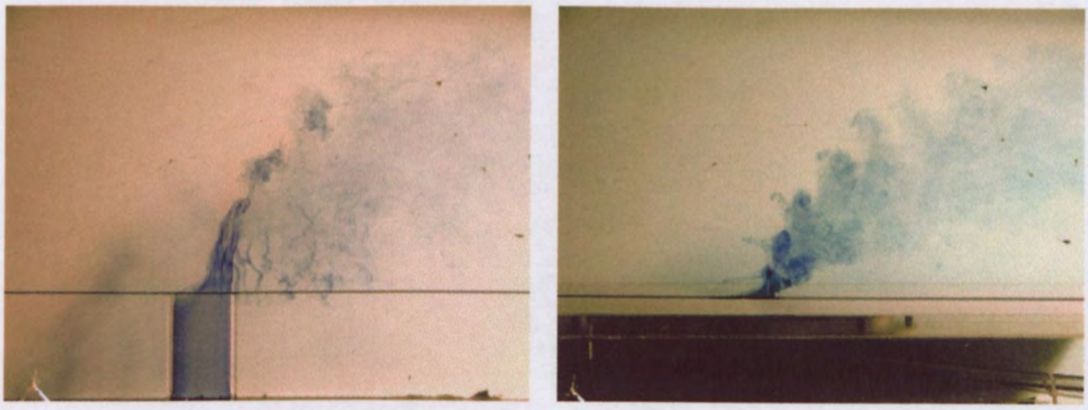

R=4 elevated

R=4 flush

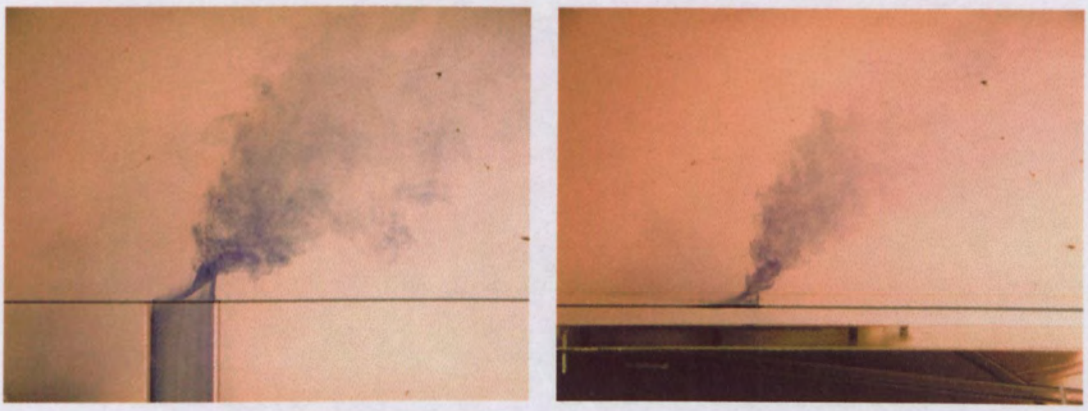

R≈4.5 elevated

R≈4.5 flush

Figure 7-48 Dye visualisation of the jet shear layer. Dye was bled into the jet shear layer from the circumferential dye slot positioned upstream of the jet exit. The images on the left correspond to the elevated jet case, and the images on the right to the flush-mounted case. Re=2000

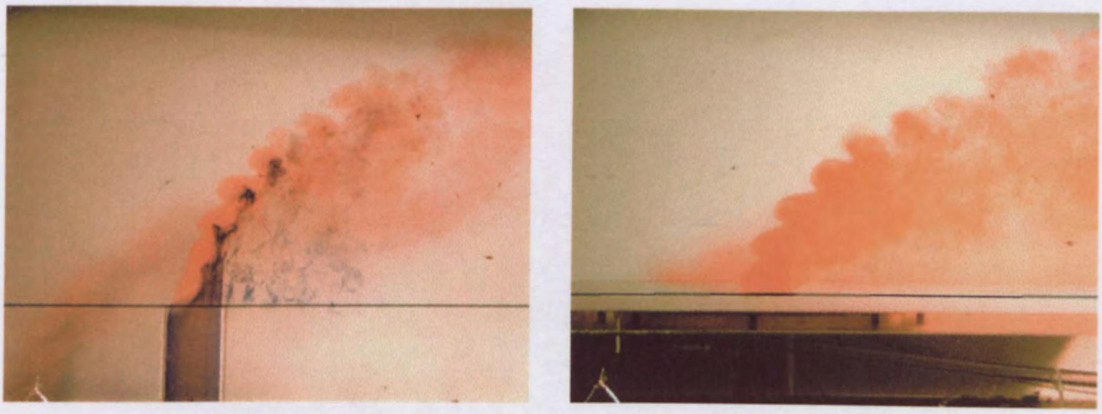

R=4 elevated

R=4 flush

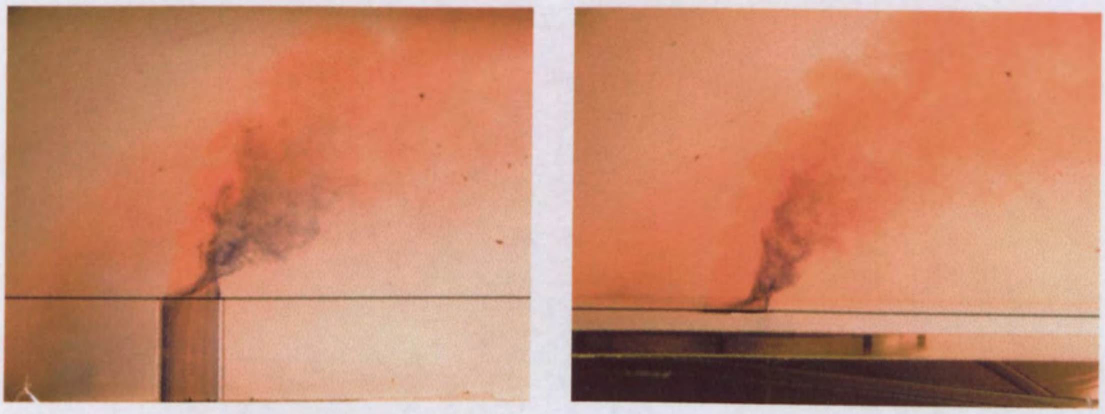

R≈4.5 elevated

R≈4.5 flush

Figure 7-49 Dye visualisation of the jet shear layer. Blue dye was bled into the jet shear layer from the circumferential dye slot positioned upstream of the jet exit while the entire jet fluid was marked with red dye. The images on the left correspond to the elevated jet case, and the images on the right to the flush-mounted case. Re=2000

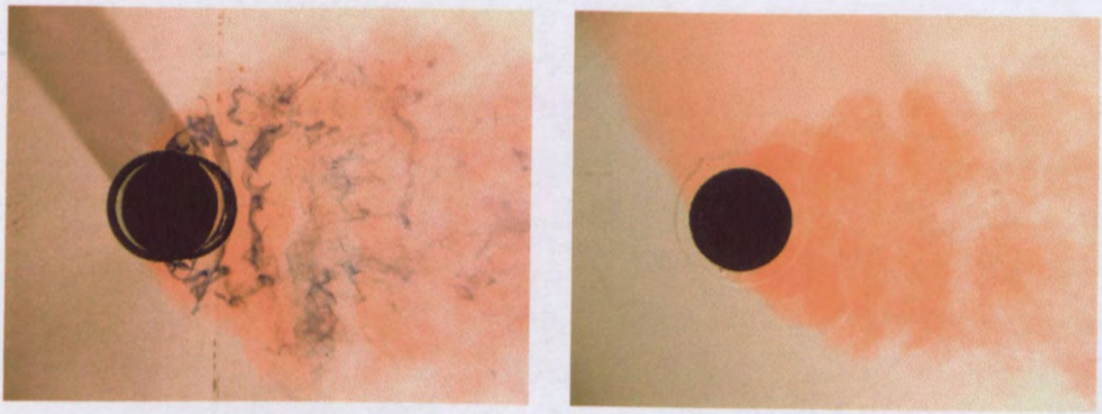

R=4 elevated

R=4 flush

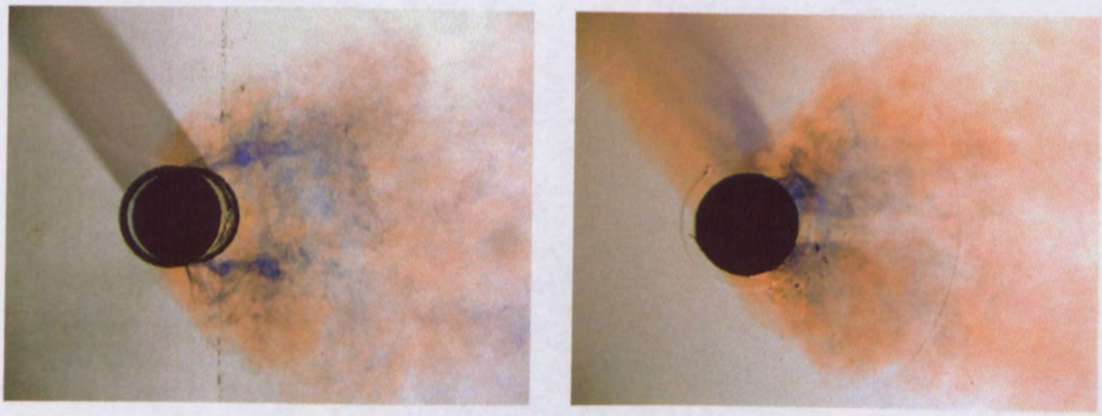

R≈4.5 elevated

R≈4.5 flush

Figure 7-50 Dye visualisation of the jet shear layer. Blue dye was bled into the jet shear layer from the circumferential dye slot positioned upstream of the jet exit while the entire jet fluid was marked with red dye. The images on the left correspond to the elevated jet case, and the images on the right to the flush-mounted case. Re=2000

7.5.1 External Flow Topology

Although there are differences in the structure between the flush and elevated jets, many similarities exist between the flow topologies of the two cases. In Figure 7-51 a streamline pattern constructed by Kelso (1991) for a flush-mounted jet is reproduced. The top half of the pattern corresponds to the jet plane on the axis of symmetry and the lower half corresponds to the channel floor. By examining the external flow on the jet pipe, the features of the flow shown in the flush-mounted case were observed in the elevated case, although there were differences. The flow pattern for the case of an elevated jet at a velocity ratio of 2, and jet Reynolds number of 4000 is shown in Figure 7-52. The pattern was constructed from detailed observations of dye traces introduced by a dye probe and by dyed toothpaste placed on the pipe's exterior surface. A three-dimensional streamsurface representation of the flush-mounted case constructed by Kelso (1991) is shown in Figure 7-53. This shows that the vortices on the wall extended upwards. In the elevated case, similar vortices exist on the external surface of the jet pipe and these vortices extend approximately horizontally in the direction of the crossflow from the downstream side of the jet. Note that the details of the elevated pipe pattern are different from the details of the flush jet pattern. Whereas the flush jet pattern contained two vortices of the same direction of circulation, the elevated jet shows a vortex pair of opposing signs.

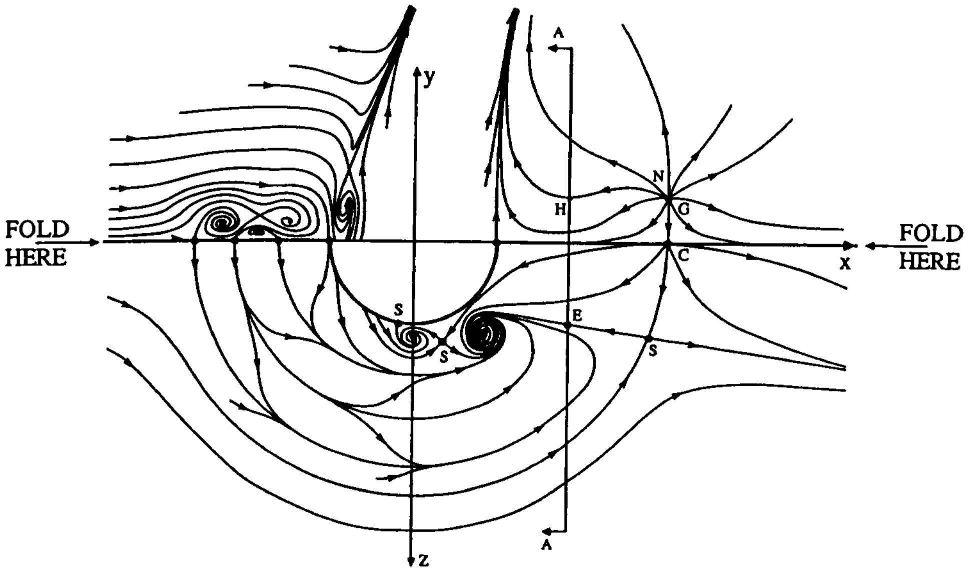

Figure 7-51 Streamline pattern for flush-mounted jet at a velocity ratio of x. The top half of the pattern corresponds to the xy plane on the jet axis of symmetry and the lower half of the pattern to the xz plane on the floor (reproduced from Kelso 1991)

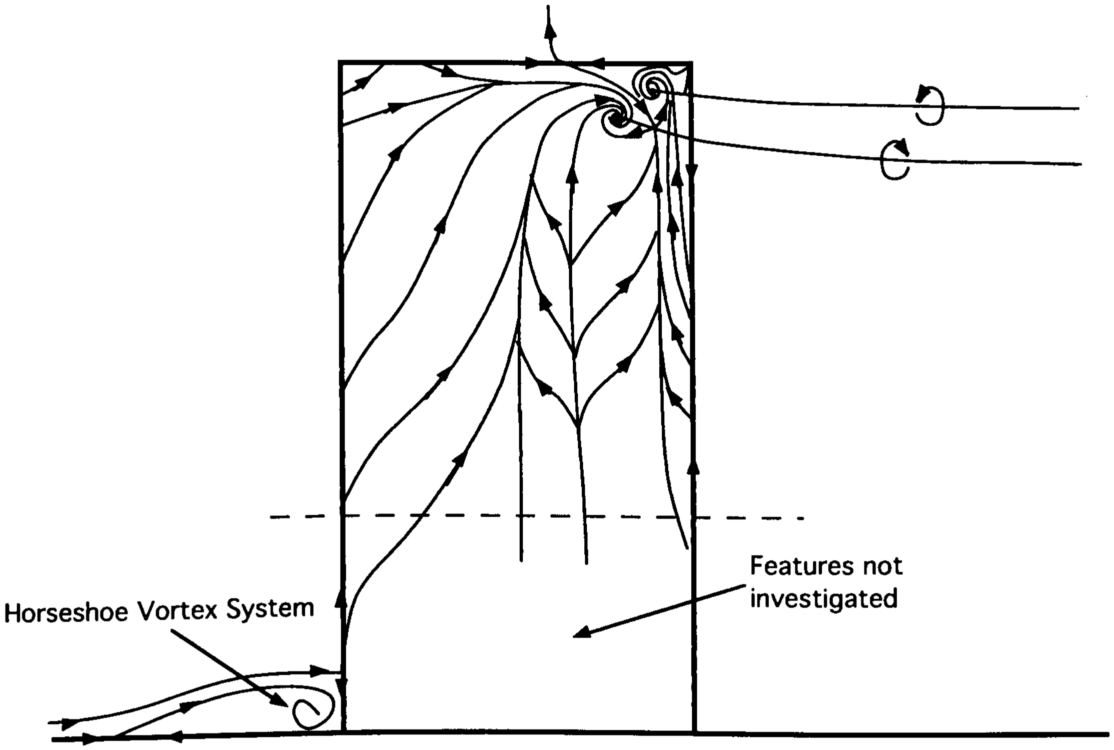

Figure 7-52 Streamline pattern, based on the flush-mounted jet topology, for an elevated jet at a velocity ratio of 2, and jet Reynolds number of 4000

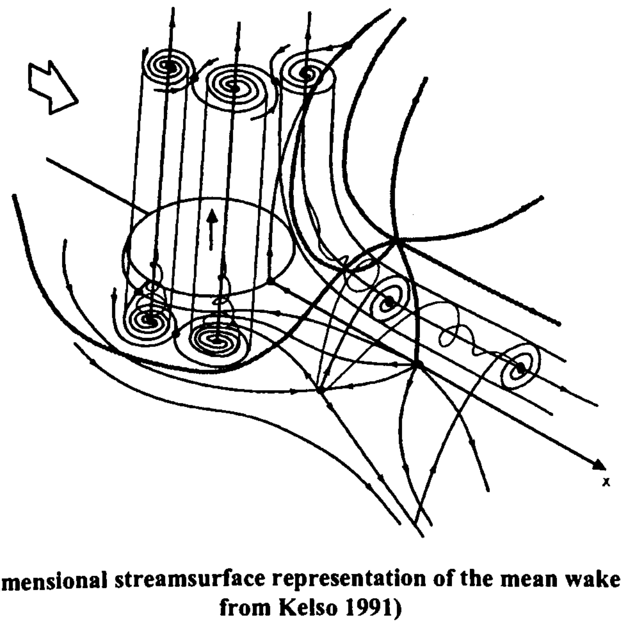

Figure 7-53 Three-dimensional streamsurface representation of the mean wake pattern (reproduced from Kelso 1991)

7.6 Conclusions

The findings from the dye visualisation of the flow cases investigated suggest that there are two stable structures of the elevated jet in crossflow. The structure of the flow is dependent both on the velocity ratio and the Reynolds number. At lower velocity ratios and Reynolds numbers the flow structure consists of upright vortices formed along the sides of the jet and the presence of a large recirculation zone downstream of the jet. At higher velocity ratios and Reynolds numbers the sides of the jet roll up into concentrated vortices and the large-scale roll-up of the leading edge jet shear layer is more likely to occur. The structure of the flow is similar in appearance to that of the flush-mounted JICF. These results are summarised in Figure 7-54 which shows the various flow characteristics that occur, depending on the velocity ratio and crossflow Reynolds number. The same results are shown in Figure 7-55 for the velocity ratio against jet Reynolds number. Dotted lines on the plots are shown passing through the two transitional cases. These lines represent a boundary between the two flow cases, however, their exact shape is as yet unknown.

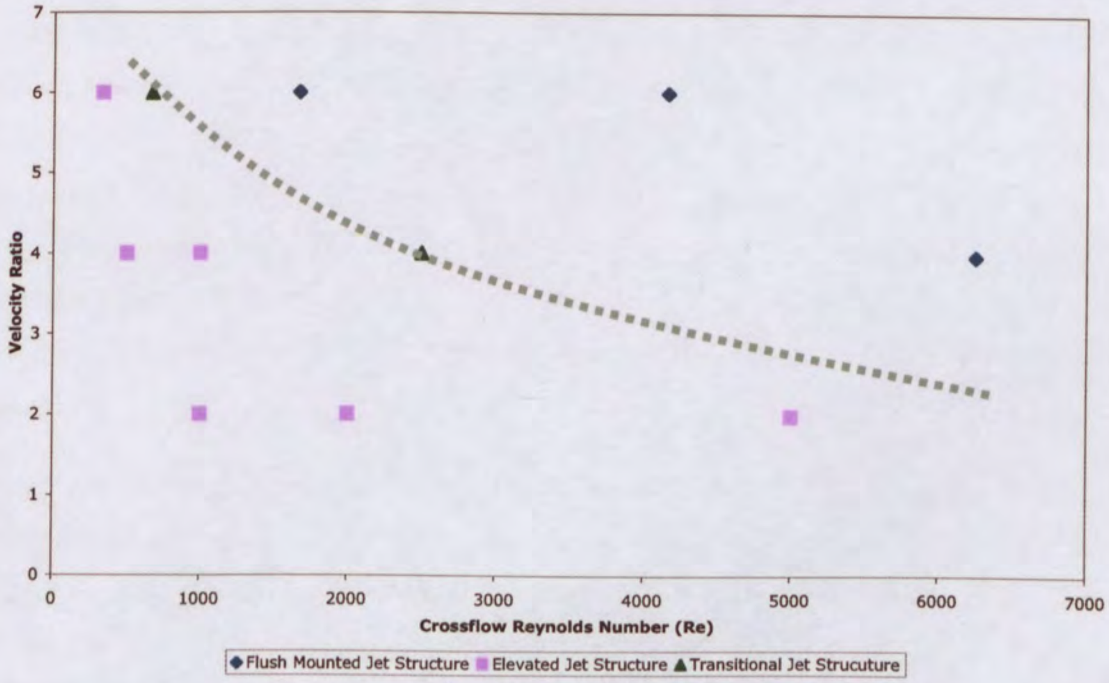

Figure 7-54 Graphical summary of the velocity ratio / crossflow Reynolds number dependence on the elevated jet structure.

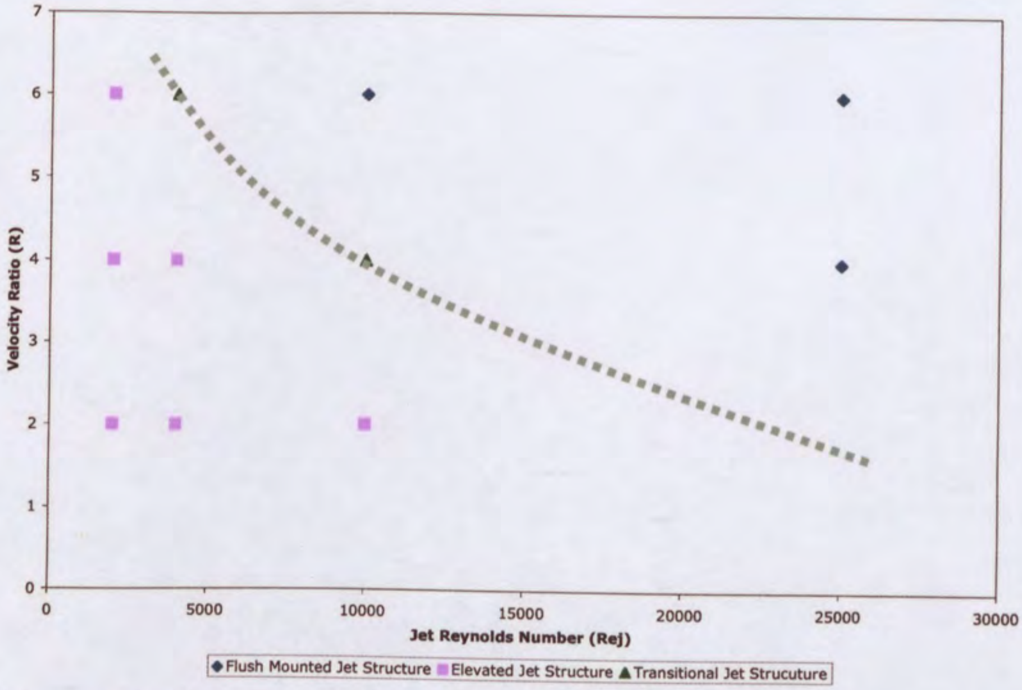

Figure 7-55 Graphical summary of the velocity ratio / jet Reynolds number dependence on the elevated jet structure.

In Chapter 5 it was shown that there was a difference in the mixing rate between elevated and flush-mounted jets at the same flow conditions. The results of the flow visualisation in the current chapter have shown that at the velocity ratios selected to undertake the mixing study there was a significant difference in the structure of the two flow cases. The combination of these findings is that for flows with Reynolds number and velocity ratios beneath the dotted lines (shown in Figure 7-54 and Figure 7-55) a flush-mounted jet provides enhanced mixing compared with an elevated jet. This suggests that, if it is required to increase the mixing rate of an elevated jet at these flow conditions, a flat wall could be installed flush with the jet exit to change from an elevated jet to a flush-mounted jet.

In addition, although it has not been directly tested in the current work, the similar overall structure of elevated jets above the structural transition (above the dotted lines shown in Figure 7-54 and Figure 7-55) to the flush-mounted cases, suggest the mixing rate may also be similar. Therefore, increasing either the velocity ratio or Reynolds number of a flow in order to position it above the structural transition condition may also increase the mixing rate.

8 Discussion and Conclusions

The work undertaken in the current thesis investigated two cases of a single round jet in crossflow; that of a flush-mounted jet and an elevated jet. The work focussed on the flows at velocity ratios of 2 and 4, however, other ratios including 0.5, 6 and 8 were also studied. The majority of the work was undertaken at a crossflow Reynolds number of 2000, although a range of values from 333 to 6250 were covered. The jet Reynolds numbers covered the range from 2000 to 25000.

1. Details of elevated jets identified for the first time.

The work presented in the current thesis has provided further evidence of the complexity of the transverse jet flow. The main focus of the work was to provide a detailed comparison between elevated and flush-mounted transverse jets with the same initial conditions; the difference between the two flow cases being the presence or absence of a wall at the exit plane of the jet. As part of this work, the structure of elevated jets in crossflow was examined in detail for the first time. A significant finding from this examination was that elevated jets in crossflow form one of two distinct structures depending on the velocity ratio and Reynolds number of the flow. The transition between the different structures was found to occur at certain values of R and Re. The low R/Re elevated jet case was characterised by the formation of upright vortices in the lateral edges of jet shear layer that were connected to the roll-up of the lee side jet shear layer. The appearance of the elevated jet at this flow condition was quite different to that of a flush-mounted jet at the same flow conditions. However, elevated jets at the high R/Re flow condition appeared very similar to flush-mounted jets at the same initial conditions.

The difference in structure between the low R/Re and high R/Re elevated jets resulted in differences in the trajectory and lateral spreading of the jet. It was established that the low R/Re elevated jet penetrates further into the crossflow than a flush-mounted jet at the same flow conditions. By contrast, the trajectories for high R/Re elevated jets were shown to appear similar to equivalent flush-mounted jets.

2. Structure/topology identified for both elevated and flush-mounted jets.

The detailed dye visualisation of elevated jets in crossflow allowed the examination of the flow structures within the jet pipe to be undertaken. From this work the existence of multiple hovering vortices was found within the leading edge of the jet pipe, upstream and close to the plane of the jet exit. In addition, by inspection of the location of the hovering vortices, and the fold in the lateral edge of the jet shear layer which forms the hanging vortices leading to the CVP, it was established that the hovering vortices represent the inception of the CVP.

In the experiments undertaken in the current thesis it was shown that the leading edge shear layer rolls up by one of two different mechanisms depending on the flow conditions, as established by Kelso (1991) and Kelso *et al.* (1996). At the flow conditions used in the current work, the leading edge shear layer of the flush-mounted jet rolled up by a large-scale periodic instability, close to or within the jet pipe. However, it was found that for elevated jets, at the same flow conditions, the roll-up of the leading edge shear layer occurred by a Kelvin-Helmholtz instability mechanism, beginning as a small disturbance in the shear layer which grew as the jet progressed downstream. It was found that the large-scale periodic roll-up of the leading edge shear layer did occur for the elevated jet, but the Reynolds number and velocity ratios at which this occurred where higher than for the flush-mounted jet. The reason for this was suggested to be the fact that the crossflow approaching the elevated jet is generally rising, resulting in a decrease in the velocity gradient across the leading edge shear layer.

An interesting effect was found for the elevated and flush-mounted flow cases at a velocity ratio of 0.5, in which the leading edge shear layer rolled-up to form wake-like vortices. Here a large-scale periodic roll-up of the leading edge shear layer occurred for the elevated jet, but the leading edge shear layer of the flush-mounted jet rolled-up by a Kelvin-Helmholtz type mechanism. This trend is opposite to that observed in the R=2, 4 and 6 flow cases.

3. A new model for the shear layer roll-up.

The shear layer structure of the elevated and flush-mounted jets is described in a series of interpretations in Figure 8-1 to Figure 8-3. These interpretations are based on the hydrogen bubble visualisation of the vortex lines in the pipe shear layer (Section 7.3.2), the dye visualisation images of the elevated and flush jets (Section 7.5) and the volume visualisation images (Section 6.2.1). In order to facilitate direct comparison with the interpretations of Lim *et al.* (2001) the interpretations have been presented using a similar format.

Figure 8-1 shows an interpretation of the flush-mounted jet and elevated jet (high R/Re) flow cases. It is proposed that the patterns for these two flow cases are essentially the same. The pattern shows the leading edge and trailing edge shear layer roll-ups to consist of loops that span the leading and trailing sides of the jet respectively and merge with the CVP. The leading and trailing edge roll-ups are depicted as separate structures - loops, not rings - that can roll-up in lock-step, but do not share vortex lines. To simplify the pattern the hovering vortices are not shown. They can be expected to merge with the CVP in the same way as do the leading edge shear layer roll-ups. Figure 8-2 shows a cut-away view of the same flow to aid in the understanding of this mechanism. Again, the hovering vortices are not shown. The underlying assumption that leads to this interpretation is that the "vertical vortices" shown in Section 6.2.1 are the vertical legs of trailing-side vortex loops, similar to those identified in the low R/Re elevated jet cases (Section 7.3.2).

Figure 8-3 shows an interpretation of the low R/Re elevated jet case where the leading edge shear layer rolls up by a Kelvin-Helmholtz mechanism. This pattern bears a strong similarity to the flow visualisation patterns in Section 7.3.4, where it can be seen that there is a large-scale periodic roll-up on the trailing edge of the jet, and a Kelvin-Helmholtz roll-up of the leading edge shear layer. This illustrates the independence of the roll-ups on the leading and trailing edges of the shear layer. Here the cores of the CVP are shown to be almost horizontal, similar to the observed behaviour. Comparison of the cross-sectional pattern in Figure 8-3 with Figure 5-21 and Figure 5-40 show some similarities in the vertical alignment of the regions of high dye concentration. A PLIF image of an elevated JICF taken through the plane aligned with the internal trailing edge of the jet pipe, is shown in Figure 8-4. The features shown provide strong support for the suggested model. The large recirculation zone observed downstream of the jet (Section 7.3.2) is also compatible with the envelope formed by the shear layer depicted in this model.

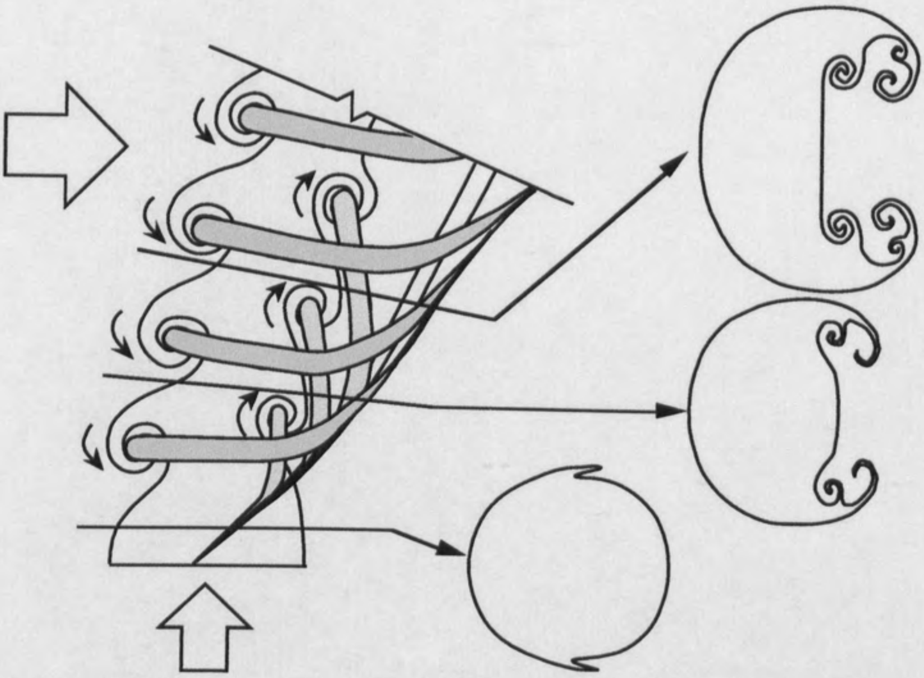

Figure 8-1 Interpretation of the shear layer roll-up of the high R/Re elevated and flush-mounted jets in crossflow.

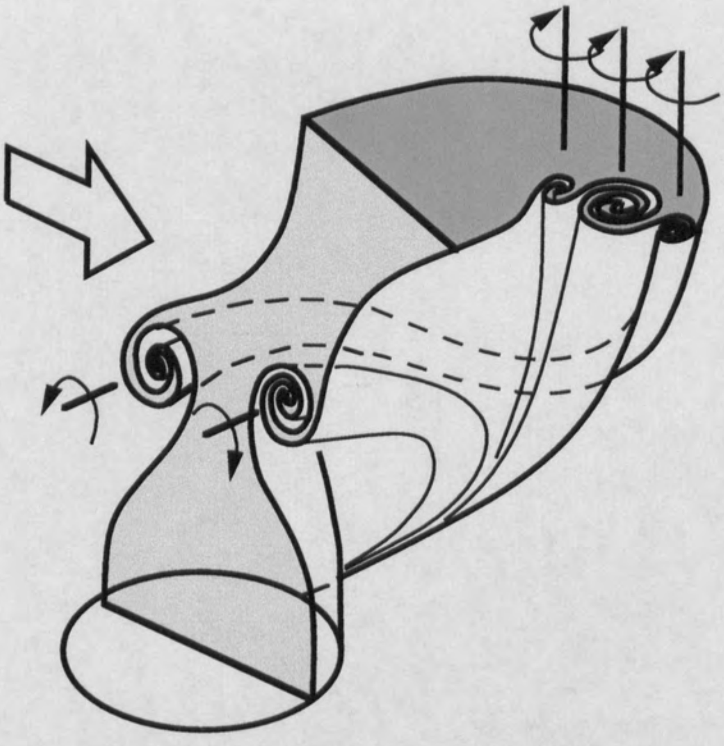

Figure 8-2 Cut-away view of the flow structure presented in Figure 8-1.

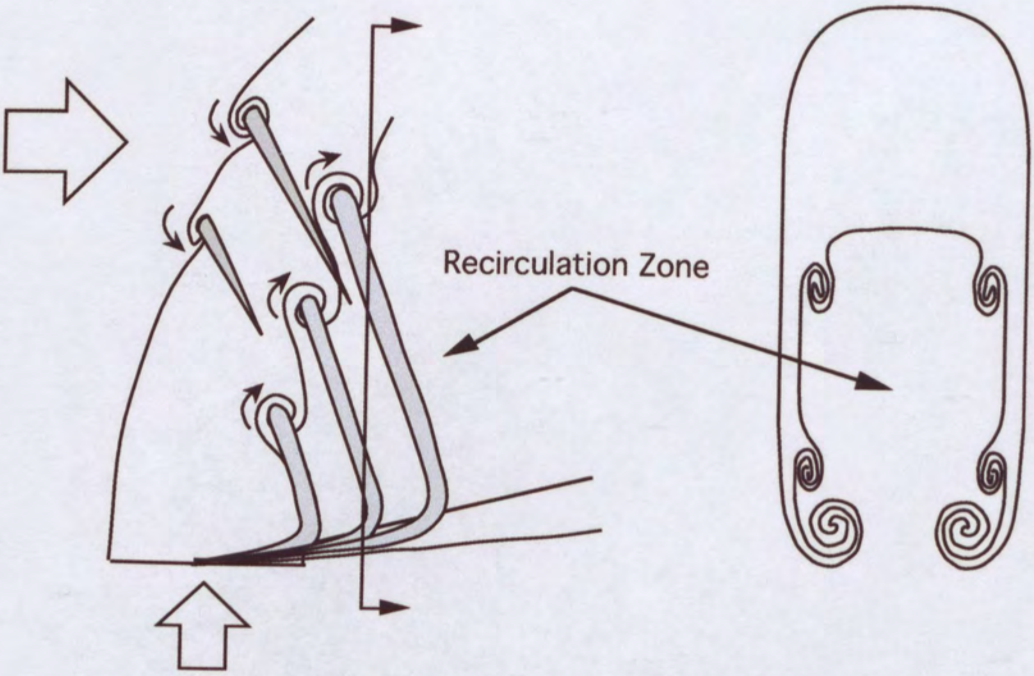

Figure 8-3 Interpretation of the shear layer roll-up of the low R/Re elevated jets in crossflow.

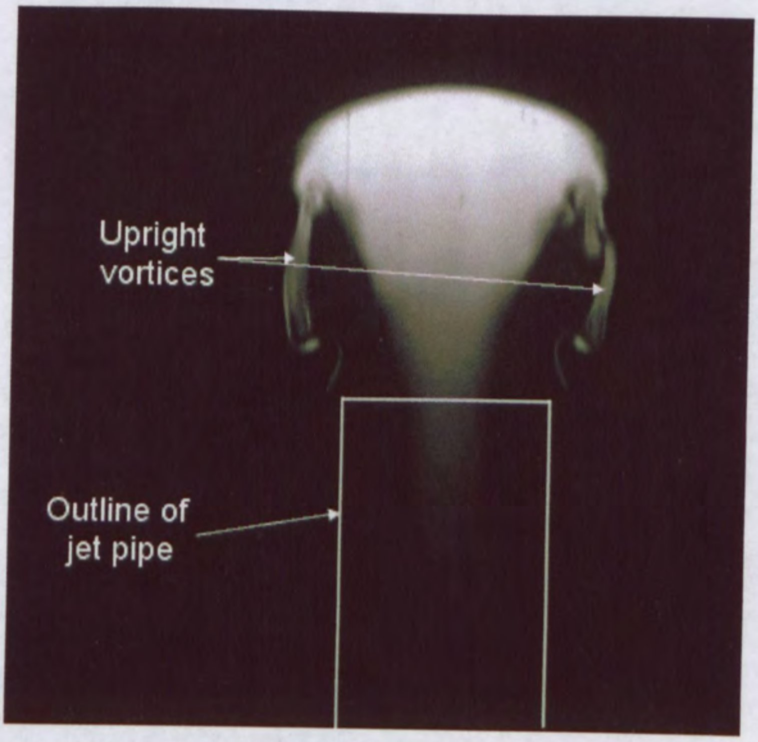

Figure 8-4 PLIF image of an elevated JICF at R=2, Re=2000. The plane on which the image is taken runs through the internal trailing edge of the jet pipe.

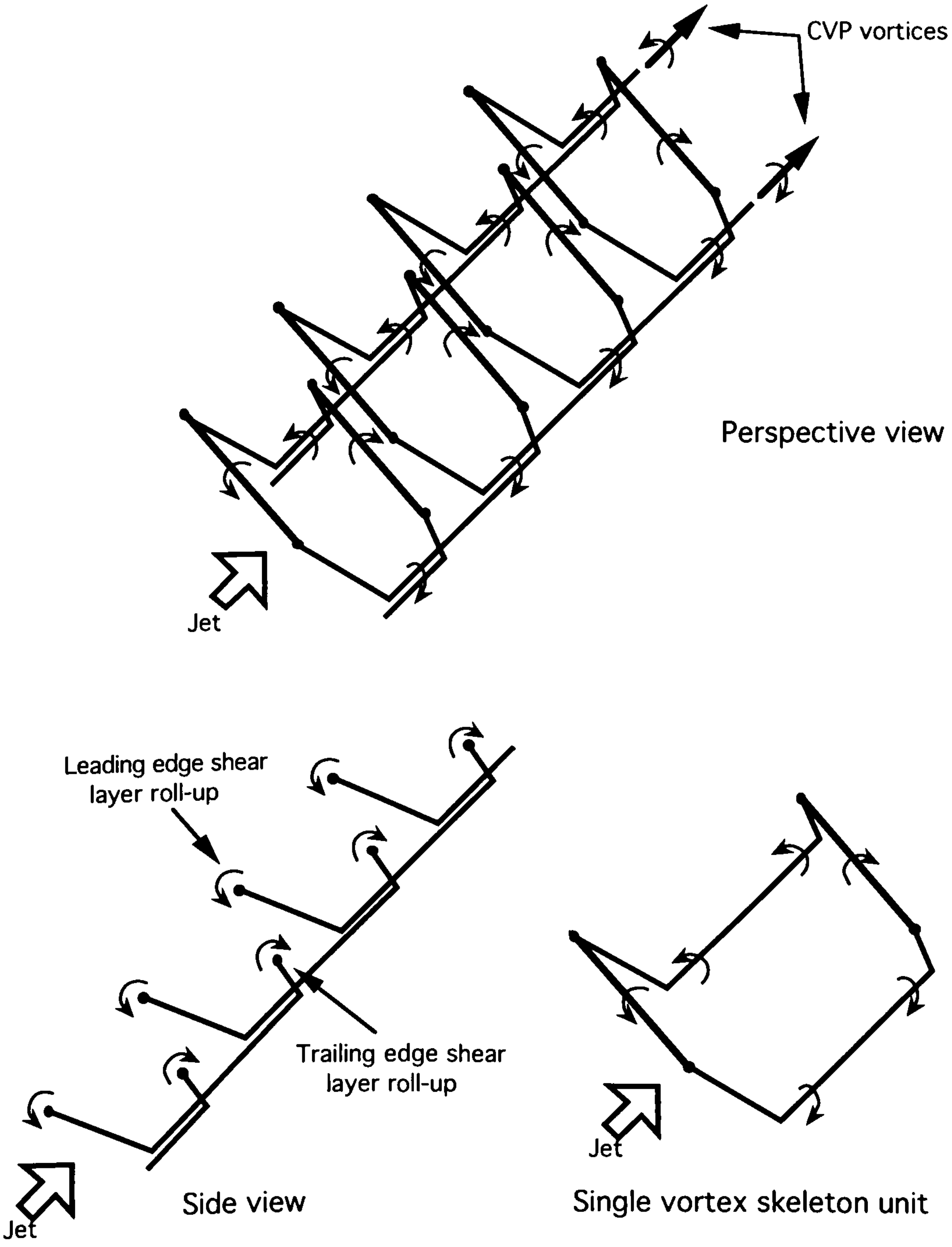

Figure 8-5 Proposed Vortex skeleton model of the shear layer roll-up of a jet in crossflow.

A vortex skeleton representation of the shear layer mechanism is proposed in Figure 8-5. Vortex skeletons in this case represent, schematically, groups of vortex lines in the cylindrical shear layer of the jet. The pattern consists of a series of ring-like vortex loops that become distorted and fold to generate roll-ups on the leading and trailing edges of the shear layer. The sides of the loops bunch together to form the CVP. The distinction between this model and previous models is that the roll-up on the leading edge of the jet is not necessarily connected in any organised way to the roll-up on the trailing edge. For example, vortex lines from a leading edge vortex may pass through more than one vortex on the trailing edge. Further information on vortex skeletons maybe found in Perry & Chong (1987).

The present interpretations are interesting as they contradict the interpretations of Lim *et al.* (2001). Lim *et al.* proposed that the side-arms of the vortex loops on the trailing-side turned downstream (not upstream) before merging with the CVP, as shown in Figure 2-5. (The evidence presented by Lim *et al.* in support of this mechanism is relatively inconclusive, especially when the LIF images are compared with similar images presented in Kelso, Lim & Perry (1998).) By contrast, the present interpretation is that the side-arms of these loops turn upstream before merging with the CVP. The present observations and interpretations agree with the observation of Lim *et al.* that the leading and trailing-side roll-ups are not the result of the deformation of individual vortex rings.

4. Importance of the wall boundary layer circulation.

The proportion of the wall boundary layer circulation that interacts with the leading edge jet shear layer was established. It was found that a significant proportion of the boundary layer circulation does not interact with the jet shear layer. This result suggests that the vortex mechanism proposed by Morton (1995) does not play a significant role in the development of the shear layer of the jet.

5. Mixing characteristics of flush and elevated jets compared.

A significant, although tentative conclusion of the mixing studies is that for all the flow cases investigated the normalised mean concentration decay data along the CVP appear to collapse when plotted against the jet-wise coordinate s. Furthermore, the normalised decay rates seem to fit the s^{-1} decay rate that is usually associated with a free jet. The reason for the tentative conclusion is that the scatter of the data is large. However, the close collapse suggests that this phenomenon deserves more detailed study. This result is also worth considering in the light of the conclusions below.

The mixing studies reported in Chapter 5 showed that the higher centreline concentration decay of the flush-mounted jet correlates with the observed lower trajectory of that configuration compared with an elevated jet at the same flow conditions. The concentration decay in the CVP itself agreed with this trend, except for the case of the R=4 flush mounted jet. The reason for this appears to be due to the structural differences observed in Chapter 7.

From the flow structure observed in Chapter 7 it is clear that large differences exist between the elevated and flush-mounted jets at R=4. The mixing and flow visualisation studies agree that the CVP formed by the flush-mounted jet is compact and well defined, and that the jet fluid appears to concentrate at its core. The elevated jet structure present in the mixing study, however, is substantially different as it corresponds to the low R/Re case. In the low R/Re elevated jet the CVP roll-up is much less concentrated, and it appears to exist below the main body of the jet, as discussed above. Here the jet fluid that is entrained into the CVP will be mixed over a very large cross-sectional area. Thus, the highest concentration in the jet cross-section will not exist at the cores of the CVP in this flow case. Sectional views (such as Figure 5-21) show that the main body of the jet contains a considerably higher concentration than does the CVP region below. This result demonstrates that the velocity centreline and concentration centrelines diverge considerably for this particular flow case, unlike previously documented observations of flush-mounted jets. The result also shows the error in the assumption that the locus of maximum concentration corresponds to the CVP in the present study. However, the above conclusions and observations about the mixing rate still hold.

The scatter in the data were, in part, a result of the small sample size (100 images) and short running time (3.3 seconds) at each measurement plane, as well as a small number (10) of measurement planes. The sampling arrangements were dictated by the small total running time available for each experiment, which was itself dictated by the need to avoid contamination of the cross-flow fluid by the recirculated dye. The sampling arrangements were a trade-off between the various spatial and temporal resolution requirements. Future experiments should seek to extend the running time of the experiments and so improve the resolution and convergence of the data.

6. Use of volumetric experimental techniques.

A significant component of the work involved the development of experimental techniques – volume visualisation in particular. Overall, the volume visualisation technique has been under-exploited in this work, but the benefits of the technique are obvious, especially in identifying the details of the instantaneous flow structure. This aspect alone has allowed the topology of the trailing edge shear layer roll-up to be identified.

7. Future work.

Although progress has been made toward a better understanding of the nature of the transverse jet at the two configurations tested, the work has also generated issues that require additional work to resolve. Three main of areas work, summarised below, are considered necessary to provide a more complete understanding of the results presented in the current work.

The finding that the elevated jet undergoes a transition between two different structures, depending on the velocity ratio and Reynolds numbers of the flow, was made after the mixing study had been completed. Therefore, the mixing characteristics of the elevated jet for each of the flow structures have not been determined. It is probable, given the differences between the structures, that there will also be a difference in between mixing characteristics of these flows. Further, given the similarity of the structure of the elevated jet at the higher R/Re to that of a flush-mounted jet, it is likely that the mixing characteristics may also be similar for these cases. However, these conclusions need to be verified. Such work will also provide additional information about the effect of the floor and its associated boundary layer in the flush-mounted case. Given that the flow structures are similar, differences in the mixing would suggest effects due to the presence of the floor.

The location of the point of transition between the two structures of an elevated jet was plotted for various velocity ratios and Reynolds numbers in Section 7.6 of this thesis. However, only a limited number of flow cases have been investigated. It is therefore recommended that a broader range of Reynolds numbers and velocity ratios are tested to better define the transition region of the elevated jet. It is also necessary to establish over what range of Reynolds numbers and velocity ratios the two structures occur and how broad the transition region is for each flow case. The relationship between the structural transition and the transition between the two types of roll-up of the leading edge shear layer also needs to be investigated further.

The results from the extensions of the current work suggested above may be valuable in industrial applications of the elevated jet. From such results it may be possible to change the mixing characteristics of certain elevated jets that have flow conditions that fall close to the transition condition between the different flow structures.

Part of the work for the current thesis applied volume visualisation techniques in order to gain a clearer understanding of the flow. In the current work the techniques were applied in order to visualise the large-scale structure of the flow. However there is also great potential for the techniques to be applied to smaller regions in order to provide information about the formation of individual components within the flow. An example may be the visualisation of the region on just one side of the jet as it exits the pipe in order to provide a high-resolution rendering of the initial formation of the CVP. This would allow a better understanding of the interactions between the various roll-ups identified within the elevated jet case to be made.

Bibliography

Andreopoulos, J. & Rodi, W. (1984) Experimental Investigations of Jets in Cross-Flow, *Journal of Fluid Mechanics*, vol. 138, pp. 93-127

Andreopoulos, J. (1982) Measurements in a Jet-Pipe Flow Issuing Perpendicularly into a Cross Stream, *Journal of Fluids Engineering*, vol. 104, pp. 493-499

Andreopoulos, J. (1983) Heat Transfer Measurements in a Heated Jet-pipe Flow Issuing into a Cold Cross Stream, *Physics of Fluids*, vol. 26, no. 11, pp. 3201-3210

Andreopoulos, J. (1984) Initial Conditions, Reynolds Number Effects and the Near Field Characteristics of the Round Jet in a Cross Flow, *Journal of Flight Sciences and Space Research*, vol. 8, Heft 2

Andreopoulos, J. (1985) On the Structure of Jets in a Crossflow, *Journal of Fluid Mechanics*, vol. 157, pp. 163-197

Birch, A. D., Brown, D. R. Fairweather, M. & Hargrave, G. K. (1989) An Experimental Study of a Turbulent Natural Gas Jet in a Cross-flow, *Combustion Science and Technology*, vol. 66, pp. 217-232

Blanchard, J. N., Brunet, Y. & Merlen, A. (1999) Influence of a Counter Rotating Vortex Pair on the Stability of a Jet in Cross Flow: An Experimental Study by Flow Visualizations, *Experiments in Fluids*, vol. 26, pp. 63-74

Bousgarbiès, J. L., Brizzi, L. E. & Foucault, E. (nd) *Coherent Structures Generation from a Circular Jet issuing into a Cross Boundary Layer. Low Reynolds Study*, Laboratoire d'Etudes Aérodynamiques, Poitiers

Bradshaw, P. (1970) *Experimental Fluid Mechanics*, Pergamon Press, Oxford

Broadwell, J. E. & Breidenthal, R. E. (1984) Structure and Mixing of a Transverse Jet in Incompressible Flow, *Journal of Fluid Mechanics*, vol. 148, pp. 405-412

Brücker, C. & Althaus, W. (1992) Study of Vortex Breakdown by Particle Tracking Velocimetry (PTV): Part 1: Bubble-Type Vortex Breakdown, *Experiments in Fluids*, vol. 13, pp. 339-349

Brücker, C. (1995) *Study of the 3D Flow in a T-Junction Using a Dual-Scanning Method for 3-D Scanning-Particle-Image-Velocimetry (3-D SPIV)*, Tenth Symposium on Turbulent Shear Flows, The Pennsylvania State University, University Park, PA, USA, August 14-16

Camussi, R., Guj, G. & Stella, A. (2002) Experimental Study of a Jet in a Crossflow at Very Low Reynolds Number, *Journal of Fluid Mechanics*, vol. 454, pp. 113-144

Chong, M. S., Perry, A. E. & Cantwell, B. J. (1990) A General Classification of Three-dimensional Flow Fields, *Physics of Fluids*, vol. 2, no. 5, pp. 765-777

Coelho, S. L. V. & Hunt, J. C. R. (1989) The Dynamics of the Near Field of Strong Jets in Crossflows, *Journal of Fluid Mechanics*, vol. 200, pp. 95–120

Cortelezzi, L. & Karagozian (2001) On the Formation of the Counter-Rotating Vortex Pair in Transverse Jets, *Journal of Fluid Mechanics*,

Crowe, C. T., Gore, R. A. & Troutt, T. R. (1985) Particle Dispersion by Coherent Structures in Free Shear Flows, *Part. Sci. Technol.*, vol. 3, pp. 149-158

Dahm, W. J. A., Southerland, K. B. & Buch, K. A. (1991) Direct, High Resolution, Four-Dimensional Measurements of the Fine Scale Structure of Sc >> 1 Molecular Mixing in Turbulent Flows, *Physics of Fluids*, vol. 3, no. 5

Dahm, W. J. A., Su, L. K. & Southerland, K. B. (1992) A scalar imaging velocimetry technique for fully resolved four-dimensional vector velocity field measurements in turbulent flows, *Physics of Fluids*, vol. 4, no. 10

Delo, C. & Smits, A. J. (1997) Volumetric Visualisation of the Three-Dimensional, Time-Evolving Scalar Concentration Field in a Low Reynolds Number Turbulent Boundary Layer. *Near Wall Turbulent Flows*, ed. Speziale, C. G. & Launder, B. E., Elsevier Science Publishers, pp. 573-582

Diep, J. & Sigurdson, L. (2001) Cross-Jet Influenced by a Concentric Synthetic Jet, *Physics of Fluids*, vol. 13, no. 9, p. S16

Doligalski, T. L., Smith, C. R. & Walker, J. D. A. (1994) Vortex Interactions with Walls, *Annual Review of Fluid Mechanics*, vol. 26, pp. 573-616

Eiff, O. S. & Keffer, J. F. (1997) On the Structures in the Near-wake Region of an Elevated Turbulent Jet in Crossflow, *Journal of Fluid Mechanics*, vol. 333, pp. 161-195

Eiff, O. S., Kawall, J. G. & Keffer, J. F. (1995) Lock-in of Vortices in the Wake of an Elevated Round Turbulent Jet in a Crossflow, *Experiments in Fluids*, vol. 19, pp. 203-213

Fohl, T. & Turner, J. S. (1975) Colliding vortex rings, *Physics of Fluids*, vol. 18, p. 443-436

Foss, J. F. (1980) Flow *Visualisation Studies of Jets in a Crossflow*, Sonderforschungsbereich 80, Ausbreitungs- Und Thansprotvorgänge in Strömungen, Universität Karlsruhe

Fric, T. F. (1990) *Structure in the Near Field of a Transverse Jet*, Ph.D. Thesis, California Institute of Technology, 1990

Fric, T. F. & Roshko, A. (1989) *Structure in the Near Field of the Transverse Jet*, Seventh Symposium on Turbulent Shear Flows, Stanford University

Fric, T. F. & Roshko, A. (1994) Vortical Structure in the Wake of a Transverse Jet, *Journal of Fluid Mechanics*, vol. 148, pp. 405-412

Gad-el-Hak, M. (1989) Review of Flow Visualisation Techniques for Unsteady Flows, *Handbook of Flow Visualisation*, Hemisphere Publishing Corporation

Garcfa, J. C. A. & Hesselink, L. (1986) 3-D Reconstruction of Flow Visualisation Images, *Flow Visualisation IV*, Proceedings of the Fourth International Symposium on Flow Visualisation, Ecole Nationale Superieure de Techniques Avancés, Paris, France, August 26-29, 1986

Gibbings, J. C. (1973) The Pyramid Gauze Diffuser, *Ing.-Arch*, 42, 225

Goldstein, J. E. & Smits, A. J. (1994) Flow Visualisation of the Three-Dimensional, Time-Evolving Structure of a Turbulent Boundary Layer, *Physics of Fluids*, vol. 6, no. 2, pp. 577-587

Hasselbrink, E. F. & Mungal, M. G. (1996) *An Analysis of the Time-Averaged Properties of the Far Field of the Transverse Jet*, AIAA 34th Aerospace Sciences Meeting & Exhibit, Reno, NV, USA, January 15-18

Haven, B. A. & Kurosaka, M. (1997) Kidney and Anti-kidney Vortices in Crossflow Jets, *Journal of Fluid Mechanics*, vol. 352, pp. 27-64

Hornung, H. & Perry, A. E. (1982) *Streamsurface Bifurcation, Vortex Skeletons and Separation*, Institut für Experimentelle Strömungsmechan, Aerodynamische Versuchsanstalt, Gottingen

Johari, H., Pacheco-Tougas, M. & Hermanson, J. C. (1999) Penetration and Mixing of Fully Modulated Turbulent Jets in Crossflow, *AIAA Journal*, vol. 37, no. 7, pp. 842-850

Kavsaoglu, M. S. & Schetz, J. A. (1989) Effects of Swirl and High Turbulence, J. Aircraft, vol. 26, pp. 539-546

Kelso, R. M. & Smits, A. J. (1995) Horseshoe Vortex Systems Resulting form the Interaction Between a Laminar Boundary Layer and a Transverse Jet, *Physics of Fluids*, vol. 7, no. 1, January 1995, pp. 153-158

Kelso, R. M. (1991) *A Study of Free Shear Flows Near Rigid Boundaries*, Ph.D. Thesis, University of Melbourne

Kelso, R. M., Delo, C. & Smits, A. J. (1993) *Unsteady Wake Structures in Transverse Jets*, AGARD Conference Proceeding 534, Advisory Group for Aerospace Research & Development, Fluid Dynamics Panel Symposium, Winchester, UK, April 19-22

Kelso, R. M., Lim, T. T. & Perry, A. E. (1996) An Experimental Study of a Round Jet In Cross-Flow, *Journal of Fluid Mechanics*, vol 306, pp. 111-114

Kelso, R. M., Lim, T. T. & Perry, A. E. (1998) New Experimental Observations of Vortical Motions in Transverse Jets, *Physics of Fluids*, vol. 10, no. 9, pp. 2427-2429

Krothapalli, A. & Shih, C. (1993) *Separated Flow Generated by a Vectored Jet in a Crossflow*, AGARD Symposium on Computational and Experimental Assessment of Jets in Crossflow, Winchester, UK, April 19-22, 1993

Krothapalli, A., Lourenco, L. & Buchlin, J. M. (1990) Separated Flow Upstream of a Jet in a Crossflow, *AIAA Journal*, vol. 28, no. 3, pp. 414-420

Landman, M. J. & Saffman, P. G. (1987) The Three-Dimensional Instability of Strained Vortices in a Viscous Fluid, Physics of Fluids, vol. 30, pp. 2339-2342

Lim T. T., Kelso, R. M. & Perry, A. E. (1998*) A Visual Study of Vortex Rings Fired Transversely into a Cross-flow*, Thirteenth Australasian Fluid Mechanics Conference, Monash University, Melbourne, Australia

Lim, T. T., New, T. H. & Luo, S. C. (2001) On the Development of Large-Scale Structures of a Jet Normal to a Cross Flow, *Physics of Fluids*, vol. 13, no. 3, pp. 770-774

Margason, R. J. (1993) *50 Years of Jet in Cross Flow Research*, AGARD Conference Proceeding 534, Advisory Group for Aerospace Research & Development, Fluid Dynamics Panel Symposium, Winchester, UK, April 19-22

Mason, P.J. & Morton, B.R. (1987) Trailing vortices in the wakes of surface-mounted obstacles, *Journal of Fluid Mechanics*, vol. 175, pp. 247-293

McMahon, H. M., Hester, D. D. & Palfery, J. G. (1971) Vortex Shedding from a Turbulent Jet in a Cross-wind, *Journal of Fluid Mechanics*, vol. 48, part 1, pp. 73-80

Mehta, R. D. (1977) The Aerodynamic Design of Blower Tunnels with Wide-Angle Diffusers, *Progress in Aerospace Science*, vol. 18, pp. 59-120

Mehta, R. D. & Bradshaw, P. (1979) Design Rules for Small Low Speed Wind Tunnels, *Aeronautical Journal*, November, pp. 443-449

Mikolowsky, W. & McMahon H. (1973) An Experimental Investigation of a Jet Issuing from a Wing in a Crossflow, *Journal of Aircraft*, vol. 10, no. 9, pp. 546-553

Morton, B. R. (1984) The Generation and Decay of Vorticity, *Geophys. Astrophys. Fluid Dyn.*, vol. 28, pp. 277-308

Morton, B. R. (1995) *The Vortical Structure of Jets in Crossflow*, Twelfth Australasian Fluid Mechanics Conference, The University of Sydney, Australia

Moussa, Z. M., Trischka, J. W. & Eskinazi, S. (1977) The Near Field in the Mixing of a Round Jet with a Cross-stream, *Journal of Fluid Mechanics*, vol. 80, part 1, pp. 49-80

Mungal, M. G. & Lozano, A. (1996) Some Observations of a Large, Burning Jet in Crossflow, *Experiments in Fluids*, vol. 21, pp. 264-267

Niederhaus, C. E., Champagne, F. H. & Jacobs, J. W. (1997) Scalar Transport in a Swirling Transverse Jet, *AIAA Journal*, vol. 35, no. 11, pp. 1697-1704

Papaspyros, J. N. E., Papanicolaou, P. N., Kastrinakis, E. G. & Nychas, S. G. (1996) Buoyant Jet in Cross Flow: Study of Turbulent Transport Terms, *Engineering Turbulence Modelling and Experiments 3*

Perry, A. E. & Chong, M. S. (1987) A Description of Eddying Motions and Flow Patterns Using Critical-Point Concepts, *Annual Review of Fluid Mechanics*, vol. 19, pp. 125-155

Perry, A. E. & Chong, M. S. (1994) Topology of Flow Patterns in Vortex Motions and Turbulence, *Appl. Scientific Research*, vol. 54 (3/4), pp. 357-374

Perry, A. E. & Lim, T. T. (1978) Coherent Structures in Co-flowing Jet and Wakes, *Journal of Fluid Mechanics*, vol. 88 part 3, pp. 451-463

Perry, A. E., Kelso, R. M. & Lim, T. T. (1993) *Topological Structure of a Jet in Crossflow*, AGARD Conference Proceeding 534, Advisory Group for Aerospace Research & Development, Fluid Dynamics Panel Symposium, Winchester, UK, April 19-22

Prasad, R. R. & Sreenivasan, K. R. (1990) Quantitative Three-Dimensional Imaging and the Structure of Passive Scalar Fields in Fully Turbulent Flows, *Journal of Fluid Mechanics*, vol. 216. pp. 1-34

Pratte & Baines (1967) Profiles of the Round Turbulent Jet in a Cross Flow, *J. Hydraulics Division, Proc. A.S.C.E.*, vol. 92, no. HY 6, pp. 53-64

Rivero, A., Ferré, J. A. & Giralt, F. (2001) Organised Motions in a Jet in Crossflow, *Journal of Fluid Mechanics*, vol. 444, pp. 117-149

Rudman, M. J. (1995) *The Wake Vortex System of a Jet in a Cross-flow*, Twelfth Australasian Fluid Mechanics Conference, Sydney, Australia

Simeons, S. and Ayrault, M. (1994) Concentration Flux Measurements of a Scalar Quantity in Turbulent Flows, *Experiments in Fluids*, vol. 16, pp. 273-281

Smith, S. H. & Mungal, M. G. (1998) Mixing, Structure and Scaling of the Jet in Crossflow, *Journal of Fluid Mechanics*, vol. 357, pp. 83-122

Smith, S. H., Lozano, A., Mungal, M. G. & Hanson, R. K. (1993) *Scalar mixing in The Subsonic Jet in Crossflow*, AGARD Conference Proceeding 534, Advisory Group for Aerospace Research & Development, Fluid Dynamics Panel Symposium, Winchester, UK, April 19-22

Smits, A. J. & Lim, T. T. (2000) *Flow Visualisation: Techniques and Examples*, Imperial College Press

Steiner, T. R. (1984) *A Study of Turbulent Wakes and the Vortex Formation Process*, Ph.D. Thesis, University of Melbourne

Sugiyama, Y. (1991) *A Calculation of Penetration of the Jet Issuing Normally into a Cross Flow Across a Wall Boundary Layer*, SAE Technical Paper 912029, Proceedings of the International Air & Space Technology Conference and 29th Aircraft Symposium, Gifu, Japan, October 7-11

Sykes, R. I., Lwewellen, W. S. & Parker, S. F. (1986) On the Vorticity Dynamics of a Turbulent Jet in a Crossflow, *Journal of Fluid Mechanics*, vol. 168, pp. 393-413

Tobak, M. & Peake, D. J. (1979*) Topology of Two-dimensional and Three-dimensional Separated Flows*, AIAA 12th Fluid and Plasma Dynamics Conference, Williamsburg, Virginia, July 23-25

Tobak, M. & Peake, D. J. (1982) Topology of Three-dimensional Separated Flows, *Annual Review of Fluid Mechanics*, vol. 14, pp. 61-85

Toy, N., Savory, E., McCusker, S. & Disimile, P.J. (1993) *The Interaction Region Associated with Twin Jets and a Normal Crossflow*, AGARD Conference Proceedings 534, Advisory Group for Aerospace Research & Development, France

Visbal, M. R. and Gordnier, R. E. (1993) Crossflow Topology of Vortical Flows, *AIAA Journal*, vol. 32, no. 5, pp. 1085-1087

Vogel, D .T. (1996) The Influence of the Film-Cooling Coolant Channel Geometry on Jet-Mixing – Numerical Investigation using a 3D Navier-Stokes Model, *Engineering Turbulence Modelling and Experiments 3*

Werlé, H. (1973) Hydrodynamic Flow Visualisation, *Annual Review of Fluid Mechanics*, vol. 5

White, F. M. (1994) *Fluid Mechanics*, Third Edition, McGraw-Hill, Inc.

Wu, J. M., Vakili, A. D. & Yu, F. M. (1988) Investigation of the Interacting Flow of Nonsymmetric Jets in Crossflow, *AIAA Journal*, vol. 26, no. 8, pp. 940-947

Yoda, M. and Hesselink, L. (1989) Three-Dimensional Measurement, Display, and Interpretation of Fluid Flow Datasets, *Three-Dimensional Visualisation and Display Technologies*, SPIE The International Society for Optical Engineering, Vol. 1083, pp. 112 - 117

Yoda, M. and Hesselink, L. (1990) A Three-Dimensional Visualisation Technique Applied to Flow Around a Delta Wing, *Experiments in Fluids*, Vol. 10, pp. 102-108

Yuan, L. L., Street, R. L. & Ferziger, J. H. (1999) Large-Eddy Simulations of a Round Jet in Crossflow, *Journal of Fluid Mechanics*, vol. 379, pp. 71-104

A Appendix A - MATLAB Code

A.1 Summary of Code

A summary of the MATLAB code used to process the PLIF data in order to generate the volume renderings is given in Table A-1. The full code is also included following the table.

Table A-1 Description of MATLAB code used to process volume data

Script	Summary
run_all.m	The following variables are required to be entered for each data set: file_name: the prefix for the name of each file batch_letter: the batch letter for the data set start: the number of the first image to process image_no: the total number of images to be processed layers: the number of slices (planes) in each volume plane_interval_mm: the distance between image planes in millimetres Note: the name of each image file to be processed needs to be of the form prefix_batchletter???.tif Contains a loop to ensure that there are sufficient images to generate a complete data set (ie the total number of images divided by the number of image slices is a whole number). Produces an error and exits if sufficient images are not present. Generates an 'Open' dialogue box from which an image file for the data set to be processed must be selected (does not need to be the first image) in order to determine the path for each image Generates an 'Open' dialogue box from which the background image file for the data set can be selected. If no background image was captured the dialog box can be cancelled and no background image is used during the processing of the data set Calculates and displays the number of time steps to be processed Allows the data to be processed for the different rendering packages or to generate plots for display display_flag: set to 1 to display images and histograms during processing vis5d_flag: set to 1 to re-write the processed data for use with Vis5D iunterpolation_loop: set to 1 to apply three-dimensional interpolation of the image data requires interval for interpolation to be entered (fraction between 0 & 1) If more than one level is being processed runs the function set_scaling_factor.m to calculate the physical size of the data in pixels Runs the function run_process.m to undertake the processing of the data Generates a text file output of the text written to the screen while the processing is taking place, in Matlab_run.txt Incorporates tic/toc functions to obtain and display the overall processing time
set_scaling_factor.m	Used to provide details of the spacing between image planes and interpolated planes, and the entire volume depth, in pixels for the volume rendering packages Requires the full captured image width and height in millimetres to be entered into the file Determines the scaling factor for the data set, defined as the number of millimetres per pixels Calculates the interval between image planes, in pixels

	Calculates the interval between interpolated planes, in pixels Calculates the entire volume depth, (third-dimension) in pixels
run_process.m	Retrieves and stores background image, if one was selected, and runs the pre_process function on the image Loops for each time step Loops for each layer Uses the function call_filexxx.m to generate the filename of the next image to be opened based on the current image number Opens the corresponding image file and stores the image data in an array Runs the main_process function to undertake the processing of the image Stores threshold value for the current image in the array volume_threshold Uses the function name_filexxx.m to generate a new binary file with a file name of the form proc_i???.bin, where ??? are three digits based on the current number in the filename of the image currently being processed Writes the processed image data to the binary file for the current image, as a 32 byte floating point number (IEEE floating point with little-endian byte ordering) Loops for the required number of layers in each volume Concatenates the array volume_threshold to the array complete_threshold Loops for the required number of time steps Determines the maximum threshold value for the entire data set, from the array complete_threshold If there is more than one image being processed applies the functions threshold_shift_loop.m, followed by volumetric_interpolation_loop if the interpolatioon_flag was set to 1 If the vis5d_flag was set to one runs the function v5d_loop
pre_process.m	Runs the function read_tiff16.m to open and read a 16 byte TIFF image Transposes the array (to set coordinates as for an image) Changes data to class double Runs a cropping function, specific to each data set, to reduce the image size If display flag is set to 1 the image currently being processes is displayed and the region cropped is shown by a red border
read_tiff16.m	Reads a 16-byte TIFF data generated by the EPIX XCAP software used in conjunction with the Kodak MEGAPLUS camera Reads data as IEEE floating point with little-endian byte ordering Returns the width and height of the image read, in pixels Returns an error if the data in the file is not in the correct format
crop_'dataset'.m	Cropping function to remove the margins of an image A new file must be created for each data set which specifies the top left pixel and width and height for the image to be cropped
call_filexxx.m	Generates the name of the file to be processed Ensures the name of the file is of the form, filename_a???.tif, where ??? must be 3 digits
main_process.m	Runs the function pre_process.m Runs the function set_threhold_parameters to calculate the variables minimum pixel count and threshold guess value Runs the process_image function to carry out any processing required Runs the function threshold.m to calculate the threshold for the processed image
set_threshold_parameters.m	Generates a histogram for the current image Smooths the histogram using the MATLAB function *medfilt1* Runs the function set_min_level to calculate the minimum pixel count Calculates the threshold guess value defined to be the grey level half way to the end of the jet peak (based on the minimum pixel count)
set_min_level.m	Scans across the image histogram (and tries) to locate the minimum pixel counts between the two peaks If search fails a default level is returned of 100 counts
process_image.m	Checks to see whether there was a background image selected and if there was subtracts it from the current image using element by element subtraction If display flag was set to 1, the function display_doc.m is run to display the resulting image

	and histogram followed by the function threshold_image.m to generate and display a binary threshold image Runs the function intensity_norm.m to generate to normalise the current image If display flag was set to 1, the function display_doc.m is run to display the resulting image and histogram followed by the function threshold_image.m to generate and display a binary threshold image
intesity_norm.m	Normalises each element in an array against the maximum intensity of the dyed fluid Runs the function threshold.m to calculate the maximum intensity value for the dyed region If the intensity value returned is greater than zero, the intensity values of each pixel in the current image is divided by the intensity value maximum intensity value Runs the function over_value_check to check the resulting image for intensity levels greater than one, which are assumed to occur due to noise, and sets the values to zero (so they do not imfluence the remaining processing steps) If the intensity value returned is not greater than zero the image is not normalised (results if there was no dye in the image captured)
threshold.m	Determines the intensity levels of the dyed and un-dyed regions in each image Generates a histogram using 256 grey-levels for the current layer Smooths the histogram using the MATLAB function *medfilt1* Searches for the intensity level of the background peak, by finding the maximum number of pixel counts in the intensity levels from 0 to a pre-defined threshold_guess value Searches for the boundaries of the jet-peak, by finding the first and last intensity levels above a pre-defined minimum pixel count, in the intensity levels from 0 to a pre-defined threshold_guess value to the level 256 Calculates the intensity value for the jet by averaging the jet boundary intensity levels Runs the function curve_fitter.m to fit a third order polynomial to the histogram counts, and returns the position of the second peak of the curve Calculates the threshold value for the current layer by determining the mid-point between the jet intensity level and background intensity level
curve_fitter.m	Uses the MATLAB function *polyfit* to generate a polynomial which best fits the histogram counts Uses the MATLAB function *polyder* to differentiate the polynomial and determine the positions of the peaks
over_value_check.m	Scans the current image element by element and checks for intensity levels greater than a defined value Where this is the case the intensity level is set to a new value The function is used to check for intensity levels greater than one after the image has been normalised, and any cases which occur sets the level to zero, and to produce the binary threshold images, in which case all of the intensity levels above the determined threshold value are set to 1.
name_filexxx.m	Generates a name for the file to store the current processed data Ensures the name of the file is of the form, filename_a???.tif, where ??? must be 3 digits, and a is a single letter
threshold_shift_loop.m	Function is used to shift the intensity values of each pixel in an image to ensure the threshold value for every image within a data set is the same Loops for each time step Loops for each layer Checks the value in the complete_threshold array for the current time step and layer number to determine whether the corresponding image has a zero threshold value, if true the intensity values are not shifted If the threshold is greater than zero, the threshold shift value is determined, which is defined as the difference between the threshold value for the current image and the maximum threshold value for the entire data set If the intensity shift value is greater than zero, the function name_filexxx.m is run to generate the file name for the current image The image is re-openned and stored The threshold shift value is added to the data using element by element addition Runs the function over_value_check.m to check the modified data for intensity levels greater than one, and sets any such levels to one. If the intensity shift value for the current time step and level was zero the intensity levels are not shifted

volumetric_interpolation_loop.m	Function is used to apply a three-dimensional interpolation to the data to produce additional layers to allow smoother renderings of the data to be generated The function uses the MATLAB function interp3 to apply the interpolation. Three different interpolation methods are available; nearest neighbour, linear and cubic. To produce the 'smoothest' interpolation the linear or cubic methods are best Note the interpolation process is very processor intensive and therefore very slow Due to memory constraints, the interpolation is applied over four images at a time. Four images are required since the cubic interpolation method needs three or more images, and to ensure the same three images are used between interpolation steps, four images are necessary to be used. Set the interval for interpolation Runs the function set_scaling_factor.m to provide details of the overall volume size, and distance between image planes and interploted planes in pixels. Uses the MATLAB function *meshgrid* to generate a mesh, based on the interval of interpolation, to apply the interpolation over Loops for the required number of times to process each image. For each loop the four image used are displaced by one level from the previous group to ensure the interpolation is applied correctly Uses the function name_filexxx.m to open the next four images to be processed, and stores each image in a three-dimensional array Applies the interpolation using the MATLAB function *interp3*, and the interpolation method selected Uses the function bin_store.m to store the result of the interpolation in separate binary files, one file for each data level Note, depending on whether the interpolation loop is the first, last or intermediate, a different set of images are saved (see the figure in the section on interpolation in the main text)
bin_store.m	Uses the function name_filexxx.m to generate a new file name for the data to be stored Writes the data to the binary file
display_doc.m	Used to display the data during processing, in the form of images and histograms, for checking method used, and to generate figures for publication Applied during the processing only if the display_flag is set to 1 Displays the current processed image and its corresponding histogram as two separate images and a combined image (figure 1 in text) Runs the functions set_threshold_parameters.m and threshold.m to determine and display the variables Image threshold Background Intensity Level Jet Minimum Intensity Level Jet Maximum Intensity Level Jet Intensity Level Uses the function curve_fitter.m to provide the data to generate a plot of the histogram for the current image with the polynomial of best fit superimposed, along with the position of the second polynomial peak, minimum pixel count and threshold value shown (figure 2 in text) Generates a plot of the histogram for the current image with position of the minimum pixel count and maximum jet value superimposed (figure 3 in text)
threshold_image.m	Used to generate a threshold binary image for the current image The threshold binary image is generated by changing all of the intensity levels for the image above the threshold intensity level determined to one, and leaving the remaining levels at their initial value, to qualitatively show how well the threshold level found defines the boundary between the dyed and undyed fluid. That is if the binary image produced still shows many dyed features as a grey level, the threshold value found may not be sufficiently low to ensure the small scale structures are retained during the volumetric rendering Runs the function threshold.m to determine the threshold value for the current image Uses the function over_value_check.m to change the intensity levels above the threshold level to 1. Displays the resulting image
tic_toc.m	Returns the total processing time converted into hours, minutes and second

A.2 MATLAB Code Files

A.2.1 run_all.m

```
%run_all.m

clear all

clc
diary Matlab_run.txt
diary on
fprintf('************************************************\n')
fprintf('****                                        ****\n')
fprintf('****  TIFF image processing to binary files  ****\n')
fprintf('****      Code written by Philip Cutler     ****\n')
fprintf('****                 2000                   ****\n')
fprintf('****                                        ****\n')
fprintf('************************************************\n\n')

fprintf('**** Data maybe processed for use with either T3D or Vis5D ****\n\n')

file_name =     input('Enter the prefix for the names of the data to be processed: ','s');
batch_letter =          input('Enter the batch letter of the data to be processed: ','s');
start =         input('Enter the number of the first image to be processed: ');
image_no =      input('Enter the total number of images to be processed: ');
layers =        input('Enter the number of slices in each image volume: ');
fprintf('\n')

plane_interval_mm = input('Enter the distance between image planes in millimetres: ');

% Need to check image_no/layers is a whole number
if rem(image_no,layers) == 0
        %determine the file path for the files
        [file_not,file_path]=uigetfile('*.tif','Determine location of the image data');

        %determine location of the background image
        [file_back,file_back_path]=uigetfile('*.tif','Determine location and file name of
the background image');

        %determine the number of time steps
        time_steps = image_no/layers;
        message = strcat('The number of time steps to process is: ', int2str(time_steps));
        fprintf('\n')
        disp(message);
        fprintf('\n')

        display_flag = input('Enter 1 to display images and processed data: ');
        vis5d_flag = input('Enter 1 to format binary data for Vis5d: ');
        fprintf('\n')

        interpolation_flag = input('Enter 1 to apply interpolation to the image data: ');
        z_plane_precision = [];
        if interpolation_flag == 1
                if image_no < 6
                        errordlg('Must have more than six images to apply
interpolation','ERROR')
                        fprintf('\n****                      ERROR:
****\n')
                        fprintf('**** Must have more than six images to apply interpolation
****\n');
                        fprintf('****              Do not apply interpolation
****\n\n\n');
                        break
                end
                z_plane_precision = input('Enter interval for interpolation (best to use
0.5): ');
                fprintf('\n')
        else
                fprintf('\n')
        end

        if layers ~= 1
```

```
        set_scaling_factor(z_plane_precision,layers,plane_interval_mm,interpolation_flag)
        end

        tic;

        if vis5d_flag == 1
                disp('Processing data for T3D and Vis5D');
        else
                disp('Processing data for T3D');
        end
        if display_flag == 1
                disp('All images and processed data will be displayed');
        end
        if interpolation_flag == 1
                disp('Image data will be interpolated')
        end

        fprintf('\n')

        run_process(file_path,file_name,batch_letter,start,image_no,layers,time_steps,file_
back,file_back_path,plane_interval_mm,interpolation_flag,display_flag,vis5d_flag,z_plane_pr
ecision);

        t = toc;
        [message] = tic_toc(t);
        disp(message);

else
        errordlg('Number of images and layers do not create a full image set','ERROR')
        fprintf('\n****                          ERROR:                          ****\n')
        fprintf('**** Number of images and layers do not create a full image set ****\n');
        fprintf('****        Check the number of images and slices entered
****\n\n\n');
end
diary off
```

A.2.2 set_scaling_factor.m

```
%set_scaling_factor.m
%used by volumetric_interpolation_loop.m function to calculate volume depth in pixels

function set_scaling_factor(z_plane_precision,layers,plane_interval_mm,interpolation_flag)

%captured image size in pixels
%       for MEGAPLUS camera use width = 1018, height = 1008
%       for PHANTOM camera use width = 512, height = 512
full_img_width_pixels = 1018;
full_img_height_pixels = 1008;

%set full image width captured (before image cropping) in  millimetres
full_img_width_mm = 400;

%set full image height captured (before image cropping) in  millimetres
full_img_height_mm = 400;

%determine scaling factor (millimetres/pixel)
A = [full_img_width_mm/full_img_width_pixels full_img_height_mm/full_img_height_pixels];
scaling_factor = mean(A);

disp(strcat('Image scaling factor is ', num2str(scaling_factor,4), ' millimetres/pixel'));

%determine distance between image planes in pixels
plane_interval_pix = plane_interval_mm/scaling_factor;
complete_volume_pix = (layers-1) * plane_interval_pix;

if interpolation_flag == 1
        %determine distance between interpolated planes in the z-plane
        interp_interval_pix = z_plane_precision * plane_interval_pix;
        disp(strcat('Distance between each interpolated layer is ',
num2str(interp_interval_pix,3), ' pixels'));
end
```

```
disp(strcat('Distance between each image layer is ', num2str(plane_interval_pix,3), '
pixels'));
disp(strcat('Total volume height is ', num2str(complete_volume_pix,3), ' pixels'));
fprintf('\n')
```

A.2.3 run_process.m

```
%run_process.m

function
run_process(file_path,file_name,batch_letter,start,image_no,layers,time_steps,file_back,fil
e_back_path,plane_interval_mm,interpolation_flag,display_flag,vis5d_flag,z_plane_precision)

%initialise variables
n = start; bins = 256;
volume_threshold = [];
complete_threshold = [];

%retrieve and store background image
if file_back == 0
        disp('No background image used')
        im_back = 0;
else
        back_img = [file_back_path file_back];
        message = strcat('Using background image: ',back_img);
        disp(message);

        [im_back,image_width,image_height] = pre_process(back_img, display_flag);
end

fprintf('\n')

for t = 1:time_steps
        m = 0;
        threshold = [];
        message = strcat('Processing time step: ', int2str(t));
        disp(message);
        for l = 1:layers
                message = strcat('Processing level: ',int2str(l));
                disp(message)

                % Determine Filename
                file_img = call_filexxx(file_path, file_name, batch_letter, n);
                message = strcat('Image: ',file_img);
                disp(message);

                [im_data,threshold_value,image_width,image_height] =
main_process(file_img,display_flag,bins,im_back);

                volume_threshold = [volume_threshold , threshold_value];

                % Generate a new filename for output file
                blank_file_path = [];
                file_bin = name_filexxx(blank_file_path, n, 'i');

                % writes a binary file in real*4 format
                fid_w = fopen(file_bin,'w','l');
                fwrite(fid_w,im_data,'float32');
                fclose(fid_w);

                message = strcat('Image written to binary file: ',file_bin);
                disp(message);

                % increment image number
                n = n + 1; m = m + 1;
                fprintf('\n')
        end
        % END LAYERS LOOP

        complete_threshold = [complete_threshold ; volume_threshold];
        clear volume_threshold;
```

```
        % increment timestep
        t = t+1;
        fprintf('\n')
end
% END TIME STEP LOOP

%find maximum threshold value
max_threshold = max(max(complete_threshold));
message = strcat('The maximum threshold value is ', num2str(max_threshold/256,4));
disp(message);
fprintf('\n')

clear im_data im_back

if layers ~= 1
        %apply threshold shift loop
        disp('*****      APPLYING THRESHOLD SHIFTING LOOP      *****')
        threshold_shift_loop(start,time_steps,layers,complete_threshold,max_threshold,bins,
image_height,image_width);

        fprintf('\n')
        message = strcat('The threshold value for the data set is ',
num2str(max_threshold/256,4));
        disp(message);
        fprintf('\n')

        clear complete_threshold threshold_shift img_bin

        %apply volumetric interpolation loop
        if interpolation_flag == 1
                disp('*****      APPLYING VOLUMETRIC INTERPOLATION LOOP      *****')

        volumetric_interpolation_loop(image_width,image_height,layers,time_steps,start,plan
e_interval_mm,z_plane_precision);
        end
end

if vis5d_flag == 1
        %Format binary files for use with Vis5D
        disp('*****      RE-WRITING DATA TO VIS5D FORMAT      *****')
        v5d_loop(start,time_steps,layers,image_height,image_width,interpolation_flag,blank_
file_path)
end
```

A.2.4 pre_process.m

```
%pre_process.m

function [im_data,image_width,image_height] = pre_process(file_img, display_flag)

% Read image data
[im_orig, im_width, im_height] = read_tiff16(file_img);
disp('Image data read');

%transpose matrix
im_orig = im_orig';

%change to class double
im_orig = double(im_orig)/(2^16-1);

% Crop image to size specified in crop_func.m
%crop_000629
%crop_000919runb
[im_data,image_width,image_height, top_left_col, top_left_row, bottom_right_col,
bottom_right_row]=crop_000629(im_orig);
message = strcat('Image cropped to ',int2str(image_width),' x ',int2str(image_height),'
pixels');
disp(message);

if display_flag == 1
        figure, imshow(im_orig, [0 1]), title('Original Image')
```

```
        line([top_left_col bottom_right_col bottom_right_col top_left_col
top_left_col],[top_left_row top_left_row bottom_right_row bottom_right_row top_left_row],
'Color', 'red')
        figure, imshow(im_data, [0 1]), title('Original Cropped Image')
end
```

A.2.5 read_tiff16.m

```
%read_tiff16.m Version 170500b1       Written by Philip Cutler
%Opens multiple 16-bit TIFF image generated by EPIX Software
%Based on code by David Nobes and Jordan Parham

function [im_X, im_width, im_height] = read_tiff16(file_img)

info = imfinfo(file_img);
[fid_i,message] = fopen(file_img,'r','l');
status = fseek(fid_i,info.FileSize-info.Width*info.Height*info.BitsPerSample/8,'bof');
position = ftell(fid_i);

if info.BitsPerSample == 16;
        im_X = fread(fid_i,[info.Width,info.Height],'ubit16');
        fclose(fid_i);
        im_width = info.Width;
        im_height = info.Height;
else
        errordlg('This image format cannot be processed!','ERROR')
end;
```

A.2.6 crop_'dataset'.m

```
%crop_func.m
%for the MEGAPLUS camera the original image size is 1008 pixels wide and 1018 pixels high
%for the PHANTOM camera the original image size is 512 pixels wide and 512 pixels high
%to be used with data from 000629run_c data set

function [im_C,image_width,image_height, top_left_col, top_left_row, bottom_right_col,
bottom_right_row] = crop_func(im_X)

%specify top left-hand pixel
%coordinates begin in top-left and move down and to the right
x = 415;
y = 475;

%size of cropped image
image_width = 815-x;
image_height = 875-y;

top_left_col = x;
top_left_row = y;

bottom_right_col = top_left_col + (image_width-1);
bottom_right_row = top_left_row + (image_height-1);

im_C = im_X(top_left_row:bottom_right_row,top_left_col:bottom_right_col);
```

A.2.7 call_filexxx.m

```
%call_filexxx.m        Version 170500b1        Written by Philip Cutler
%Reads filenames with the form filename_a000.tif
%Version 1.0

function [file_img] = call_file(file_path, file_name, batch_letter, image)

if image <= 9
        file_img = [file_path file_name '_' batch_letter '00' num2str(image) '.tif'];
elseif (image >= 10 & image <= 99)
```

```
        file_img = [file_path file_name '_' batch_letter '0' num2str(image) '.tif'];
else
        file_img = [file_path file_name '_' batch_letter num2str(image) '.tif'];
end;
```

A.2.8 main_process.m

```
%main_process.m

function [im_data,threshold_value,image_width,image_height] =
main_process(file_img,display_flag,bins,im_back)

%pre-process image
[im_data,image_width,image_height] = pre_process(file_img, display_flag);

[threshold_guess_value,background_level] = set_threshold_parameters(im_data,bins);

%       *****   SET THRESHOLD PARAMETERS HERE   *****
%find new threshold value
%set parameters for thresholding
%peaks found either side of the threshold_guess (set to a value between 0 and 1)
%       threshold_guess_value = 0.5;
%bins selected with any number of counts above background_level
%       background_level = 100;

%process_image
[im_data] =
process_image(im_data,im_back,bins,image_width,image_height,threshold_guess_value,backgroun
d_level,display_flag);

%       *****   SET THRESHOLD PARAMETERS HERE   *****
%find new threshold value
%set parameters for thresholding
%peaks found either side of the threshold_guess (set to a value between 0 and 1)
        threshold_guess_value = 0.5;
%bins selected with any number of counts above background_level
        background_level = 100;

[threshold_value,x_back,x_jet_min,x_jet_max,x_jet,counts] =
threshold(im_data,bins,threshold_guess_value,background_level);
```

A.2.9 set_threshold_parameters.m

```
%set_threshold_parameters.m

function [threshold_guess_value,min_level] = set_threshold_parameters(im_data,bins)

%generate a histogram
[counts,x] = imhist(im_data,bins);

%smooth the histogram by averaging
counts = medfilt1(counts,4);

%manually set the min_level
min_level = 100;

start_level = 300;
[auto_min_level] = set_min_level(counts,x,start_level,bins);
min_level = auto_min_level;

%set threshold guess to value half way to end of jet peak
for a = 1:bins
        if counts(a) > min_level
                jet_max = a;
        end
```

```
end

%define threshold guess
threshold_guess = floor(jet_max/2);
threshold_guess_value = threshold_guess/bins;

%  *****   manually reset threshold values to override automatic values   *****
%peaks found either side of the threshold_guess (set to a value between 0 and 1)
%       threshold_guess_value = 0.1;
%bins selected with any number of counts above min_level
%       min_level = 100;
```

A.2.10 set_min_level.m

```
%set_min_level.m

function [auto_min_level] = set_min_level(counts,x,start_level,bins)

step = 1;
level = start_level;
default_level = 100;
auto_min_level = [];

for a = 1:((bins-1)-step)
        if counts(a) > level & counts(a+step) < level
                for b = a:((bins-1)-step)
                        if counts(b) < level & counts(b+step) > level
                                        auto_min_level = level;
                        else
                                level = level - 1;
                        end
                end
        end
end

if isempty(auto_min_level) == 1
        auto_min_level = default_level;
end
```

A.2.11 process_image.m

```
%process_image.m

function [im_data] =
process_image(im_data,im_back,bins,image_width,image_height,threshold_guess_value,backgroun
d_level,display_flag)

%subtract background
if im_back == 0
        disp('*****No background image used*****')
        mess = ('Original Cropped');
else
        im_data = im_data - im_back;
        disp('*****Background image subtracted from data*****')
        mess = ('Background Subtracted');
end
if display_flag == 1
        display_doc(im_data,bins,mess)
        threshold_image(im_data,image_width,image_height,bins,threshold_guess_value,backgro
und_level);
end

%apply median low pass filter to remove noise
%[im_data] = img_filter(im_data,'gaussian');
%if display_flag == 1
%       display_doc(im_data,bins,'Low Pass Filtered')
```

```
%
        threshold_image(im_data,image_width,image_height,bins,threshold_guess_value,backgro
und_level);
%end

%normalise image
[im_data] =
intensity_norm(im_data,bins,image_width,image_height,threshold_guess_value,background_level
);
if display_flag == 1
        display_doc(im_data,bins,'Normalised')
        threshold_image(im_data,image_width,image_height,bins,threshold_guess_value,backgro
und_level);
end

%apply filter to image
%[im_data] = img_filter(im_data,'unsharp');
%if display_flag == 1
%       display_doc(im_data,bins,'Filtered')
%
        threshold_image(im_data,image_width,image_height,bins,threshold_guess_value,backgro
und_level);
%end
```

A.2.12 intensity_norm.m

```
%intensity_norm.m

function [im_norm] =
intensity_norm(im_data,bins,image_width,image_height,threshold_guess_value,background_level
);

%find maximum jet value
        [threshold_value,x_back,x_jet_min,x_jet_max,x_jet] =
threshold(im_data,bins,threshold_guess_value,background_level);
        jet_value = x_jet_max/bins;

if jet_value > 0
        %normalise image
        im_norm = im_data/jet_value;

        %check for values greater than one and set to zero
        [im_norm] = over_value_check(im_norm,image_width,image_height,1,1);

        disp('*****Image has been normalised*****')
else
        im_norm = im_data;
        disp('*****Image has not been normalised*****')
end
```

A.2.13 threshold.m

```
%threshold.m
%determines the threshold value from the image histogram
%uses the value midway between the two peaks

function [threshold_value,x_back,x_jet_min,x_jet_max,x_jet,counts] =
threshold(image_data,bins,threshold_guess_value,background_level)

%   ****   generates histogram for current image
[counts,x] = imhist(image_data,bins);
%smooth the histogram by averaging
counts = medfilt1(counts,4);

threshold_guess = round(threshold_guess_value*bins);

%   ****   initialise variables
peak_1 = 0; peak_2 = 0; y = 0;
```

```
x_back = 0;
x_jet = threshold_guess;
x_jet_min = 0; x_jet_max = 0;

%find the intensity level of the background peak
for a = 1:(threshold_guess-1)
        if counts(a) > peak_1
                peak_1 = counts(a);
                x_back = a;
        end
end

%   ****   find the intensity levels of the jet minima and maxima
for a = threshold_guess:bins
        if counts(a) > background_level
                if y == 0
                        x_jet_min = a;
                        y = 1;
                end
                x_jet_max = a;
        end
end

%   ****   find the intensity level of the jet peak (using curve)
[plot_curve,peak_pos] = curve_fitter(bins,counts,x,3);

%   ****   find the intensity level of the jet peak (using jet maxima and minima)
x_jet = x_jet_min + (x_jet_max - x_jet_min)/2;

%   ****   determine the threshold value for the image
% set threshold constant
% generally 0.5
threshold_constant = 0.5;
threshold_value = round(threshold_constant*(peak_pos - x_back)) + x_back;
```

A.2.14 curve_fitter.m

```
%curve_fitter.m

function [plot_curve,peak_pos] = curve_fitter(bins,counts,x,order_fit)

curve_fit = polyfit(x,counts,order_fit);

curve_derivative = polyder(curve_fit);

values = roots(curve_derivative);

peak_pos = 0;

for a = 1:(order_fit-1)
        if values(a) < bins & values(a) > peak_pos
                peak_pos = values(a);
        end
end

plot_curve = polyval(curve_fit,x);
```

A.2.15 over_value_check.m

```
%over_value_check.m

function [data] = over_value_check(data,columns,rows,value_check,new_value)

for a = 1:rows
        for b = 1:columns
                if data(a,b) > value_check
                        data(a,b) = new_value;
                end
        end
end
```

A.2.16 name_filexxx.m

```
%name_filexxx.m
%Generates a filename with the form img_000.bin

function [file_bin] = name_filexxx(file_path,x,l)

if x <= 9
        file_bin = [file_path 'proc_' l '00' num2str(x) '.bin'];
elseif (x >= 10 & x <= 99)
        file_bin = [file_path 'proc_' l '0' num2str(x) '.bin'];
else
        file_bin = [file_path 'proc_' l num2str(x) '.bin'];
end
```

A.2.17 threshold_shift_loop.m

```
%threshold_shift_loop.m

function
threshold_shift_loop(start,time_steps,layers,complete_threshold,max_threshold,bins,image_he
ight,image_width)
n = start;
file_path = [];

for t = 1:time_steps
        for l = 1:layers

                %check to see whether image has a zero threshold
                %set at 10 of 256 bins (≈ 0.04)
                if complete_threshold(t,l) > 10

                        %determine threshold shift required
                        threshold_shift = (max_threshold - complete_threshold(t,l))/bins;

                        if threshold_shift > 0
                                message = strcat('Image: ', int2str(n), ' intensity values to
be shifted by ',num2str(threshold_shift,4));
                                disp(message);

                                %re-opens image data
                                %generates file name
                                file_bin = name_filexxx(file_path, n, 'i');
                                message = strcat('Reading file: ', file_bin);
                                disp(message)

                                %reads a binary file in real*4 format
                                fid_r = fopen(file_bin,'r','l');
                                img_bin = fread(fid_r,[image_height image_width],'float32');
                                fclose(fid_r);

                                %add the threshold difference from image
                                img_bin = img_bin + threshold_shift;

                                %check data for intensity values greater than 1
                                [img_bin] =
over_value_check(img_bin,image_width,image_height,1,1);

                                %writes data back to binary file in real*4 format
                                fid_w = fopen(file_bin,'w','l');
                                fwrite(fid_w,img_bin,'float32');
                                fclose(fid_w);
                                message = strcat('Re-Writing file: ', file_bin);
                                disp(message)
                        else
                                message = strcat('Image: ', int2str(n), ' intensity values
were not shifted');
                                disp(message);
                        end
```

```
            else
                    message = strcat('Image: ', int2str(n), ' intensity values were not
shifted');
                    disp(message);
            end

            %increment image number
            n = n+1;
        end
end
```

A.2.18 volumetric_interpolation_loop.m

```
%volumetric_interpolation_loop.m

function
volumetric_interpolation_loop(image_width,image_height,layers,time_steps,start,plane_interv
al_mm,z_plane_precision)

%       due to memory considerations the interpolation is applies for four
%       image at a time (to allow the use of the cubic method).  The interpolated
%       data from the first two images is then stored and the grid moved

%interpolation methods:
%       'linear' for linear interpolation (default)
%       'cubic' for cubic interpolation
%       'nearest' for nearest neighbor interpolation
%best to use linear or cubic which provide smoother results

interpolation_method = 'cubic';
disp(strcat('Using interpolation method: ', interpolation_method))

no_interp_images = 1/z_plane_precision; % number of images generated for each plane

%generate grid for interpolation
disp('Generating interpolation grid')
[XI,YI,ZI] = meshgrid(1:image_height,1:image_width,1:z_plane_precision:4);
disp('Interpolation grid generated and stored')
fprintf('\n')

f = 1;  %image count for storing interpolation layers
file_path = [];

for t = 1:time_steps
        for l = start:(start+(layers-1)-3)
                %open four images to apply interpolation across
                c = 1;
                for n = l:l+3
                        %generates file name
                        file_bin = name_filexxx(file_path, n, 'i');
                        message = strcat('Reading file: ', file_bin);
                        disp(message)

                        %reads a binary file in real*4 format
                        fid_r = fopen(file_bin,'r','l');
                        img_bin = fread(fid_r,[image_height image_width],'float32');
                        fclose(fid_r);

                        %store image in 3D array
                        im_store(:,:,c) = img_bin';

                        %increment image number
                        c = c+1;
                end

                save td_store im_store
                clear im_store img_bin
                disp('Stored 3D array to file td_store.mat')
                fprintf('\n')

                load td_store

                disp('Interpolating data')
```

```
                im_interp = interp3(im_store,XI,YI,ZI,interpolation_method);
                disp('Image data has been interpolated')
                fprintf('\n')

                clear im_store

                %writes data back to binary file in real*4 format
                if n == (start + 3)
                        %save interpolated data between first two image slices
                        disp('Using first storage loop')
                        no_img_store = 2*no_interp_images;            %image 10 in the
interpolation array
                        disp(strcat('Storing image 1 to ', int2str(no_img_store)))
                        for h = 1:no_img_store                        %10 images
                                bin_store(f,im_interp(:,:,h))
                                f = f + 1;
                        end
                elseif  n == start + (layers-1)
                        %save interpolated data between last two image slices
                        disp('Using final storage loop')
                        no_img_store_start  = no_interp_images + 1;   %image 6 in the
interpolation array
                        no_img_store_finish = 3*no_interp_images + 1;         %image 16 in the
interpolation array
                        disp(strcat('Storing image ',  int2str(no_img_store_start), ' to ',
int2str(no_img_store_finish)))
                        for h = no_img_store_start:no_img_store_finish        %11 images
                                bin_store(f,im_interp(:,:,h))
                                f = f + 1;
                        end
                else
                        %(start + 3) < n < (start+(layers-1))
                        %save interpolated data between second and third image slices
                        disp('Using intermediate storage loop')
                        no_img_store_start  = no_interp_images + 1;   %image 6 in the
interpolation array
                        no_img_store_finish = 2*no_interp_images;     %image 10 in the
interpolation array
                        disp(strcat('Storing image ',  int2str(no_img_store_start), ' to ',
int2str(no_img_store_finish)))
                        for h = no_img_store_start:no_img_store_finish        %5 images
                                bin_store(f,im_interp(:,:,h))
                                f = f + 1;
                        end
                end

                fprintf('\n')
                clear im_interp
        end
end
```

A.2.19 bin_store.m

```
function bin_store(n,data)

file_path = [];
file_bin = name_filexxx(file_path, n, 'f');
fid_w = fopen(file_bin,'w','l');
fwrite(fid_w,data,'float32');
fclose(fid_w);
message = strcat('Writing file: ', file_bin);
disp(message)
```

A.2.20 display_doc.m

```
%display_doc.m
%generates images for inclusion in image processing document

function display_doc(image_data,bins,title_text)
```

```
%display image
title_text = [title_text ' Image'];
figure,imshow(image_data,[0 1]), title(title_text)

%diplay histogram
hist_text = ['Histogram of ' title_text];
[counts,x] = imhist(image_data,bins);
figure, imhist(image_data,bins), title(hist_text)

%***   GENERATES FIGURE 1   ***
figure, subplot(1,2,1), imshow(image_data,[0 1]), title(title_text)
        subplot(1,2,2), imhist(image_data,bins), title(hist_text)

%display parameters
[threshold_guess_value,min_level] = set_threshold_parameters(image_data,bins);

[threshold_value,x_back,x_jet_min,x_jet_max,x_jet] =
threshold(image_data,bins,threshold_guess_value,min_level);

mess=strcat('The threshold value found is ', num2str((threshold_value),4));
disp(mess)
mess = strcat('Background intensity level: ', num2str(x_back,4));
disp(mess)
mess = strcat('Jet minimum intensity level: ', num2str(x_jet_min,4));
disp(mess)
mess = strcat('Jet maximum intensity level: ', num2str(x_jet_max,4));
disp(mess)
mess = strcat('Jet intensity level: ', num2str(x_jet,4));
disp(mess)

counts = medfilt1(counts,4);
[plot_curve,peak_pos] = curve_fitter(bins,counts,x,3);

%***   GENERATES FIGURE 2   ***
figure, bar(counts)
hold on
        axis([1 bins 0 1000])
        title(hist_text)
        plot(x,plot_curve,'-')
        line([peak_pos peak_pos],[0 max(counts)], 'Color', 'red')
        line([x_back x_back],[0 max(counts)], 'Color', 'red')
        line([threshold_value threshold_value],[0 max(counts)], 'Color', 'black')
hold off

disp(strcat('Position of peak is: ', num2str(peak_pos,4)));


%***   GENERATES FIGURE 3   ***
figure, bar(counts)
hold on
        axis([1 bins 0 1000])
        title(hist_text)
        line([0 bins],[min_level min_level], 'Color', 'red')
        line([x_jet_max x_jet_max],[0 max(counts)], 'Color', 'green')
hold off

disp(strcat('Minimum pixel counts is: ', num2str(min_level,4)));

%figure, bar(counts)
%hold on
%       plot(x,plot_curve,'-')
%       line([peak_pos peak_pos],[0 max(counts)], 'Color', 'red')
%       grid on
%       axis([1 bins 0 1000])
%       title(hist_text)
%       line([0 bins],[min_level min_level], 'Color', 'red')
%       line([x_back x_back],[0 max(counts)], 'Color', 'red')
%       line([x_jet_min x_jet_min],[0 max(counts)], 'Color', 'green')
%       line([x_jet_max x_jet_max],[0 max(counts)], 'Color', 'green')
%       line([x_jet x_jet],[0 max(counts)], 'Color', 'green')
%       line([threshold_value threshold_value],[0 max(counts)], 'Color', 'black')
%hold off
```

A.2.21 threshold_image.m

```
%threshold_image.m
%generates a binary image, showing all of the pixels above a certain threshold value and
displays the resulting image

function
threshold_image(img_data,image_width,image_height,bins,threshold_guess_value,background_lev
el)

%determine the threshold value for the current image
[threshold_value,x_back,x_jet_min,x_jet_max,x_jet,counts] =
threshold(img_data,bins,threshold_guess_value,background_level);

%change all intensity levels above the threshold value to 1
[bin_thresh_img] =
over_value_check(img_data,image_width,image_height,(threshold_value/bins),1);

%display the resulting figure
figure, imshow(bin_thresh_img,[0 1]), title('Normalised Threshold Binary Image')
```

A.2.22 open_image.m

```
%open_image.m  Version 1.1b1  June 21, 2000  Written by Philip Cutler

clear all

clc
fprintf('**************************************************\n')
fprintf('****                                          ****\n')
fprintf('****           Open 16-bit TIFF Image         ****\n')
fprintf('****        Code written by Philip Cutler     ****\n')
fprintf('****               May/June 2000              ****\n')
fprintf('****                                          ****\n')
fprintf('**************************************************\n\n')

%determine the file path or the files
[file_not,file_path] = uigetfile('*.tif','Determine location of the image to open');

% Determine Filename
file_img = strcat(file_path, file_not);
message = strcat('Processing Image:',file_img);
disp(message)

[im_data,image_width,image_height] = pre_process(file_img, 1);

bins = 256;
[counts,x] = imhist(im_data,bins);

[threshold_guess_value, background_level, threshold_guess] =
set_threshold_parameters(im_data, bins);

%   *****   manually set threshold values to override automatic values   *****
%set parameters for thresholding
%peaks found either side of the threshold_guess (set to a value between 0 and 1)
%       threshold_guess_value = 0.5;
%bins selected with any number of counts above background_level
%       background_level = 100;

[threshold_value,x_back,x_jet_min,x_jet_max,x_jet] =
threshold(im_data,bins,threshold_guess_value,background_level);

mess = strcat('Background intensity level: ', num2str(x_back,4));
disp(mess)
mess = strcat('Jet minimum intensity level: ', num2str(x_jet_min,4));
disp(mess)
mess = strcat('Jet maximum intensity level: ', num2str(x_jet_max,4));
disp(mess)
mess = strcat('Jet intensity level: ', num2str(x_jet,4));
disp(mess)

figure, bar(counts)
axis([0 bins 0 max(counts)])
title('Histogram of Cropped Original Image')
```

```
line([0 bins],[background_level background_level])
line([threshold_guess threshold_guess],[0 max(counts)])
line([x_back x_back],[0 max(counts)], 'Color', 'red')
line([x_jet_min x_jet_min],[0 max(counts)], 'Color', 'green')
line([x_jet_max x_jet_max],[0 max(counts)], 'Color', 'green')
line([threshold_value threshold_value],[0 max(counts)], 'Color', 'black')
```

A.2.23 read_bin_image.m

```
%read_bin_img.m                Written by Philip Cutler
%Use to open and display a binary image in real*4 (float) format

%specify image size and file type
image_width = 295;
image_height = 285;

%determine the file path for the files
[file_name,file_path]=uigetfile('*.bin','Determine location of the image data');

%generates file name
file_img = [file_path file_name];
message = strcat('Reading file: ', file_img);
disp(message)

%reads a binary file in real*4 format
fid_r = fopen(file_img,'r','l');
img_bin = fread(fid_r,[image_width image_height],'float32');
fclose(fid_r);

%invert array
img_bin = img_bin';

%displays image
figure,imshow(img_bin,[0 1])

bins = 256;

[counts,x] = imhist(img_bin,bins);

%smooth the histogram by averaging
[new_counts] = smooth_histogram(counts,bins);
counts_medfilt = medfilt1(counts,4);

[auto_min_level,temp_bin] = set_min_level(new_counts,x,1500,bins);

figure, bar(counts)
axis([1 bins 0 3000])
title('Image Histogram')
hold on
line([0 bins],[auto_min_level auto_min_level], 'Color', 'red')
line([temp_bin temp_bin],[1 max(counts)], 'Color', 'red')
bar(counts_medfilt,0.5,'r')
hold off

figure, bar(new_counts)
axis([1 256 0 3000])
title('Averaged Histogram')
hold on
line([0 bins],[auto_min_level auto_min_level], 'Color', 'red')
line([temp_bin temp_bin],[1 max(new_counts)], 'Color', 'red')
hold off
```